Mathematical Modelling of Silicon Furnaces



Benjamin Matthew Sloman

St. Anne's College

University of Oxford

A thesis submitted for the degree of

Doctor of Philosophy

Trinity 2018

Acknowledgements

First of all, I would like to thank my supervisors Colin Please and Robert Van Gorder for their advice and encouragement throughout the DPhil. Having two excellent supervisors has made the world of difference.

This doctoral research has been supported by the EPSRC Centre for Doctoral Training in Industrially Focused Mathematical Modelling (EP/L015803/01). I extend thanks to Chris Breward, who along with Colin Please has directed the CDT, and to all those who have made InFoMM a success, including the late Chris Reddick. I have thoroughly enjoyed my time as a doctoral student, in large part due to the friendship of fellow students. Thanks to Ferran for being a top office-mate for three years, and to Caoimhe and Attila, who have put up with us for a year each. Thanks also to Niall, Rachel, Roxana, Helen, Fabian, Raquel, Ali, Jess, Andrew, and Ousman.

This work has also been financially supported by Elkem. I am thankful to Aasgeir Valderhaug and Rolf Birkeland at Elkem Technology, for all their scientific insights and drive to make the research practical. The pilot furnace experiments conducted by Harald Wegge have been crucial to the modelling and analysis in this thesis. I am grateful to Elkem for the opportunity for on-site work, and for the many conversations about my research with those at Elkem Fiskaa, especially Kjetil, Knut Åge, Lars, Antoine, and Fei. Interactions with NTNU, Teknova, and Cybernetica have also proved useful. I have been made to feel welcome during my visits to Norway, and I would especially like to thank Åslaug, Kjell Arne, Ådne, and Guro for their hospitality.

On a personal note, I am grateful for the love, support, and prayer of my parents Richard and Susan, brother Peter, father-in-law George, and brother-in-law James. Thanks to friends at St. Aldate's Church, and Worcester College and Mansfield Road football clubs, for helping to make this time in Oxford so enjoyable.

Finally, I express deep gratitude to my wife Alicia for her constant love, prayer, encouragement, patience, and friendship.

Abstract

Silicon is a widely utilised material, with use in the production of semiconductors, textiles, and metallic alloys. It is produced by feeding quartz rock and carbon into huge furnaces, which are heated by electrodes. In this thesis, we develop mathematical models to better understand furnace behaviour. Of particular interest is crust formation, a phenomenon whereby a blockage emerges, preventing the raw materials from falling naturally under gravity to the lower, hotter part of the furnace where the necessary chemical reactions occur.

We begin by developing a continuum model for the evolution of chemical concentrations, temperature, and gas flow in a vertical cross-section of the furnace. This model is analysed in the context of 'pilot furnace' experiments, which are smaller, cylindrical furnaces heated in laboratory conditions. Numerical simulations of our model are shown to compare well with these experiments. We further perform parameter sweeps of our model, to give recommendations for operating strategies.

Next, we undertake an asymptotic analysis of this model, to identify the dominant chemical and thermal behaviour within the pilot furnace. We determine chemical balances in different spatial and temporal regions by imposing a temperature profile. We also obtain a simplified thermo-chemical furnace model, which captures the main behaviour of our original model, but comprises only two partial differential equations.

We then present a model of crust formation, in which furnace crust is treated as a single fluid of thermally-dependent viscosity, located between two moving boundaries. Numerical simulations show that solutions of this model can either tend towards a steady state, indicative of crust formation in practice, or the raw materials can fall indefinitely. The latter case is desirable in real furnaces, although it may not always be feasible. We discuss bifurcations between these two behaviours in our model, and the significance of such bifurcations to avoiding the build-up of crust.

Finally, we focus on the reaction between solid carbon particles and silicon monoxide gas. This motivates us to develop a homogenised model for reactions between solid particles and gas, which has many possible applications. We comment on simplifications of this model for both diffusion-limited and chemically-limited reactions.

Statement of Originality

All of the work that is presented in this thesis has been carried out by the author. The experiments that are referred to throughout the thesis have been conducted by either Harald Wegge or Fei Li, whilst working at Elkem Technology, and are attributed accordingly. The pilot furnace model that is presented in Chapter 2 has been published in [87], and the asymptotic analysis of this model, presented in Chapter 3, has been published in [86]. The homogenised model for gas-solid reactions that is presented in Chapter 5 has been submitted for publication in [85], with the exception of Section 5.8.

Contents

1 Introduction **1**

1.1 The silicon process and silicon furnaces 1

1.1.1 Crust formation 1

1.1.2 Operational efficiency 3

1.2 Pilot furnace experiments 5

1.3 Current models of silicon furnaces 8

1.3.1 The stoichiometric model 8

1.3.2 The dynamic model 9

1.3.3 (Fe)SiMod 9

1.4 Thesis outline 10

2 One-Dimensional Model of a Silicon Pilot Furnace **12**

2.1 Introduction 12

2.2 Modelling 13

2.2.1 Species and reactions 13

2.2.2 Geometry and transport 14

2.2.3 Conservation of chemical species 14

2.2.4 No voids condition 16

2.2.5 Constant total pressure 16

2.2.6 Ideal gas mixture 17

2.2.7 Conservation of energy 17

2.2.8 Reaction kinetics 20

2.2.9 Equilibrium pressure functions 21

2.2.10 Boundary and initial conditions 23

2.2.11 Full dimensionless model 25

2.3 Behaviour of the pilot furnace 27

2.3.1 Numerical scheme 27

2.3.2 Model behaviour 28

2.4 Influence of model parameters on silicon production 30
2.5 Conclusions 35

3 Asymptotic Analysis of One-Dimensional Model of a Silicon Pilot Furnace 38
3.1 Introduction 38
3.2 Alternative non-dimensionalisation 40
3.3 Prescribed temperature asymptotics 43
3.3.1 Region IIa - early time cavity and crater 45
3.3.2 Region IIb - order one time crater and cavity 46
3.3.3 Region Ia - early time furnace charge 49
3.3.4 Region Ib - order one time furnace charge 50
3.4 Full model asymptotics 53
3.5 Special limits of the simplified model 57
3.5.1 Early time 57
3.5.2 Small diffusion limit 57
3.5.3 Small heating limit 64
3.6 Crust formation 65
3.7 Conclusions 67

4 Thermo-Mechanical Crust Model 69
4.1 Introduction 69
4.2 Model derivation 72
4.3 Tall, thin cylinder limit 78
4.3.1 Derivation of leading order system 80
4.3.2 Averaged velocity from inner region 83
4.3.3 Statement of model 85
4.4 Analysis of the tall, thin cylinder model 85
4.4.1 Numerical solution 86
4.4.2 Steady state solutions 90
4.4.3 Bifurcation diagrams 98
4.5 Special limits of the tall, thin model 100
4.5.1 Thin crust limits (cases A and B) 101
4.5.2 Order one crust thickness limits (cases C, D, E, and F) 105
4.5.3 Summary of special limits 108
4.6 Model extensions 108
4.6.1 Radiative flux 108

4.6.2 Chemical reactions . . . 110
4.6.3 Numerics of the full model . . . 111
4.7 Conclusions . . . 111

5 Homogenised Model for Gas-Solid Reactions 114
5.1 Introduction . . . 114
5.2 Shrinking core model . . . 116
5.2.1 Physical derivation . . . 116
5.2.2 Dimensionless model . . . 119
5.2.3 Quasi-steady limit . . . 120
5.3 Homogenisation of a granular particle . . . 121
5.4 Distinguished limits . . . 124
5.4.1 The $\boldsymbol{D_S/D_V = \delta^2\nu}$ limit . . . 125
5.4.2 The $\boldsymbol{D_S/D_V = \delta\nu}$ limit . . . 128
5.4.3 The $\boldsymbol{D_S/D_V = \nu}$ limit . . . 128
5.4.4 Other limits . . . 129
5.4.5 Summary . . . 129
5.5 Model behaviour . . . 129
5.5.1 Numerical simulations . . . 130
5.5.2 Asymptotics . . . 130
5.6 Influence of product gas . . . 141
5.7 Comparison to existing results . . . 144
5.7.1 Comparison with existing shrinking core models . . . 144
5.7.2 Physical results from our asymptotics . . . 146
5.7.3 Comparison with the law of additive reaction times . . . 147
5.7.4 Continuum models . . . 147
5.8 Coupling to a furnace model . . . 148
5.9 Conclusions . . . 152

6 Discussions 155
6.1 Summary of results . . . 155
6.2 Industrial applications . . . 157
6.2.1 Practical use of models . . . 158
6.2.2 Crust formation and the need for stoking . . . 159
6.2.3 Selection of carbon particles . . . 163
6.3 Future work . . . 166
6.3.1 Homogenised furnace model . . . 166

6.3.2 Distribution of particle sizes 167
6.3.3 Improved gas-solid reaction model 168
6.3.4 Crater behaviour 169
6.3.5 Two-dimensional model 169
6.3.6 Industrial scale furnace geometry and electrical effects 169
6.4 Outlook 170

A Further Comments about Species and Reactions **171**

B Asymptotic Expansions for Chapter 3 **174**
B.1 Prescribed temperature - Region IIa 174
B.2 Prescribed temperature - Region IIb 175
B.3 Prescribed temperature - Region Ia 177
B.4 Prescribed temperature - Region Ib 178
B.5 Simplified model asymptotics - small diffusion limit 178

Bibliography **180**

List of Figures

1.1 Schematic of the silicon process, reproduced from Schei, Tuset, and Tveit [82]. 2
1.2 Drawing of (ferro) silicon furnaces, by Thorsteinn Hannesson [40]. We have added anotations to highlight certain key features. 3
1.3 Four pilot furnace process simulators. The furnaces were initially filled up to the blue horizontal line with the same 99% pure quartz but different reducing agent, with increasing SiO reactivity from left to right. Furnace 1 has graphitised coke which has been pre-heated to at least 2500°C. Furnace 2 has graphitised coke and char, which has been heat treated to around 1000°C. Furnace 3 has char only, and furnace 4 has char and charcoal, that is woodchips which have gone through a pyrolsis process at 400-500°C. Furnace 1 has a normal level of carbon reactivity, furnace 2 has a lower level, and furnace 3 the lowest. Furnace 4 has the highest level of carbon reactivity. The grey regions labelled 'droplets of silicon' could also contain some slag (that is waste product containing impurities). Some black particles in the base contain a mixture of carbon and silicon carbide, others are just carbon. We acknowledge Harald Wegge for conducting the experiments and taking the photographs, whilst working at Elkem Technology. . 6
1.4 Photographs of three central slices of the bottom, centre, and top of furnace 1 previously shown in Figure 1.3. We acknowledge Harald Wegge for conducting the experiments and Anders Amundsen for taking the photographs, whilst both were working at Elkem Technology. 7

2.1 The red box in the left hand image shows a typical vertical section in the pilot furnace. The horizontal variations are smoothed out in the right hand image to illustrate the approximation of the furnace geometry with a one-dimensional model. 15

2.2 Schematic diagram of heating in experiment. A direct current runs through the copper tubes around the graphite crucible, which acts as a susceptor. The raw materials in the pilot furnace are heated from the walls and bottom of the graphite crucible by conduction, with any induction heating of furnace material negligible. Carbon felt is present as heat resistant insulation between the refractory and the hot walls of the graphite crucible. The carbon black is positioned to raise the crucible relative to the coils, so that there is less heating in the upper part of the crucible. There have been no indications that the inside of the graphite crucible has participated in the reactions. However, some oxidation of the upper outside region of the graphite crucible has been observed, though this is not relevant for our model. The original image is from Harald Wegge, whilst working at Elkem Technology. 19

2.3 On the top are equilibrium pressure functions (in solid lines) compared with read in data from the image on the bottom (in dashed lines). Temperature is in Celsius to allow for comparison, even though the equilibrium pressure functions are used with temperature in kelvin. On the bottom is the diagram of equilibrium SiO pressures reproduced from [82]. 24

2.4 Temperature profiles (left) and the total solid and liquid volume fraction θ_S (right) at ten minute intervals. 29

2.5 Comparison of numerical simulations and an experiment. The plot shows the volume fractions of each of the solid and liquid chemical species (left), with the height lined up with the experiment (right). The top of the green epoxy-filled region in the experiment (taking the place of the gas cavity) matches up with the kink in the blue and yellow curves, so we have captured the upper region (the charge), which is dominated by solid quartz and carbon. 30

2.6 Plots of numerical simulations of the solid and liquid concentrations (left), and the reaction rates (right). In rows from top to bottom: times $t = 40$ min, $t = 60$ min, and end time $t = 80$ min. 31

2.7 Output metrics (2.38), (2.39), and (2.40) against reactivity of carbon, for three different values of effective heating into the pilot furnace. . 34

2.8 Output metrics (2.38), (2.39), and (2.40) against the mixture ratio of C to SiO_2(s), for four different values of carbon reactivity. 35

2.9 Output metrics (2.38), (2.39), and (2.40) against the rate of the condensation reaction, R_2, for four different values of carbon reactivity. 36

3.1 Schematic diagram of asymptotic regimes. Hashed regions correspond to early time and solid regions to larger time. The blue region, where the temperature is below the melting point of quartz, corresponds to the furnace charge. The red region, where melting of quartz occurs, corresponds to the mixed cavity and crater region in the model. . . . 44

3.2 Dimensionless concentration of carbon, in blue, and solid quartz, in red, at height $z = 0.3$. We compare numerical solutions of the full system with $T(z)$ in solid lines to asymptotic solutions in dashed lines, with parameter values $\epsilon = 0.16$, $\delta = 3.2 \times 10^{-4}$, and $\alpha = 0.45$. 47

3.3 Comparison of early time, late time, and composite asymptotics, with numerics of the full system with prescribed temperature profile at height $z = 0.3$. On the left is the concentration of liquid quartz, and on the right is the gas flux (both dimensionless). Parameter values used are $\epsilon = 0.16$, $\delta = 3.2 \times 10^{-4}$, $\alpha = 0.45$, $\chi_1 = 0.15$, and $\chi_2 = 0.25$. . . 48

3.4 Comparison of numerical simulations and asymptotic solutions at $z = 0.9$. On the left are plots of the dimensionless concentration of carbon, showing numerics in blue and asympotics in red. On the right are plots of the dimensionless concentrations of SiC (in blue) and Si (in red), showing numerics in solid lines and asympotics in dashed lines. There is agreement to $\mathcal{O}(\epsilon)$ but noticeable $\mathcal{O}(\epsilon^2)$ disagreement, which would be reduced through addition of more terms in the ϵ expansion. Notice that the scale for the left plot is between 0.7 and 1, so there is an approximate 5% error for C_C, and the scale on the right plot is only up to 0.1, so the absolute error for C_{SiC} and C_{Si} is also small, since these are order one dimensionless variables. Parameter values used are $\epsilon = 0.16$, $\delta = 3.2 \times 10^{-4}$, $\chi_1 = 0.15$, and $\chi_2 = 0.25$. 52

3.5 Comparison of numerics of the full system (3.3) - (3.10) (with a constant heat capacity) in solid lines and numerics for the simplified system (3.56) - (3.58) in dotted lines. On the left are plots of temperature and on the rights are plots of $C_{SiO_{2(s)}}$ (both dimensional). Parameter values used are $\epsilon = 0.16$, $\delta = 3.2 \times 10^{-4}$, and $\alpha = 0.45$. 56

3.6 Comparison of the analytical solution (3.62) with numerical simulations. On the left is the dimensionless temperature for fixed height $z = 0.3$, while on the right are spatial profiles at different times, with the analytic solution in dotted lines and numerics in solid lines. . . . 58
3.7 Contour plots for dimensionless T (left) and C (right), in the cases $K = 0.01$ (top) and $K = 0$ (bottom), with $b = 0.3$ and $\omega = 0.15$ in all cases. 58
3.8 Schematic diagram of the different regions in the variable temperature problem. In Region A the temperature is too cold for the reaction to take place, whilst in Region B the chemical reacts. These regions are separated by the interface $z = s(t)$, given by the isotherm $T = 0$. . . 59
3.9 Numerical simulations of dimensionless T and C from the system (3.56) - (3.58), displayed for fixed height $z = 0.3$. Region A is to the left of the dashed line, Region B is between the dashed and the dot-dashed lines, and Region C is to the right of the dot-dashed line. The dashed line has label $z = s(t)$, because it is showing the time for which there is a transition between Regions A and B for the given height $z = 0.3$. The dot-dashed line is in a possible, illustrative location. Parameter values used are $K = 0.01$, $\omega = 0.15$, and $b = 0.3$. 60
3.10 Comparison of first order asymptotic solutions, shown in dotted lines, and numerical solutions of the simplified system (3.56) - (3.58), shown in solid lines, at height $z = 0.3$ for the dimensionless temperature, concentration, and time taken to reach the interface between Regions A and B. Parameter values used are $K = 0.01$, $\omega = 0.15$, and $b = 0.3$. 63
3.11 Comparison of asymptotic solutions, shown in dotted lines, and numerical solutions of the simplified system (3.56) - (3.58), shown in solid lines, for the dimensional temperature (left) and concentration (right). Since the smooth heating source was used, the simplified numerics are different to those in Figure 3.5, which use a Heaviside function. Parameter values used are $K = 0.01$, $\omega = 0.15$, and $b = 0.3$. 63

4.1 Image of pilot furnace experiments, with (left) and without (right) epoxy injected to take the place of the gas cavity. Note in the experiments the bottom region indicated 'fallen material' will contain some solids that started there. However, in industrial furnaces this will be comprised almost entirely of fallen material. We acknowledge Harald Wegge for conducting the experiments and taking the photographs, whilst working at Elkem Technology. 70
4.2 A schematic diagram of the two-dimensional geometry, with moving interfaces at $z = a(r, t)$ and $z = b(r, t)$. 73
4.3 Schematic diagram of the inner region near $z = a_0(t)$. In this image the correction term is drawn below the leading order interface, i.e., $a_I < 0$. 83
4.4 Schematic diagram of the tall thin model. The viscous region is in hashed blue and the granular region is in hashed red. 86
4.5 Plots showing the evolution of temperature over time. On the left are plots of $T(x, \tau)$ in the fixed domain. On the right are plots of $T(z, t)$ in the original domain. Curves of the same colour are at the same time. Parameter values used are $St = 1$, $Pe = 1$, $\lambda = 0.1$, $T_b = 0.5$, and $\gamma = 20$. A spatial step size of $\Delta x = 4 \times 10^{-3}$ and timestep of $\Delta\tau = 10^{-4}$ are used. 89
4.6 Plot showing $a(\tau)$ in solid lines and $b(\tau)$ in dashed lines for varying T_b. Other parameter values used are $St = 0.1$, $Pe = 1$, $\lambda = 0.1$, and $\gamma = 30$. A spatial step size of $\Delta x = 4\times10^{-3}$ and timestep of $\Delta\tau = 10^{-4}$ are used. 90
4.7 Plot showing $a(\tau)$ in solid lines and $b(\tau)$ in dashed lines for varying Pe. Other parameter values used are $St = 0.1$, $\lambda = 0.1$, $\gamma = 20$, and $T_b = 0.1$. A spatial step size of $\Delta x = 4 \times 10^{-3}$ and timestep of $\Delta\tau = 10^{-4}$ are used. 91
4.8 Plot showing $a(\tau)$ for varying Pe. Other parameter values used are $St = 0.1$, $\lambda = 0$, $\gamma = 20$, and $T_b = 0$. A spatial step size of $\Delta x = 4 \times 10^{-3}$ and timestep of $\Delta\tau = 10^{-4}$ are used. Note the purple curve for $Pe = 2$ does not tend to a steady state, but decreases to $z = -\infty$. 91

4.9 Trajectories from ten randomly selected initial positions for $a(t)$ in solid and $b(t)$ in corresponding dashed lines. The initial positions were selected randomly from independent Uniform $[-2, 1]$ distributions. Parameter values used are $\gamma = 30$, $St = 0.1$, $Pe = 0.1$, $\lambda = 0.1$, and $T_b = 0.2$. A spatial step size of $\Delta x = 4 \times 10^{-3}$ and timestep of $\Delta\tau = 10^{-4}$ are used. 92
4.10 Contour plots of roots of (4.129) for ϑ, given a value of λ and T_b, for $Pe = 1$, $St = 2$, and $\gamma = 30$. The multiple roots for $\lambda = 1$ and $T_b = 0.8$ are circled. 95
4.11 Plot showing the evolution of trajectories from a stable steady state (solid) and unstable steady state (dashed) for $a(t)$ (red) and $b(t)$ (blue). Parameter values used are $Pe = 1$, $St = 2$, $\gamma = 30$, $T_b = 0.8$, and $\lambda = 1$. A spatial step size of $\Delta x = 4 \times 10^{-3}$ and a timestep of $\Delta\tau = 10^{-6}$ are used. 96
4.12 Plots of the value of the steady state a^*, comparing Pe and St, for fixed $\gamma = 8$, $\lambda = 0$, and $T_b = 0$. 98
4.13 Plots showing the interface between where the solutions tend to steady states a^* and b^* and where it undergoes free fall, with $\gamma = 8$ in both cases. Plots were generated in Mathematica by letting $\vartheta = 1+10^{-6}$. In the left panel, we vary λ, with values shown $\lambda = 10^{-6}, 0.1, 0.2, 0.3, 0.4, 0.5$, and $T_b = 0$. In the right panel, we vary T_b, with values shown $T_b = 10^{-1}, 10^{-2}, 10^{-3}, 10^{-4}, 0$, and $\lambda = 0.1$. 99
4.14 Plots showing the interface between where the solutions tend to steady states a^* and b^* and where it undergoes free fall, with $St = 1$ in both cases. Plots were generated in Mathematica by letting $\vartheta = 1 + 10^{-6}$. In the left panel we vary γ, with values shown $\gamma = 10, 20, 30, 40, 50$, and $\lambda = 0.1$. In the right panel we vary λ, with values shown $\lambda = 10^{-6}, 1, 2, 3, 4, 5$, and $\gamma = 30$. 100

5.1 Schematic diagram of the shrinking core model, showing the fixed outside radius $r = R_p$ and the moving internal radius $r = l(t)$ of a spherical shell. 117
5.2 Schematic diagram of the problem geometry, with macroscale in the left wedge and microscale in the right square. Note that this is a two-dimensional plane-view of the cubic packing, whereas the problem we are concerned with is three-dimensional. 122

5.3 Numerical simulations of (5.63) - (5.66), with $\lambda = 0$, for p (left) and b (right). From top to bottom, we tkae $\kappa = 0.01$, $\kappa = 10$, and $\kappa = 1000$. Note how the timescale is different for each choice of κ. 131
5.4 Extent of reaction against time. In the left plot, κ is varied, with $\lambda = 0$ fixed. In the right plot, λ is varied, with $\kappa = 10$ fixed. 132
5.5 Numerical simulations of (5.63) - (5.66), for p (left) and b (right). From top to bottom parameter values used are $\kappa = 1$ and $\lambda = 1$, $\kappa = 10$ and $\lambda = 1$, and $\kappa = 100$ and $\lambda = 20$. Note how the timescale is different in the bottom row. 133
5.6 Comparison of numerics (solid) and asymptotics (dashed) for the extent of the reaction $X(t)$, with $\lambda = 3$. Even for $\kappa = 10$, the small κ asymptotics give a decent agreement with numerics. 135
5.7 Numerical plots of $F(\eta; \lambda)$, for varying λ. 138
5.8 Comparison of numerics and asymptotics for $s(t)$ (red) and $X(t)$ (black) for $\kappa = 10^4$ and $\lambda = 0$. 140
5.9 Comparison of asymptotics and numerics for time for complete reaction t^* for varying κ, with $\lambda = 0$ in blue and $\lambda = 10$ in red. The plot is on a logarithmic scale. Note how the combined asymptotic result $t^* = 1 + \lambda/6 + \kappa/18$ matches well with the numerics for both values of λ. 141
5.10 Plot of concentration of carbon at $z = 0.3$ (left) and $z = 0.7$ (right). Solid lines are shown of different values of $\hat{\beta}$ in (5.162), with the dashed line found using our original reaction rate, given in (5.150). Note that the vertical axes are different in each case. 151

6.1 Comparison of an Arrhenius and exponential fit for data from Tang and Tangstad [99]. We have read in the data and plotted $\ln(\eta)$ in units of Pa s, rather than Poise. 160
6.2 Bifurcation plot for Pe/γ against λ, for curves of constant T_b, increasing in intervals of 0.1 from 0 to 0.9. Above and to the left of the curves, steady states are possible, while below and to the right of curves the system is in free fall. Plots were generated in Mathematica by letting $\vartheta = 1 + 10^{-6}$. The left circle is the value for $\lambda = 0$ and $T_b = 0$, corresponding to $Pe/\gamma = 1$. The right circle is the value for $\lambda = 10.4$ and $T_b = 0.4$, corresponding to $Pe/\gamma = 7.40$. 161

6.3 Illustration of a possible explanation for the change in furnace behaviour with added iron content. 163
6.4 Image of a partially reacted carbon cylinder, which has been sliced along its central axis and folded outwards, so that up and down correspond to radial distances. The inner core of unreacted carbon and the outer shell of silicon carbide can be seen. The presence of silicon carbide next to a crack suggests that the cracks were not caused by the reaction. Instead, it is likely that cracks formed to allow moisture and volatiles to escape in the initial heating. We acknowledge Fei Li for conducting the experiment and taking the photograph, whilst working at Elkem Technology. 164
6.5 Image of a partially reacted carbon particle, which is about 10 mm in diameter. The black region contains a mixture of carbon and some silicon carbide crystals, so is a transition region, despite the colour. We acknowledge Fei Li for conducting the experiment and taking the photograph, whilst working at Elkem Technology. 165
6.6 Schematic diagram of a log-log plot demonstrating how the reaction completion time varies with the particle radius. 166

Chapter 1

Introduction

1.1 The silicon process and silicon furnaces

Silicon (Si) is found in high quantities in the earth's crust, second in abundance only to oxygen as an element [82]. It naturally occurs in quartz and quartzite (both as silicon dioxide) and other rock, from which it can be extracted. Elkem ASA is one of several global companies which extract silicon and sell it to a range of industries. Customers use Elkem's silicon for semiconductors in solar panels and computers, for silicone in kitchenware and textiles, and for use in other metallic alloys. To produce silicon, a submerged-arc furnace [82, 103, 104] is continually fed with carbon (C) and quartz (SiO_2) [39, 48, 64, 82], as shown in Figure 1.1. Liquid silicon is tapped out of the taphole at the base of the furnace [39, 47, 48, 82] and undergoes further processes to produce silicon with the desired purity and size distribution for the customers' needs [6, 5, 12]. The hot off-gases that rise through the furnace are cooled, extracted, and filtered. A typical medium-sized furnace has a height of $2.2 - 3.5$ m, a diameter of $5 - 12$ m, and operates at $15 - 45$ MW. A drawing of a silicon furnace is given in Figure 1.2. Silicon is also commonly produced with iron content as ferrosilicon. However, throughout our research, we will only be interested in pure silicon and the associated furnace dynamics in the pure silicon process.

1.1.1 Crust formation

Conventionally raw materials are added in a homogenised batch at roughly $10 - 15$ minute intervals. Ideally they should be added to balance the average rate at which material is consumed. However, in practice a solid and viscous liquid crust region builds up, forming a ceiling-like structure above a gaseous region where no solids or liquids are present, known as the gas cavity. This crust is comprised of a mixture

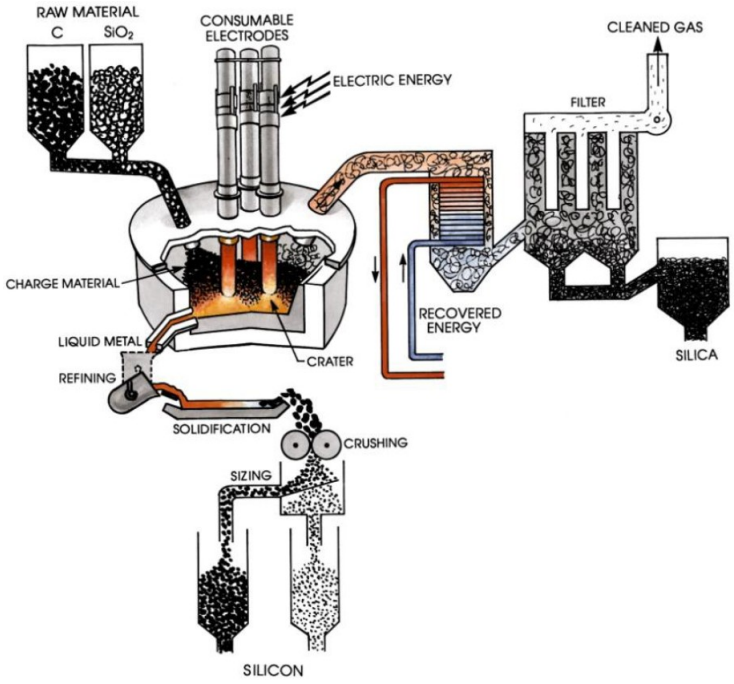


Figure 1.1: Schematic of the silicon process, reproduced from Schei, Tuset, and Tveit [82].

of carbon, molten quartz, silicon carbide, and condensated material. The presence of the crust slows the motion of solids and liquids to the lower part of the furnace, restricting their access to the heat required to facilitate the necessary reactions. The bulk region in the furnace where the solids and viscous liquid are present is known as the furnace charge [82]. Material at the lower interface of the charge can melt and fall to the bottom of the furnace, through the gas cavity; alternatively, this material may react to form gas. The crust thus rises in the furnace, with the charge replenished by additional material deposited on the top. Since the products from the lower part of the crust are tapped out of the furnace base or convected away as gas, this rising crust corresponds to a volumetric increase in the gas cavity. Some of this gas may escape out of the taphole during routine tapping, but it is also possible for the crust to be so thick that high volumes of gas rapidly escape, in a disastrous situation known as 'blowing' or 'gassing' [46, 82]. In order to counter the crust build-up, operators 'stoke' the furnace, where the crust is manually broken up by a bar from a 'stoking car' on an hourly basis. Research into silicon furnaces is thus important in order to better understand, and subsequently control, this crust formation. In particular, an improved understanding of crust formation is crucial if Elkem are to achieve the long-term aim of removing the need for stoking.

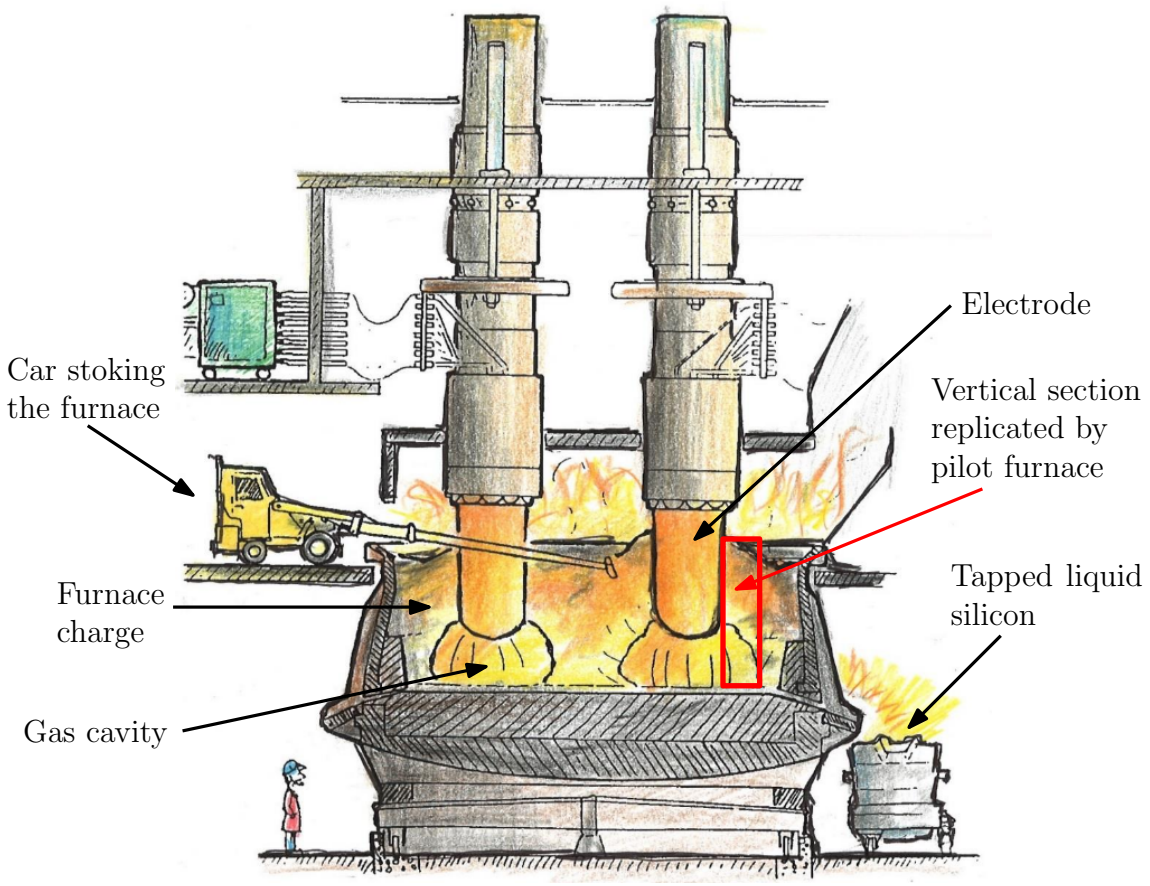


Figure 1.2: Drawing of (ferro) silicon furnaces, by Thorsteinn Hannesson [40]. We have added anotations to highlight certain key features.

1.1.2 Operational efficiency

Operating silicon furnaces is a highly complex process, requiring the balancing of chemical and electrical effects. The main inputs that can be controlled are the types of carbon and quartz used as raw materials, the molar ratio of carbon to quartz in the feeding mixture, and the height of the electrodes relative to the base of the furnace (the electrodes can be raised or lowered). These inputs must be tweaked in order to maintain safe working conditions and keep a high level of silicon production. The silicon monoxide (SiO) gas convects out of the top of the furnace where it combusts in air to form microsilica. This microsilica can be filtered from the gas, as it is a common material used to strengthen concrete [82]. Depending on demand, it can sometimes be favourable to operate the furnace to obtain a high quantity or quality of microsilica production, and not to maximise the silicon yield.

The source of carbon is typically in the form of coal, charcoal, or petroleum coke. These materials have different levels of carbon content, with volatiles present which

will evaporate when the particles are added to the furnace. Of particular importance is how well these particles react with silicon monoxide, since this reaction is a crucial mechanism for retaining silicon atoms in the process. The strength of this reaction is influenced by the porosity and size of the particles, since larger particles have a smaller relative surface area for the reaction with the gas. However, if carbon particles are too small then they will be advected out of the furnace with the gas stream. The term 'reactivity' and phrase 'SiO reactivity' are commonly used to quantify and compare the rate of this reaction between different carbon materials [53, 82]. Woodchips are often used to change the permeability of the upper furnace, even though they contribute little carbon to the process [53]. As quartz heats up, it transitions to cristobalite, which has the same chemical composition but different crystal structure [2, 16, 77, 82], and can undergo cracking. The thermal and cracking properties of the quartz rock varies from source to source, but the influence of different types of quartz on furnace behaviour is not as well understood as that of carbon sources. Mechanical properties are also considered in raw material selection, since a steady downwards flow of material is desired.

Operators seek to balance the molar ratio of carbon to quartz input into the furnace, in order to achieve an overall, idealised, reaction of

$$\mathrm{SiO_2} + 2\mathrm{C} \rightarrow \mathrm{Si} + 2\mathrm{CO}. \tag{1.1}$$

If too much carbon is present, then there will be a build-up of silicon carbide, which, if left unreacted, will decrease the size of the active region in the furnace. However, if too little carbon is added, then not all the quartz will be reduced.

The furnace is heated by arcs from the three electrodes into the craters, which are liquid pools at the base of the furnace. The length of each arc, and hence the current through the arc and resulting power into the furnace, can be controlled by slipping the electrode up and down. The voltage can also be controlled [82]. The thermal energy put into the furnace will influence the chemical reaction rates, and thus the productivity of the furnace. The electrodes are consumed at their lower tips, and so are a further source of carbon for the reduction of quartz. These electrodes can sometimes crack and break, causing highly costly and potentially dangerous interruptions. A thorough study into electrical conditions in furnace operation was undertaken by Valderhaug in [103]. In particular, the electrical properties of the carbon particles are considered when selecting raw materials. Although the carbon used is an electrical insulator at room temperature, it can become conductive as it is heated and cracks develop, potentially causing an undesired electric current along the crust at the base

of the charge. The electrical resistivity will be influenced by the particle size, since a granular material composed of smaller particles will have more contacts between particles, as explained by Valderhaug [103].

Understanding the fundamental relationships between physical and chemical effects is necessary to improve furnace operation, through better use of process inputs, and will also provide vital guidance for the construction of future furnaces.

1.2 Pilot furnace experiments

Taking measurements in a silicon furnace is extremely difficult due to the high temperatures involved. The cost of lost production prohibits experiments on industrial scale furnaces, although excavations are possible on the rare occasions that operation has been stopped for safety reasons. Thus, to gain insight into the furnace environment, Elkem have carried out experiments on 'Pilot Furnace Process Simulators.' In this thesis these will be referred to as pilot furnaces, to avoid confusion with computational simulations of process models. These pilot furnaces are cylinders of inner height 43 cm and inner diameter 13 cm which are filled with raw material and heated from room temperature by an induction furnace. Standard production quartz is used, but different carbon materials are used as the reducing agent. Once the furnaces have cooled down at the end of the experiment, epoxy is injected so that the material stays in the final state when they are cut open. In particular, the gas cavity is filled, so that the charge material will not fall down after the experiment has finished. Photographs of the results are shown in Figure 1.3. Similar experiments are described by Tangstad et al. [100].

Considerable variability is seen between the four furnaces. For example, the upper charge layer is thinnest for the most reactive carbon, which is found in furnace 4. However, some general properties are shared by the furnaces. The gas cavity, preserved by the green epoxy in the centre, is similar in size for each furnace. The brown arch shape corresponds to condensate from SiO gas to liquid Si and SiO_2, with the shape of the arch likely corresponding to an isotherm in the furnace. The induction furnace provided a spatially constant heat flux up to a level just above the gas cavity, and is discussed more in Chapter 2.

In furnace 1 a high density of quartz particles at the top of the furnace can be seen, which have undergone little melting or reaction with other materials. Further down the furnace these particles are fewer in number and slightly smaller in size, suggesting a zone of melting and reaction. At the furnace base (crater), there are

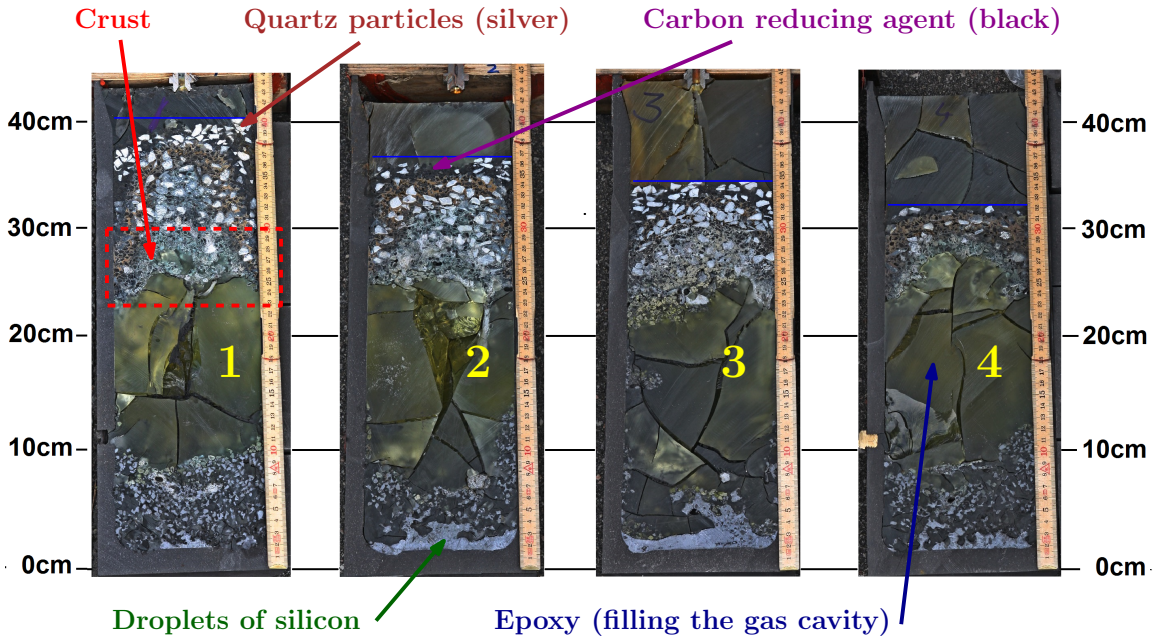
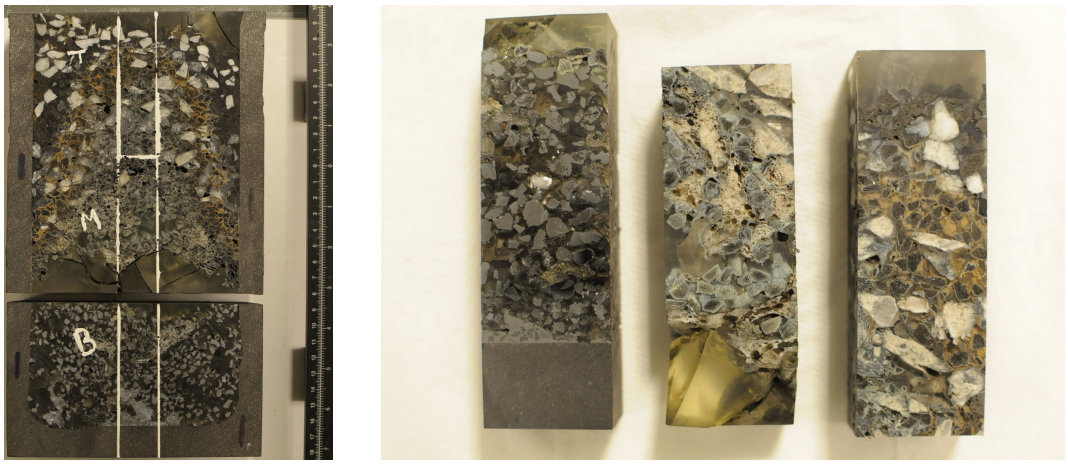


Figure 1.3: Four pilot furnace process simulators. The furnaces were initially filled up to the blue horizontal line with the same 99% pure quartz but different reducing agent, with increasing SiO reactivity from left to right. Furnace 1 has graphitised coke which has been pre-heated to at least 2500°C. Furnace 2 has graphitised coke and char, which has been heat treated to around 1000°C. Furnace 3 has char only, and furnace 4 has char and charcoal, that is woodchips which have gone through a pyrolsis process at 400-500°C. Furnace 1 has a normal level of carbon reactivity, furnace 2 has a lower level, and furnace 3 the lowest. Furnace 4 has the highest level of carbon reactivity. The grey regions labelled 'droplets of silicon' could also contain some slag (that is waste product containing impurities). Some black particles in the base contain a mixture of carbon and silicon carbide, others are just carbon. We acknowledge Harald Wegge for conducting the experiments and taking the photographs, whilst working at Elkem Technology.



(a) Furnace 1, with epoxy cavity removed.

(b) Slices from the bottom, centre, and top of furnace 1.

Figure 1.4: Photographs of three central slices of the bottom, centre, and top of furnace 1 previously shown in Figure 1.3. We acknowledge Harald Wegge for conducting the experiments and Anders Amundsen for taking the photographs, whilst both were working at Elkem Technology.

light grey silicon particles suspended in a pool of other materials. This situation is undesirable in industrial furnaces, where operators seek to tap out liquid silicon into a ladle, before undergoing solidification and other post-processing occurs. The liquid pool of silicon in furnaces 2 and 3 would therefore be preferred. Note, however, that since there is no tapping from the base of pilot furnaces, or electric arcs mixing the crater, these experiments do not replicate behaviour of the craters in industrial furnaces as well as they replicate behaviour in the charge.

In Figure 1.4 we show photographs of slices taken from the bottom, centre, and top of furnace 1. In the bottom sample we can see light grey particles suspended in a black liquid. In the central sample there is a coating on the dark particles close to the base of the charge, and in the middle white liquid quartz can be seen, contrasting with the solid particles further up. In the top sample, an orange/light-brown layer exists where the condensation of SiO to liquid Si and SiO_2 has taken place.

The majority of the modelling and analysis conducted in this thesis will relate to these pilot furnace experiments. Not only does this allow for validation and comparison of our models with real experimental results, which would be difficult to do with industrial furnaces, but also the geometry is simpler. The spatial effects are at most two-dimensional, and can be represented simply by circularly symmetric cylindrical co-ordinates. Accurately recreating the geometry of an industrial furnace, which has cavities and craters interacting around three electrodes, is a difficult task. In addition,

electrical effects do not have to be considered in pilot furnaces. Instead, we are able to focus on the interaction between chemical, material transport, mechanical, and thermal effects (simplified without ohmic heating). Many of the results discussed will be transferable to industrial furnaces, due to similarity of the environments, although caution is needed, due to the differences involved. Hence, ours is a suitable approach to better understand furnace behaviour in a qualitative sense.

1.3 Current models of silicon furnaces

Several models of silicon furnaces have been obtained in the literature, under various assumptions and modelling approaches. These models have been created to aid furnace operators, and are used both as training tools and to allow operators to simulate the result of different operating conditions, particularly the influence of carbon content on silicon yield. The stoichiometric model is a steady state, lumped parameter calculation, whilst the dynamic model and SiMod capture the temporal nature of silicon production, but are focussed on changes over the timescale of days, or even weeks. These models are briefly discussed below, but differ from the approach taken in this thesis, which is to examine in detail the chemical, thermal, and mechanical interactions in the pilot furnace over a shorter, hour-long timescale, in order to provide new understanding into furnace behaviour.

In addition to these models, valuable background material on the chemical species present in the silicon furnace is given in [2], and the relevant kinetics are discussed in [109]. Myrhaug et al. [64] give details about the reactions between carbon materials and silicon monoxide. Lund [57] applies these existing furnace models to improve process operations, and the energy balances in the silicon furnace are considered in [49, 98].

1.3.1 The stoichiometric model

Developed by Schei and Larsen [81], and discussed in [80, 82], the stoichiometric model captures the main reactions between furnace materials, calculating arithmetic balances between these species to determine how much of each material is found in an inner, hotter zone at the furnace base and an outer, colder zone at the furnace top. Different reactions occur in each zone. The model uses lumped parameters, which represent a range of physical parameters, and considers the steady state, but not how the furnace moves to this condition as it does not include time dependence. The (molar) amounts of raw materials, as well as the fraction of carbon available

for reaction, are input into the model, with the resulting amounts of each chemical species output.

1.3.2 The dynamic model

The dynamic model, developed by Halvorsen et al. [39], is an improvement on the stoichiometric model. The model considers spatial and temporal variations in a vertical region next to an electrode. Thus, instead of calculating a steady state in an inner and an outer zone, the model discretises the furnace height into several spatial zones, with an additional region for the crater. Reactions take place in each zone and material and enthalpy transfers between zones at each timestep. Convection of gases upwards and liquids downwards is assumed to be sufficiently fast that a quasi-steady limit is imposed, meaning that time derivatives in conservation equations are neglected. Instead, there are constant material fluxes between zones. One temperature is used for all material, with a thermal source at the crater due to the electrode and conduction between zones. The model can capture a continuous feeding of raw materials at the top of the furnace, or a stoking cycle, whereby the size of the crater increases until the charge material is stoked downwards.

1.3.3 (Fe)SiMod

The dynamic model is a basis for SiMod - 'a Silicon Furnace Process Model' [106]. This software was developed by Stein Wasbø and Andreas Hammervold at Cybernetica, based on previous simulators created in cooperation with Elkem researchers, and is used by furnace operators and scientists at Elkem. As with the dynamic model, material is transferred between, and reactions take place within, spatial zones representing height in the furnace. Although the number of zones can be input by the user, in practice around ten are typically used, with the size of each zone varying throughout each simulation. At each timestep solid (and liquid) materials flow into the zone below, in proportion to the concentration in the zone being exited. To represent the dripping of material from the base of the charge through the gas cavity, a user-determined 'hang-factor' regulates how much material leaves the bottom shaft zone and falls into the crater. Raw material is added to the top of the furnace semi-continuously and silicon is tapped from the crater. Stoking can also occur, with the load applied to the furnace from the stoking car replicated by transferring further material from the lowest charge zone down to the crater. The rates of charging, tapping, and stoking can all be input by the user before running a simulation. In

addition to the temperature of the solids and liquids in each zone, there is also a separate gas temperature, but this has no influence on reaction rates. At the top zone there is heat loss from radiation and convection, and in the middle zones conduction and convection effects are included. No electrical effects are included, apart from a thermal energy source in the crater. In 2017, SiMod was extended to FeSiMod, which includes reactions present in ferrosilicon furnaces.

Kinetic parameters used in both the dynamic model [39] and SiMod [106] are not found experimentally, but rather are chosen in order to produce sensible results that compare well with observations in industrial furnaces. Both models use existing knowledge of the silicon process and are used by Elkem for training purposes, allowing employees to see the impact of certain furnace operating conditions.

1.4 Thesis outline

In this thesis, we seek to understand the role of chemical, thermal, transport, and mechanical effects inside silicon furnaces. We are particularly interested in understanding the mechanisms behind crust formation, and improving furnace operation through controlling the raw materials and power input to the furnaces. Our models and subsequent analysis are focussed on the pilot furnace experiments, where electrical effects do not need to be considered and the geometry is simplified.

In Chapter 2 we develop a one-dimensional model, with our spatial variable representing height in the pilot furnace. This model builds upon many of the ideas used in the dynamic model and SiMod, but has the advantage of being a continuum model. Further, we do not impose a gas velocity, but allow this to be solved as part of the model. We are interested in thermal and chemical interactions, and so simplify the mechanical effects found physically. Numerical simulations are conducted, which show a rising interface at the base of the charge, with motion caused by heating of the pilot furnace. The influence of changing model inputs on certain proposed output metrics is also discussed.

In Chapter 3 we perform an asymptotic analysis of the one-dimensional model proposed in Chapter 2, in order to determine the dominant chemical and thermal behaviour of the system. We exploit the fact that the timescale for melting quartz is slow compared to that of quartz reacting with carbon, and that the timescale for gas convection is fast compared to all chemical timescales. First, by prescribing a steady state temperature profile in the furnace, we explore the leading order reactions in different spatial regions, as well as early time behaviour. Then, utilising the dominant

balances found when the temperature is prescribed, we next reduce the full model to two coupled partial differential equations for the time-variable temperature profile within the furnace and the concentration of solid quartz. These equations account for diffusion, an endothermic reaction, and the external heating input to the system, and highlight the key energy balance between the heating and the carbon-quartz reaction.

In Chapter 4 we present a thermo-mechanical model of crust formation, in which we model the crust as a viscous fluid with temperature-dependent viscosity, and the granular upper charge as a region of hydrostatic pressure. A radiative heat source causes material to be eaten away from the lower interface of the crust, and we assume that the charge is continually replenished, so that the top is maintained at a constant height. We use a cylindrical geometry, and take a tall, thin limit to obtain a radially averaged system. Numerical simulations demonstrate that this system either evolves in time to a steady state or the charge keeps falling. We present bifurcation diagrams to classify behaviour in parameter space, and consider some further simplifications upon taking relevant parameter limits. We then highlight ways in which our approach could be extended.

The reaction between gaseous silicon monoxide and solid carbon particles is believed to have an important influence on both the silicon yield and crust formation. Such gas-solid reactions are commonly modelled using a shrinking core framework, where a sharp interface in each particle between an inner unreacted core and an outer product shell moves inwards until the reaction is complete. In Chapter 5 we develop a homogenised model which captures interactions between microscale granular and macroscale particulate effects, and allows a diffuse reaction front. The resulting model is analysed in the asymptotic limits that the reaction time is rate-limited by chemical kinetics, and separately by diffusion. We comment on the new insights this model brings to the selection of carbon materials as reduction agents in the silicon production process.

Finally, in Chapter 6, we summarise the main results from the thesis, comment on the industrial applications, and suggest recommendations for future work.

Throughout this thesis, we have chosen notation such that there is consistency within in each chapter. However, due to a shortage of Latin and Greek letters, there are occasions where the same symbol represents different variables. For example, ϵ is used for different small dimensionless parameters in Chapters 3, 4, and 5. Each time we define a new variable we have tried to present its meaning clearly, and so hope such inevitable clashes will not cause confusion for the reader.

Chapter 2

One-Dimensional Model of a Silicon Pilot Furnace

2.1 Introduction

We begin the mathematical research in this thesis by developing a one-dimensional model of a silicon pilot furnace. Our model accounts for the relevant chemistry, heat flow, and material transfer processes occurring within such a furnace. We take a continuum modelling approach, resulting in a system of partial differential equations which depend upon time and height in the furnace. Numerical simulations of the model solutions are shown to agree with results from pilot furnace experiments, and may better inform future experimental or theoretical work involving more complicated chemical reactions or more involved geometries. We take parameter sweeps of the model, and in particular find that more reactive carbon reduces the silicon monoxide losses, and that reducing the carbon content in the raw material mixture causes more solid and liquid material to build-up in the charge region, which is indicative of crust formation. Since we have little *a priori* understanding of which effects will dominate furnace behaviour, our model is quite complex. Later, in Chapter 3, we will simplify the model using asymptotic analysis.

This chapter is organised as follows. In Section 2.2, we derive a heat and mass transfer model for the silicon pilot furnace. In Section 2.3, we perform numerical simulations in order to understand the model behaviour. Then, in Section 2.4, we use these simulations to ascertain the influence of certain controllable parameters on the silicon production process. Finally, concluding remarks are given in Section 2.5. The work presented in this chapter has been published in [87].

2.2 Modelling

In this section we develop a mathematical model which can be used to examine behaviour in a silicon pilot furnace. We start by indicating which chemical species and reactions we will consider and what geometry we will use. We then formulate the framework of our model, by considering conservation of chemical species and energy, and closing the system through the constitutive relations that there are no voids, that the gas is ideal, and that the total gas pressure is constant. We then obtain the full dimensionless model.

2.2.1 Species and reactions

We are interested in modelling the dynamics of the following chemical species which are found in a silicon furnace: C(s) - carbon; SiC(s) - silicon carbide; SiO_2(s) - silica (solid quartz or quartzite); SiO_2(l) - liquid 'sticky' silica; Si(l) - liquid silicon; CO(g) - carbon monoxide; and SiO(g) - silicon monoxide. Here the parenthetical notation (s) denotes a solid, (l) a liquid, and (g) a gas. Other compounds (such as the impurities Al, Ca and their oxides [82], and Ti) can be found in small quantities in industrial furnaces and may contribute to the dynamics, but are not believed to be important in the pilot furnace experiments.

The most important reactions in the furnace are (see [2, 109]):

$$\mathrm{SiO(g)} + 2\mathrm{C(s)} \xrightarrow{R_1} \mathrm{SiC(s)} + \mathrm{CO(g)}, \tag{2.1}$$

$$2\mathrm{SiO(g)} \underset{R_{-2}}{\overset{R_2}{\rightleftharpoons}} \mathrm{SiO_2(l)} + \mathrm{Si(l)}, \tag{2.2}$$

$$\mathrm{SiO_2(s)} \xrightarrow{R_3} \mathrm{SiO_2(l)}, \tag{2.3}$$

$$\mathrm{SiO(g)} + \mathrm{SiC(s)} \xrightarrow{R_4} 2\mathrm{Si(l)} + \mathrm{CO(g)}, \tag{2.4}$$

$$\mathrm{SiO_2(l)} + \mathrm{C(s)} \xrightarrow{R_5} \mathrm{SiO(g)} + \mathrm{CO(g)}. \tag{2.5}$$

We treat the chemical species as existing in one of either a joint solid and liquid bulk phase or a gas phase. We will measure chemical compositions as concentrations, using the notation C_X for the concentration of species X [mol/m^3]. This is an effective concentration, since C_{Si} measures the number of moles of Si per unit volume of the mixture of all species in the furnace. A more detailed discussion on the choice of species and reactions modelled is given in Appendix A.

2.2.2 Geometry and transport

For simplicity, we model a one-dimensional vertical section in the furnace. Although some multi-dimensional effects are visible, such as the arched isotherms in the pilot furnace (see Figures 1.3 and 2.1) and the bridging of the crust away from the electrodes in industrial furnaces, the dominant structure is uni-dimensional. We are interested in where and how the crust occurs and this can be captured by considering height in the furnace as the spatial independent variable. Letting z denote furnace height, we take the base at $z = 0$ and the top at $z = h$, as illustrated in Figure 2.1. We allow for there to be a mixture of charge material and gas throughout the furnace, so that we do not capture the interfaces between the gas cavity and the furnace charge, or the crater and the gas cavity. We refer to the joint cavity and crater region as the base of the furnace. Since we estimate the Péclet number to be $Pe \sim 10^3$, diffusion of the chemicals is neglected, meaning that transport of chemical species is assumed to be entirely due to advection of the gas phase and the solid and liquid bulk phase. It is assumed that both gases, CO and SiO, move with the same velocity $\mathbf{v}_g = U_g\mathbf{k}$ and solid and liquid components move at constant velocity $\mathbf{v}_s = -U_s\mathbf{k}$, where $\mathbf{k}$ is a unit vector in the positive $z-$direction. Note that these are the actual velocities of the gas and of the solid and liquid matrix, and not superficial velocities.

In practice the solid materials are irregular particles, with a typical characteristic length scale of the quartz used being $40 - 100$ mm. The size of carbon depends on the material used, with coke being $3 - 12$ mm in size, but charcoal and briquettes can be up to 100 mm in length. Liquid quartz is highly viscous, unlike silicon which can flow freely. Thus granular effects are present, and the interactions between solids, viscous and inviscid liquids, and gases are highly complex. The variable motion of the charge is considered in the context of a crust model in Chapter 4, but for this one-dimensional model a constant bulk motion of solids and liquids, along with a variable motion of gases, is sufficient.

2.2.3 Conservation of chemical species

We define the effective mass density of species X to be π_{X} [kg/m^3], which measures the mass of the species in 1 m^3 of the total mixture of all species. We define the mass density ρ_{X} [kg/m^3] to be the mass of species X in 1 m^3 of that species alone. We assume that the mass density of solid and liquid species is constant, but that the mass density of the two gases can vary. For each species the mass density and the effective mass density can be related through a volume fraction θ_{X} (dimensionless), by

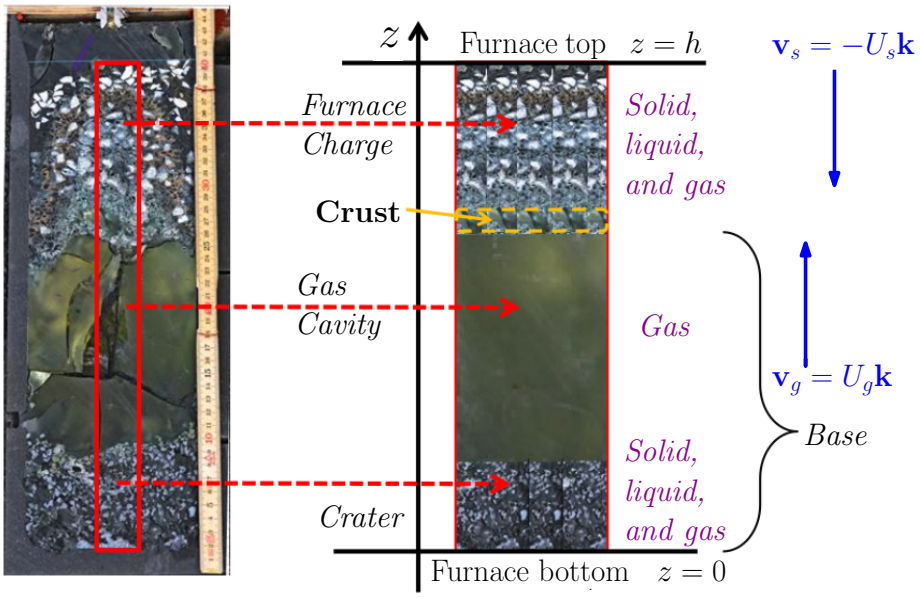


Figure 2.1: The red box in the left hand image shows a typical vertical section in the pilot furnace. The horizontal variations are smoothed out in the right hand image to illustrate the approximation of the furnace geometry with a one-dimensional model.

$\pi_{\mathrm{X}} = \rho_{\mathrm{X}}\theta_{\mathrm{X}}$. We note that for species X the effective mass density π_{X} [kg/m^3], molar mass M_{X} [kg/mol], and concentration $\mathrm{C_X}$ [mol/m^3] are related through $\pi_{\mathrm{X}} = M_{\mathrm{X}}\mathrm{C_X}$. Hence we have the relation

$$\rho_{\mathrm{X}}\theta_{\mathrm{X}} = M_{\mathrm{X}}\mathrm{C_X}. \tag{2.6}$$

We consider the conservation of carbon, given by

$$\frac{\partial \mathrm{C_C}}{\partial t} + \frac{\partial\left(-U_s \mathrm{C_C}\right)}{\partial z} = -2R_1 - R_5, \tag{2.7}$$

where R_1 and R_5 (both mol/m^{3}s) denote the degradation of carbon in the reactions (2.1) and (2.5), respectively. The same process can be implemented to obtain PDEs

for the other chemical species, and we thus obtain the following system of equations:

$$\frac{\partial \mathrm{C_C}}{\partial t} - \frac{\partial\left(U_s \mathrm{C_C}\right)}{\partial z} = -2R_1 - R_5, \tag{2.8}$$

$$\frac{\partial \mathrm{C_{SiC}}}{\partial t} - \frac{\partial\left(U_s \mathrm{C_{SiC}}\right)}{\partial z} = R_1 - R_4, \tag{2.9}$$

$$\frac{\partial \mathrm{C_{SiO_2(s)}}}{\partial t} - \frac{\partial\left(U_s \mathrm{C_{SiO_2(s)}}\right)}{\partial z} = -R_3, \tag{2.10}$$

$$\frac{\partial \mathrm{C_{SiO_2(l)}}}{\partial t} - \frac{\partial\left(U_s \mathrm{C_{SiO_2(l)}}\right)}{\partial z} = R_2 - R_{-2} + R_3 - R_5, \tag{2.11}$$

$$\frac{\partial \mathrm{C_{Si}}}{\partial t} - \frac{\partial\left(U_s \mathrm{C_{Si}}\right)}{\partial z} = R_2 - R_{-2} + 2R_4, \tag{2.12}$$

$$\frac{\partial \mathrm{C_{CO}}}{\partial t} + \frac{\partial\left(U_g \mathrm{C_{CO}}\right)}{\partial z} = R_1 + R_4 + R_5, \tag{2.13}$$

$$\frac{\partial \mathrm{C_{SiO}}}{\partial t} + \frac{\partial\left(U_g \mathrm{C_{SiO}}\right)}{\partial z} = -R_1 - 2R_2 + 2R_{-2} - R_4 + R_5. \tag{2.14}$$

2.2.4 No voids condition

For each solid and liquid species i, there is an associated volume fraction θ_i. There is only one volume fraction to describe the gas, θ_g, which will be comprised of a perfect mixture of CO and SiO wherever both of these exist. If only one gas is present then the gas volume fraction is comprised entirely of that gas. We make the assumption that there are no voids in the furnace, but that any arbitrary volume is filled with a combination of C, SiO_2(s), SiO_2(l), SiC, Si, and the gaseous CO and SiO. Thus, in terms of our volume fractions, we have that

$$\theta_g + \sum_i \theta_i = 1. \tag{2.15}$$

2.2.5 Constant total pressure

The total gas pressure in industrial furnaces has been observed to vary up to around 4 kPa [46] above atmospheric pressure (101 kPa). For simplicity we will follow the approach used in the dynamic model of Halvorsen et al. [39] by assuming that the total pressure is constant. This constant, called P_{TOT}, is set to 1 bar. Since a pipe allows gas to escape from the top of the pilot furnace, and the distance through which gas has to travel in the packed bed is small, this is a reasonable approximation.

This assumption can be seen as taking Darcy's law in the limit of high permeability and low viscosity, which is reasonable for a gas convecting through granular material in a furnace. Imposing constant total pressure and a no voids conditions means that gas moves in order to equilibrate pressure. If gas is produced through reactions in one

part of the furnace, then it will move away from that region to keep the total pressure steady. Thus the gas velocity is not explicitly stated, but is determined implicitly as part of the model.

2.2.6 Ideal gas mixture

We model the gas as being ideal, relating the gas pressure P_{TOT}, concentration C_g, volume fraction θ_g, gas constant $R_g = 8.314$ J/molK, and temperature T [K] through the equation

$$P_{\mathrm{TOT}} = \mathrm{C}_g R_g T/\theta_g. \tag{2.16}$$

The gas comprises of a mixture of CO and SiO, so that the total gas concentration can be found as

$$\mathrm{C_g} = \mathrm{C_{CO}} + \mathrm{C_{SiO}}. \tag{2.17}$$

Similarly, the total gas pressure is comprised solely of CO and SiO partial pressures, so that

$$P_{\mathrm{TOT}} = P_{\mathrm{CO}} + P_{\mathrm{SiO}}. \tag{2.18}$$

Gaskell [32] outlines Dalton's law of partial pressures, from which we can infer that

$$\frac{P_{\mathrm{CO}}}{P_{\mathrm{TOT}}} = \frac{\mathrm{C_{CO}}}{\mathrm{C}_g} \quad \text{and} \quad \frac{P_{\mathrm{SiO}}}{P_{\mathrm{TOT}}} = \frac{\mathrm{C_{SiO}}}{\mathrm{C}_g}. \tag{2.19}$$

We can then re-write the no voids condition (2.15) in terms of concentrations, temperature, and pressure, obtaining

$$\frac{R_g T}{P_{\mathrm{TOT}}} \left(\mathrm{C_{CO}} + \mathrm{C_{SiO}}\right) + \sum_{\text{solids and liquids } i} \mathrm{C}_i \frac{M_i}{\rho_i} = 1. \tag{2.20}$$

2.2.7 Conservation of energy

We now consider how the temperature is determined. In our model we use one temperature $T(z,t)$, which corresponds to an assumption of instantaneous heat transfer between the gas, the solid and liquid, and the graphite crucible. The temperature is influenced by heat from reactions, convection of the material in the furnace, conductive and radiative heat fluxes within the material, conduction in the graphite crucible, and external heat sources. We utilise the equation

$$\begin{aligned} &\frac{\partial}{\partial t}\left(T\left(A_f(\sigma_s+\sigma_g)+A_{gr}\sigma_{gr}\right)\right)+\frac{\partial}{\partial z}\left(TA_f\left(-U_s\sigma_s+U_g\sigma_g\right)\right) \\ &\quad=\frac{\partial}{\partial z}\left(\left(A_f k_f+A_{gr}k_{gr}\right)\frac{\partial T}{\partial z}+A_f\beta T^3\frac{\partial T}{\partial z}\right)+A_f H+\left(A_f+A_{gr}\right)F, \end{aligned} \tag{2.21}$$

which arises from considering conservation of energy. Equation (2.21) was derived following the approach of Byrne and Norbury [14] used in their model for a catalytic converter, and here we will explain the meaning of each term. For each chemical species X, we let $C_{p,\mathrm{X}}^{kg}$ be the mass specific heat [J/kgK] at constant pressure. We can relate this to the molar specific heat, $C_{p,\mathrm{X}}$ [J/molK], through the relation $C_{p,\mathrm{X}}^{kg} = C_{p,\mathrm{X}}/M_{\mathrm{X}}$. The effective heat capacity of the solid and liquid per total unit volume is given by $\sigma_s := \sum_i \rho_i \theta_i C_{p,i}^{kg}$. Although the density and specific heat of solids and liquids is assumed to be constant, σ_s is not constant, since the volume fractions vary. We similarly sum over the two gases to define $\sigma_g := \theta_g \sum_l \rho_l C_{p,l}^{kg}$, which is likewise not constant. We can write the effective heat capacities in the solid and liquid, and in the gas, respectively, as

$$\sigma_s = \sum_{\text{solids and liquids } i} \rho_i \theta_i C_{p,i}^{kg} = \sum_{\text{solids and liquids } i} \mathrm{C}_i C_{p,i}, \tag{2.22a}$$

$$\sigma_g = \theta_g \sum_{\text{gases } l} \rho_l C_{p,l}^{kg} = \sum_{\text{gases } l} \mathrm{C}_l C_{p,l}. \tag{2.22b}$$

Heat conducts through contact points between solid particles in the furnace and radiates across the gaseous voids between the particles. Thus, the diffusive heat transfer will vary with each chemical species and the size and packing arrangement of solid particles. However, we do not incorporate such complexity in our model. Instead, the terms k_f and k_{gr} are the effective thermal conductivity of the material inside the pilot furnace and graphite crucible respectively, and β is a radiative constant in the furnace associated with radiation between particles. A_f and A_{gr} are the cross-sectional areas of the furnace and the graphite crucible respectively.

The rate of heat release to the furnace due to reaction j is denoted dH_j. Typically the notation ΔH is used in the literature to denote change in enthalpy, with $\Delta H > 0$ for an endothermic reaction, where heat is required, and $\Delta H < 0$ for an exothermic reaction, where heat is produced (for example, see [45]). However, we are interested in the change in temperature in the local surrounding region caused by the reaction, and so have $dH_j < 0$ for endothermic reactions, and $dH_j > 0$ for exothermic reactions. $H(z,t)$, the overall heat source due to the chemical reactions, is given by $H := \sum_j dH_j R_j$.

The term $F(z,t)$ denotes the external heat source going into the furnace. In the experiment the pilot furnace starts from room temperature and is heated up to furnace temperatures by an induction heater. As can be seen in Figure 2.2, the bottom part of the furnace is surrounded and heated by copper coils, up to a height h_T, with the

top left exposed. We take $h_T = 0.234$ m from experimental data. We neglect heating into the base of the graphite crucible.

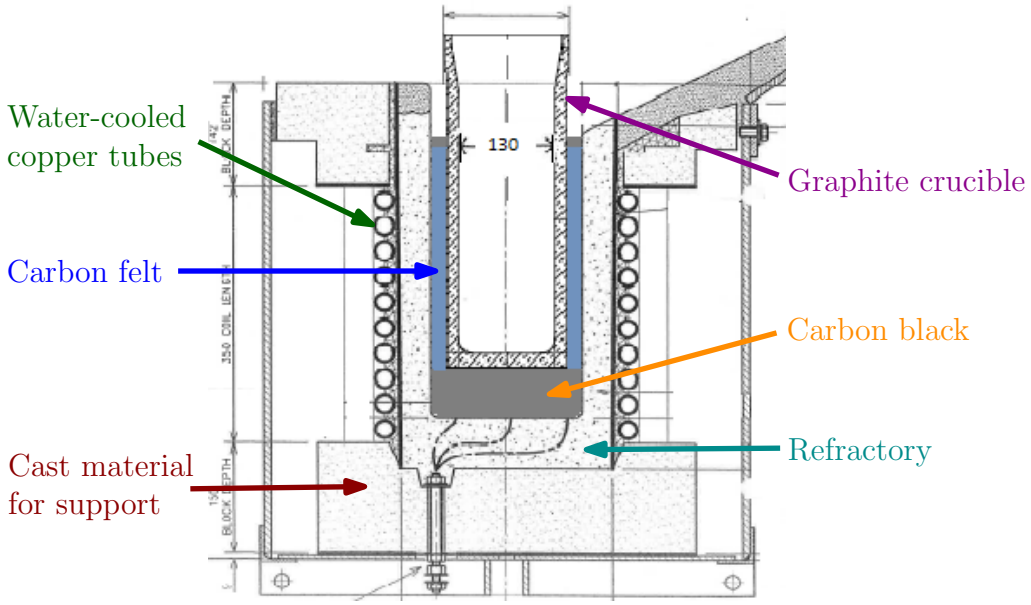


Figure 2.2: Schematic diagram of heating in experiment. A direct current runs through the copper tubes around the graphite crucible, which acts as a susceptor. The raw materials in the pilot furnace are heated from the walls and bottom of the graphite crucible by conduction, with any induction heating of furnace material negligible. Carbon felt is present as heat resistant insulation between the refractory and the hot walls of the graphite crucible. The carbon black is positioned to raise the crucible relative to the coils, so that there is less heating in the upper part of the crucible. There have been no indications that the inside of the graphite crucible has participated in the reactions. However, some oxidation of the upper outside region of the graphite crucible has been observed, though this is not relevant for our model. The original image is from Harald Wegge, whilst working at Elkem Technology.

For simplicity we assume a constant power going into the pilot furnace up to a height $z = h_T$, so that $F = Q\mathcal{H}(h_T - z)$, where Q is a scalar and the Heaviside function $\mathcal{H}(h_T - z)$ takes the value one for $z \leq h_T$ and the value zero for $z > h_T$. However, a different functional form of $F(z)$ could readily be used, and in particular in Sections 3.5.2 and 3.5.3 of the next chapter, our asymptotic solutions require an invertible $F(z)$. We let the effective power dissipated from the induction furnace into the pilot furnace be $\mathcal{P}$ [W]. Since Q is defined per unit volume, then we have $Q = \mathcal{P}/V_H$, where $V_H = h_T(A_f + A_{gr})$ is the heated volume of the pilot furnace.

In the model we have allowed convection, reaction heat release, and radiation to only act in the furnace, but allow all other forms of heat transfer to act in both the furnace and the graphite.

2.2.8 Reaction kinetics

The reaction rates R_j are dependent upon the local environment in the furnace, including chemical concentrations, partial pressures, and temperature. The functional dependence of the rate of each reaction was chosen after taking ideas from relevant literature [2, 39, 109] and the simulator SiMod [106]. Wiik [109] discusses many factors that can influence kinetic rates, including the crystal structure, level of impurities, porosity, and grain size of both the quartz and the carbon used. However, we adopt the ethos of Halvorsen et al. [39], utilising simplified kinetic rates that sufficiently capture furnace behaviour. In practice, the kinetic rates in silicon furnaces are not well known, due to the difficulty of measurements at high temperature conditions. For example, it is difficult to measure precisely how the rate of reaction R_2 varies with temperature and partial pressure, since it only occurs at high temperature. Thus using rates that have been calibrated to furnace data in previous models is the best that can be done at this stage. Once experimentally determined data has been found for more sophisticated rates, these can be included without detriment to the continuum model developed in this chapter.

The kinetic rates used are given in Table 2.1. The reaction constants k_j have units chosen to ensure that the overall reaction rate has units mol/m^{3}s. We use concentrations to model solid and liquid reactants and a partial pressure difference from equilibrium, $P_{\mathrm{SiO}} - P_{\mathrm{SiO,equ,j}}(T)$, for the gas reactants. Here $(f)^+$ denotes the positive part of the function f, so that $(f)^+ = \max\{f, 0\}$. The calculations to determine the equilibrium partial pressure functions are outlined in Section 2.2.9. Where appropriate, an Arrhenius term e^{-E_j/R_gT} is used, which is dependent on the activation energy E_j, gas constant $R = 8.314$ J/molK, and temperature T. This is a commonly used empirical relationship to model how the rate of a chemical reaction depends upon temperature. The activation energy acts as a barrier to the reaction; the lower the activation energy, the faster the reaction will be.

In reaction R_1, SiO gas reacts with solid carbon on the surface of particles, forming solid SiC and CO gas. Since the carbon is fed into the furnace as a raw material in the form of coal, coke or otherwise [64], some reaction models incorporate the particle size and reactivity of the carbon particles. We define this reactivity, $\mathrm{r_C}$, as the fraction of carbon that is available for reaction at each height and time in the furnace. One approach found in the literature to determine reactivity is to use a shrinking core model, described by [63, 64, 82, 97], where a spherical carbon particle reacts from the outside, with SiC product forming around a decreasing core until all of the original particle has reacted. Thus the reactivity changes with height, since carbon particles

Reaction	**Kinetic Rate**
R_1	$k_1 \mathrm{r_C} \mathrm{C_C} \left(P_{\mathrm{SiO}} - P_{\mathrm{SiO,equ},1}(T) \right)^+$
R_2	$k_2 e^{-E_2/R_g T} \left(P_{\mathrm{SiO}} - P_{\mathrm{SiO,equ},2}(T) \right)^+$
R_{-2}	$k_{-2} e^{-E_{-2}/R_g T} \mathrm{C}_{\mathrm{SiO_2(l)}} \mathrm{C_{Si}}$
R_3	$k_3 \mathrm{C}_{\mathrm{SiO_2(s)}} (T - T_M)^+$
R_4	$k_4 e^{-E_4/R_g T} \mathrm{C_{SiC}} \left(P_{\mathrm{SiO}} - P_{\mathrm{SiO,equ},4}(T) \right)^+$
R_5	$k_5 e^{-E_5/R_g T} \mathrm{C}_{\mathrm{SiO_2(l)}} \mathrm{C_C}$

Table 2.1: Kinetic rates used for each reaction.

move down the furnace as they react. Andresen [2] adds further complexity by having a square dependence on carbon reactivity, arguing that the reaction takes place in the porous volume of the carbon particles. In Chapter 5 we develop a homogenised model for gas-solid reactions that incorporates porosity. However, for simplicity in this model we will treat the reactivity of carbon, $\mathrm{r_C}$, as a constant which takes a value between zero and one. A similar approach is taken in the stoichiometric model described in [80, 82], where a reactivity number, describing the fraction of carbon that will react in the upper part of the furnace, is chosen to be a constant. This approach still allows observation of the influence of more or less reactive materials on furnace dynamics.

The reaction R_3 represents the change of state of quartz, from a solid to a sticky liquid. We assume that solid quartz is unreactive with other substances, but that once it has melted it may subsequently react with silicon and carbon. Alternatively, one could model SiO_2 as having solely one state. We have assumed that no SiO_2(l) solidifies back to SiO_2(s), and that SiO_2(s) only melts at temperatures higher than the melting point $T_M = 1996$ K (1723°C) [2]. We model the rate of melting, R_3, to be increasing with temperature and the concentration of solid quartz.

2.2.9 Equilibrium pressure functions

To calculate the equilibrium functions $P_{\mathrm{SiO,equ,j}}(T)$, we relate the change in Gibbs free energy of a reaction, ΔG_R [J/mol], and the equilibrium constant, K_{equ}, through the

reaction isotherm

$$\ln(K_{\text{equ}}) = -\frac{\Delta G_R}{R_g T}, \tag{2.23}$$

as discussed in [32]. The chemical reaction constant, K_{equ}, is given as a ratio of the activity of products k_+ to reactants k_-, that is, $K_{\text{equ}} = \frac{k_+}{k_-}$. Using the common assumption that the activity of gases is given by their partial pressures and that the activity of solids and liquids is unitary [2, 39, 82, 109], for reaction R_1 we have that K_{equ} is given by the relation

$$K_{\text{equ}} = \frac{1 \cdot P_{\text{CO}}}{P_{\text{SiO}} \cdot 1^2} = \frac{P_{\text{CO}}}{P_{\text{SiO}}}. \tag{2.24}$$

We can utilise the relation $P_{\text{CO}} = P_{\text{TOT}} - P_{\text{SiO}}$ and (2.23) to find

$$P_{\text{SiO,equ,1}} = \frac{P_{\text{TOT}}}{1 + \exp(-\frac{\Delta G_{R1}}{R_g T})}. \tag{2.25}$$

Similarly, for reactions R_2 and R_4, we obtain

$$P_{\text{SiO,equ,2}} = P_{\text{TOT}} \min\left\{1, \exp\left(\frac{\Delta G_{R2}}{2R_g T}\right)\right\} \tag{2.26}$$

and

$$P_{\text{SiO,equ,4}} = \frac{P_{\text{TOT}}}{1 + \exp(-\frac{\Delta G_{R4}}{R_g T})}, \tag{2.27}$$

respectively. All that is left is to relate the change in Gibbs free energy, ΔG_{Rj}, to temperature for each reaction. The simplest means of doing this, as outlined by Gaskell [32], is to data fit for the constants a_j, b_j, and d_j in

$$\Delta G_{Rj}(T) = a_j + b_j T \ln T + d_j T. \tag{2.28}$$

Using values from [69] we find these constants, which are listed in Table 2.2. We shall use these values throughout the remainder of this chapter. In Figure 2.3 we show that (2.25), (2.26), and (2.27) using data from Table 2.2 compare well with the diagram of equilibrium SiO pressures found in [82]. Note this thermodynamic diagram represents where different condensed phases, that is solids and liquids, will be present for a given temperature and partial pressure of SiO, if the furnace were to be in equilibrium. The regions have one condensed phase present, the lines have two condensed phases, and at intersections between lines three condensed phases can co-exist. The dashed lines indicate a region where the gas in unstable (and hence reactive). However, silicon furnaces are rarely in equilibrium, and so all condensed

phases could exist in practice in any region, depending on material transfer and how fast reactions occur. We follow the approach of Halvorsen et al. [39] and SiMod [106], to use partial pressure difference from equilibrium curves as driving mechanisms in reactions which have SiO as a reactant.

j	a_j	b_j	d_j
1	-8.183×10^4	-1.687	1.528×10
2	-8.178×10^5	-9.903×10	1.141×10^3
4	-9.901×10^4	-1.264×10^2	1.019×10^3

Table 2.2: Table of parameter values for equilibrium partial pressure functions, calculated using data from [69].

2.2.10 Boundary and initial conditions

The model comprises the seven equations (2.8) - (2.14) with reaction rates described in Section 2.2.8, in addition to the no voids condition (2.20) and the temperature equation (2.21), for the nine variables C_C, C_{SiC}, $C_{SiO_2(s)}$, $C_{SiO_2(l)}$, C_{Si}, C_{CO}, C_{SiO}, U_g, and T. We also have the algebraic relationships (2.19) to relate the gas partial pressures to concentrations. We take the constant velocity U_s to be zero in our model analysis as material is not fed in from the top of the pilot furnace. We take kinetic rates k_j from SiMod [106]. These were calibrated to industrial furnace data under the assumption that there is little variation in the Arrhenius term e^{-E_j/R_gT} over the temperature range present in the furnace. We follow this approach here, so that the Arrhenius terms are not included from here on. In addition, we have the reactivity of carbon, r_C, as discussed in Section 2.2.8, as a free parameter which we can vary in our model.

To determine what boundary and initial conditions are needed for the system, we consider the characteristics of the system with direction $\frac{dz}{dt} = \lambda_c$ in the $(z,t)-$plane. An explanation of how to find these is given in [67]. We find that there are characteristics with directions given by $\lambda_c = -U_s$, $\lambda_c = U_g$, and $\lambda_c = \infty$.

The direction $\lambda_c = -U_s$ has multiplicity five, corresponding to equations (2.8) - (2.12) for the evolution of the solid and liquid concentrations. Since we take $U_s = 0$, this gives $\lambda_c = 0$ and hence $z =$ constant. Thus, we need initial conditions for each of the solid and liquid concentrations, which we take from experimental data. In the majority of the pilot furnace there is carbon and solid quartz at the start of the experiment. However, solid quartz and silicon carbide were placed in the

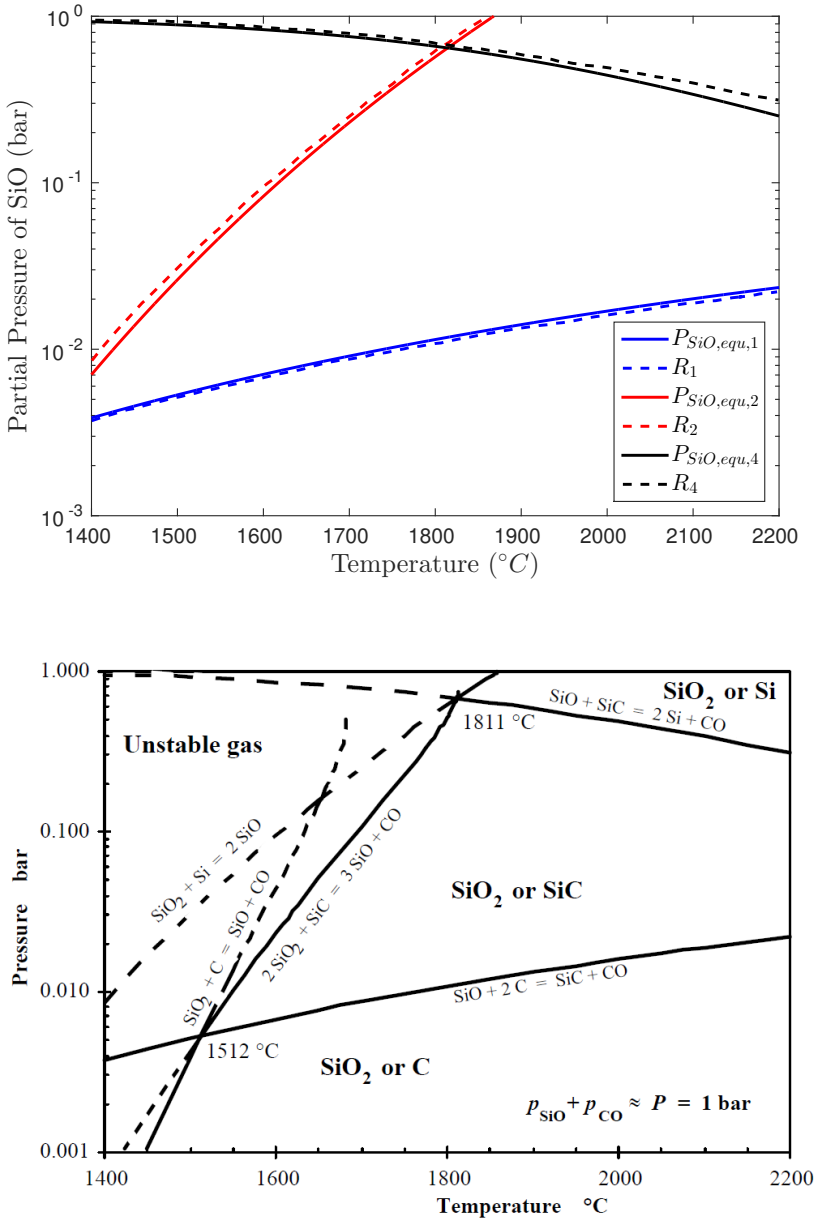


Figure 2.3: On the top are equilibrium pressure functions (in solid lines) compared with read in data from the image on the bottom (in dashed lines). Temperature is in Celsius to allow for comparison, even though the equilibrium pressure functions are used with temperature in kelvin. On the bottom is the diagram of equilibrium SiO pressures reproduced from [82].

bottom (roughly 10%) of the furnace to generate the SiO furnace gas. We make the simplification that all of the furnace is initially filled with carbon and solid quartz, and that there is CO and SiO initially.

Multiplying the no voids condition (2.20) by $\mathrm{P_{TOT}}/R_gT$, then taking a time derivative, we can substitute in equations (2.13) and (2.14) to give an equation with a spatial derivative of $U_g(\mathrm{C_{CO}} + \mathrm{C_{SiO}})$ and a time derivative of a function of temperature and the solid and liquid concentrations. This tells us that the no voids condition (2.20) has characteristics with direction $\lambda_c = \infty$, corresponding to t = constant. Hence, we need a boundary condition for $U_g(z,t)$. As particles touching the very bottom of the furnace remain there, we use the no-flux condition $U_g(0,t) = 0$. In all practical situations $U_g(h,t) > 0$, so no boundary condition is needed at the top of the furnace.

The characteristics corresponding to equations (2.13) and (2.14) are given by $\frac{dz}{dt} = U_g(z,t)$. Since we have set $U_g(0,t) = 0$, the characteristic emanating from the origin is given by $z = 0$. As such, only initial conditions are needed for the gas concentrations. The total initial concentration of gas must satisfy the no voids condition (2.20), along with the initial conditions of the solid and liquid concentrations and the temperature. However, we are free to choose the initial conditions of $\mathrm{C_{CO}}$ and $\mathrm{C_{SiO}}$ up to this constraint, or equivalently, to choose the initial condition of the partial pressure of SiO, P_{SiO}. Since CO and SiO gas are initially produced in roughly even quantities in the experiments, we take the initial gas concentrations to be equal, $\mathrm{C_{CO}} = \mathrm{C_{SiO}}$. This is the same as taking $P_{\mathrm{SiO}} = \frac{1}{2}P_{\mathrm{TOT}}$.

The parabolic equation for temperature (2.21) requires two boundary conditions and one initial condition. Since we are heating the pilot furnace from room temperature, we use the initial condition $T(z,0) = 300$ K. We assume that the furnace is suitably insulated so that there is no heat loss from conduction or radiation at the top or bottom, giving $\frac{\partial T}{\partial z} = 0$ at $z = 0, h$. However, note that energy can escape from the top via convection, since gas leaves the furnace.

2.2.11 Full dimensionless model

We use the dimensionless scalings:

$$\begin{aligned} &\mathrm{C_X} = c_0\bar{\mathrm{C}}_{\mathrm{X}}, \quad T = (T_{\mathrm{bottom}} - T_{\mathrm{top}})\bar{T} + T_{\mathrm{top}}, \quad t = \tau\bar{t}, \quad z = h\bar{z}, \\ &U_g = V\bar{U}_g, \quad P_{\mathrm{SiO}} = P_{\mathrm{TOT}}\bar{P}_{\mathrm{SiO}}, \quad P_{\mathrm{SiO,equ,j}} = P_{\mathrm{TOT}}\bar{P}_{\mathrm{SiO,equ,j}}, \\ &\sigma_s = c_0C_{p,C}\bar{\sigma}_s, \quad \sigma_g = c_0C_{p,C}\bar{\sigma}_g. \end{aligned} \tag{2.29}$$

We take $T_{\mathrm{bottom}} = 2400$ K (2127°C) and $T_{\mathrm{top}} = 1400$ K (1127°C) as typical temperatures found at the bottom and the top of the furnace, respectively, since there is no

scaling from the boundary conditions. A scale for τ can be found through a balance with any of the reaction terms or the gas transport. We choose to balance with the melting of quartz reaction, so take $\tau = (k_3 T_0)^{-1}$, where we have used the shorthand $T_0 := T_{\text{bottom}} - T_{\text{top}}$. This gives $\tau = 1091$s, which is 18 min 11 s. We take c_0 to be the initial concentration of carbon in the bulk of the pilot furnace, found to be 38000 mol/m^{3}s. Upon non-dimensionalisation we can define the following dimensionless parameters:

$$\begin{aligned}
&\nu = \frac{V\tau}{h}, \quad \xi_1 = \frac{k_1 P_{\text{TOT}}}{k_3 T_0}, \quad \xi_2 = \frac{k_2 P_{\text{TOT}}}{k_3 T_0 c_0}, \quad \xi_{-2} = \frac{k_{-2} c_0 P_{\text{TOT}}}{k_3 T_0}, \\
&\xi_4 = \frac{k_4 P_{\text{TOT}}}{k_3 T_0}, \quad \xi_5 = \frac{k_5 c_0}{k_3 T_0}, \qquad T_m = \frac{T_M - T_{\text{top}}}{T_{\text{bottom}} - T_{\text{top}}}, \\
&a = \left(k_f + \frac{A_{gr} k_{gr}}{A_f}\right) \frac{\tau}{h^2 C_{p,\mathrm{C}} c_0}, \quad \gamma_j = \frac{dH_j}{C_{p,\mathrm{C}} T_0}, \quad \beta^* = \frac{\beta T_0^3 \tau}{h^2 C_{p,\mathrm{C}} c_0}, \\
&\sigma^*_{gr} = \frac{A_{gr} \rho_{gr} C^{kg}_{p,gr}}{A_f c_0 C_{p,C}}, \quad q = \frac{\tau}{T_0 c_0 C_{p,C}} \left(1 + \frac{A_{gr}}{A_f}\right) Q, \quad h^*_T = \frac{h_T}{h}.
\end{aligned} \tag{2.30}$$

We drop the overbar notation, and use the relations $\mathrm{C}_{\mathrm{CO}} + \mathrm{C}_{\mathrm{SiO}} = \mathrm{C}_g$, $\mathrm{C}_{\mathrm{CO}} = \mathrm{C}_g(1 - P_{\mathrm{SiO}})$, and $\mathrm{C}_{\mathrm{SiO}} = \mathrm{C}_g P_{\mathrm{SiO}}$, to write the dimensionless equations as

$$c_0 \left(\frac{R_g (T_0 T + T_{\text{top}}) \mathrm{C}_g}{P_{\text{TOT}}} + \sum_{\text{solids and liquids } i} \mathrm{C}_i \frac{M_i}{\rho_i} \right) = 1, \tag{2.31}$$

$$\begin{aligned}
\frac{\partial}{\partial t} \begin{pmatrix} \mathrm{C}_{\mathrm{C}} \\ \mathrm{C}_{\mathrm{SiC}} \\ \mathrm{C}_{\mathrm{SiO_2(s)}} \\ \mathrm{C}_{\mathrm{SiO_2(l)}} \\ \mathrm{C}_{\mathrm{Si}} \\ \mathrm{C}_g(1 - P_{\mathrm{SiO}}) \\ \mathrm{C}_g P_{\mathrm{SiO}} \end{pmatrix} + \nu \frac{\partial}{\partial z} \begin{pmatrix} 0 \\ 0 \\ 0 \\ 0 \\ 0 \\ U_g \mathrm{C}_g (1 - P_{\mathrm{SiO}}) \\ U_g \mathrm{C}_g P_{\mathrm{SiO}} \end{pmatrix} \\
= \begin{pmatrix} -2 & 0 & 0 & 0 & 0 & -1 \\ 1 & 0 & 0 & 0 & -1 & 0 \\ 0 & 0 & 0 & -1 & 0 & 0 \\ 0 & 1 & -1 & 1 & 0 & -1 \\ 0 & 1 & -1 & 0 & 2 & 0 \\ 1 & 0 & 0 & 0 & 1 & 1 \\ -1 & -2 & 2 & 0 & -1 & 1 \end{pmatrix} \begin{pmatrix} r_1 \\ r_2 \\ r_{-2} \\ r_3 \\ r_4 \\ r_5 \end{pmatrix},
\end{aligned} \tag{2.32}$$

$$\begin{aligned}
&\frac{\partial}{\partial t} \left(\left(\frac{T_{top}}{T_0} + T \right) (\sigma_s + \sigma_g + \sigma^*_{gr}) \right) + \nu \frac{\partial}{\partial z} \left(\left(\frac{T_{top}}{T_0} + T \right) U_g \sigma_g \right) \\
&\quad = a \frac{\partial T^2}{\partial z^2} + \beta^* \frac{\partial}{\partial z} \left(\left(\frac{T_{top}}{T_0} + T \right)^3 \frac{\partial T}{\partial z} \right) + \sum_j \gamma_j r_j + q \mathcal{H}(h^*_T - z),
\end{aligned} \tag{2.33}$$

where

$$\begin{pmatrix} r_1 \\ r_2 \\ r_{-2} \\ r_3 \\ r_4 \\ r_5 \end{pmatrix} = \begin{pmatrix} \xi_1 \mathrm{r_C} \mathrm{C_C} \big(P_{\mathrm{SiO}} - P_{\mathrm{SiO,equ},1}(T)\big)^+ \\ \xi_2 \big(P_{\mathrm{SiO}} - P_{\mathrm{SiO,equ},2}(T)\big)^+ \\ \xi_{-2} \mathrm{C}_{\mathrm{SiO_2(l)}} \mathrm{C_{Si}} \\ \mathrm{C}_{\mathrm{SiO_2(s)}} (T - T_m)^+ \\ \xi_4 \mathrm{C_{SiC}} \big(P_{\mathrm{SiO}} - P_{\mathrm{SiO,equ},4}(T)\big)^+ \\ \xi_5 \mathrm{C}_{\mathrm{SiO_2(l)}} \mathrm{C_C} \end{pmatrix}. \tag{2.34}$$

We have the dimensionless initial conditions

$$\begin{aligned} &\mathrm{C_C} = 1, \quad \mathrm{C_{SiC}} = 0, \quad \mathrm{C}_{\mathrm{SiO_2(s)}} = \alpha, \quad \mathrm{C}_{\mathrm{SiO_2(l)}} = 0, \quad \mathrm{C_{Si}} = 0, \quad P_{\mathrm{SiO}} = \frac{1}{2}, \\ &U_g = 0, \quad T = -1.1, \quad \mathrm{C}_g = \frac{P_{\mathrm{TOT}}}{300 R_g} \left(\frac{1}{c_0} - \left(\frac{M_{\mathrm{C}}}{\rho_{\mathrm{C}}} + \frac{M_{\mathrm{SiO_2}(s)}}{\rho_{\mathrm{SiO_2}(s)}} \alpha \right) \right), \end{aligned} \tag{2.35}$$

for $0 \leq z \leq 1$, and the dimensionless boundary conditions

$$U_g(0,t) = 0, \quad \frac{\partial T(0,t)}{\partial z} = 0, \quad \frac{\partial T(1,t)}{\partial z} = 0. \tag{2.36}$$

2.3 Behaviour of the pilot furnace

2.3.1 Numerical scheme

We perform numerical simulations of our model to capture the behaviour in the pilot furnace. We run the simulations for 80 minutes in dimensional time, as this is the length of the pilot furnace experiments.

For our numerical simulations, we use first order finite difference schemes, with a spatial step Δz and a timestep Δt. We first step forward in time for the solid and liquid concentrations using a forward Euler explicit scheme. Then, we find the temperature by using a forward Euler scheme which is implicit for diffusive derivatives but explicit for the diffusive coefficient, $a + \beta^* T^3$, as well as the convective and wall source terms. The reaction heat release is implicit in solid and liquid concentrations but explicit in temperature and pressure. We use a Godunov-type method with upwinding for the convective fluxes. In the time partial derivative we neglect the heat capacity in the gas σ_g, which is 10^{-4} times the size of the other heat capacities σ_s and σ^*_{gr}. Using the temperature we then find the concentration of gas using the no voids condition (2.31). We next update for the gas velocity and partial pressure of SiO using a Godunov-type upwinding method. In order to ensure numerical stability, we choose Δt based on Δz to obey the Courant-Friedrichs-Lewy (CFL) condition. The scheme implemented is grid scalable, and our numerical experiments show a slightly better than first order rate of convergence.

Dimensionless Parameter	Value
ξ_1	$10^{-1} - 1$
ξ_2	$10^{-2} - 10^{-1}$
ξ_{-2}	$1 - 10$
ξ_4	$1 - 10$
ξ_5	$1 - 10$
γ_1	3.09
γ_2	1.22×10
γ_{-2}	-2.41×10
γ_3	0
γ_4	-6.65
γ_5	-3.16×10
h_T^*	0.544
T_m	0.596
ν	3.17×10^3
a	0.177
β^*	3.51×10^{-3}
σ_{gr}^*	1.013
q	3.685
α	0.454

Table 2.3: Dimensionless parameter values or ranges.

2.3.2 Model behaviour

Typical dimensionless parameters are given in Table 2.3. These were calculated from dimensional parameters found in [28, 42, 45, 51, 55, 69, 71, 82, 101, 106]; for brevity we do not list all of these values here, as they are never used individually. Unless stated otherwise, we use the value $\mathrm{r_C} = 0.2$ for the reactivity of carbon in simulations.

In the first 40 minutes the furnace heats up and no substantial reactions occur. Then in the second 40 minutes the pilot furnace is hot enough for typical industrial furnace behaviour to be observed. We are interested in the amount of solids and liquids, as opposed to gas, and so define the total solid volume fraction, θ_S, to be

$$\theta_S = \theta_{\mathrm{C}} + \theta_{\mathrm{SiC}} + \theta_{\mathrm{SiO_2(s)}} + \theta_{\mathrm{SiO_2(l)}} + \theta_{\mathrm{Si}}, \tag{2.37}$$

with liquids incorporated because they are treated like solids in our model. In the second half of the experiment, a separation emerges between lower and upper regions of the pilot furnace. In the lower region, θ_S decreases substantially, due to the melting of SiO_2(s) and degradation of carbon. In the upper region, θ_S increases slightly, due to condensation of SiO gas. The interface between these regions moves upwards as

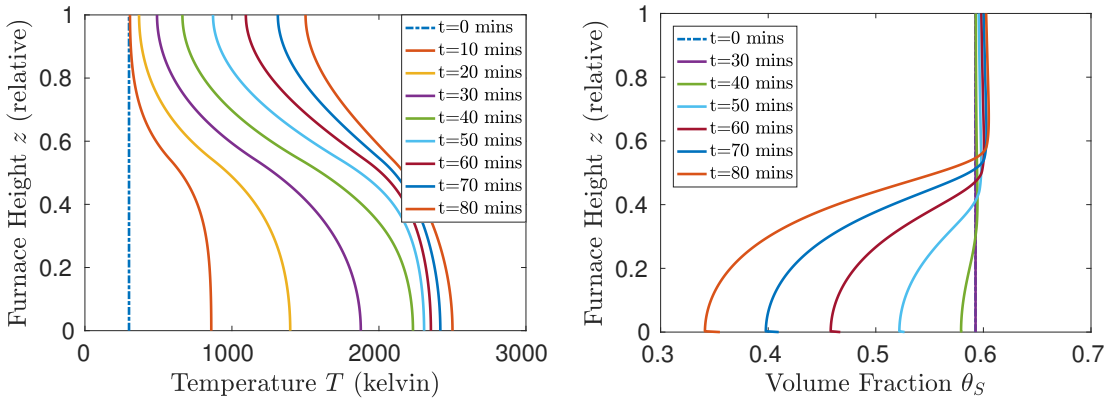


Figure 2.4: Temperature profiles (left) and the total solid and liquid volume fraction θ_S (right) at ten minute intervals.

the temperature rises throughout the furnace and more of the quartz becomes hot enough to melt. Plots of temperature and the total solid volume fraction are given in Figure 2.4.

In Figure 2.5 we compare our numerical simulations with one of the pilot furnace experiments, displaying results in terms of volume fractions. In the top region, where $z \geq h_T^* \approx 0.54$, we have unmelted SiO_2(s). Carbon has reacted away in part, and there is deposition of SiC, Si, and SiO_2(l). The SiO_2(l) comes from condensation of SiO, rather than from the melting of SiO_2(s).

In the bottom of the furnace, where $z \leq h_T^* \approx 0.54$, SiO_2(s) has melted and there has been degradation of carbon, through reaction R_5 with the SiO_2(l). There is some build-up of SiO_2(l) and SiC, as well as production of Si. Around the highest position of heating $z = h_T^* \approx 0.54$, in approximately the region $0.45 \leq z \leq 0.6$, the volume fractions of Si and SiO_2(l) seem to interchange between their behaviour in the upper and lower regions of the furnace. This crossover region corresponds to a temperature of around 2000 K, where both quartz first starts to melt and the SiO gas begins to condensate.

Our one-dimensional model captures a distinct upper charge region, and shows the interface of this region moving upwards as temperature increases. To understand how the crust supports the weight of the granular particles in the charge, mechanical effects need to be modelled. These are considered in Chapter 4. In the experiment there is a separation between the gas cavity and the crater comprising solid and liquid materials. This is not replicated in our model, as we treat solids and liquids as being stationary.

In Figure 2.6 we plot the solid and liquid concentrations, as well as the reaction

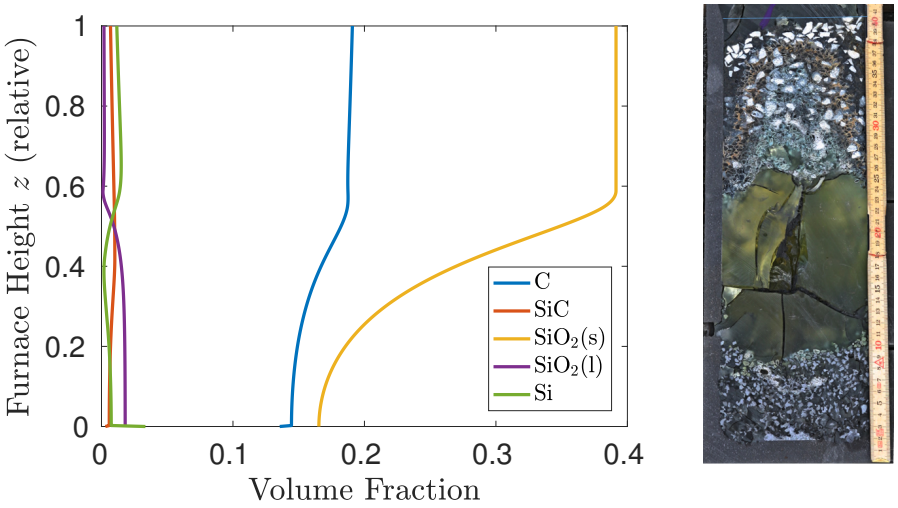


Figure 2.5: Comparison of numerical simulations and an experiment. The plot shows the volume fractions of each of the solid and liquid chemical species (left), with the height lined up with the experiment (right). The top of the green epoxy-filled region in the experiment (taking the place of the gas cavity) matches up with the kink in the blue and yellow curves, so we have captured the upper region (the charge), which is dominated by solid quartz and carbon.

rates, showing the dynamics in the pilot furnace at 40 min, 60 min, and the end time of 80 min. The temperature increases with time throughout the furnace in a monotone profile which is hotter at the base and cooler at the top. Two regions can be seen, with distinct behaviour of the concentrations. SiO_2(s) melts in the bottom of the furnace and forms SiO_2(l), which reacts with carbon to produce CO and SiO gas. This can be seen through R_3, the reaction governing the melting of quartz, and R_5, the carbon and SiO_2(l) reaction, which dominate in this lower region. The height of this region increases with the temperature. In the top region of the furnace, SiO gas condenses to form Si and SiO_2(l). The SiO_2(l) then reacts with carbon to produce gas, as occurs in the furnace base. Some of the SiO gas reacts with carbon to produce CO gas and SiC. Thus our model gives a decent representation of reality, and so we now turn to consider the effect of model inputs.

2.4 Influence of model parameters on silicon production

In the silicon process, and the pilot furnace experiments, various inputs can be changed, including the reactivity of the carbon particles used, the heating applied

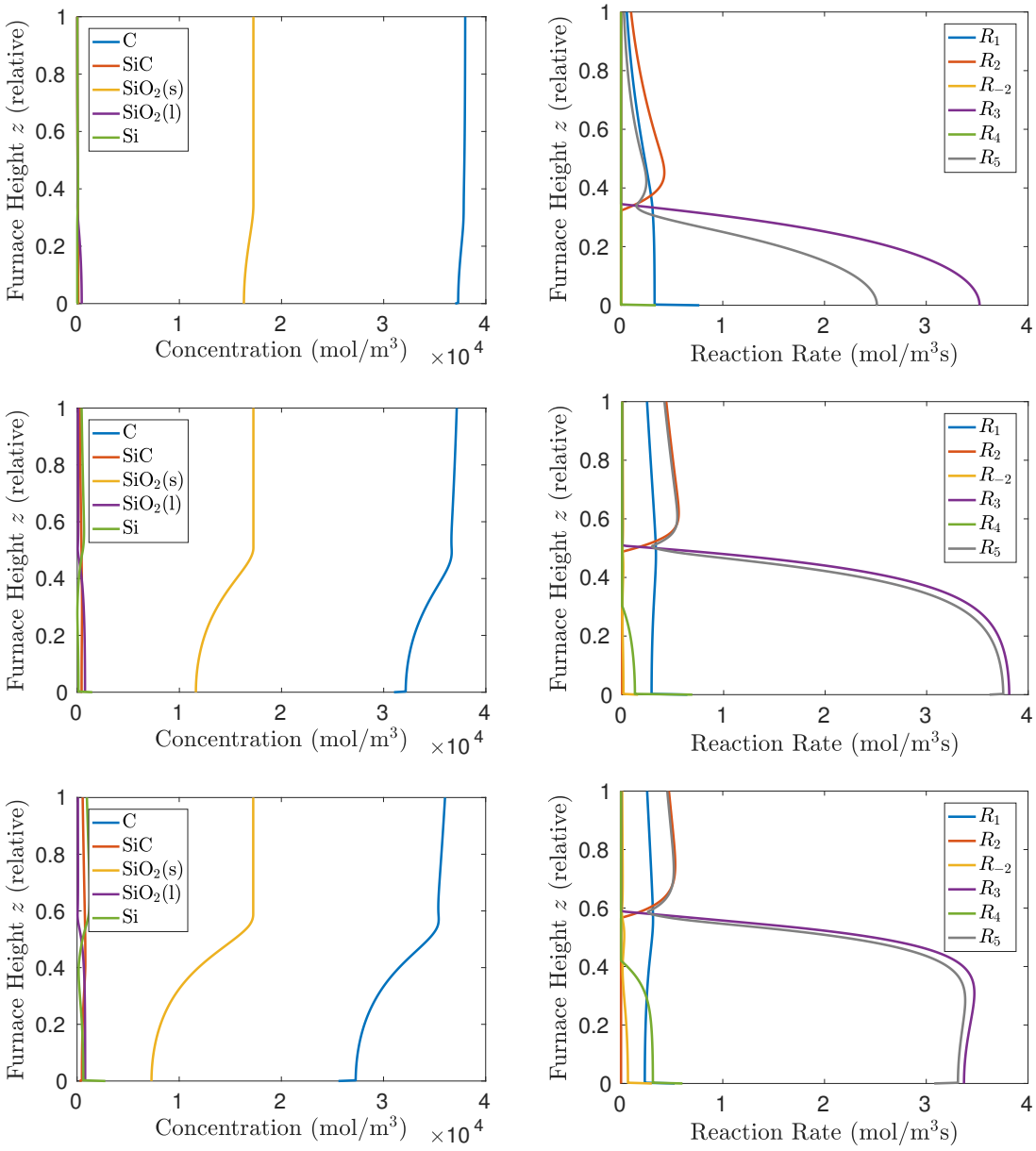


Figure 2.6: Plots of numerical simulations of the solid and liquid concentrations (left), and the reaction rates (right). In rows from top to bottom: times $t = 40$ min, $t = 60$ min, and end time $t = 80$ min.

to the furnace, and the ratio of carbon to quartz used as raw materials. These inputs are varied in our model to observe the influence on furnace dynamics. Similarly, although the kinetic rates cannot be changed in reality, since they are not known accurately we will adjust them in our simulations. Of particular interest is the condensation reaction, R_2, since this has been hypothesised as a mechanism for crust formation in [82]; accordingly, we vary the kinetic rate ξ_2.

We want systematic ways of measuring how furnace behaviour changes with varying inputs, and so use the metrics of silicon yield, SiO losses, and solid build-up, described below.

We define the silicon yield (%) as:

$$\text{Silicon Yield (\%)} = \frac{\text{Total Final Silicon}}{\text{Total Input SiO}_2} \times 100, \tag{2.38}$$

where we measure the yield in terms of concentrations. This permits us to calculate the amount of silicon that is created from the raw material quartz. The more silicon that is created, the better. Due to the uncertainty of kinetic parameters and the purity of quartz used, these calculated values are not intended to be used to a high level of accuracy, but are useful for comparison between different model inputs. The values will be lower in the pilot furnace experiment than in industrial furnaces, because the experiment only runs for 80 minutes and quartz in the upper furnace remains unmelted and unreactive. In addition, silicon in the base of the pilot furnace reacts with liquid quartz to produce silicon monoxide, through reaction R_{-2} (2.2), as demonstrated by the yellow curve in the bottom right plot of Figure 2.6. In industrial furnaces the tapping of silicon reduces this effect. Thus, results should not be directly transferred to the operational setting.

We define the SiO losses as

$$\text{SiO Losses (\%)} = \frac{\text{Total SiO Convected Away}}{\text{Total Input SiO}_2} \times 100, \tag{2.39}$$

where again we measure the losses in terms of concentrations. This allows us to determine how much of the silicon put into the furnace (as SiO_2(s)) is lost from the process through SiO gas escaping out of the furnace top, but does not include losses in the tapping process or during post treatment. This is an important measure, capturing the efficiency of production, since the majority of silicon that is not lost from industrial furnaces through SiO convection will eventually be tapped as liquid silicon.

We want to have a measure for crust formation and so, as a proxy, we consider the build-up of solids and liquids. We define the solid build-up as

$$\text{Solid Build-up } (\%) = \max_{z} \left\{ \frac{\text{Final } \theta_S - \text{Initial } \theta_S}{\text{Initial } \theta_S} \right\} \times 100, \tag{2.40}$$

where θ_S is the total solid and liquid volume fraction. We are thus finding the greatest increase in θ_S relative to the initial condition. The higher this value is, the more clogging up of solids and liquids we see in the upper part of the furnace.

We run simulations with varying inputs and calculate the output metrics described. In Figure 2.7 we show plots for varying the reactivity of carbon and applying three different levels of effective heating. For the higher heating powers 15 kW and 20 kW, there is a trade-off between silicon yield and SiO losses. Higher heating brings higher yield, but also higher losses, as more SiO escapes from the system. It is difficult to apply these results to industrial furnaces, where there is feeding of raw material and the heat source is from electrodes, rather than an induction heater. However, if the power input is too high, it is possible that much of the silicon will be lost from the process as gas. For all levels of heating in the pilot furnace, SiO losses decrease as the carbon reactivity is increased, since reaction R_1 between SiO and carbon is faster, hence less SiO escapes the furnace, and more SiC is produced. For a heating of 10 kW and 15 kW, the solid build-up is approximately constant for varying reactivity of carbon. Higher reactivity causes greater SiC production, which takes up more space than does the carbon it replaces (the volume taken by two moles of carbon is $2 \times M_{\mathrm{C}}/\rho_{\mathrm{C}} = 1.06 \times 10^{-5}$ m^3, yet the volume taken by one mole of SiC is $M_{\mathrm{SiC}}/\rho_{\mathrm{SiC}} = 1.25 \times 10^{-5}$ m^3). However, an increase in R_1 produces more CO(g), lowering the partial pressure P_{SiO}. This lower P_{SiO} decreases the rate of R_2, reducing the deposition of SiO_2(l) and Si, and balancing the build-up of SiC.

In Figure 2.8 we show plots for varying the mixture between carbon and solid quartz used at the start and applying four different values for $\mathrm{r_C}$. The mixture ratio is the initial value of $\mathrm{C_C}$ to $\mathrm{C_{SiO_2(s)}}$. Note that when we increase the carbon we also decrease the quartz, in order to ensure the initial values of θ_S is the same. Thus the silicon yield and SiO losses are measured with respect to the initial amount of quartz, which is different in each simulation. We see that more reactive carbon leads to a lower silicon yield and lower SiO losses, since more SiC is produced through the reaction R_1 and less SiO can escape from the top of the furnace. However, silicon yield increases with reactivity for effective heating of 15 kW and 20 kW (see Figure 2.7). Also, in an industrial furnace, most of the silicon atoms remaining in the process will eventually be tapped as liquid silicon, so SiO losses may be a more useful metric than silicon yield.

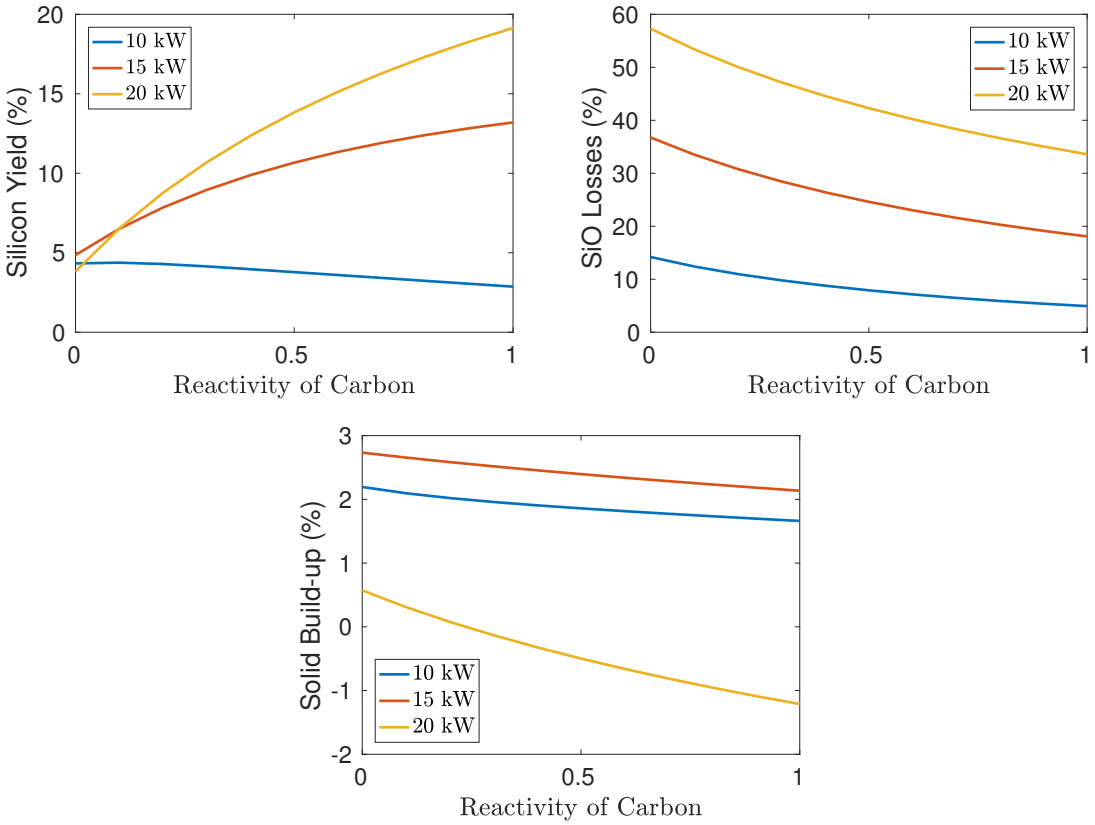


Figure 2.7: Output metrics (2.38), (2.39), and (2.40) against reactivity of carbon, for three different values of effective heating into the pilot furnace.

We see that as the concentration of carbon in the initial mixture increases (and, correspondingly, the amount of solid quartz decreases) there is a higher silicon yield and lower level of SiO losses, due to a faster rate of R_1. As with Figure 2.7, this faster R_1 decreases the rate R_2, due to lower P_{SiO}, causing less SiO_2(l) and Si to be deposited. However, in this case this effect dominates over the build-up of SiC, and hence the solid build-up decreases with more carbon in the initial mixture.

In Figure 2.9 we see the effect of changing the strength of the condensation reaction, R_2, in our simulations, by altering the kinetic rate parameter, ξ_2. We find that the silicon yield increases, the SiO losses decrease, and the solid build-up increases with an increase in the value of ξ_2. This is expected, since a faster reaction R_2 results in a greater rate of condensation of SiO gas to SiO_2(l) and Si.

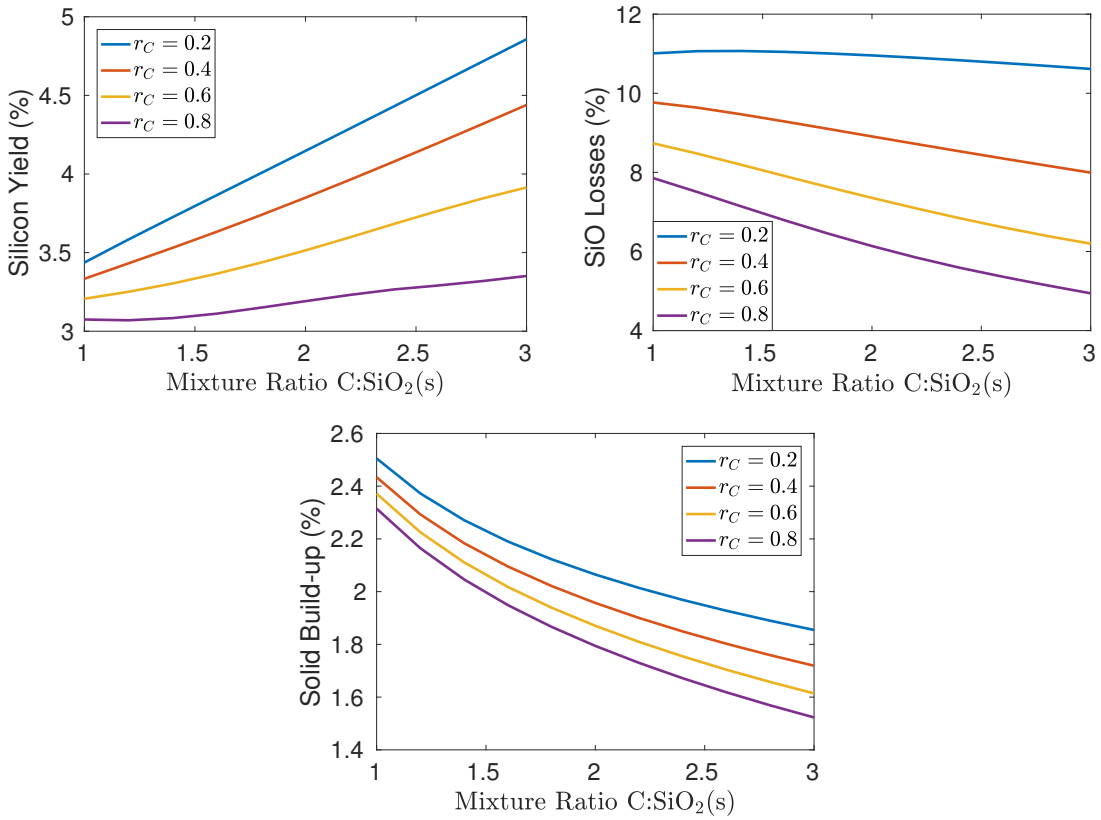


Figure 2.8: Output metrics (2.38), (2.39), and (2.40) against the mixture ratio of C to SiO_2(s), for four different values of carbon reactivity.

2.5 Conclusions

We have developed a mathematical model for the chemistry, heat flow, and material transfer in a silicon pilot furnace, and we have applied this model to better understand real silicon pilot furnace experiments. In order to ensure higher process yields and energy efficiency in the silicon production process, it is important to understand crust formation within the furnace. Our numerical simulations replicated the reacting away of the lower part of the furnace, which corresponds to the creation of a gas cavity and crater region. Comparisons with experiments show a good fit for the position of the interface between the charge and the lower regions, without the need to fit any model parameters artificially. The location of this interface is largely dictated by the temperature within the furnace, with our results suggesting that increasing the temperature will result in an increase in the size of the gas cavity, along with a rising of the crust within the furnace.

Key to modelling the furnace dynamics is understanding the gaseous SiO molecules convecting up the furnace. Due to the partial pressures and temperatures found in

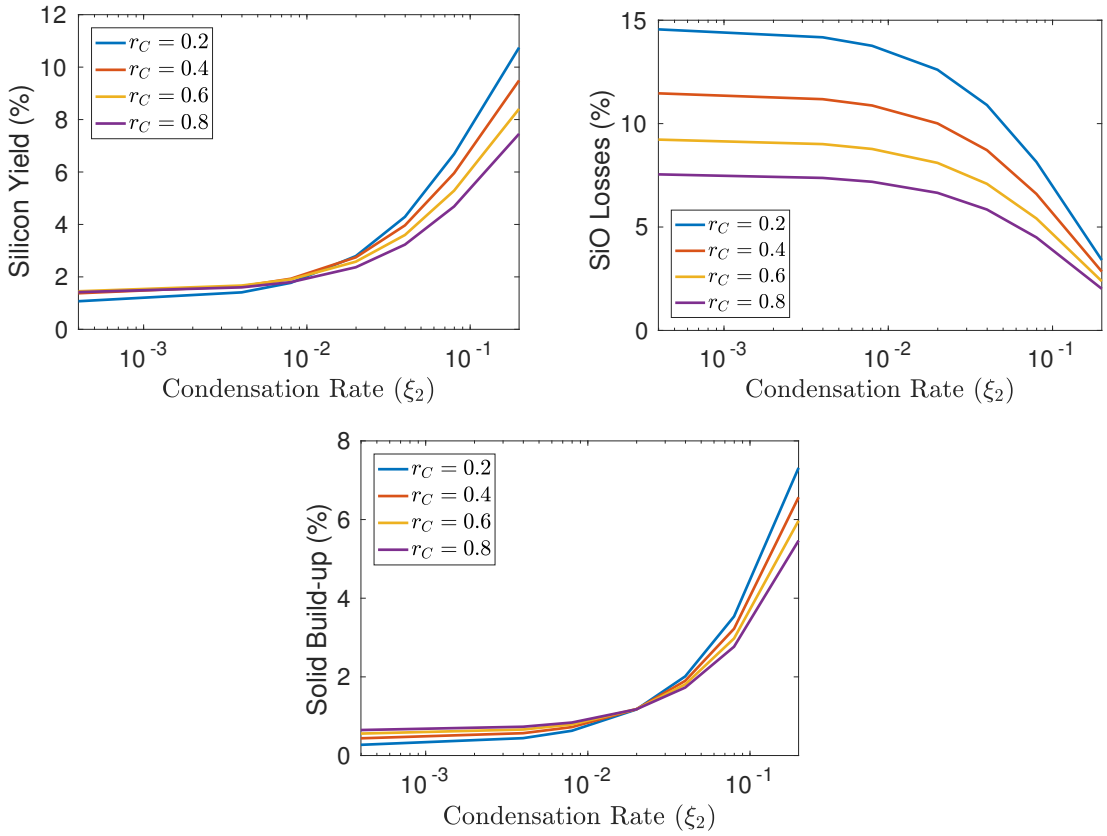


Figure 2.9: Output metrics (2.38), (2.39), and (2.40) against the rate of the condensation reaction, R_2, for four different values of carbon reactivity.

the upper region of the furnace, these molecules can either condense to form Si and SiO_2(l), react with carbon to form SiC and CO, or convect out of the furnace (resulting in silicon loss). It is primarily the balance of these three processes which determines the productivity of the silicon furnace. In furnace operation, the SiO losses and crust formation can be reduced simultaneously. Increasing the mixture ratio and the reactivity of the carbon particles decreases the crust formation, seen through the proxy of solid build-up and the amount of SiO convecting out of the furnace. However, using highly reactive carbon particles is costly, so the financial benefits of reduced SiO losses should be considered when determining what constitutes optimal production.

Our simulations suggest that material builds up in the upper region of the furnace due to the production of SiC and the condensation of SiO gas. We find that having more carbon in the initial mixture plays a larger role in the reduction of the solid build-up than does using more reactive carbon particles. Yet, using too much carbon and too little quartz may reduce the overall amount of silicon produced, even if the silicon

yield and SiO losses are favourable, as these are measured relative to the amount of initial quartz. On the other hand, using more reactive carbon particles decreases both silicon yield and SiO losses for the effective heating used in the experiment, as more SiC is produced. Since SiO loss is a more helpful metric for industrial operation, the finding that these diminish as reactivity of carbon increases confirms the intuition presented in [82].

All analysis of the one-dimensional model in this chapter has been in the form of numerical simulations. In Chapter 3, we undertake an asymptotic analysis of the model, in order to find analytic representations of the dominant behaviour in the pilot furnace, and to better understand the interplay between temperature and chemistry. Then, in Chapter 4, we develop a model of the furnace crust, which addresses some of the shortcomings of the model we have studied in this present chapter, by incorporating material transfer of materials in the charge.

Chapter 3

Asymptotic Analysis of One-Dimensional Model of a Silicon Pilot Furnace

3.1 Introduction

In Chapter 2 we derived a one-dimensional continuum model of a silicon pilot furnace, accounting for chemical, thermal, and gas flow effects. In the present chapter, we build on this work by examining asymptotic limits of this model, in order to capture and better understand the underlying behaviour.

There is a wealth of mathematical literature on problems of coupled chemical and thermal effects which is relevant for this chapter. In [14, 65, 74], the authors consider catalytic converters and combustion. Here an exothermic reaction heats the system, causing an initial light-off behaviour [74] and the mechanisms by which the reaction switches off [14] are studied by asymptotic means. A separate, but linked, body of work examines competing exothermic and endothermic reactions [38, 75, 84, 107]. If there is just a single exothermic reaction, or two exothermic reactions, travelling wave solutions exist. However, the presence of the endothermic reaction, removing heat from the system, means these travelling waves can exist only for certain regions of the parameter space. In [3], premixed flames are considered and in [1] a model of coupled heat transfer and an endothermic reaction is analysed. Useful analogues of the behaviour in the model outlined in Chapter 2 can be found in work set in different physical contexts. In [29], the authors find a moving drying front in the roasting of a coffee bean, which separates a dry region from a saturated region. The behaviour of this narrow transition layer is analysed using asymptotic methods. The processing of glass in a furnace is considered in [31], where a melted upper region and an unmelted

lower batch region are separated by a downwards moving travelling front. In the context of tumour cells, the authors of [59] find new discontinuous travelling waves for different hyperbolic PDE models. Although many chemical processes contain numerous reactions, it is possible to reduce the number of equations in mathematical models describing these processes by making certain simplifications. One of these is the quasi-steady state assumption [83], or pseudo-steady state hypothesis. There is a separation of timescales, so that after the initial fast timescale some of the variables can be assumed to be in steady state, reducing the number of equations to be solved to find the other variables, which vary over a longer timescale.

In Section 3.2, we discuss a new non-dimensionalisation of the model developed in Chapter 2, choosing scalings to ensure that all dimensionless variables are order one in size, while parameters are also order one, except for two which are small. In Section 3.3, we examine this dimensionless model with the simplification of a prescribed steady state temperature profile in the limit of these small parameters going to zero. This corresponds physically to the reaction between liquid quartz and carbon being instantaneous when compared to the melting of solid quartz, and gas advection being instantaneous when compared to both these effects. Using a prescribed temperature profile makes the leading order system of equations easier to solve and allows us to capture the behaviour of the dominant chemical effects. We find that two spatial regions emerge; a lower, hot region where gas is produced from the solid carbon and quartz, and a cold, upper region where SiO gas reacts with carbon particles and also condenses. We also find two timescales, with an initial fast transience followed by a slower outer timescale. In Section 3.4, we consider asymptotics of the full problem, where the varying temperature is coupled with chemistry and gas transport. We find that the leading order problem comprises an endothermic chemical reaction acting as a sink in the heat equation, which has an external source. This differs from much of the literature discussed, which largely deals with exothermic reactions (e.g. [14, 65, 74]). We find spatial regions similar to those which arise in Section 3.3 with a prescribed temperature profile, with the difference being that the spatial interface rises in the furnace with a travelling wave type behaviour. We consider subsequent sub-limits of this simplified model in Section 3.5. We are particularly interested in both crust formation and the interface between the charge and the gas cavity, given in this model by the isotherm where quartz begins to melt. There is discussion of the melting isotherm throughout Sections 3.3 and 3.4, and in Section 3.6 we give insights into crust formation. Concluding remarks are given in Section 3.7. The work presented in this chapter has been published in [86].

3.2 Alternative non-dimensionalisation

In Section 2.3 of the previous chapter, we performed numerical simulations of the one-dimensional model to replicate behaviour in the pilot furnace, and conducted parameter sweeps to determine the influence of various input parameters on the output metrics silicon yield, SiO losses, and solid build-up. There is, however, much to be learned by exploiting the relative sizes of the various parameters that are found in the model to determine the asymptotic behaviour of solutions. Many of the parameters in the model are not known accurately, but have been calibrated with industrial furnaces to give sensible results from previous models (see the dynamic model [39] and SiMod [106]). Thus, finding the general qualitative behaviour when certain parameters are small or large helps us to understand the interplay of the chemical, thermal, and transport effects.

In this chapter we use two small parameters, ϵ and δ, to seek asymptotic solutions to the model presented in Chapter 2, and to help formulate a simplified model. The small parameter ϵ emerges by considering a balance between reactions R_3 and R_5 (see equations (2.3) and (2.5)). Liquid quartz is formed through R_3 and then reacts with C through R_5 to form CO and SiO. The timescale used in Section 2.2.11 was that of the melting reaction R_3, so $\tau = (k_3 T_0)^{-1}$, where $T_0 := T_{\text{bottom}} - T_{\text{top}} = 1000$ K is the typical temperature difference between the top and bottom of the furnace. We let ϵ be the ratio of the rate of R_3 to R_5, or ratio of the timescale of R_5 to R_3. We let δ be the ratio of time taken for the gas to convect the height of the furnace to the timescale for R_3. We thus have

$$\epsilon = \frac{k_3 T_0}{k_5 c_0} = \frac{1/(k_5 c_0)}{1/(k_3 T_0)}, \quad \delta = \frac{h/V}{1/(k_3 T_0)}, \tag{3.1}$$

where h is the height of the furnace and V is a typical value of the magnitude of the gas velocity. We have $0 < \delta \ll \epsilon \ll 1$, and will consider the joint limits $\epsilon \to 0$ and $\delta \to 0$, with $\delta/\epsilon \to 0$. The limit $\epsilon \to 0$ corresponds to the reaction between C and SiO_2(l) being instantaneous when compared to the melting of SiO_2(s), so that as soon as quartz melts to liquid quartz, it will react with any available carbon. The limit $\delta \to 0$ corresponds to instantaneous gas flow when compared with the melting of quartz, but as $\delta/\epsilon \to 0$, this gas flow is also faster than the chemical timescale for R_5.

In (2.29) all concentrations were scaled with the initial concentration of carbon, c_0. However, in the numerical simulations shown in Section 2.3, we found that the

concentrations of SiC, SiO_2(l), and Si remain around 30 times smaller than the concentrations of C and SiO_2(s) (see Figures 2.5 and 2.6). Also, the concentration of gas was found to be around 10^4 times smaller than the concentrations of C and SiO_2(s). By considering dominant balances, we find that the most appropriate scales for the concentrations, when compared to c_0, are that C and SiO_2(s) are $\mathcal{O}(1)$, SiC, SiO_2(l), and Si are $\mathcal{O}(\epsilon)$, and the gases CO and SiO are $\mathcal{O}(\delta)$. We thus utilise the new dimensionless scalings given below in (3.2).

$$\begin{aligned}
&\mathrm{C_C} = c_0\bar{\mathrm{C}}_\mathrm{C}, \quad \mathrm{C_{SiO_2(s)}} = c_0\bar{\mathrm{C}}_{\mathrm{SiO_2(s)}}, \quad \mathrm{C_{SiC}} = \epsilon c_0\bar{\mathrm{C}}_\mathrm{SiC}, \quad \mathrm{C_{SiO_2(l)}} = \epsilon c_0\bar{\mathrm{C}}_{\mathrm{SiO_2(l)}},\\
&\mathrm{C_{Si}} = \epsilon c_0\bar{\mathrm{C}}_\mathrm{Si}, \qquad \mathrm{C_g} = \delta c_0\bar{\mathrm{C}}_\mathrm{g}, \quad T = (T_\mathrm{bottom} - T_\mathrm{top})\bar{T} + T_\mathrm{top},\\
&t = \tau\bar{t}, \quad z = h\bar{z}, \quad U_g = V\bar{U}_g, \quad P = P_\mathrm{TOT}\bar{P},\\
&P_j = P_\mathrm{TOT}\bar{P}_j, \quad \sigma_s = c_0C_{p,C}\bar{\sigma}_s, \quad \sigma_g = \delta c_0C_{p,C}\bar{\sigma}_g, \quad F(z) = Q\bar{F}(\bar{z}).
\end{aligned} \tag{3.2}$$

Notice that the scalings in (3.2) are the same as in (2.29), apart from the chemical concentrations and the heat capacity in the gas. To make the presentation of the asymptotics appear cleaner, we have changed the notation of two variables from Chapter 2. The partial pressure of silicon monoxide and the equilibrium partial pressure functions, previously denoted P_SiO and $P_{\mathrm{SiO,equ,j}}$, are now written as P and P_j, respectively. Dropping the overbar notation from variables in (3.2), we have the dimensionless equations

$$\begin{aligned}
\frac{\partial}{\partial t}\begin{pmatrix} \mathrm{C_C} \\ \epsilon\mathrm{C_{SiC}} \\ \mathrm{C_{SiO_2(s)}} \\ \epsilon\mathrm{C_{SiO_2(l)}} \\ \epsilon\mathrm{C_{Si}} \\ \delta\mathrm{C}_g(1-P) \\ \delta\mathrm{C}_gP \end{pmatrix} + \frac{\partial}{\partial z}\begin{pmatrix} 0 \\ 0 \\ 0 \\ 0 \\ 0 \\ U_g\mathrm{C}_g(1-P) \\ U_g\mathrm{C}_gP \end{pmatrix} \\
= \begin{pmatrix} -2 & 0 & 0 & 0 & 0 & -1 \\ 1 & 0 & 0 & 0 & -1 & 0 \\ 0 & 0 & 0 & -1 & 0 & 0 \\ 0 & 1 & -1 & 1 & 0 & -1 \\ 0 & 1 & -1 & 0 & 2 & 0 \\ 1 & 0 & 0 & 0 & 1 & 1 \\ -1 & -2 & 2 & 0 & -1 & 1 \end{pmatrix}\begin{pmatrix} \epsilon r_1 \\ \epsilon r_2 \\ \epsilon r_{-2} \\ r_3 \\ \epsilon r_4 \\ r_5 \end{pmatrix},
\end{aligned} \tag{3.3}$$

$$\begin{aligned}
&g_0\left(T + \frac{T_\mathrm{top}}{T_0}\right)\mathrm{C}_g + m_\mathrm{C}\mathrm{C_C} + \epsilon m_\mathrm{SiC}\mathrm{C_{SiC}} + m_{\mathrm{SiO_2(s)}}\mathrm{C_{SiO_2(s)}} + \epsilon m_{\mathrm{SiO_2(l)}} + \mathrm{C_{SiO_2(l)}}\\
&+ \epsilon m_\mathrm{Si}\mathrm{C_{Si}} = 1,
\end{aligned} \tag{3.4}$$

$$\frac{\partial}{\partial t}\left(\left(T+\frac{T_{\text{top}}}{T_0}\right)\left(\sigma_s+\delta\sigma_g+\sigma_{gr}^*\right)\right)+\frac{\partial}{\partial z}\left(\left(T+\frac{T_{\text{top}}}{T_0}\right)U_g\sigma_g\right)$$
$$=a\frac{\partial^2 T}{\partial z}+\beta^*\frac{\partial}{\partial z}\left(\left(\frac{T_{\text{top}}}{T_0}+T\right)^3\frac{\partial T}{\partial z}\right)+\epsilon\left(\gamma_1 r_1+\gamma_2 r_2+\gamma_{-2}r_{-2}+\gamma_4 r_4\right)+\gamma_5 r_5+qF, \tag{3.5}$$

where

$$\begin{pmatrix} r_1 \\ r_2 \\ r_{-2} \\ r_3 \\ r_4 \\ r_5 \end{pmatrix}=\begin{pmatrix} \chi_1 \mathrm{C_C}(P-P_1(T))^+ \\ \chi_2(P-P_2(T))^+ \\ \chi_{-2}\mathrm{C_{SiO_2(l)}}\mathrm{C_{Si}} \\ \mathrm{C_{SiO_2(s)}}(T-T_m)^+ \\ \chi_4\mathrm{C_{SiC}}(P-P_4(T))^+ \\ \mathrm{C_{SiO_2(l)}}\mathrm{C_C} \end{pmatrix}, \tag{3.6}$$

$$\sigma_s=\mathrm{C_C}+\epsilon\mathrm{C_{SiC}}C_{P,\mathrm{SiC/C}}+\mathrm{C_{SiO_2(s)}}C_{P,\mathrm{SiO_2(s)/C}}+\epsilon\mathrm{C_{SiO_2(l)}}C_{P,\mathrm{SiO_2(l)/C}}+\epsilon\mathrm{C_{Si}}C_{P,\mathrm{Si/C}}, \tag{3.7}$$

$$\sigma_g=\mathrm{C}_g\left((1-P)C_{P,\mathrm{CO/C}}+PC_{P,\mathrm{SiO/C}}\right),\quad g_0=\delta\frac{R_gT_0c_0}{P_{\text{TOT}}},\quad m_{\mathrm{X}}=c_0\frac{M_{\mathrm{X}}}{\rho_{\mathrm{X}}}, \tag{3.8}$$

and parameters a, β^*, σ_{gr}^*, γ_j, and q are given in (2.30). We have the same dimensionless initial conditions (2.35) and boundary conditions (2.36) as in Chapter 2. For the sake of the reader we present them again below:

$$\begin{aligned}&\mathrm{C_C}=1,\quad \mathrm{C_{SiC}}=0,\quad \mathrm{C_{SiO_2(s)}}=\alpha,\quad \mathrm{C_{SiO_2(l)}}=0,\quad \mathrm{C_{Si}}=0,\quad P_{\mathrm{SiO}}=\frac{1}{2},\\ &U_g=0,\quad T=-1.1,\quad \mathrm{C}_g=\frac{P_{\text{TOT}}}{300R_g}\left(\frac{1}{c_0}-\left(\frac{M_{\mathrm{C}}}{\rho_{\mathrm{C}}}+\frac{M_{\mathrm{SiO_2}(s)}}{\rho_{\mathrm{SiO_2}(s)}}\alpha\right)\right),\end{aligned} \tag{3.9}$$

$$U_g(0,t)=0,\quad \frac{\partial T(0,t)}{\partial z}=0,\quad \frac{\partial T(1,t)}{\partial z}=0. \tag{3.10}$$

We have scaled the kinetic rates χ_j such that each is an order one constant, taking a typical value $\mathrm{r_C}=0.2$ when choosing the appropriate scale for r_1 (in line with Chapter 2). Each variable and parameter listed in equations (3.9) - (3.10) is order one. g_0 is an order one constant, since $R_gT_0c_0/P_{\text{TOT}}$ is $\mathcal{O}(\delta^{-1})$, as are the m_{X}. We have used the shorthand notation $C_{P,\mathrm{X/C}}:=C_{P,\mathrm{X}}/C_{P,\mathrm{C}}$ in the heat capacities σ_s and σ_g. T_m is the dimensionless melting temperature of quartz. There is no heat release associated with r_3 in the model, so $\gamma_3=0$.

To understand the behaviour of solutions to our model (3.3) - (3.10), we begin by constraining the temperature to be fixed, with a prescribed steady state temperature $T(z)$ considered in Section 3.3, and we neglect the energy equation (3.5). Although neither pilot or industrial furnaces operate with a steady state temperature, this allows us to focus on the chemical and gas transport dynamics, and makes the

analysis more tractable. In Section 3.4, we will return to the problem with time-variable temperature. Although less analytical progress can be made in that case, the simplifications developed allow for a reduced model to be identified.

In the model analysis in Chapter 2 we took the dimensionless heating function to be the discontinuous Heaviside function, $F(z) = q\mathcal{H}(h_T^* - z)$. In Section 3.5.1 we will use this function to ease the analysis of the resulting series solution. However, since an invertible $F(z)$ is required for asymptotic solution in Sections 3.5.2 and 3.5.3, when a specific heating profile is needed in these sections, we will use the smooth function $F(z) = \frac{q}{2}\left(1 + \tanh(\zeta(h_T^* - z))\right)$, which tends to $q\mathcal{H}(h_T^* - z)$ as $\zeta \to \infty$.

As in Chapter 2, all numerical simulations in this chapter are found using first order finite difference schemes, with upwinding for convective fluxes and the timestep chosen to obey the Courant-Friedrichs-Lewy (CFL) condition.

3.3 Prescribed temperature asymptotics

We analyse the dimensionless equations (3.3) - (3.4), but with a prescribed temperature profile, $T(z)$, instead of the energy equation (3.5). Initial conditions (3.9) and boundary conditions (3.10) are used for the concentrations, partial pressure, and gas velocity. Where possible we will work in terms of a general $T(z)$, but any time a specific profile is used we will utilise the piecewise linear profile $T(z) = \min\left(1, \frac{1-z}{1-h_T^*}\right)$. With this function, the furnace is at constant unitary temperature up to a dimensionless height $h_T^* = 0.544$, and above this height linearly decays to zero at the top of the furnace. This is to replicate the experimental behaviour, where the induction furnace creates a temperature gradient by inputting more heat into the bottom of the furnace, as discussed in Chapter 2 (see Figure 2.2).

There are different spatial regions in the problem, due to the behaviour of the melting reaction $r_3 = \mathrm{C}_{\mathrm{SiO_2(s)}}(T - T_m)^+$. In the lower, hotter part of the furnace we have $T > T_m$, and hence $r_3 = \mathcal{O}(1)$. In the upper, colder region of the furnace we have $T < T_m$, and hence $r_3 = 0$. These regions are separated by an interface given by the isotherm $T = T_m$. With a prescribed temperature profile, we do not consider any temperature transient as it heats from cold, but the process starts from the prescribed hot profile. Hence, the chemistry has a rapid transient period, before getting near typical operating conditions. There are thus four main regimes of behaviour of the chemistry in height-time space. A schematic diagram is shown in Figure 3.1.

There is a separation between the blue region, where the temperature is too cold for solid quartz to melt, and the red region, where quartz melts. There is also a

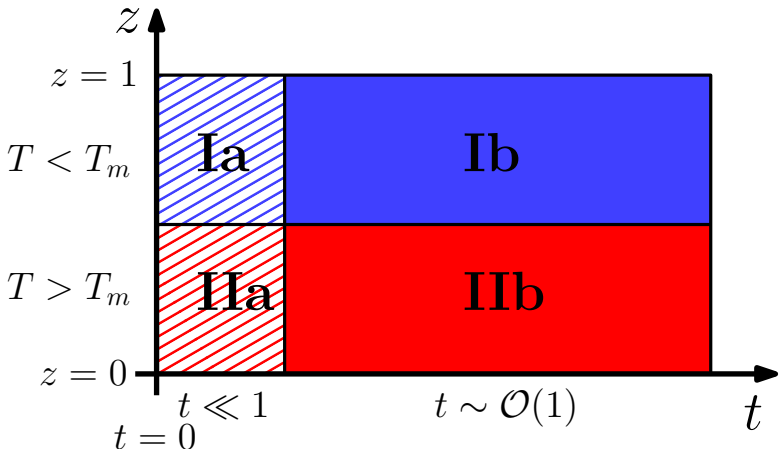


Figure 3.1: Schematic diagram of asymptotic regimes. Hashed regions correspond to early time and solid regions to larger time. The blue region, where the temperature is below the melting point of quartz, corresponds to the furnace charge. The red region, where melting of quartz occurs, corresponds to the mixed cavity and crater region in the model.

separation between the early time regions (shown as hashed), where the pilot furnace moves away from the initial conditions to dynamics more likely to be seen in the industrial furnace, and the $\mathcal{O}(1)$ time regions (shown as solid). Since in all practical situations $U_g \geq 0$, and we have assumed no solid or liquid motion, we have that information propagates upwards in Figure 3.1 (so from Region II to Region I) as well as rightwards (from Region a to Region b). We now give details of the behaviour in each region found through expanding each variable in terms of the small parameter ϵ. That is, for a variable Y, we have $Y = Y^0 + \epsilon Y^1 + \mathcal{O}(\epsilon^2)$. We begin by considering Region II, since the gas produced in this region influences the dynamics in Region I. We find analytic solutions in Regions IIa and IIb and, where appropriate, give composite solutions that replicate both the inner and outer time behaviour. We then examine the upper part of the furnace, which is Region I. In Region Ia, we list the leading order equations, but find that the solid and liquid concentrations are solved by the initial conditions. Hence the corresponding leading order equations arising in Region Ib can be solved with these initial conditions, and analytic solutions are found for all of Region I. Matching occurs between Regions I and II in terms of continuity of the gas flux across the interface $T = T_m$. We give a summary of the main asymptotic behaviour in each region, but do not include all the details. A summary of leading and first order solutions is given in Appendix B.

3.3.1 Region IIa - early time cavity and crater

We find that the appropriate timescale is $t = \epsilon\hat{t}$, where $\hat{t}$ is an order one variable. With this rescaling, we find that the leading order equations from the matrix system (3.3) are at $\mathcal{O}(\epsilon^{-1})$, and are given by

$$\frac{1}{\epsilon}\frac{\partial \mathrm{C}^0_{\mathrm{C}}}{\partial \hat{t}} = \mathcal{O}(1), \quad \frac{1}{\epsilon}\frac{\partial \mathrm{C}^0_{\mathrm{SiO_2(s)}}}{\partial \hat{t}} = \mathcal{O}(1), \tag{3.11}$$

which have solutions $\mathrm{C}^0_{\mathrm{C}} = 1$ and $\mathrm{C}^0_{\mathrm{SiO_2(s)}} = \alpha$. We use these solutions when finding the leading order terms for the other variables. For the concentrations of SiC, $\mathrm{SiO_2(l)}$, and Si, we have

$$\frac{\partial \mathrm{C}^0_{\mathrm{SiC}}}{\partial \hat{t}} = \mathcal{O}(\epsilon), \quad \frac{\partial \mathrm{C}^0_{\mathrm{SiO_2(l)}}}{\partial \hat{t}} = \alpha(T - T_m) - \mathrm{C}^0_{\mathrm{SiO_2(l)}} + \mathcal{O}(\epsilon), \quad \frac{\partial \mathrm{C}^0_{\mathrm{Si}}}{\partial \hat{t}} = \mathcal{O}(\epsilon). \tag{3.12}$$

With the zero initial conditions, we have $\mathrm{C}^0_{\mathrm{SiC}} = 0$, $\mathrm{C}^0_{\mathrm{Si}} = 0$, and

$$\mathrm{C}^0_{\mathrm{SiO_2(l)}} = \alpha\left(T(z) - T_m\right)\left(1 - e^{-\hat{t}}\right) = \alpha\left(T(z) - T_m\right)\left(1 - e^{-t/\epsilon}\right). \tag{3.13}$$

We can find the leading order gas flux, $U^0_g \mathrm{C}^0_g$, and pressure, P^0, from the equations

$$\frac{\partial}{\partial z}\left(U^0_g \mathrm{C}^0_g (1 - P^0)\right) = \mathrm{C}^0_{\mathrm{SiO_2(l)}} + \mathcal{O}(\epsilon), \tag{3.14a}$$

$$\frac{\partial}{\partial z}\left(U^0_g \mathrm{C}^0_g P^0\right) = \mathrm{C}^0_{\mathrm{SiO_2(l)}} + \mathcal{O}(\epsilon). \tag{3.14b}$$

Utilising the no-flux boundary condition $U_g(0, \hat{t}) = 0$, we can add the above equations and integrate, to find

$$U^0_g \mathrm{C}^0_g = 2\alpha\left(1 - e^{-t/\epsilon}\right)\int_{y=0}^{y=z}\left(T(y) - T_m\right)dy, \tag{3.15}$$

and hence $P^0 = \frac{1}{2}$. We can find C^0_g from the reduced, leading order no-voids condition

$$g_0\left(T + \frac{T_{\mathrm{top}}}{T_0}\right)\mathrm{C}^0_g + m_{\mathrm{C}} + m_{\mathrm{SiO_2(s)}}\alpha + \mathcal{O}(\epsilon) = 1, \tag{3.16}$$

so that for prescribed $T(z)$, we obtain

$$\mathrm{C}^0_g = \frac{1 - m_{\mathrm{C}} - m_{\mathrm{SiO_2(s)}}\alpha}{g_0\left(T(z) + \frac{T_{\mathrm{top}}}{T_0}\right)}. \tag{3.17}$$

Thus, the concentration of gas increases as the temperature decreases higher up in the furnace. The leading order gas velocity U^0_g can then be found using (3.15) and (3.17). Note that on an even smaller $\mathcal{O}(\delta)$ timescale, different behaviour would be found, with the time derivative of $\mathrm{C}^0_g(1 - P^0)$ and $\mathrm{C}^0_g P^0$ balancing with the convective flux and reaction r^0_5 in (3.3). However, the resulting wave-like behaviour only describes the very fast transient behaviour of the gas flux and pressure, and so is not discussed for the sake of brevity.

3.3.2 Region IIb - order one time crater and cavity

We next examine behaviour in the outer-in-time crater and cavity region. Here we have the order one timescale, t. The order one equations are found to be

$$\frac{\partial \mathrm{C}_{\mathrm{C}}^0}{\partial t} = -r_5^0, \quad \frac{\partial \mathrm{C}_{\mathrm{SiO_2(s)}}^0}{\partial t} = -r_3^0, \quad 0 = r_3^0 - r_5^0, \tag{3.18a}$$

$$\frac{\partial}{\partial z}\left(U_g^0 \mathrm{C}_g^0 (1 - P^0)\right) = r_5^0, \quad \frac{\partial}{\partial z}\left(U_g^0 \mathrm{C}_g^0 P^0\right) = r_5^0, \tag{3.18b}$$

which all have $\mathcal{O}(\epsilon)$ corrections, while the no-voids equation is

$$g_0 \left(T + \frac{T_{\mathrm{top}}}{T_0}\right) \mathrm{C}_g^0 + m_{\mathrm{C}} \mathrm{C}_{\mathrm{C}}^0 + m_{\mathrm{SiO_2(s)}} \mathrm{C}_{\mathrm{SiO_2(s)}}^0 = 1 + \mathcal{O}(\epsilon). \tag{3.19}$$

From the third equation in (3.18a), we have a leading order balance between the melting of quartz r_3^0 and the production of CO and SiO gas from liquid quartz and carbon, r_5^0. This corresponds to a quasi-steady state assumption, since the time rate of change of liquid quartz is an order smaller than the reaction rates r_3 and r_5. This reaction balance was the motivation for choosing $\epsilon = k_3 T_0 / k_5 c_0$ and scaling the concentrations of SiC, SiO_2(s), and Si to be $\mathcal{O}(\epsilon)$ in Section 3.2. We have the reaction rate $r := r_3^0 = r_5^0$ from this balance, and find it is easiest to work with

$$r := \mathrm{C}_{\mathrm{SiO_2(s)}}^0 (T - T_m). \tag{3.20}$$

As the leading order terms for the concentrations of carbon and solid quartz in Region IIa are the initial conditions, the solutions in Region IIb are found to be

$$\mathrm{C}_{\mathrm{C}}^0 = \alpha e^{-(T-T_m)t} + (1 - \alpha), \quad \mathrm{C}_{\mathrm{SiO_2(s)}}^0 = \alpha e^{-(T-T_m)t}. \tag{3.21}$$

In Figure 3.2 we compare these solutions with numerical simulations corresponding to a fixed temperature profile, showing a good fit. We find $\mathrm{C}_{\mathrm{SiO_2(l)}}^0$ from the balance between r_3^0 and r_5^0, obtaining

$$\mathrm{C}_{\mathrm{SiO_2(l)}}^0 = \frac{\mathrm{C}_{\mathrm{SiO_2(s)}}^0 (T - T_m)}{\mathrm{C}_{\mathrm{C}}^0} = \frac{(T - T_m)\alpha e^{-(T-T_m)t}}{\alpha e^{-(T-T_m)t} + (1 - \alpha)}. \tag{3.22}$$

Although $\mathrm{C}_{\mathrm{SiO_2(l)}}^0$ given by (3.22) tends to zero as t increases, it does not satisfy the initial condition of $\mathrm{C}_{\mathrm{SiO_2(l)}} = 0$. This is accounted for in Section 3.3.1, where the early time behaviour is examined.

To find the gas flux, we add the equations in (3.18b) and integrate spatially, applying the no-flux boundary condition $U_g^0(0,t) = 0$, to give

$$U_g^0(z,t)\mathrm{C}_g^0(z,t) = 2\alpha \int_{y=0}^{y=z} e^{-(T(y)-T_m)t} \left(T(y) - T_m\right) dy = -2\alpha \frac{\partial}{\partial t} \int_{y=0}^{y=z} e^{-(T(y)-T_m)t} dy. \tag{3.23}$$

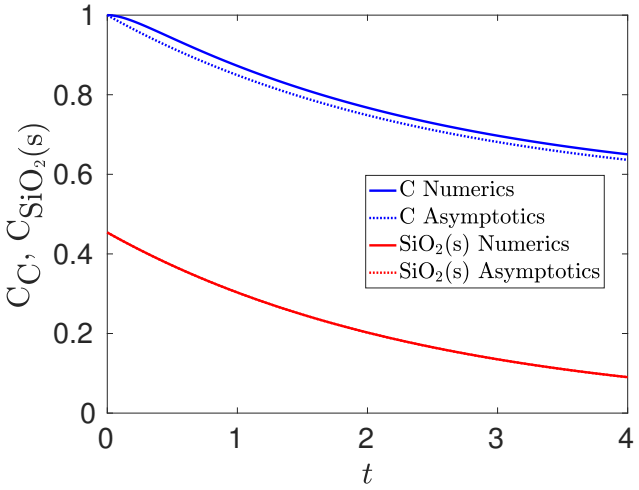


Figure 3.2: Dimensionless concentration of carbon, in blue, and solid quartz, in red, at height $z = 0.3$. We compare numerical solutions of the full system with $T(z)$ in solid lines to asymptotic solutions in dashed lines, with parameter values $\epsilon = 0.16$, $\delta = 3.2 \times 10^{-4}$, and $\alpha = 0.45$.

We can find the leading order pressure by integrating the second equation in (3.18b), and noting that

$$U_g^0 \mathrm{C}_g^0 P^0 = \frac{1}{2} U_g^0 C_g^0 + g(t). \tag{3.24}$$

The arbitrary function of time, $g(t)$, is zero from the no-flux boundary condition for velocity, and since $U_g^0 \mathrm{C}_g^0 \neq 0$ in general, we again have $P^0 = \frac{1}{2}$.

We can find the concentration of gas through (3.19), which gives

$$\mathrm{C}_g^0 = \frac{1}{g_0\left(T + \frac{T_{\mathrm{top}}}{T_0}\right)} \left(1 - (m_{\mathrm{C}} + m_{\mathrm{SiO_2(s)}})\alpha e^{-(T-T_m)t} - m_{\mathrm{C}}(1-\alpha)\right). \tag{3.25}$$

Notice that although this is not a separable solution, we can decompose the solution (3.25) as $\mathrm{C}_g^0(z,t) = X(z)Y(t,z)$ for

$$X(z) := \frac{1}{g_0\left(T + \frac{T_{\mathrm{top}}}{T_0}\right)}, \quad Y(t,z) := 1 - (m_{\mathrm{C}} + m_{\mathrm{SiO_2(s)}})\alpha e^{-(T-T_m)t} - m_{\mathrm{C}}(1-\alpha). \tag{3.26}$$

Thus $Y(0,z) = 1 - m_{\mathrm{SiO_2(s)}}\alpha - m_{\mathrm{C}}$ and $Y(t,z) \to 1 - m_{\mathrm{C}}(1-\alpha)$ as $t \to \infty$. This means that there is a saturation level for the gas concentration, which happens as the concentrations of carbon and solid quartz tend towards their long time behaviour.

If required, we could calculate the velocity from the solutions for the gas flux and the gas concentration. For example, using our specific example temperature profile

$T(z) = \min\left(1, \frac{1-z}{1-h_T^*}\right)$, in the region $0 \le z \le h_T^*$ where $T(z) \equiv 1$, we have

$$U_g^0(z,t) = 2\alpha \frac{(1-T_m)e^{-(1-T_m)t}z}{\mathrm{C}_g^0(z,t)}. \tag{3.27}$$

We can find composite asymptotic solutions valid for all time by combining our inner-in-time and outer-in-time solutions. Letting y_I denote an inner solution, y_O an outer solution, and $y_{overlap}$ the overlap, we have that the composite solution, y_c, is given by $y_c = y_I + y_O - y_{overlap}$. The composite solution for the concentration of SiO_2(l) is thus

$$\mathrm{C}^0_{\mathrm{SiO_2(l)}} = \alpha(T - T_m)\left(\frac{e^{-(T-T_m)t}}{\alpha e^{-(T-T_m)t} + (1-\alpha)} - e^{-\frac{t}{\epsilon}}\right). \tag{3.28}$$

Similarly, for the gas flux, we have

$$U_g^0(z,t)\mathrm{C}_g^0(z,t) = 2\alpha \int_{y=0}^{y=z} (T(y) - T_m)\left(e^{-(T(y)-T_m)t} - e^{-\frac{t}{\epsilon}}\right) dy. \tag{3.29}$$

In Figure 3.3 we compare the early time, late time, and composite asymptotics with numerics for the full system, for the concentration of liquid quartz and the gas flux. The numerical and composite asymptotic curves match in long time, as the variables go to zero. The difference between the curves is due to the reactions r_2 and r_{-2}, which do not appear in the leading order asymptotics.

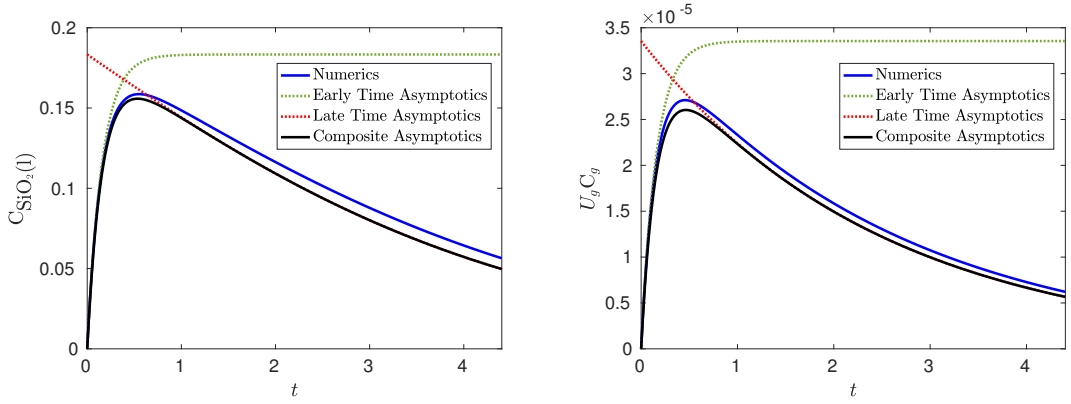


Figure 3.3: Comparison of early time, late time, and composite asymptotics, with numerics of the full system with prescribed temperature profile at height $z = 0.3$. On the left is the concentration of liquid quartz, and on the right is the gas flux (both dimensionless). Parameter values used are $\epsilon = 0.16$, $\delta = 3.2 \times 10^{-4}$, $\alpha = 0.45$, $\chi_1 = 0.15$, and $\chi_2 = 0.25$.

The equations for the leading order concentrations of SiC and Si are

$$\epsilon \frac{\partial \mathrm{C}^0_{\mathrm{SiC}}}{\partial t} = \epsilon\chi_1\left(\alpha e^{-(T-T_m)t} + (1-\alpha)\right)\left(\frac{1}{2} - P_1\right)^+ - \epsilon\chi_4 \mathrm{C}^0_{\mathrm{SiC}}\left(\frac{1}{2} - P_4\right)^+ + \mathcal{O}(\epsilon^2), \tag{3.30}$$

$$\epsilon\frac{\partial \mathrm{C}_{\mathrm{Si}}^0}{\partial t} = \epsilon\chi_2\left(\frac{1}{2}-P_2\right)^+ - \epsilon\chi_{-2}\left(\frac{(T-T_m)\alpha e^{-(T-T_m)t}}{\alpha e^{-(T-T_m)t}+(1-\alpha)}\right)\mathrm{C}_{\mathrm{Si}}^0 + 2\epsilon\chi_4\mathrm{C}_{\mathrm{SiC}}^0\left(\frac{1}{2}-P_4\right)^+ + \mathcal{O}(\epsilon^2). \tag{3.31}$$

Equations (3.30) and (3.31), along with the zero initial conditions (3.9), may be solved analytically by first solving (3.30) and then substituting the result into (3.31). In the typical temperature range found in Region II, we find $P_1 < \frac{1}{2}$, but P_2 and P_4 can be smaller or larger than $\frac{1}{2}$, hence the different cases would need to be considered individually. We do not include these cases here, but they are listed in Appendix B for completeness.

3.3.3 Region Ia - early time furnace charge

We now consider the upper region in the furnace, which corresponds to the furnace charge. In this region, $T < T_m$, so the solid quartz does not melt, and $r_3 \equiv 0$. Hence, $\mathrm{C}_{\mathrm{SiO_2(s)}} = \alpha$ for all time, and we now have seven equations for the remaining seven unknowns, consisting of the concentrations of C, SiC, $\mathrm{SiO_2(l)}$, Si, and gas, the partial pressure, P, and the gas flux, U_g. We begin with Region Ia, where we analyse the early time behaviour. Using the same timescale as in Region IIa, namely $t = \epsilon\hat{t}$, we find that the leading order equations for each variable are given by

$$\frac{1}{\epsilon}\frac{\partial \mathrm{C}_{\mathrm{C}}^0}{\partial \hat{t}} = \mathcal{O}(1), \quad \frac{\partial \mathrm{C}_{\mathrm{SiC}}^0}{\partial \hat{t}} = \mathcal{O}(\epsilon), \quad \frac{\partial \mathrm{C}_{\mathrm{SiO_2(l)}}^0}{\partial \hat{t}} = -r_5^0 + \mathcal{O}(\epsilon), \quad \frac{\partial \mathrm{C}_{\mathrm{Si}}^0}{\partial \hat{t}} = \mathcal{O}(\epsilon), \tag{3.32a}$$

$$\frac{\partial}{\partial z}\left(U_g^0\mathrm{C}_g^0(1-P^0)\right) = r_5^0 + \mathcal{O}(\epsilon), \quad \frac{\partial}{\partial z}\left(U_g^0\mathrm{C}_g^0P^0\right) = r_5^0 + \mathcal{O}(\epsilon), \tag{3.32b}$$

$$g_0\left(T+\frac{T_{\mathrm{top}}}{T_0}\right)\mathrm{C}_g^0 + m_{\mathrm{C}}\mathrm{C}_{\mathrm{C}}^0 + m_{\mathrm{SiO_2(s)}}\alpha = 1 + \mathcal{O}(\epsilon). \tag{3.32c}$$

We immediately see that $\mathrm{C}_{\mathrm{C}}^0 = 1$, $\mathrm{C}_{\mathrm{SiC}}^0 = 0$, and $\mathrm{C}_{\mathrm{Si}}^0 = 0$. Since $r_5^0 = \mathrm{C}_{\mathrm{C}}^0\mathrm{C}_{\mathrm{SiO_2(l)}}^0 = \mathrm{C}_{\mathrm{SiO_2(l)}}^0$, we find the third equation in (3.32a) leads to $\mathrm{C}_{\mathrm{SiO_2(l)}}^0 = 0$, since the pre-exponential factor is zero from the initial condition. Thus, the leading order concentrations of the solid and liquid species are given by their initial conditions, and they do not significantly change in early time. When analysing their dynamics in Region Ib, we use initial conditions for the whole model (3.9). Similarly, since $\mathrm{C}_{\mathrm{C}}^0 = 1$ and $\mathrm{C}_{\mathrm{SiO_2(s)}}^0 = \alpha$, C_g^0 is constant, given by (3.32c). We then find that $U_g^0\mathrm{C}_g^0$ and P^0 are both functions of time only, since $r_5^0 = 0$. We can find these functions by imposing continuity of the gas flux and pressure across the interface $z = z_m$ (which is $z : T(z) = T_m$), and utilising solutions from Region IIa below. Hence, $P^0 = \frac{1}{2}$ and

$$U_g^0\mathrm{C}_g^0 = 2\alpha\left(1-e^{-t/\epsilon}\right)\int_{y=0}^{y=z_m}(T(y)-T_m)\,dy, \tag{3.33}$$

where we have used the gas flux at $z = z_m$ from (3.15).

3.3.4 Region Ib - order one time furnace charge

We now consider order one time behaviour in the upper furnace, where $T < T_m$. We find the leading order equations for the solid and liquid concentrations are

$$\begin{aligned} \frac{\partial \mathrm{C}_{\mathrm{C}}^0}{\partial t} &= -r_5^0 + \mathcal{O}(\epsilon), \quad \epsilon\frac{\partial \mathrm{C}_{\mathrm{SiC}}^0}{\partial t} = \epsilon r_1^0 - \epsilon r_4^0 + \mathcal{O}(\epsilon^2), \\ 0 &= -r_5^0 + \mathcal{O}(\epsilon), \quad \epsilon\frac{\partial \mathrm{C}_{\mathrm{Si}}^0}{\partial t} = \epsilon r_2^0 - \epsilon r_{-2}^0 + \epsilon r_4^0 + \mathcal{O}(\epsilon^2), \end{aligned} \tag{3.34}$$

along with the gas flux equations (3.32b) and the reduced no-voids equation (3.32c) from Region Ia. Since $r_5^0 = 0$, then $\mathrm{C}_{\mathrm{C}}^0 = 1$ and the partial pressure and gas flux are again given by imposing continuity from below, this time with Region IIb, to give $P^0 = \frac{1}{2}$, and

$$U_g^0 \mathrm{C}_g^0 = 2\alpha \int_{y=0}^{y=z_m} e^{-(T(y)-T_m)t}\,(T(y) - T_m)\,dy, \tag{3.35}$$

using (3.23). Also, since $r_5^0 = 0$ and $r_5^0 = \mathrm{C}_{\mathrm{C}}^0 \mathrm{C}_{\mathrm{SiO_2(l)}}^0$, then $\mathrm{C}_{\mathrm{SiO_2(l)}}^0 = 0$, and hence $r_{-2}^0 = \chi_{-2}\mathrm{C}_{\mathrm{SiO_2(l)}}^0 \mathrm{C}_{\mathrm{Si}}^0 = 0$. We now examine the $\mathcal{O}(\epsilon)$ equations for the concentrations of solid and liquid species,

$$\begin{aligned} \frac{\partial \mathrm{C}_{\mathrm{C}}^1}{\partial t} &= -2r_1^0 - r_5^1 + \mathcal{O}(\epsilon), \quad \frac{\partial \mathrm{C}_{\mathrm{SiC}}^0}{\partial t} = r_1^0 - r_4^0 + \mathcal{O}(\epsilon), \\ 0 &= r_2^0 - r_5^1 + \mathcal{O}(\epsilon), \quad \frac{\partial \mathrm{C}_{\mathrm{Si}}^0}{\partial t} = r_2^0 + 2r_4^0 + \mathcal{O}(\epsilon). \end{aligned} \tag{3.36}$$

There is a balance between r_2 and r_5, so that the liquid quartz, which condenses through r_2, reacts with the available carbon through r_5. Since reaction r_5 is limited by the amount of liquid quartz available, it is of size $\mathcal{O}(\epsilon)$ in the upper furnace, which is much smaller than the $\mathcal{O}(1)$ reaction in the lower furnace, in which the available liquid quartz is provided through reaction r_3, the melting of solid quartz. Indeed, to order one, no reactions take place in the furnace charge and the chemical species remain in their initial state. To find the $\mathcal{O}(\epsilon)$ changes to the chemical species, we utilise the balance $r_2^0 = r_5^1$ and solutions $\mathrm{C}_{\mathrm{C}}^0 = 1$ and $P^0 = \frac{1}{2}$. In addition, when $T < T_m$, we have that $P_4 > \frac{1}{2}$, but $P_1, P_2 < \frac{1}{2}$ (see the equilibrium partial pressure diagram in Figure 2.3). Hence, we have that

$$\frac{\partial \mathrm{C}_{\mathrm{C}}^1}{\partial t} = -2\chi_1\left(\frac{1}{2} - P_1\right) - \chi_2\left(\frac{1}{2} - P_2\right), \tag{3.37a}$$

$$\frac{\partial \mathrm{C}_{\mathrm{SiC}}^0}{\partial t} = \chi_1\left(\frac{1}{2} - P_1\right), \tag{3.37b}$$

$$\frac{\partial \mathrm{C}_{\mathrm{Si}}^0}{\partial t} = \chi_2 \left(\frac{1}{2} - P_2 \right). \tag{3.37c}$$

In Section 3.3.3 we calculated $\mathrm{C_C}$ only to first order, but we can easily find that $\mathrm{C}_{\mathrm{C}}^1 = 0$ in Region Ia. Hence, we use the zero Dirichlet condition for $\mathrm{C}_{\mathrm{C}}^1$ in Region Ib, as well as for $\mathrm{C}_{\mathrm{SiC}}^0$ and $\mathrm{C}_{\mathrm{Si}}^0$, to find

$$\mathrm{C}_{\mathrm{C}}^1 = -\left(2\chi_1 \left(\frac{1}{2} - P_1 \right) + \chi_2 \left(\frac{1}{2} - P_2 \right) \right) t, \tag{3.38a}$$

$$\mathrm{C}_{\mathrm{SiC}}^0 = \chi_1 \left(\frac{1}{2} - P_1 \right) t, \tag{3.38b}$$

$$\mathrm{C}_{\mathrm{Si}}^0 = \chi_2 \left(\frac{1}{2} - P_2 \right) t. \tag{3.38c}$$

We show comparisons of these solutions with numerics in Figure 3.4. We have that carbon is being lost to gas through reaction r_5 (reacting with the liquid quartz produced through r_2) and to silicon carbide through reaction r_1. The production of silicon through r_2 is equal to the loss of carbon through r_5, since all the available liquid quartz reacts with carbon (to leading order). The dynamics in the furnace charge are driven by the behaviour of convecting SiO molecules, which can condense through r_2, leading to silicon production, react with carbon, through r_1 to produce silicon carbide, or convect out of the furnace unreacted. The parameter ratio χ_2/χ_1 determines the relative importance of reactions r_1 and r_2. The larger χ_2/χ_1 is, the more silicon will be produced. The smaller χ_2/χ_1 is, the more silicon carbide will build up.

We now find the $\mathcal{O}(\epsilon)$ corrections to the gas flux and the pressure. Adding the last two rows in (3.3) gives an equation for the gas flux, which we treat as one variable (so that $U_g \mathrm{C}_g = U_g^0 \mathrm{C}_g^0 + \epsilon U_g^1 \mathrm{C}_g^1 + \mathcal{O}(\epsilon^2)$). We have that $U_g^0 \mathrm{C}_g^0 = f(t)$, given by (3.35), and we find that

$$\epsilon \frac{\partial}{\partial z} \left(U_g^1 \mathrm{C}_g^1 \right) = -2\epsilon r_2^0 + 2\epsilon r_5^1 + \mathcal{O}(\epsilon^2). \tag{3.39}$$

By the balance $r_2^0 = r_5^1$ in (3.36), we have that $U_g^1 \mathrm{C}_g^1$ is also a function of time only, which may be given from matching with the region below, Region IIb, if we desired. The $\mathcal{O}(\epsilon)$ equation for P^1 is

$$\epsilon \frac{\partial}{\partial z} \left(U_g^0 \mathrm{C}_g^0 P^1 + U_g^1 \mathrm{C}_g^1 P^0 \right) = -\epsilon r_1^0 - 2\epsilon r_2^0 + \epsilon r_5^1 + \mathcal{O}(\epsilon^2), \tag{3.40}$$

where we have noted that $r_{-2}^0 = r_4^0 = 0$. Using $r_5^1 = r_2^0$, and since $U_g^0 \mathrm{C}_g^0 = f(t)$ and $U_g^1 \mathrm{C}_g^1 P^0$ are both spatially independent, we have

$$f(t) \frac{\partial P^1}{\partial z} = -\left(\chi_1 \left(\frac{1}{2} - P_1(T(z)) \right) + \chi_2 \left(\frac{1}{2} - P_2(T(z)) \right) \right). \tag{3.41}$$

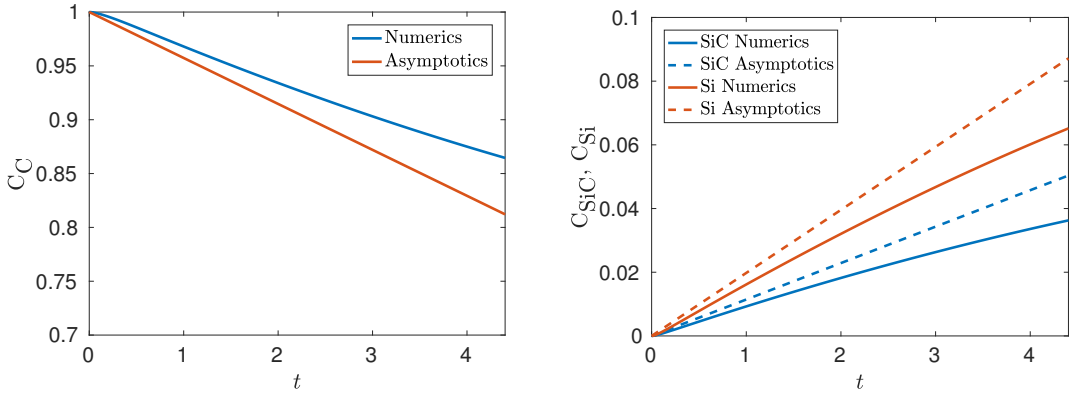


Figure 3.4: Comparison of numerical simulations and asymptotic solutions at $z = 0.9$. On the left are plots of the dimensionless concentration of carbon, showing numerics in blue and asympotics in red. On the right are plots of the dimensionless concentrations of SiC (in blue) and Si (in red), showing numerics in solid lines and asympotics in dashed lines. There is agreement to $\mathcal{O}(\epsilon)$ but noticeable $\mathcal{O}(\epsilon^2)$ disagreement, which would be reduced through addition of more terms in the ϵ expansion. Notice that the scale for the left plot is between 0.7 and 1, so there is an approximate 5% error for C_C, and the scale on the right plot is only up to 0.1, so the absolute error for C_{SiC} and C_{Si} is also small, since these are order one dimensionless variables. Parameter values used are $\epsilon = 0.16$, $\delta = 3.2 \times 10^{-4}$, $\chi_1 = 0.15$, and $\chi_2 = 0.25$.

This implies

$$P^1 = \frac{A(z)}{f(t)} + b(t), \tag{3.42}$$

where $A(z)$ is a decreasing function in z and $b(t)$ is an arbitrary function of time. Since $f(t) \to 0$ as $t \to \infty$, this form of P^1 breaks down after a long time. The timescale on which $P^1 = \mathcal{O}(\epsilon^{-1})$, thus breaking down the asymptotic expansion, is the timescale on which $f(t) = U_g^0 C_g^0$ given by (3.35) is $\mathcal{O}(\epsilon)$ (assuming $A(z) = \mathcal{O}(1)$). Assuming $M/2\alpha := \max|T'(y)|$ is an order one constant and letting $x := T(y) - T_m$, we have

$$|f(t)| \leq M \left| \int_{x=0}^{1-T_m} x e^{-xt} dx \right| \leq M t^{-2}, \tag{3.43}$$

and so this happens for $t = \mathcal{O}(\epsilon^{-1/2})$. In numerical simulations we find that $P \to P_2$ in long time behaviour, so that the condensation of SiO stops, but the reaction r_1 with carbon continues (as $P_2 > P_1$, see Figure 2.3).

By prescribing a temperature profile $T(z)$, we have identified two spatial regions - a lower crater and cavity region, in which there is a balance between reactions r_3 and r_5, and an upper furnace charge region in which chemical changes occur in smaller $\mathcal{O}(\epsilon)$ quantities and there is a balance between reactions r_2 and r_5. By expanding variables

in terms of the small parameter ϵ, we have found analytic solutions throughout the furnace, with composite solutions for early time and order one time behaviour in Region II, where appropriate. Information propagates upwards from the crater and cavity to the charge through the gas flux - an effect that we have quantified. In the charge there is competition between reactions r_1, producing SiC, and r_2, producing Si.

3.4 Full model asymptotics

We now consider asymptotics of the full model, comprising equations (3.3) - (3.5), initial conditions (3.9), and boundary conditions (3.10). We utilise the balances developed in Section 3.3 and extend our analysis to consider a spatially and temporally varying temperature $T(z,t)$. In the pilot furnace experiments we see that the interface between the furnace charge and the cavity region rises as the furnace heats up. We would thus expect to have regions similar to Regions I and II as in Figure 3.1, except that the interface $z = z_m$ moves with time. Considering the full model with varying temperature is thus important, because it captures this rising interface. In this section we reduce our model to two coupled equations for temperature and the concentration of solid quartz, which are dependent on three parameters. This simplified coupled model captures much of the qualitative behaviour of the full model, which has nine variables and over thirty parameters. We analyse early time behaviour, before reactions occur significantly, and consider the limit of small diffusion. We also comment on the joint limits of small diffusion and small external heating.

We consider leading order terms in the conservation of energy equation (3.5) in the joint limit $\epsilon \to 0$ and $\delta/\epsilon \to 0$. The superscript notation ^{0} used in Section 3.3 is dropped, with the assumption that all variables used to determine the simplified system are $\mathcal{O}(1)$. Although there are different equations in Regions I and II in Section 3.3, the changes in Region II are of higher order than in the other regions, so our leading order equations capture these effects primarily. To $\mathcal{O}(1)$, no chemical changes occur in the top of the furnace, but reactions and chemical transformations happen in the base. There is a balance between reactions r_3 and r_5 in the furnace base, so we integrate the first two equations in (3.18a) to get the algebraic relation $\mathrm{C_C} = \mathrm{C_{SiO_2(s)}} + (1-\alpha)$. Note that this does not hold in the top of the furnace, where carbon slowly decays but the concentration of solid quartz remains constant. However, this is an $\mathcal{O}(\epsilon)$ effect only. Noting that $P = \frac{1}{2}$ to leading order, we then have

$$\sigma_s = \mathrm{C_{SiO_2(s)}}\left(1 + C_{P,\mathrm{SiO_2(s)/C}}\right) + (1-\alpha) + \mathcal{O}(\epsilon), \tag{3.44a}$$

$$\sigma_g = \frac{1}{2}\mathrm{C}_g\left(C_{P,\mathrm{CO/C}} + C_{P,\mathrm{SiO/C}}\right) + \mathcal{O}(\epsilon), \tag{3.44b}$$

as leading order terms to equations (3.7) and (3.8). Combining these with the leading order terms in (3.5), and using $r = \mathrm{C}_{\mathrm{SiO_2(s)}}(T - T_m)^+$ as the functional form for $r := r_3 = r_5$, we obtain the leading order equations, with $\mathcal{O}(\epsilon)$ corrections,

$$\begin{aligned}\frac{\partial}{\partial t}\left(\left(\frac{T_{\mathrm{top}}}{T_0} + T\right)\left(\sigma_s + \sigma^*_{gr}\right)\right) + \frac{\partial}{\partial z}\left(\left(\frac{T_{top}}{T_0} + T\right)\frac{U_g\sigma_g}{2}\right)\\ = a\frac{\partial T^2}{\partial z^2} + \beta^*\frac{\partial}{\partial z}\left(\left(\frac{T_{top}}{T_0} + T\right)^3\frac{\partial T}{\partial z}\right) + \gamma_5\mathrm{C}_{\mathrm{SiO_2(s)}}(T - T_m)^+ + qF(z),\end{aligned} \tag{3.45}$$

$$\frac{\partial}{\partial z}\left(U_g\mathrm{C}_g\right) = 2\mathrm{C}_{\mathrm{SiO_2(s)}}(T - T_m)^+, \tag{3.46}$$

$$\frac{\partial \mathrm{C}_{\mathrm{SiO_2(s)}}}{\partial t} = -\mathrm{C}_{\mathrm{SiO_2(s)}}(T - T_m)^+, \tag{3.47}$$

$$g_0\left(T + \frac{T_{\mathrm{top}}}{T_0}\right)\mathrm{C}_g + \mathrm{C}_{\mathrm{SiO_2(s)}}(m_{\mathrm{C}} + m_{\mathrm{SiO_2(s)}}) + (1 - \alpha)m_{\mathrm{C}} = 1, \tag{3.48}$$

along with boundary and initial conditions

$$\frac{\partial T(0,t)}{\partial z} = 0 = \frac{\partial T(1,t)}{\partial z}, \quad T(z,0) = T_a = -1.1, \quad U_g(0,t) = 0, \quad \mathrm{C}_{\mathrm{SiO_2(s)}}(z,0) = \alpha. \tag{3.49}$$

We further simplify our system by neglecting radiation, since $\beta^*\left(\frac{T_{\mathrm{top}}}{T_0} + T\right)^3/a \sim 0.27$ at the hottest part of the furnace, and thermal convection from (3.45). Although these are both order one effects, we seek to get the simplest model which represents the main physical and chemical effects, thus making the analysis more tractable. We thus replace (3.45) with

$$\begin{aligned}\frac{\partial}{\partial t}\left(\left(\frac{T_{\mathrm{top}}}{T_0} + T\right)\left(\mathrm{C}_{\mathrm{SiO_2(s)}}\left(1 + C_{P,\mathrm{SiO_2(s)/C}}\right) + (1 - \alpha) + \sigma^*_{gr}\right)\right)\\ = a\frac{\partial T^2}{\partial z^2} + \gamma_5\mathrm{C}_{\mathrm{SiO_2(s)}}(T - T_m)^+ + qF(z).\end{aligned} \tag{3.50}$$

The gas flux equation (3.46) decouples and we are left with the system (3.50) and (3.47) to be solved for the temperature and concentration of solid quartz. This is still quite complex, so we make an additional approximation. Since the model assumes a constant thermal conductivity, it is not unreasonable to replace the varying heat capacity with a constant heat capacity. We take this to be the average of the minimum and maximum values of the heat capacity, that is

$$\sigma = \frac{\alpha}{2}\left(1 + C_{P,\mathrm{SiO_2(s)/C}}\right) + (1 - \alpha) + \sigma^*_{gr}. \tag{3.51}$$

We note that γ_5 is negative (see Table 2.3), so for clarity we use the notation $\gamma := -\gamma_5$. This gives the system

$$\sigma \frac{\partial T}{\partial t} = a \frac{\partial T^2}{\partial z^2} - \gamma \mathrm{C}_{\mathrm{SiO_2(s)}} (T - T_m)^+ + qF(z), \tag{3.52}$$

$$\frac{\partial \mathrm{C}_{\mathrm{SiO_2(s)}}}{\partial t} = -\mathrm{C}_{\mathrm{SiO_2(s)}} (T - T_m)^+, \tag{3.53}$$

$$\frac{\partial T(0,t)}{\partial z} = 0 = \frac{\partial T(1,t)}{\partial z}, \quad T(z,0) = T_a = -1.1, \quad \mathrm{C}_{\mathrm{SiO_2(s)}}(z,0) = \alpha. \tag{3.54}$$

We have the furnace heating up from cold due to a wall source term $F(z)$, up to a time when the temperature reaches the melting point of quartz, T_m, in the base of the furnace. Then solid quartz melts to form liquid quartz, at a rate $r_3 = \mathrm{C}_{\mathrm{SiO_2(s)}}(T - T_m)^+$. This melting does not release any heat in our full model, but we have a reaction balance between the reactions r_3 and r_5, in which carbon reacts with the newly formed liquid quartz to produce gaseous CO and SiO. This pair of reactions is highly endothermic, taking in heat from the surroundings. Thus, energy needs to be input from the walls for the carbon and quartz to react, but since this reaction is endothermic it slows down the rate of temperature increase.

In order to write this system in a cleaner mathematical form, we choose to rescale time to balance with the endothermic heat of reaction, and so introduce the scalings

$$T = T_m + \hat{T}(T_m - T_a), \quad \mathrm{C}_{\mathrm{SiO_2(s)}} = \alpha \hat{C}, \quad t = \frac{\sigma}{\gamma \alpha} \hat{t}. \tag{3.55}$$

Dropping the hat notation we have the system

$$\frac{\partial T}{\partial t} = K \frac{\partial^2 T}{\partial z^2} - CT^+ + \omega F(z), \tag{3.56}$$

$$\frac{\partial C}{\partial t} = -bCT^+, \tag{3.57}$$

with initial and boundary conditions

$$T(z,0) = -1, \quad C(z,0) = 1, \quad \frac{\partial T(0,t)}{\partial z} = 0 = \frac{\partial T(1,t)}{\partial z}. \tag{3.58}$$

The three dimensionless parameters are written in terms of previous dimensionless parameters as

$$K = \frac{a}{\gamma \alpha}, \quad b = \frac{(T_m^* - T_a)\sigma}{\gamma \alpha}, \quad \omega = \frac{q}{(T_m^* - T_a)\gamma \alpha}. \tag{3.59}$$

Typical parameter sizes are $K = 0.01$, $b = 0.3$, and $\omega = 0.15$. We will use these values throughout this section unless otherwise stated. In Figure 3.5 we show

plots comparing the numerical solutions of this simplified system with the full system presented in Section 3.1. In the full system heat equation (3.5) the heat capacity can vary, so for a fair comparison we restrict the heat capacity in the time derivative of the full numerics to be the constant σ given in (3.51). We could alternatively have kept a varying heat capacity in the simplified system, but this would make the asymptotic analysis more difficult. The heat capacity of the gas in the spatial derivative of (3.5) is still allowed to vary, since this is not included in the simplified model. The temperatures of the two systems match well for the first 40 minutes in the base of the furnace, but the simplified numerics become hotter in the base after this. This is because thermal convection and radiation, which transfer heat from the base to the top of the furnace, are present in the full model, but not in the simplified model. The effect of this is to produce more SiO_2(s) in the base in the simplified model. Also, the exothermic heat sources from reactions r_1 and r_2 are present in the full model only, adding to the discrepancy of the temperature in the upper furnace. However, despite these differences, the overall qualitative behaviour is similar between the two models. We have the base of the furnace heating up faster than the top and, upon reaching a critical temperature, solid quartz melting then reacting to form gas. It is thus instructive to consider this simplified model to develop understanding as to the qualitative effects in the pilot furnace.

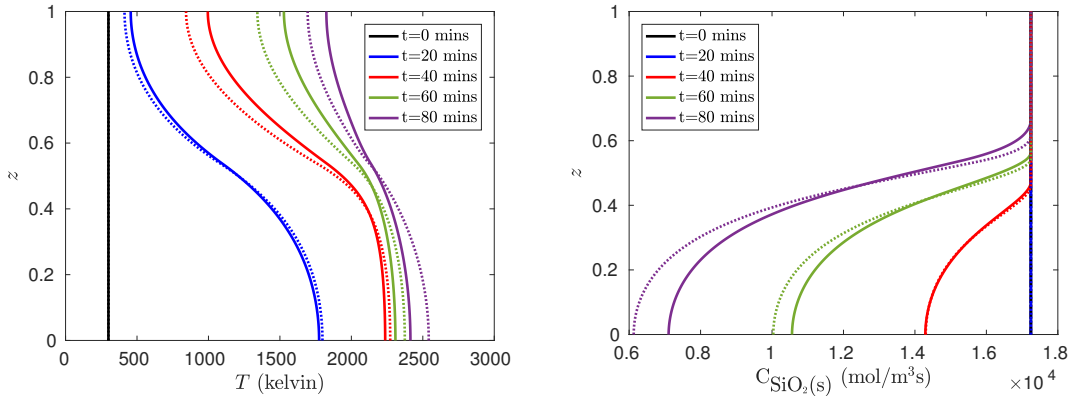


Figure 3.5: Comparison of numerics of the full system (3.3) - (3.10) (with a constant heat capacity) in solid lines and numerics for the simplified system (3.56) - (3.58) in dotted lines. On the left are plots of temperature and on the rights are plots of $C_{SiO_2(s)}$ (both dimensional). Parameter values used are $\epsilon = 0.16$, $\delta = 3.2 \times 10^{-4}$, and $\alpha = 0.45$.

3.5 Special limits of the simplified model

We have used asymptotics to reduce the full model (3.3) - (3.10), obtaining a simplified model (3.56) - (3.58) which captures the dominant behaviour of the full system. We now explore this simplified model further. We examine early time dynamics in Section 3.5.1, analyse a small diffusion limit in Section 3.5.2, and comment on a small heating limit in Section 3.5.3.

3.5.1 Early time

For early time, the temperature is not hot enough for the reaction to take place, meaning no energy is consumed by the reaction. Taking the heat source from the wall to be the step function $F(z) = \mathcal{H}(h_T^* - z)$ in this case, for ease of analysis, we have

$$\frac{\partial T}{\partial t} = K\frac{\partial^2 T}{\partial z^2} + \omega\mathcal{H}(h_T^* - z), \tag{3.60}$$

with initial condition and boundary conditions

$$T(z,0) = -1, \quad \frac{\partial T(0,t)}{\partial z} = \frac{\partial T(1,t)}{\partial z} = 0. \tag{3.61}$$

We can find a series solution to this problem, and this takes the form

$$T(z,t) = T_a + \omega h_T^* t + \frac{2\omega}{K}\sum_{n=1}^{\infty}\frac{\sin(n\pi h_T^*)}{n^3\pi^3}\left(1 - \exp(-Kn^2\pi^2 t)\right)\cos(n\pi z). \tag{3.62}$$

In Figure 3.6, we compare this solution to numerics of the system (3.56) - (3.58). There is good agreement in the early time pre-heating region, while the solutions diverge later when $T > 0$, where the endothermic reaction occurs.

3.5.2 Small diffusion limit

In Figure 3.7 we show contour plots for T and C for the cases $K = 0.01$ and $K = 0$, with $b = 0.3$ and $\omega = 0.15$ in each case. When there is no diffusion, so that $K = 0$, we see a sharp interface between a pre-heating region in the upper-left of the (z,t)-plane and a reaction zone in the lower-right of the plane. Throughout this section and Section 3.5.3, we use the smooth heating function $F(z) = \frac{1}{2}\left(1 + \tanh(10(h_T^* - z))\right)$, with $h_T^* = 0.544$, in both the numerical simulations and asymptotic solutions shown in figures.

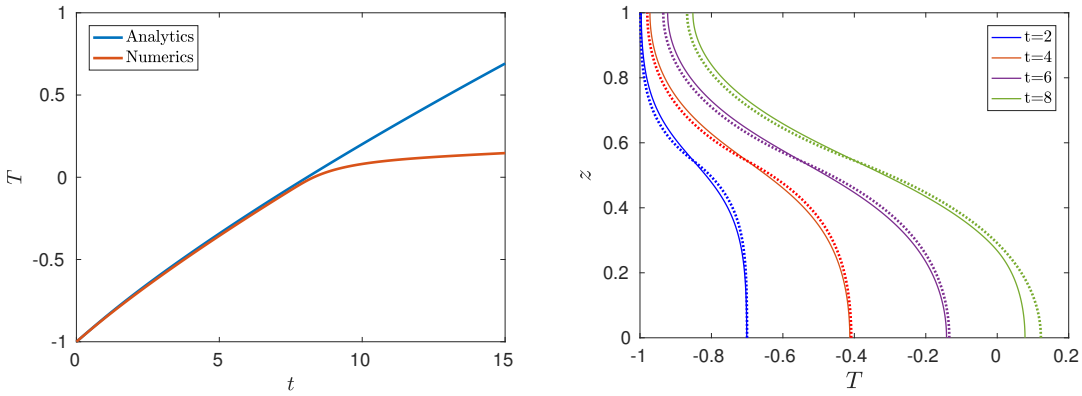


Figure 3.6: Comparison of the analytical solution (3.62) with numerical simulations. On the left is the dimensionless temperature for fixed height $z = 0.3$, while on the right are spatial profiles at different times, with the analytic solution in dotted lines and numerics in solid lines.

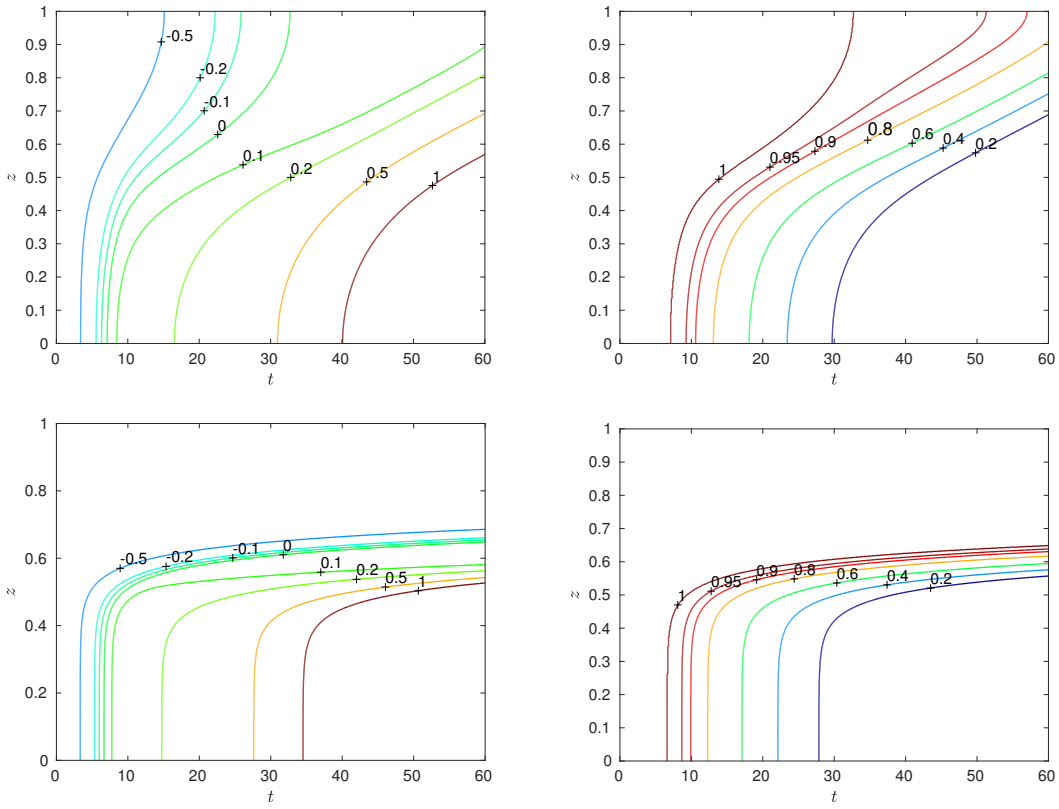


Figure 3.7: Contour plots for dimensionless T (left) and C (right), in the cases $K = 0.01$ (top) and $K = 0$ (bottom), with $b = 0.3$ and $\omega = 0.15$ in all cases.

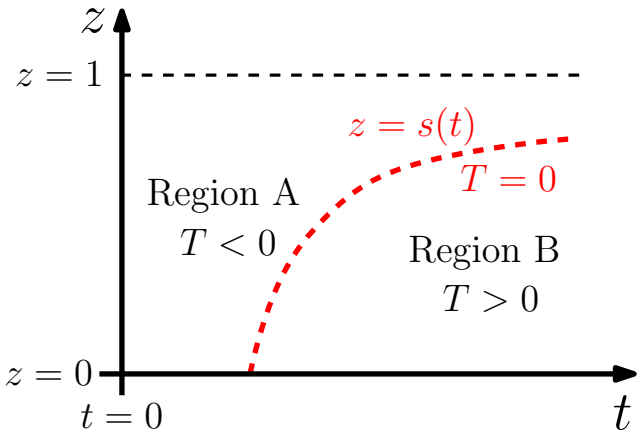


Figure 3.8: Schematic diagram of the different regions in the variable temperature problem. In Region A the temperature is too cold for the reaction to take place, whilst in Region B the chemical reacts. These regions are separated by the interface $z = s(t)$, given by the isotherm $T = 0$.

A schematic diagram of the two regions is given in Figure 3.8. Region A is the pre-heating region, where the temperature is too cold for the reaction to take place. In Region B the temperature is positive, so the chemical reacts. Let $z = s(t)$ be defined as the interface between these regions. We plot numerical solutions for a fixed height $z = 0.3$ in Figure 3.9, indicating where these regions occur. A third region, Region C, occurs where all the chemical is nearly used up and the temperature increases linearly in the graphite crucible due to the heat source from the wall. We are not interested in this region in this chapter, since it corresponds to all the solid material being used up in the furnace, and the pilot furnace experiments do not run for long enough for this to be observed. Unlike the sharp interface between Regions A and B at $z = s(t)$ (shown by the dashed line), there is no sharp interface between Regions B and C; however, we have put an interface between these regions (shown by the dot-dashed line) to illustrate a possible location to distinguish between the regions.

Our simplified model has the small parameter K. We treat ω and b as order one constants and expand in terms of K, with $0 < K \ll 1$, so that we write

$$\begin{aligned} T^{A/B} &= T_0^{A/B} + KT_1^{A/B} + \mathcal{O}(K^2), \\ C^{A/B} &= C_0^{A/B} + KC_1^{A/B} + \mathcal{O}(K^2), \\ s(t) &= s_0(t) + Ks_1(t) + \mathcal{O}(K^2), \end{aligned} \tag{3.63}$$

where $T^{A/B}$ and $C^{A/B}$ refer to T and C in Regions A and B, respectively. The first order equations correspond to the limit of zero diffusion. In this case, the spatial dependency for the problem comes through the general heating source term $F(z)$, which we take to be order one and hotter at the base than at the top.

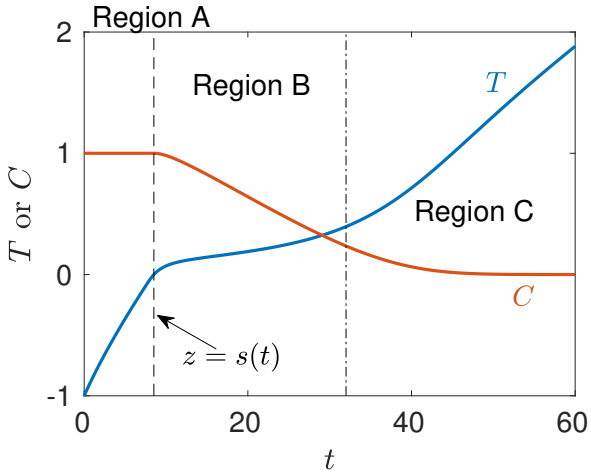


Figure 3.9: Numerical simulations of dimensionless T and C from the system (3.56) - (3.58), displayed for fixed height $z = 0.3$. Region A is to the left of the dashed line, Region B is between the dashed and the dot-dashed lines, and Region C is to the right of the dot-dashed line. The dashed line has label $z = s(t)$, because it is showing the time for which there is a transition between Regions A and B for the given height $z = 0.3$. The dot-dashed line is in a possible, illustrative location. Parameter values used are $K = 0.01$, $\omega = 0.15$, and $b = 0.3$.

In Region A, we have the following system at leading order,

$$\frac{\partial T_0^A}{\partial t} = \omega F(z) + \mathcal{O}(K), \quad T_0^A(z,0) = -1 + \mathcal{O}(K), \tag{3.64a}$$

$$\frac{\partial C_0^A}{\partial t} = \mathcal{O}(K), \quad C_0^A(z,0) = 1 + \mathcal{O}(K), \tag{3.64b}$$

which has the solution

$$T_0^A(z,t) = -1 + \omega F(z)t, \quad C_0^A(z,t) = 1. \tag{3.65}$$

We find that $C^A \equiv 1$, and that the higher order equations for temperature are given by

$$\frac{\partial T_n^A}{\partial t} = \frac{\partial^2 T_{n-1}^A}{\partial z^2}, \quad n \geq 1. \tag{3.66}$$

Thus we have the following expansion in K for temperature in Region A:

$$T^A(z,t) = -1 + \omega F(z)t + \omega \sum_{n=1}^{\infty} K^n F^{(2n)}(z) \frac{t^{n+1}}{(n+1)!}. \tag{3.67}$$

To find the coefficients in the expansion of $s(t)$, we note that the curve $z = s(t)$ is given implicitly by

$$T^A(s(t), t) = 0. \tag{3.68}$$

Hence, we have that

$$\begin{aligned}
0 &= T^A(s_0(t) + Ks_1(t) + \cdots, t) \\
&= T^A(s_0(t), t) + (Ks_1(t) + \cdots)\frac{\partial T^A}{\partial z}(s_0(t), t) + \cdots \\
&= T_0^A(s_0(t), t) + K\left(T_1^A(s_0(t), t) + s_1(t)\frac{\partial T_0^A}{\partial z}(s_0(t), t)\right) \\
&\quad + K^2\Bigg(T_2^A(s_0(t), t) + s_1(t)\frac{\partial T_1^A}{\partial z}(s_0(t), t) + s_2(t)\frac{\partial T_0^A}{\partial z}(s_0(t), t) \\
&\qquad + \frac{1}{2}s_1(t)^2\frac{\partial^2 T_0^A}{\partial z^2}(s_0(t), t)\Bigg) + \mathcal{O}(K^3).
\end{aligned} \tag{3.69}$$

Looking at leading order, we find

$$\mathcal{O}(1): \quad s_0(t) = F^{-1}\left(\frac{1}{\omega t}\right), \tag{3.70}$$

which requires that F be invertible. At next order, we obtain

$$\mathcal{O}(K): \quad s_1(t) = -\frac{1}{2}\frac{F''(s_0(t))}{F'(s_0(t))}t, \tag{3.71}$$

and then looking at terms quadratic in K, we find

$$\mathcal{O}(K^2): \quad s_2(t) = \left(\frac{F''(s_0(t))F'''(s_0(t))}{4(F'(s_0(t)))^2} - \frac{F^{IV}(s_0(t))}{6F'(s_0(t))} - \frac{(F''(s_0(t)))^3}{8(F'(s_0(t)))^3}\right)t^2. \tag{3.72}$$

This iterative process can be continued to find the correction for $s(t)$ to any order of K, if desired.

In Region B, we have obtained the leading order equations

$$\frac{\partial T_0^B}{\partial t} = -C_0^B T_0^B + \omega F(z) + \mathcal{O}(K), \tag{3.73a}$$

$$\frac{\partial C_0^B}{\partial t} = -bC_0^B T_0^B + \mathcal{O}(K), \tag{3.73b}$$

with the boundary conditions

$$T_0^B(s_0(t), t) = \mathcal{O}(K), \quad C_0^B(s_0(t), t) = 1 + \mathcal{O}(K), \tag{3.74}$$

which we can write as

$$T_0^B = 0 \quad \text{and} \quad C_0^B = 1 \quad \text{on} \quad t = \frac{1}{\omega F(z)}. \tag{3.75}$$

We can then write equations (3.73a) and (3.73b) as

$$\frac{\partial}{\partial t}\left(T_0^B - \frac{1}{b}C_0^B\right) = \omega F(z), \tag{3.76a}$$

$$\frac{\partial C_0^B}{\partial t} = -bC_0^B T_0^B. \tag{3.76b}$$

Integrating (3.76a), we obtain the relation

$$T_0^B = \frac{1}{b}(C_0^B - 1) - 1 + \omega F(z)t, \tag{3.77}$$

which can be substituted (3.76b) to obtain the ODE

$$\frac{\partial C_0^B}{\partial t} = -(C_0^B)^2 + C_0^B\left(1 + b - b\omega F(z)t\right). \tag{3.78}$$

Equation (3.78), along with the boundary condition in (3.75), has the solution

$$C_0^B(z,t) = \frac{\exp\left(-\frac{2+b}{2\omega F(z)} + (b+1)\,t - \frac{b\omega F(z)}{2}t^2\right)}{1 + \sqrt{\frac{\pi}{2b\omega F(z)}}\exp\left(\frac{1}{2b\omega F(z)}\right)\left[\operatorname{erf}\left(\frac{1}{\sqrt{2b\omega F(z)}}\right) + \operatorname{erf}\left(\frac{b\omega F(z)t - b - 1}{\sqrt{2b\omega F(z)}}\right)\right]}, \tag{3.79}$$

and hence the temperature is given by

$$\begin{aligned} T_0^B(z,t) = &-1 - \frac{1}{b} + \omega F(z)t \\ &+ \frac{\exp\left(-\frac{2+b}{2\omega F(z)} + (b+1)\,t - \frac{b\omega F(z)}{2}t^2\right)}{b + \sqrt{\frac{\pi b}{2\omega F(z)}}\exp\left(\frac{1}{2b\omega F(z)}\right)\left[\operatorname{erf}\left(\frac{1}{\sqrt{2b\omega F(z)}}\right) + \operatorname{erf}\left(\frac{b\omega F(z)t - b - 1}{\sqrt{2b\omega F(z)}}\right)\right]}. \end{aligned} \tag{3.80}$$

The $\mathcal{O}(K)$ equations are solvable, but require tedious calculations, especially to determine the required $\frac{\partial^2 T_0^B}{\partial z^2}$, so we do not include the functional form of solutions here, but instead give solutions in integral form in Appendix B.

In Figure 3.10 we compare the leading order asymptotic solutions with the numerical results of the simplified system, at a fixed height in the bottom of the furnace. In Figure 3.11 we show spatial comparisons at different fixed times for temperature on the left and the concentration of solid quartz on the right. In the base of the furnace the leading order asymptotics capture the qualitative behaviour of temperature increasing and quartz melting, but are off by a noticeable error. This is because diffusion does not feature, so the bottom of the furnace is too hot, whilst the top remains cold. Consequently, the quartz melts too quickly in the asymptotic solutions. The errors are larger than might be expected because the smooth heating source used, $F(z) = \frac{1}{2}\left(1 + \tanh(10(h_T^* - z))\right)$, changes rapidly in the region close to $z = h_T^*$.

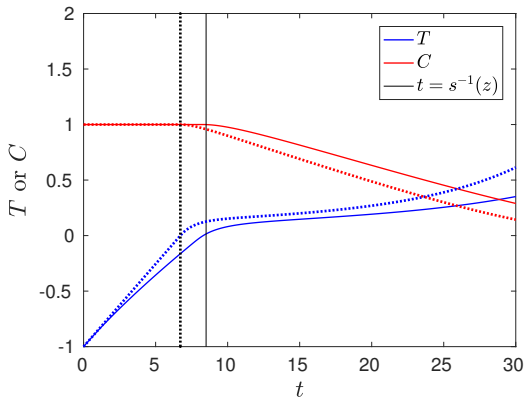


Figure 3.10: Comparison of first order asymptotic solutions, shown in dotted lines, and numerical solutions of the simplified system (3.56) - (3.58), shown in solid lines, at height $z = 0.3$ for the dimensionless temperature, concentration, and time taken to reach the interface between Regions A and B. Parameter values used are $K = 0.01$, $\omega = 0.15$, and $b = 0.3$.

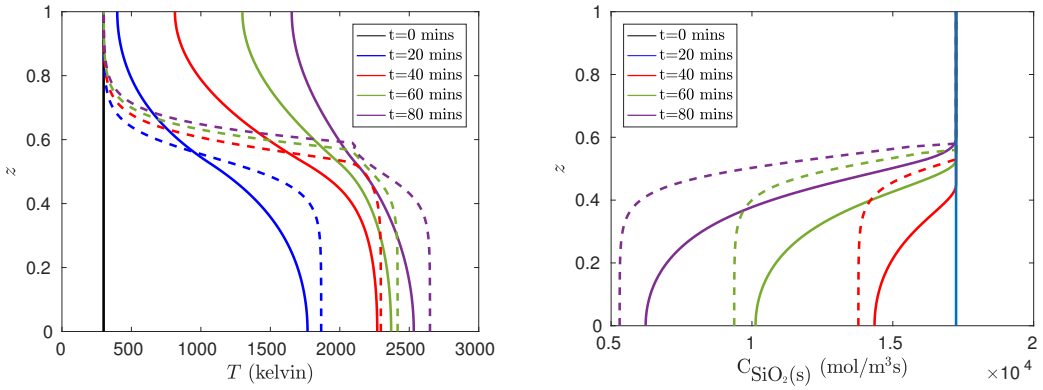


Figure 3.11: Comparison of asymptotic solutions, shown in dotted lines, and numerical solutions of the simplified system (3.56) - (3.58), shown in solid lines, for the dimensional temperature (left) and concentration (right). Since the smooth heating source was used, the simplified numerics are different to those in Figure 3.5, which use a Heaviside function. Parameter values used are $K = 0.01$, $\omega = 0.15$, and $b = 0.3$.

3.5.3 Small heating limit

We next consider the case where ω is also a small parameter, with $0 < K \ll \omega \ll 1$. Here the heat absorbed by the endothermic reaction between the melted quartz and the carbon is larger than the heat input from the electrode or the induction furnace, but the heat transfer from this source term dominates over diffusion as the main heating mechanism. An asymptotic analysis can be performed by first assuming $K = \mathcal{O}(\omega^2)$ and then considering the limit $\omega \to 0$. We will not give the details of this analysis here, but find behaviour in Region A similar to that discussed in the small diffusion limit in Section 3.5.2. The chemical C remains unreacted and the temperature increases due to the heat source $F(z)$, with spatial variation again arising from derivatives of $F(z)$. The interface $z = s(t)$ can be determined using the same method employed to find (3.70) - (3.72), and similar functional forms are found, with the leading order location of the interface being given by the heat source $F(z)$. In Region B the concentration reacts away, with the $\mathcal{O}(1)$ changes found to be larger than the $\mathcal{O}(\omega)$ changes in temperature. Since the temperature is small, the dominant balance is between the heating and the endothermic reaction. Thus, the whole problem is heat controlled and the temperature in the furnace changes to balance the energy input. However, the leading order solution for temperature in Region B blows up in finite time, as temperature changes increase. This issue does not occur in the small diffusion limit in Section 3.5.2, where ω is treated as an $\mathcal{O}(1)$ parameter.

By considering the full model we have reduced the number of equations to a simplified system, which captures the coupled evolution of temperature and concentration of solid quartz in the furnace. This model has two regions of interest: the pre-heating Region A and the reaction zone Region B. An analytic series solution was found for Region A and the simplified model was considered in the limit of small diffusion, and a small heat source. When diffusion is small, the location of the interface between Regions A and B is determined to leading order by the functional form of the heating source. When the parameter ω is also considered to be small, then the temperature is small in Region B, and the main balance in the problem is between the energy input from the induction furnace and the energy absorbed by the endothermic reaction. Numerical simulations of the simplified model compare well with those of the full model, therefore the simplifications discussed will be useful for future models.

3.6 Crust formation

We are particularly interested in furnace crust formation, since this slows down the industrial operation and requires 'stoking'. We derive a model focussed on this phenomenon in Chapter 4. However, general insights into the crust can be found from the reaction pathways in (2.1) - (2.5), with additional understanding from the analysis of the dimensionless equations with prescribed temperature profile in Section 3.3 and the full model in Section 3.4.

In (2.37), we introduced the solid volume fraction θ_S as a proxy for crust formations. We can look at whether the time rate of change of θ_S is positive or negative in the upper part of the furnace, to determine if crust is building up. An equivalent definition for θ_S is

$$\theta_S = \sum_{\text{solids and liquids } i} \frac{M_i}{\rho_i} \mathrm{C}_i, \tag{3.81}$$

for dimensional C_i, so taking a time derivative we can substitute in the reaction rates from the equations (2.8) - (2.14). We can make progress even if we do not define functional forms of the reaction rates or the associated parameter values. This is helpful, since one can still study crust formation regardless of the functional forms chosen. We thus refer to the rates as R_j, as described in (2.1) - (2.5). Note that these are dimensional variables. In the upper part of the furnace, where the temperature is too cold for quartz to melt, we impose $R_3 = 0$, obtaining

$$\frac{\partial \theta_S}{\partial t} = \frac{M_{\mathrm{C}}}{\rho_{\mathrm{C}}}(-2R_1 - R_5) + \frac{M_{\mathrm{SiC}}}{\rho_{\mathrm{SiC}}}(R_1 - R_4) + \frac{M_{\mathrm{SiO_2(l)}}}{\rho_{\mathrm{SiO_2(l)}}}(R_2 - R_{-2} - R_5) + \frac{M_{\mathrm{Si}}}{\rho_{\mathrm{Si}}}(R_2 - R_{-2} - R_4). \tag{3.82}$$

In the top of the furnace, carbon reacts with the available $\mathrm{SiO_2(l)}$, which is produced from the condensation reaction R_2. Since we expect quantities of Si and $\mathrm{SiO_2(l)}$ to be small compared to the amount of carbon, we can write $R_{-2} \ll R_5$ and $R_5 = R_2$. If we further assume a functional dependence of R_4 on $(P - P_4)^+$, as done in Table 2.1, then $R_4 = 0$ in the upper part of the furnace, because the partial pressure of SiO is too low. With these assumptions, we can simplify equation (3.82) to

$$\frac{\partial \theta_S}{\partial t} = \left(\frac{M_{\mathrm{SiC}}}{\rho_{\mathrm{SiC}}} - 2\frac{M_{\mathrm{C}}}{\rho_{\mathrm{C}}} \right) R_1 + \left(\frac{M_{\mathrm{Si}}}{\rho_{\mathrm{Si}}} - \frac{M_{\mathrm{C}}}{\rho_{\mathrm{C}}} \right) R_2. \tag{3.83}$$

The molar masses are known constants and can be found in [69]. We take the density of carbon, silicon carbide, and silicon from [55], [71], and [54], respectively. With this data, we have

$$\frac{M_{\mathrm{C}}}{\rho_{\mathrm{C}}} = 5.298 \times 10^{-6}, \quad \frac{M_{\mathrm{SiC}}}{\rho_{\mathrm{SiC}}} = 1.249 \times 10^{-5}, \quad \frac{M_{\mathrm{Si}}}{\rho_{\mathrm{Si}}} = 1.206 \times 10^{-5}. \tag{3.84}$$

This means that $\frac{\partial \theta_S}{\partial t} > 0$, and as such we will see a build-up of solid in our model. This corresponds, in turn, to crust formation, regardless of the functional form of reaction rates R_1, R_2, and R_5, and regardless of how large the kinetic parameters are. Notice though that the sign of $\frac{M_{SiC}}{\rho_{SiC}} - 2\frac{M_C}{\rho_C}$ is quite sensitive to the data used in [54] and [55]. A decrease in the value of ρ_C by 15% or an increase in the value of ρ_{SiC} by 18% would change the sign, and it would not then be true that solid always builds up.

We can also incorporate the solutions from Section 3.3, with a prescribed temperature profile $T(z)$. With these we find

$$\theta_S = m_{\mathrm{C}} + \alpha m_{\mathrm{SiO_2(s)}} + \epsilon \left[\chi_1 \left(\frac{1}{2} - P_1 \right) (m_{\mathrm{SiC}} - 2m_{\mathrm{C}}) + \chi_2 \left(\frac{1}{2} - P_2 \right) (m_{\mathrm{Si}} - m_{\mathrm{C}}) \right] t + \mathcal{O}(\epsilon^2), \tag{3.85}$$

and so we can quantify how the crust grows. Taking a spatial partial derivative and using the chain rule, we see

$$\frac{\partial \theta_S}{\partial z} = -\epsilon \left[\chi_1 \frac{dP_1}{dT} (m_{\mathrm{SiC}} - 2m_{\mathrm{C}}) + \chi_2 \frac{dP_2}{dT} (m_{\mathrm{Si}} - m_{\mathrm{C}}) \right] \frac{dT}{dz} t + \mathcal{O}(\epsilon^2). \tag{3.86}$$

Since $\frac{dP_1}{dT}, \frac{dP_2}{dT} > 0$ (see the equilibrium partial pressures in Figure 2.3) and $\frac{dT}{dz} < 0$ (because of the temperature gradient in the furnace), we have

$$\frac{\partial \theta_S}{\partial z} > 0. \tag{3.87}$$

Hence, the solid volume fraction increases with height in the furnace, according to this model, and the charge is most porous at the lower interface with the gas cavity.

Our analysis in Section 3.4 did not consider solid build-up in the upper furnace, since this is an $\mathcal{O}(\epsilon)$ effect when compared to the $\mathcal{O}(1)$ changes taking place in the lower, hotter region. However, we tracked the location of the interface at the base of the charge through the isotherm $T = 0$ (or $T = 1996$ K in dimensional units). This position is largely driven by the external heat source, since diffusion effects are small. Temperature remains monotone throughout when we assume a monotone heat source F. This means that to leading order r_1 and r_2 increase with furnace height, and thus the rate of crust increase in (3.83) will increase as well.

3.7 Conclusions

We have investigated asymptotic limits of the silicon furnace model developed in Chapter 2, extending the analysis that was undertaken through numerical simulations there. Natural small parameters are the ratio of the timescale for the reaction between carbon and liquid quartz to the timescale for the melting of quartz, and the ratio of timescale of gas advection to the timescale of the melting of quartz. With appropriate scalings for the concentrations, we have been able to determine the leading order chemical behaviour for different spatial regions in the furnace, when a prescribed temperature is imposed in the model. In Region II, we find the dominant behaviour is solid quartz melting to liquid quartz, which then reacts with the available carbon particles to form gaseous CO and SiO. In Region I, this SiO gas condenses into silicon and liquid quartz, and also reacts with carbon to form silicon carbide and CO. This competition between reactions, determining how much SiC and Si is produced, is represented in the size of the parameter ratio χ_2/χ_1. We have also been able to capture early time behaviour in these regions, where the variables move from the initial conditions to typical furnace behaviour.

In Section 3.4, we considered asymptotics of the full model with temperature allowed to vary in time. Through systematic reductions we have derived a simplified system of two coupled equations for temperature and the concentration of solid quartz, which depends on three parameters, ten times fewer than the number used in the full model. These three parameters represent the heating from the external source, the thermal diffusion, and the rate of melting of solid quartz. Numerical simulations of the simplified system compare well with those of the full model, showing the same qualitative behaviour. In Section 3.5.2, we found asymptotic solutions to the reduced system, treating the diffusivity, K, as a small parameter. The leading order solutions, where no diffusion occurs, are representative of the behaviour in the reaction zone. This suggests that the dominant heat transfer mechanisms are the energy input from the induction furnace into the pilot furnace, and the heat absorption of the endothermic reaction between carbon and quartz. The pilot furnace is most thermally conductive along the graphite walls, since conduction between solid particles is relatively small. In an industrial furnace the subdominance of diffusion is likely to be even more pronounced, since energy is input directly from the electrodes.

By examining crust formation in Section 3.6, we found that crust builds up in this model regardless of the functional forms or kinetic parameters of reaction rates R_1 and R_2. However, the model assumes that there is no solid or liquid motion and that

there is a mixture of solid, liquid, and gas at every location in the furnace. In practice, liquid silicon has very low viscosity, and so will drip to the crater when produced. This would have an impact on crust formation, as silicon would not contribute to the solid fraction in the upper furnace, as it does in (3.83). In addition, the porosity will become so low at the bottom of the charge that solid and liquid material will fall to the furnace base. Clearly there needs to be a failure criterion for this falling material. One possibility is to use the melting isotherm, so that all material hotter than this will have fallen to the base. The reduced system in Section 3.4 will be useful when further physical effects are incorporated in future models, such as the dripping of silicon, the falling of material from the charge to the crater, and the two-dimensional mechanical bridging of the crust. In Chapter 4 we develop a more accurate model of crust formation that takes into account mechanical effects.

Chapter 4

Thermo-Mechanical Crust Model

4.1 Introduction

In Chapter 2 we presented a one-dimensional furnace model, which captured the emergence of an interface at the base of the charge, likely corresponding to the location of crust growth. We explored how model input parameters influenced the 'solid build-up', introduced as a proxy for crust formation. In Chapter 3 we took asymptotic limits of this model, and in Section 3.6 explained that a crust could emerge regardless of the particular kinetic rates used. The modelling in Chapters 2 and 3 focussed on thermal and chemical effects, albeit with additional gas transport in Chapter 2. In all numerical simulations and analysis, solids and liquids were assumed to be stationary. Thus although these models have explanatory power as to the location of the crust, they do not address the fundamental question of how the crust is able to support the weight of the material above it. The cause of crust formation in silicon furnaces, and the factors influencing its strength, is not well understood. In this chapter, we develop a crust model to bring insight to this problem. We consider mechanical effects, but to keep the model and analysis tractable, we do not include the influence of the background gas or the many chemical reactions that occur. The mechanical and thermal model presented here is kept sufficiently general in order to provide insight to other application areas.

Solid particles of quartz and carbon are fed into the top of the furnace, so that the upper charge is granular. Lower down in the furnace, the quartz has softened and begun to melt, and silicon monoxide gas has condensed, so that there is a mixture of solids and viscous liquids, with porous spaces for gas to flow. Material drips from the base of the charge through the gas cavity into the liquid pool. Annotated images of pilot furnace experiments are shown in Figure 4.1.

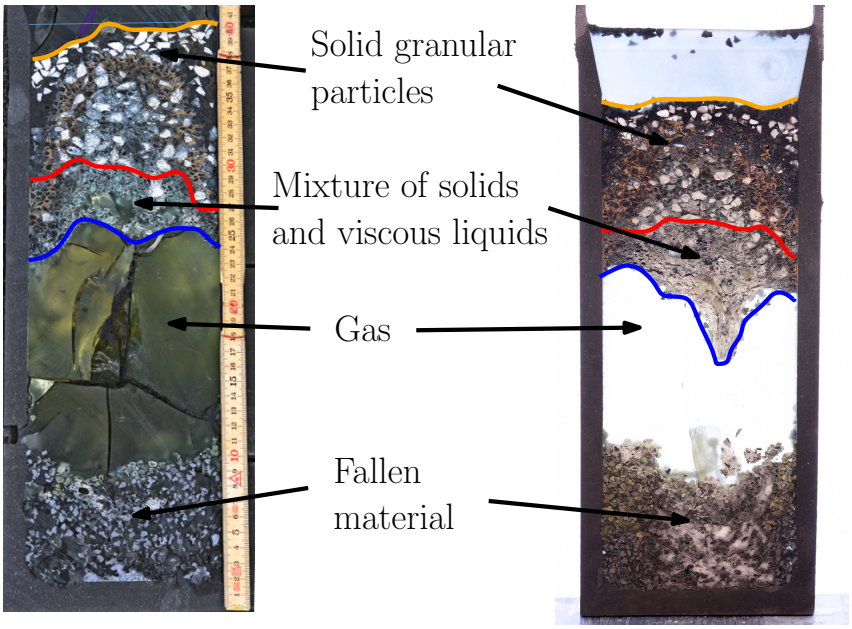


Figure 4.1: Image of pilot furnace experiments, with (left) and without (right) epoxy injected to take the place of the gas cavity. Note in the experiments the bottom region indicated 'fallen material' will contain some solids that started there. However, in industrial furnaces this will be comprised almost entirely of fallen material. We acknowledge Harald Wegge for conducting the experiments and taking the photographs, whilst working at Elkem Technology.

Two possible simple modelling approaches are to treat the charge as either a viscous or a granular material. Although in practice there are local interactions between viscous and granular materials, a model capturing both effects in the same region would introduce too much complexity. In both industrial and pilot furnaces, the distance between supporting vertical surfaces is too large for the crust to form due to granular bridging, whereby the horizontal pressure exerted on the walls supports the load from above. Given that the crust is highly viscous and is our main region of interest, it is reasonable to choose a viscous rather than granular modelling route for this region. A similar physical configuration has been considered by Ceseri and Stockie [15], where a horizontal cylinder comprises three ordered regions of gas, liquid, and solid, respectively. In this paper heating from the gas influences a Stefan condition at the gas-liquid interface, and a long, thin limit is considered. However, the convection of the liquid is given by the velocity of the gas-liquid interface, moving in the same direction. In our problem there is a gravity-driven downwards convection, with the gas-charge interface having been observed to move upwards.

There is a wealth of mathematical literature concerning temperature-dependent fluid mechanics problems. For example, Ockendon and Ockendon [66] consider a

channel of Newtonian fluid that is instantaneously heated or cooled from the walls. A Cartesian channel is assumed, but results are also given for an axisymmetric cylindrical channel. The dependence of viscosity on temperature is considered to be either exponential ($e^{-\beta T}$) or algebraic ($1 - \beta T$). Pearson [73] also considers a channel heated from the wall with viscosity having an exponential dependence on temperature. Bergstrøm et al. [8] and Fitt and Howell [30] analyse two-phase flow with thermally-dependent viscosity in furnace electrodes, which is similar to our application of interest. The problem of a warm liquid flowing over a cold semi-infinite solid is examined by Huppert [44], with freezing of the liquid and melting of the solid both possible. Further asymptotic limits of Huppert's model are studied by King and Riley [50]. Models of a similar flavour can also be used to describe problems in application areas such as volcanic eruptions and lava flows [37, 56, 110], welding [25], and fusion reactors [41].

There are several means of mathematically representing variations in viscosity. The dependence on temperature is discussed in [66, 73, 110]. The situation where fluid carries a suspension of solid particles is considered by Brinkman [11], Chong et al. [18], Mader, Llewellin, and Mueller [58, 62], amongst others. A dense suspension limit is examined by Stickel and Powell [93], with Chang and Powell studying the influence of the particle size on the rheology [17]. Although the crust in our problem is formed of solid particles within a viscous mixture, we do not consider such complexity at present. However, we note that our work could be extended to incorporate such effects, and comment on this in Section 4.6.2.

Tuck et al. [102] model an initially rectangular viscous liquid held fixed between two vertical walls. The fluid slumps under gravity, and they analyse the initial velocity profile. In the tall, thin limit the profile is parabolic, but is parabolic-squared (or quartic-shaped) in the short, wide limit. The same authors then consider the extensional flow of a viscous fluid forming a droplet [94]. They find a critical 'crisis time' at which break-off of a droplet occurs (when inertial effects are neglected).

We are interested in the interactions between thermal effects and flow of the furnace charge. The charge moves under gravity, subject to radiative heating below, from the base of the furnace. In Section 4.2 we develop a two-dimensional axisymmetric model comprising three regions. A middle viscous region lies above a gas region of constant pressure and underneath a granular region acting as a region of hydrostatic pressure. We assume there are sharp interfaces between these regions. The location of the upper interface of the viscous fluid is given implicitly by an isotherm, whilst the lower interface is subject to a Stefan condition. The furnace is constantly refilled, so

that the top of the granular region remains flat. We simplify this model by assuming a tall, thin geometry. The arising leading order system comprises a heat equation with a coupled Stefan condition, both subject to a radially-averaged convective term. In Section 4.4 we perform numerical simulations of this tall, thin model and find that in certain parameter regimes the system tends to a unique steady state, which we find. We present parameter bifurcation diagrams demonstrating when such steady states exist. Subsequent parameter limits of the tall, thin model are taken in Section 4.5; in particular, a thin crust limit is examined. Potential extensions to the model are highlighted in Section 4.6, and conclusions are drawn in Section 4.7.

4.2 Model derivation

The charge consists of two regions: an upper region of solid particles, behaving like a granular material, and a lower region comprising a mixture of solid and viscous liquid materials, which are reacting with each other and a background gas. For simplicity, we model the lower region as a one-phase viscous fluid, with viscosity dependent on temperature in the upper region. Since the solid particles fall down into any space below, we neglect any solid friction between particles and model the granular region as a region of hydrostatic pressure with no horizontal motion of particles. Thus, the upper charge region acts like a dead load, applying pressure to the lower region. This simplification of the granular dynamics is taken, since our motivation is to better understand the crust behaviour. We ignore the influence of the background gas and any reactions that might create or remove material in the lower charge region.

We model the domain of the furnace as a cylinder. This is partly to simplify the analysis, allowing us to consider the interaction between different physical effects, and partly because the pilot furnace experiments are cylindrical. We assume the problem is axisymmetric and so our co-ordinate system is (r, z), where r is the radius and z is the height. The viscous fluid lies above a region of constant gas pressure and no fluid, with a free boundary at $z = a(r, t)$ separating these regions. The movement and shape of this interface is of particular interest, and will be influenced by the viscous motion of the fluid and thermal heating. Physically, this interface will be formed by material dripping to the pool below, but we model it as a melting isotherm. There will be a heat source lower down in the furnace, which heats the fluid through radiation. The walls are assumed to be insulated. The upper interface of the viscous fluid is given by $z = b(r, t)$. This will also be determined by an isotherm, replicating a condensation temperature. We suppose that material is added to the top of the furnace at a rate

which ensures a flat, horizontal top at $z = h$, so that we only need to consider two free boundaries. A schematic diagram of the geometry is given in Figure 4.2.

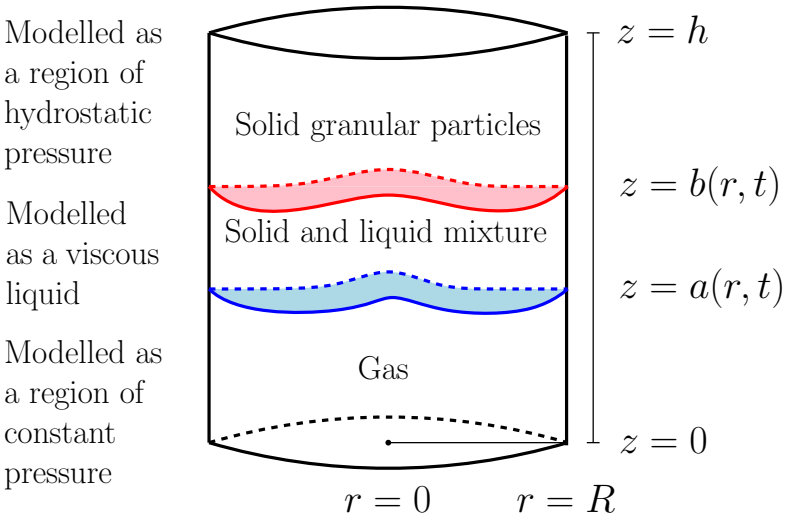


Figure 4.2: A schematic diagram of the two-dimensional geometry, with moving interfaces at $z = a(r,t)$ and $z = b(r,t)$.

Note that in practice material falls from $z = a(r,t)$ to the base of the furnace and collects in a pool or crater. We have chosen not to track the subsequent behaviour of this falling material. Thus both moving boundaries $z = a(r,t)$ and $z = b(r,t)$ are permitted to be negative, with $-\infty < a(r,t) \leq b(r,t) \leq h$.

We assume that the viscous fluid lies in the region $a(r,t) \leq z \leq b(r,t)$. The Reynolds number is such that the Stokes equations hold, and the fluid is taken to be incompressible. The fluid has a constant density, ρ, but a thermally-varying viscosity, η, giving

$$0 = -\nabla p + \nabla \cdot \left(\eta \left(\nabla \mathbf{u} + \nabla \mathbf{u}^T\right)\right) - \rho g \mathbf{k}, \text{ for } a(r,t) \leq z \leq b(r,t), \quad r \leq R, \tag{4.1}$$

$$\nabla \cdot \mathbf{u} = 0, \text{ for } a(r,t) \leq z \leq b(r,t), \quad r \leq R. \tag{4.2}$$

The region $b(r,t) \leq z \leq h$ is treated as a region of hydrostatic pressure, providing a force to the crust below. Thus the pressure in the upper region is given by

$$p = p_{\text{atm}} + \rho g(h - z), \text{ for } b(r,t) \leq z \leq h, \tag{4.3}$$

where we have assumed that the granular region has same constant density, ρ, as the fluid region. We have continuity of stresses and velocity at the interface $z = b(r,t)$.

We assume that the top is replenished with cold material, so that $T = T_c$ at $z = h$, for 'cold temperature'. On the interface $z = b(r,t)$, we have the constant temperature $T = T_k$ (for Norwegian 'kondensasjon', for want of other subscripts).

We assume, for simplicity, that the granular particles only move in the vertical direction, with no horizontal motion, and that the velocity in this region is independent of height. Since we require continuity of velocity at the interface $z = b(r,t)$, we have

$$\mathbf{u}(r,z,t) = \mathbf{u}(r,b(r,t),t), \text{ for } b(r,t) \leq z \leq h, \quad r \leq R. \tag{4.4}$$

Note that, although we are interested in the crust region, we expect that thermal convection throughout the whole domain $a(r,t) \leq z \leq h$ will be important, and hence we have determined a velocity field in the granular region.

We assume that both regions can be described by the same temperature, $T(r,z,t)$, and the same constant thermal conductivity, k. Since we neglect any heat from reactions, this gives the heat equation

$$\frac{\partial T}{\partial t} + \mathbf{u} \cdot \nabla T = \kappa \nabla^2 T, \text{ for } a(r,t) \leq z \leq h, \quad r \leq R, \tag{4.5}$$

where we have written the convective term as $\mathbf{u} \cdot \nabla T$ due to incompressibility, and κ is the thermal diffusivity. Since the problem is axisymmetric, we have that

$$T = T(r,z,t), \quad \mathbf{u}(r,z,t) = u_r(r,z,t)\mathbf{e}_r + u_z(r,z,t)\mathbf{k}. \tag{4.6}$$

We will solve the fluid problem for $\mathbf{u}$ in the viscous region $a(r,t) \leq z \leq b(r,t)$, but the thermal problem in the whole domain $a(r,t) \leq z \leq h$.

The boundary conditions for the viscous fluid are that there is no flux or slip on the radial walls,

$$u_r = 0, \quad u_z = 0, \text{ at } r = R, \tag{4.7}$$

and that velocity is bounded at $r = 0$,

$$\|\mathbf{u}\| \text{ is bounded as } r \to 0. \tag{4.8}$$

We assume that the cylinder is insulated at the walls and that temperature is bounded along the centreline, so we have

$$\frac{\partial T}{\partial r} = 0 \text{ at } r = R, \quad T \text{ bounded as } r \to 0. \tag{4.9}$$

We also have the thermal conditions

$$T = T_c, \text{ at } z = h, \tag{4.10}$$

$$T = T_k, \text{ at } z = b(r,t), \tag{4.11}$$

as already discussed. The furnace starts from cold, so we have the initial condition

$$T = T_c, \text{ at } t = 0. \tag{4.12}$$

The behaviour at the lower interface, $z = a(r,t)$, is more complex. We have not included a heat source as part of the heat equation (4.5), but energy radiates from the base of the furnace to cause the lower charge to drip down to the pool below. We thus assume that there is a heat source of constant temperature T_h (for 'hot temperature') at $z = -\infty$. We choose to model the interface $z = a(r,t)$ as an isotherm, corresponding to the temperature at which the fluid drops off instead of staying as a coherent mixture on the timescale of interest. Although the fluid does not melt at this temperature, since it is already a fluid, we use the boundary condition

$$T = T_M, \text{ at } z = a(r,t), \tag{4.13}$$

where $T_M < T_h$ is the 'melting point' of quartz. This approach ties in to the reaction rate used for the melting of quartz in Chapters 2 and 3 (see R_3 in Table 2.1 and the schematic diagram of furnace regions in Figure 3.1). To describe the motion of the interface we use the Stefan condition for convecting material. This is given by

$$\rho L \left(V_n - \mathbf{u}\cdot\mathbf{n}\right) = \left[\mathbf{q}\cdot\mathbf{n}\right]_-^+, \text{ at } z = a(r,t), \tag{4.14}$$

where L is the latent heat [$\mathrm{m}^{-2}\mathrm{s}^{-2}$], V_n is the normal velocity of the interface, $\mathbf{q}$ is the heat flux, and $\mathbf{n}$ is the normal vector to the boundary. Terms on the left hand side correspond to the interface moving upwards and the fluid moving downwards. This general approach will allow our model to be used for a range of applications. However, since no latent heat is given off when material drips in the furnace, the special limit $L \to 0$ is important for silicon production. This is considered later in Section 4.5.2.2.

Returning to (4.14), we note that V_n is given by (see [67])

$$V_n = -\frac{1}{\|\nabla a\|}\frac{\partial a}{\partial t}, \tag{4.15}$$

and that the outward normal to the boundary from the fluid is

$$\mathbf{n} = \frac{\nabla a}{\|\nabla a\|} = \frac{1}{\|\nabla a\|}\begin{pmatrix}\frac{\partial a}{\partial r}\\ -1\end{pmatrix} = \frac{1}{\sqrt{1+\left(\frac{\partial a}{\partial r}\right)^2}}\begin{pmatrix}\frac{\partial a}{\partial r}\\ -1\end{pmatrix}. \tag{4.16}$$

Taking care of the signs of the normals for the radiative and conductive fluxes on the right hand side of equation (4.16), we obtain

$$\rho L\left(\frac{1}{\|\nabla a\|}\frac{\partial a}{\partial t} + \mathbf{u}\cdot\frac{\nabla a}{\|\nabla a\|}\right) = -\epsilon_R\sigma_{\mathrm{SB}}({T_h}^4 - T_M^4)\mathbf{k}\cdot\mathbf{n} - k\nabla T\cdot\mathbf{n}, \text{ at } z = a(r,t), \tag{4.17}$$

for $\mathbf{n}$ given by (4.16), emissivity ϵ_R (dimensionless), and Stefan-Boltzmann constant σ_{SB} [kg K^{-4}s^{-3}] (where the subscript is to avoid confusion with the heat capacities in Chapter 2). The first term on the right hand side is the radiative flux from the hot heat source to the surface, and the second term is the conductive flux lost from the surface. We can thus multiply through by $\|\nabla a\|$, giving

$$\rho L\left(\frac{\partial a}{\partial t}+\mathbf{u}\cdot\nabla a\right)=-\epsilon_R\sigma_{\text{SB}}(T_h^4-T_M^4)\mathbf{k}\cdot\nabla a-k\nabla T\cdot\nabla a,\ \text{at } z=a(r,t). \quad (4.18)$$

Note that (4.18) includes a simplified radiative flux. In actuality an integral term would be needed to capture the radiative contribution for each point at the base to the surface $z=a(r,t)$. However, to do this consistently, we would need to track the height of the pool at the base of the furnace, to know the distance that heat radiates onto the surface. Instead, we have a heat source radiating from $z=-\infty$.

At the $z=a(r,t)$ surface, we have that the normal stress is equal to the atmospheric pressure in the gas. In practice there may be some over-pressure in $z<a(r,t)$, but this is not included in our model. We also have that the tangential component of stress is zero. These conditions can be written

$$\mathbf{n}\cdot\Sigma\mathbf{n}=-p_{\text{atm}},\quad \mathbf{t}\cdot\Sigma\mathbf{n}=0,\ \text{at } z=a(r,t), \quad (4.19)$$

for stress tensor, Σ, normal vector, $\mathbf{n}$, and tangential vector, $\mathbf{t}$. Angular terms do not contribute, so we only give the relevant terms in the tensor

$$\Sigma=\begin{bmatrix}\Sigma_{rr} & \Sigma_{rz}\\ \Sigma_{zr} & \Sigma_{zz}\end{bmatrix}=\begin{bmatrix}-p+2\eta\frac{\partial u_r}{\partial r} & \eta\left(\frac{\partial u_r}{\partial z}+\frac{\partial u_z}{\partial r}\right)\\ \eta\left(\frac{\partial u_r}{\partial z}+\frac{\partial u_z}{\partial r}\right) & -p+2\eta\frac{\partial u_z}{\partial z}\end{bmatrix}. \quad (4.20)$$

Since the tangent vector is given by

$$\mathbf{t}=\frac{1}{\sqrt{1+\left(\frac{\partial a}{\partial r}\right)^2}}\begin{pmatrix}1\\ \frac{\partial a}{\partial r}\end{pmatrix}, \quad (4.21)$$

and noting that $\Sigma_{rz}=\Sigma_{zr}$, we thus obtain

$$\frac{1}{1+\left(\frac{\partial a}{\partial r}\right)^2}\left[\Sigma_{rr}\left(\frac{\partial a}{\partial r}\right)^2-2\Sigma_{rz}\frac{\partial a}{\partial r}+\Sigma_{zz}\right]=-p_{\text{atm}},\ \text{at } z=a(r,t), \quad (4.22)$$

$$\frac{1}{1+\left(\frac{\partial a}{\partial r}\right)^2}\left[-\Sigma_{rr}\frac{\partial a}{\partial r}+\Sigma_{rz}\left(1-\left(\frac{\partial a}{\partial r}\right)^2\right)+\Sigma_{zz}\frac{\partial a}{\partial r}\right]=0,\ \text{at } z=a(r,t). \quad (4.23)$$

At the upper interface, we have analogous conditions arising from continuity of normal and tangential stress. The normal stress is equal to the hydrostatic pressure in the upper region, and the tangential stress is zero. Defining $\mathbf{n_b}$ and $\mathbf{t_b}$ as

$$\mathbf{n_b}=\frac{1}{\sqrt{1+\left(\frac{\partial b}{\partial r}\right)^2}}\begin{pmatrix}-\frac{\partial b}{\partial r}\\ 1\end{pmatrix},\quad \mathbf{t_b}=\frac{1}{\sqrt{1+\left(\frac{\partial b}{\partial r}\right)^2}}\begin{pmatrix}1\\ \frac{\partial b}{\partial r}\end{pmatrix}, \quad (4.24)$$

we can write the stress conditions

$$\mathbf{n_b} \cdot \Sigma \mathbf{n_b} = -p_{\text{atm}} - \rho g(h - b(r,t)), \quad \mathbf{t_n} \cdot \Sigma \mathbf{t_n} = 0, \text{ at } z = b(r,t). \tag{4.25}$$

The free surfaces start at the base of the furnace, so we have initial conditions

$$a(r,0) = 0, \quad b(r,0) = 0. \tag{4.26}$$

We are aware that this introduces a singularity into the problem, since the viscous region is non-existent initially. However, this is the case in experiments, and later in Section 4.4 we find that a viscous region develops naturally in numerical simulations.

To close the system we have the constitutive relationship for viscosity,

$$\eta = \eta_s \exp\left(-\lambda_s \left(T - T_M\right)\right), \tag{4.27}$$

motivated by the fact that the fluid becomes less viscous as it heats up, with the positive parameters η_s and λ_s representing the viscosity at the melting temperature and the rate of exponential decay, respectively. An exponential function, such as (4.27), has been used in many applications, such as the flow of lava [37], molten polymers [105], and electrodes [8]. We should remark that often an Arrhenius law is used instead, and this fits well with data for some metallic slags [99], which are similar to the charge in silicon furnaces. However, for small temperature variations, the Arrhenius can be approximated by an inverse exponential. To illustrate this, let $T = T_0(1 + \bar{T})$ for small dimensionless $\bar{T}$. We then have

$$\begin{aligned} \exp\left(\frac{A}{T}\right) &= \exp\left(\frac{A}{T_0}(1+\bar{T})^{-1}\right) \\ &= \exp\left(\frac{A}{T_0}\left(1 - \bar{T} + \mathcal{O}(\bar{T})^2\right)\right) \\ &= \exp\left(\frac{A}{T_0}\right)\exp\left(-\frac{A}{T_0}\bar{T}\right)\left(1 + \mathcal{O}(\bar{T}^2)\right). \end{aligned} \tag{4.28}$$

Since the relative temperature difference between $z = a(r,t)$ and $z = h$ is quite small, the inverse exponential is sufficient for our model. This approach is often taken in the mathematical literature [66, 73], since it eases the model analysis.

Our system is thus comprised of equations (4.1), (4.2), (4.5), boundary conditions (4.4), (4.7), (4.8), (4.9), (4.10), (4.13), (4.22), (4.23), (4.25), initial conditions (4.12), (4.26), interface conditions (4.11) and (4.18), and the viscosity relationship (4.27).

4.3 Tall, thin cylinder limit

We now non-dimensionalise our system under the assumption that the pilot furnace is tall and thin. We introduce the dimensionless parameter $\delta = h/R$, giving the ratio of lengthscales, and assume $0 < \delta \ll 1$. We introduce the scalings

$$\begin{aligned} &u_r = \delta U \bar{u}_r, \quad u_z = U\bar{u}_z, \quad r = \delta h \bar{r}, \quad z = h\bar{z}, \quad a = h\bar{a}, \quad b = h\bar{b}, \\ &p = p_{\text{atm}} + \frac{U\eta_s}{\delta^2 h}\bar{p}, \quad \eta = \eta_s\bar{\eta}, \quad T = T_c + (T_M - T_c)\,\bar{T}, \quad t = \frac{\rho L h^2}{k(T_M - T_c)}\bar{t}, \end{aligned} \tag{4.29}$$

where we have chosen the Stefan timescale balancing the movement of the interface with the conductive heat flux from the fluid. For the velocity scale, we choose the average speed for Poiseuille flow due to gravity in a cylinder of radius R for a fluid of constant viscosity η_s, namely

$$U = \frac{\rho g}{8\eta_s}R^2. \tag{4.30}$$

The leading order system will depend on the dimensionless parameters

$$\begin{aligned} St =& \frac{C_p(T_M - T_c)}{L}, \quad Pe = \frac{Uh}{\kappa}, \quad \gamma = \frac{\epsilon_R \sigma_{\text{SB}}\left(T_h^4 - T_M^4\right)}{k\left(T_M - T_c\right)/h}, \\ T_b :=& \frac{T_k - T_c}{T_M - T_c}, \quad \lambda = \lambda_s\left(T_M - T_c\right). \end{aligned} \tag{4.31}$$

The Stefan number, St, measures the ratio of sensible heat to latent heat, the thermal Péclet number, Pe, measures the ratio of the rate of thermal convection to the rate of thermal conduction, and the parameter γ is the ratio of radiative to convective thermal fluxes. T_b represents the condensation temperature and λ the sensitivity of the viscosity to temperature variations.

Dropping the overbar notation in (4.29), we obtain the system

$$\frac{\partial u_z}{\partial z} + \frac{1}{r}\frac{\partial}{\partial r}\left(r u_r\right) = 0, \tag{4.32}$$

$$0 = -\frac{\partial p}{\partial z} + \frac{1}{r}\frac{\partial}{\partial r}\left(r\eta\frac{\partial u_z}{\partial r}\right) - 8 + \mathcal{O}(\delta^2), \tag{4.33}$$

$$0 = -\frac{\partial p}{\partial r} + \mathcal{O}(\delta^2), \tag{4.34}$$

$$\frac{\partial T}{\partial t} + \frac{Pe}{St}\left(u_r\frac{\partial T}{\partial r} + u_z\frac{\partial T}{\partial z}\right) = \frac{1}{St}\left(\frac{1}{\delta^2}\frac{1}{r}\frac{\partial}{\partial r}\left(r\frac{\partial T}{\partial r}\right) + \frac{\partial^2 T}{\partial z^2}\right), \tag{4.35}$$

$$\eta = \exp\left(-\lambda\left(T - 1\right)\right). \tag{4.36}$$

We have the following boundary and initial conditions

$$T(r, a(r,t), t) = 1, \quad T(r,1,t) = 0, \quad \frac{\partial T}{\partial r}(1,z,t) = 0, \quad T \text{ bounded as } r \to 0, \tag{4.37}$$

$$T(r,z,0)=0, \tag{4.38}$$

$$u_r(1,z,t)=0, \quad u_z(1,z,t)=0, \quad \|\mathbf{u}\| \text{ is bounded as } r\to 0, \tag{4.39}$$

We note that the atmospheric pressure terms p_{atm} cancel in both stress conditions (4.22) and (4.23), and hence we find

$$\left(-\frac{p}{\delta^2}+2\eta\frac{\partial u_r}{\partial r}\right)\frac{1}{\delta^2}\left(\frac{\partial a}{\partial r}\right)^2-2\eta\left(\delta\frac{\partial u_r}{\partial z}+\frac{1}{\delta}\frac{\partial u_z}{\partial r}\right)\frac{1}{\delta}\frac{\partial a}{\partial r}-\frac{p}{\delta^2}+2\eta\frac{\partial u_z}{\partial z}=0, \text{ at } z=a(r,t), \tag{4.40}$$

$$\begin{aligned}-\left(-\frac{p}{\delta^2}+2\eta\frac{\partial u_r}{\partial r}\right)\frac{1}{\delta}\frac{\partial a}{\partial r}+\eta\left(\delta\frac{\partial u_r}{\partial z}+\frac{1}{\delta}\frac{\partial u_z}{\partial r}\right)\left(1-\frac{1}{\delta^2}\left(\frac{\partial a}{\partial r}\right)^2\right)\\ +\left(-\frac{p}{\delta^2}+2\eta\frac{\partial u_z}{\partial z}\right)\frac{1}{\delta}\frac{\partial a}{\partial r}=0 \text{ at } z=a(r,t).\end{aligned} \tag{4.41}$$

Similarly the free stress conditions (4.25) on the upper surface become

$$\begin{aligned}\left(-\frac{p}{\delta^2}+2\eta\frac{\partial u_r}{\partial r}\right)\frac{1}{\delta^2}\left(\frac{\partial b}{\partial r}\right)^2-2\eta\left(\delta\frac{\partial u_r}{\partial z}+\frac{1}{\delta}\frac{\partial u_z}{\partial r}\right)\frac{1}{\delta}\frac{\partial b}{\partial r}-\frac{p}{\delta^2}+2\eta\frac{\partial u_z}{\partial z}\\ =-8(1-b(r,t))\left(1+\frac{1}{\delta^2}\left(\frac{\partial b}{\partial r}\right)^2\right), \text{ at } z=b(r,t),\end{aligned} \tag{4.42}$$

$$\begin{aligned}-\left(-\frac{p}{\delta^2}+2\eta\frac{\partial u_r}{\partial r}\right)\frac{1}{\delta}\frac{\partial b}{\partial r}+\eta\left(\delta\frac{\partial u_r}{\partial z}+\frac{1}{\delta}\frac{\partial u_z}{\partial r}\right)\left(1-\frac{1}{\delta^2}\left(\frac{\partial b}{\partial r}\right)^2\right)\\ +\left(-\frac{p}{\delta^2}+2\eta\frac{\partial u_z}{\partial z}\right)\frac{1}{\delta}\frac{\partial b}{\partial r}=0, \text{ at } z=b(r,t).\end{aligned} \tag{4.43}$$

We also have the interface conditions

$$\frac{\partial a}{\partial t}+\frac{Pe}{St}\left(u_r\frac{\partial a}{\partial r}-u_z\right)=\gamma+\frac{\partial T}{\partial z}-\frac{1}{\delta^2}\frac{\partial T}{\partial r}\frac{\partial a}{\partial r}, \text{ at } z=a(r,t), \tag{4.44}$$

$$a(r,0)=0, \tag{4.45}$$

$$T(r,b(r,t),t)=T_b, \tag{4.46}$$

$$b(r,0)=0. \tag{4.47}$$

We now treat St, Pe, γ, T_b, and λ as $\mathcal{O}(1)$ parameters, and examine the problem in the small δ limit, so that the domain is long and thin.

4.3.1 Derivation of leading order system

Since we have taken a tall, thin limit, we would expect the lower interface to be flat to leading order. To prove this, we note that the leading order terms in (4.40) and (4.41) are

$$-p\left(\frac{\partial a}{\partial r}\right)^2 = 0, \quad p\frac{\partial a}{\partial r} - \eta\frac{\partial u_z}{\partial r}\left(\frac{\partial a}{\partial r}\right)^2 = 0. \tag{4.48}$$

If we did not take $\frac{\partial a}{\partial r} = 0$, then in addition to zero pressure $p = 0$ we would also need the vertical component of velocity to be radially independent at the interface. Due to the no-flux condition on the wall, this would require zero vertical velocity across the whole interface, and hence throughout the entire fluid and granular regions. Thus, since we want to include convection in our model, we must have that the interface is flat at leading order.

Further, letting $a = a_0(t) + \delta a_1(r,t) + \mathcal{O}(\delta^2)$, where the first term with radial dependence may well come later in the expansion than $\mathcal{O}(\delta)$, we note that the next order terms in (4.40) and (4.41) are given by

$$-p_0\left(\frac{\partial a_1}{\partial r}\right)^2 - p_0 = 0, \quad p_0\frac{\partial a_1}{\partial r} - p_0 = 0, \tag{4.49}$$

for leading order pressure p_0. We thus obtain a zero pressure condition on the flat, lower interface

$$p_0 = 0, \text{ at } z = a_0(t). \tag{4.50}$$

By similar reasoning with equations (4.42) and (4.43), we also obtain a flat upper interface to leading order, so $b = b_0(t) + \mathcal{O}(\delta)$, and we find the pressure condition

$$p_0 = 8(1 - b_0(t)), \text{ at } z = b_0(t). \tag{4.51}$$

We now expand the temperature, velocity, pressure, and viscosity variables. Due to the δ^{-2} term in the heat equation (4.35), we consider expansions of the form

$$\begin{aligned} T &= T_0 + \delta^2 T_1 + \mathcal{O}(\delta^4), \\ \mathbf{u} &= \mathbf{u}_0 + \delta^2 \mathbf{u}_1 + \mathcal{O}(\delta^4), \\ p &= p_0 + \delta^2 p_1 + \mathcal{O}(\delta^4), \\ \eta &= \eta_0 + \delta^2 \eta_1 + \mathcal{O}(\delta^4). \end{aligned} \tag{4.52}$$

The leading order heat equation is

$$0 = \frac{1}{St}\frac{1}{r}\frac{\partial}{\partial r}\left(r\frac{\partial T_0}{\partial r}\right), \tag{4.53}$$

which, combined with the boundedness of T_0 as $r \to 0$ and the vanishing normal derivative on the wall $r = 1$, gives $T_0 = T_0(z, t)$ (for finite St, which we have assumed). Thus, the leading order temperature is radially independent, which we might expect in a tall, thin cylinder. This, in turn, gives that the leading order viscosity is radially independent, with

$$\eta_0(z, t) = \exp\left(-\lambda(T_0(z, t) - 1)\right). \tag{4.54}$$

The leading order fluid equations are

$$\frac{\partial u_{z0}}{\partial z} + \frac{1}{r}\frac{\partial}{\partial r}\left(r u_{r0}\right) = 0, \tag{4.55}$$

$$0 = -\frac{\partial p_0}{\partial z} + \frac{1}{r}\frac{\partial}{\partial r}\left(r\eta_0 \frac{\partial u_{z0}}{\partial r}\right) - 8, \tag{4.56}$$

$$0 = -\frac{\partial p_0}{\partial r}, \tag{4.57}$$

$$u_{r0}(1, z, t) = u_{z0}(1, z, t) = 0, \tag{4.58}$$

$$u_{r0},\ u_{z0} \text{ bounded as } r \to 0, \tag{4.59}$$

$$p_0(r, a_0(t), t) = 0, \quad p_0(r, b_0(t), t) = 8(1 - b_0(t)). \tag{4.60}$$

Since the leading order pressure p_0 is also radially independent, (4.56) can be integrated twice radially to give

$$u_{z0} = \frac{1}{\eta_0(z, t)}\left(\frac{\partial p_0}{\partial z} + 8\right)\left(\frac{r^2}{4} - \frac{1}{4}\right). \tag{4.61}$$

Integrating the incompressibility condition (4.55) radially gives

$$\int_0^1 r\frac{\partial u_{z0}}{\partial z} dr + \left[r u_{r0}\right]_{r=0}^{r=1} = 0. \tag{4.62}$$

The boundary conditions on u_{r0}, combined with (4.61), thus give

$$\frac{\partial}{\partial z}\left(\frac{1}{\eta_0}\left(\frac{\partial p_0}{\partial z} + 8\right)\right) = 0, \tag{4.63}$$

and hence u_{z0} is independent of height z. Substituting u_{z0} from (4.61) into the incompressibility condition (4.55), we find that $u_{r0} = 0$. Thus, to leading order, the fluid moves downwards with a velocity that is the same at each height, but varies radially and temporally. We have that

$$\mathbf{u}_0 = 2f(t)(r^2 - 1)\mathbf{k}, \tag{4.64}$$

where $f(t)$ is the average speed of the fluid, since

$$\left| \frac{2\pi \int_{r=0}^{1} 2f(t)(r^2-1)rdr}{2\pi \int_{r=0}^{1} rdr} \right| = f(t). \tag{4.65}$$

We can find $f(t)$ by first substituting (4.64) into (4.56), which when rearranged gives

$$8f(t)\eta_0 = 8 + \frac{\partial p_0}{\partial z}. \tag{4.66}$$

We can then integrate (4.66) vertically between $z = a_0(t)$ and $z = b_0(t)$, giving

$$\begin{aligned} 8f(t) \int_{a_0(t)}^{b_0(t)} \eta_0(z,t)dz &= [p_0 + 8z]_{z=a_0(t)}^{z=b_0(t)} \\ &= 8(1 - b_0(t)) + 8b_0(t) - 8a_0(t), \end{aligned} \tag{4.67}$$

and hence we obtain

$$f(t) = \frac{(1 - a_0(t))}{\int_{a_0(t)}^{b_0(t)} \eta_0(z,t)dz}. \tag{4.68}$$

Thus, $f(t)$ is a ratio of the gravitational force in the numerator driving the fluid downwards to the viscous force in the denominator resisting motion. Note that the weight of the whole charge is felt, but the resistance is due only to the viscosity of the lower region. We note that in the case of constant viscosity ($\lambda = 0$), and no granular region ($T_b = 1$), we have that $f(t) \equiv 1$, and we recover the usual Poiseuille profile. As expected, the speed is fastest along the centre-line $r = 0$.

We determine an equation for $T_0(z,t)$ by considering the $\mathcal{O}(1)$ heat equation, namely

$$\frac{\partial T_0}{\partial t} + \frac{Pe}{St} u_{z0} \frac{\partial T_0}{\partial z} = \frac{1}{St} \left(\frac{1}{r} \frac{\partial}{\partial r} \left(r \frac{\partial T_1}{\partial r} \right) + \frac{\partial^2 T_0}{\partial z^2} \right). \tag{4.69}$$

Integrating (4.69) radially, noting that T_0 is independent of r, gives

$$\frac{1}{2}\frac{\partial T_0}{\partial t} - \frac{1}{2}\frac{Pe}{St} f(t) = \frac{1}{St} \int_{r=0}^{1} \frac{\partial}{\partial r} \left(r \frac{\partial T_1}{\partial r} \right) dr + \frac{1}{2}\frac{1}{St}\frac{\partial^2 T_0}{\partial z^2}. \tag{4.70}$$

Since T_1 is bounded at $r \to 0$ and has a zero normal derivative on the wall $r = 1$, we are left with

$$\frac{\partial T_0}{\partial t} - \frac{Pe}{St} f(t) \frac{\partial T_0}{\partial z} = \frac{1}{St}\frac{\partial^2 T_0}{\partial z^2}, \text{ in } a_0(t) \le z \le 1, \tag{4.71}$$

with the corresponding initial and boundary conditions

$$T_0(z,0) = 0, \quad T_0(a_0(t),t) = 1, \quad T_0(1,t) = 0. \tag{4.72}$$

We note that the location of the upper interface given by

$$T_0(b_0(t),t) = T_b. \tag{4.73}$$

We also need to determine the leading order Stefan condition. Note that considering the leading order terms in (4.44) gives

$$\frac{\partial a_0}{\partial t} - \frac{Pe}{St} 2f(t)\left(r^2 - 1\right) = \gamma + \frac{\partial T_0}{\partial z}, \text{ at } z = a_0(t), \tag{4.74}$$

which is inadmissible, since a_0 and T_0 are independent of r and $f(t) > 0$, so there is a single term with radial dependence and the equation cannot hold. The problem arises physically because we have assumed a flat interface, $z = a_0(t)$, in order to determine that T_0 is radially independent due to being insulated on the walls. However, to higher order, the interface is not flat, and may decrease away from the walls. We thus have an inner region where temperature could potentially vary radially. We expect this region to be of size $\mathcal{O}(\delta)$, corresponding to a breakdown in the assumption of a tall, thin domain. We will not consider this region in detail, but will examine its effect on the outer problem.

4.3.2 Averaged velocity from inner region

To find the full problem for the leading order behaviour we consider the inner region, and we will find this gives the average velocity, which contributes to the Stefan condition.

We consider the small inner region at the bottom of the lower, viscous region by defining the inner variables $a_I(r,t)$, $\hat{z}$, and $T_I(\hat{z},r,t)$ as

$$a = a_0(t) + \delta a_I(r,t), \quad T = 1 + \delta T_I(\hat{z},r,t), \quad z = a_0(t) + \delta\hat{z}, \tag{4.75}$$

where $r, t \geq 0$ and $\hat{z} \geq a_I$. A schematic diagram of the inner region is given in Figure 4.3.

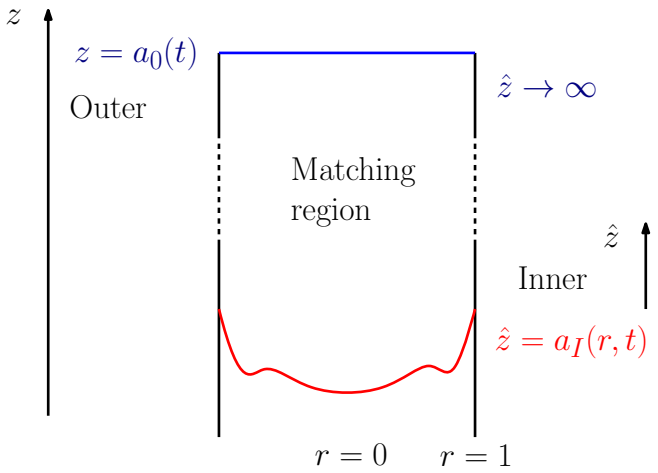


Figure 4.3: Schematic diagram of the inner region near $z = a_0(t)$. In this image the correction term is drawn below the leading order interface, i.e., $a_I < 0$.

The leading order temperature equation in the inner region is given by

$$\hat{\nabla}^2 T_I = 0, \quad \hat{z} \geq a_I(\hat{z}, t), \tag{4.76}$$

where the hat on the Laplacian denotes derivatives with respect to r and $\hat{z}$. We have the inner velocity profile, $\mathbf{u}_I$, which scales with the outer velocity and satisfies the incompressibility condition $\hat{\nabla} \cdot \mathbf{u}_I = 0$.

The leading order Stefan condition in the inner region is given by

$$\frac{da_0(t)}{dt} - \frac{Pe}{St}\mathbf{u}_I \cdot \hat{\nabla} a_I = \gamma - \hat{\nabla} T_I \cdot \hat{\nabla} a_I, \text{ at } \hat{z} = a_I, \tag{4.77}$$

or, alternatively, by

$$\frac{1}{\|\hat{\nabla} a_I\|}\frac{da_0(t)}{dt} - \frac{Pe}{St}\mathbf{u}_I \cdot \mathbf{n} = \frac{\gamma}{\|\nabla a_I\|} - \hat{\nabla} T_I \cdot \mathbf{n}, \text{ at } \hat{z} = a_I. \tag{4.78}$$

We also have that

$$T_I = 0, \quad \hat{z} = a_I, \quad \frac{\partial T_I}{\partial r} = 0 = u_{Iz} = u_{Ir}, \quad r = 1, \tag{4.79}$$

and the matching conditions with the leading order outer variables T_0 and $\mathbf{u}_0$. Using Van Dyke's matching principle, noting that $T_{0z}(a_0(t) + \delta\hat{z}, t) = T_{0z}(a_0(t), t) + \mathcal{O}(\delta)$, we have

$$\frac{\partial T_I}{\partial \hat{z}}(r, \infty, t) = \frac{\partial T}{\partial z}(a_0(t), t), \quad \mathbf{u}_I(r, \infty, t) = \mathbf{u}_0(a_0(t), t). \tag{4.80}$$

Integrating (4.78) over the surface $\hat{z} = s_I(r, t)$, we obtain

$$\iint_{\hat{z}=a_I} \frac{1}{\|\hat{\nabla} a_I\|}\frac{da_0(t)}{dt} - \frac{Pe}{St}\mathbf{u}_I \cdot \mathbf{n}\, dS = \iint_{\hat{z}=a_I} \frac{\gamma}{\|\hat{\nabla} a_I\|} - \hat{\nabla} T_I \cdot \mathbf{n}\, dS. \tag{4.81}$$

Using the divergence theorem in the region bounded by $\hat{z} = a_I$, $\hat{z} = \infty$, and the walls $r = 1$, and noting that $\hat{\nabla}^2 T_I = 0$, gives

$$\iint_{\hat{z}=a_I} \hat{\nabla} T_I \cdot \mathbf{n}\, dS = \iint_{\hat{z}=\infty} \hat{\nabla} T_I \cdot \mathbf{n}\, dS. \tag{4.82}$$

Since $\hat{\nabla} T_I \to \nabla T_0(a_0(t), t)$ as $\hat{z} \to \infty$, we obtain

$$\iint_{\hat{z}=a_I} \hat{\nabla} T_I \cdot \mathbf{n}\, dS = \int_{\theta=0}^{2\pi}\int_{r=0}^{1} r\frac{\partial T_0}{\partial z}(a_0(t), t)\, dr d\theta = \pi\frac{\partial T_0}{\partial z}(a_0(t), t). \tag{4.83}$$

Similarly, since $\mathbf{u}_I$ is incompressible and there are zero flux conditions on the walls, we can use the divergence theorem to write

$$\iint_{\hat{z}=a_I} \mathbf{u}_I \cdot \mathbf{n}\, dS = \int_{\theta=0}^{2\pi}\int_{r=0}^{1} r u_{z0}(a_0(t), t)\, dr d\theta = -f(t)\pi, \tag{4.84}$$

where we have used $u_{z0} = 2f(t)(r^2 - 1)$ from the outer problem.

Noting that

$$\iint_{\hat{z}=a_I} \frac{1}{\|\hat{\nabla} a_I\|}\, dS = \iint_{\hat{z}=a_I} -\mathbf{k}\cdot\mathbf{n}\, dS = \pi, \tag{4.85}$$

is the projected area of the surface onto the plane orthogonal to $\mathbf{k}$, and that $a_0'(t)$ and γ are constant with respect to the integrals, we find

$$\frac{da_0(t)}{dt} + \frac{Pe}{St} f(t) = \gamma + \frac{\partial T_0}{\partial z}, \text{ at } z = a_0(t). \tag{4.86}$$

Thus our analysis of the inner problem has identified that we should impose a radially averaged boundary condition (4.86), instead of (4.74), on the flat outer position of the interface.

4.3.3 Statement of model

We clean the notation used in the previous sections when we derived the lowest order behaviour by dropping the 0 subscripts, so that the problem we seek to study is given by

$$\frac{\partial T}{\partial t} - \frac{f(t)Pe}{St}\frac{\partial T}{\partial z} = \frac{1}{St}\frac{\partial^2 T}{\partial z^2}, \text{ in } a(t) \le z \le 1, \tag{4.87}$$

$$\frac{da}{dt} + \frac{f(t)Pe}{St} = \gamma + \frac{\partial T}{\partial z}, \text{ at } z = a(t), \tag{4.88}$$

$$T(a(t), t) = 1, \quad T(b(t), t) = T_b, \quad T(1, t) = 0, \tag{4.89}$$

$$T(z, 0) = 0, \tag{4.90}$$

$$f(t) = \frac{(1 - a(t))}{\int_{a(t)}^{b(t)} \exp\left(-\lambda(T(z,t) - 1)\right) dz}, \tag{4.91}$$

$$a(0) = 0, \quad b(0) = 0. \tag{4.92}$$

Upon solving this system for $T(z,t)$, $a(t)$, $b(t)$, and $f(t)$ we determine the fluid flow as $\mathbf{u} = 2f(t)(r^2 - 1)\mathbf{k}$. We could subsequently consider the higher order problems if desired, but we do not do this here. A schematic diagram of the tall, thin model is given in Figure 4.4.

4.4 Analysis of the tall, thin cylinder model

We have developed a one-dimensional model for temperature and the motion of the interfaces, which depends upon five parameters, namely Pe, St, γ, T_b, and λ. We now analyse the tall, thin model (4.87) - (4.92) presented in Section 4.3.3. First, in

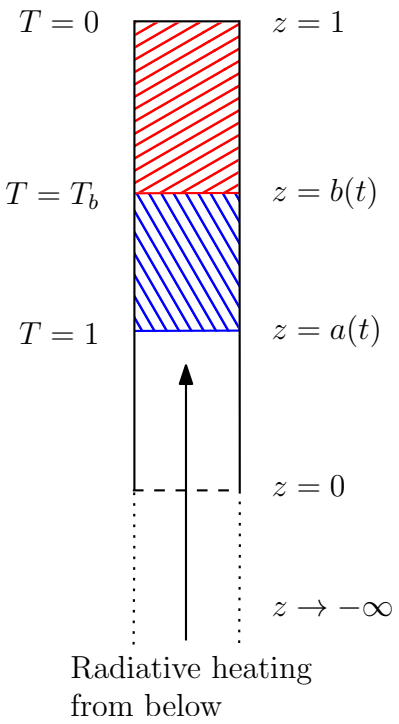


Figure 4.4: Schematic diagram of the tall thin model. The viscous region is in hashed blue and the granular region is in hashed red.

Section 4.4.1 we perform numerical simulations, by mapping the problem onto a fixed domain and using a semi-implicit finite difference scheme. Next, in Section 4.4.2 we look for steady states of the problem, and classify in which parameter regimes the system has a steady state. We do not perform a stability analysis but we use numerical evidence to motivate situations with no steady state, which result in free falling material. Later, in Section 4.5, we consider further parameter limits of the model (4.87) - (4.92) in order to better understand the qualitative behaviour of the solutions.

4.4.1 Numerical solution

It is natural to use a finite difference scheme to obtain numerical solutions of our one-dimensional problem. Potential difficulties, however, come from the moving interfaces, and the non-local convective term $f(t)$, which is determined by an integral condition. In this section, we discuss the numerical scheme implemented, and give some illustrative plots of solutions.

To account for the moving lower interface, we map the problem onto a fixed

domain, with the transformation

$$x = \frac{z - a(t)}{1 - a(t)}, \quad \tau = t. \tag{4.93}$$

Since the partial derivatives become

$$\frac{\partial T}{\partial t} = \frac{\partial T}{\partial \tau} + \frac{\partial T}{\partial x}\frac{d}{dt}\left(\frac{-a(t)}{1-a(t)}\right) = \frac{\partial T}{\partial \tau} - \frac{\partial T}{\partial x}\frac{da}{dt}\frac{1}{(1-a)^2}, \tag{4.94}$$

$$\frac{\partial T}{\partial z} = \frac{\partial T}{\partial x}\frac{1}{1-a}, \tag{4.95}$$

we have the system for $x \in [0,1]$, $\tau \geq 0$,

$$\frac{\partial T}{\partial \tau} + \left(-\frac{da}{d\tau}\frac{1}{(1-a(\tau))^2} - \frac{f(\tau)Pe}{St}\frac{1}{(1-a(\tau))}\right)\frac{\partial T}{\partial x} = \frac{1}{St}\frac{1}{(1-a(\tau))^2}\frac{\partial^2 T}{\partial x^2}, \tag{4.96}$$

$$T(0,\tau) = 1, \quad T(1,\tau) = 0, \tag{4.97}$$

$$T = T_b, \text{ at } \quad x = \frac{b(t) - a(t)}{1 - a(t)}, \tag{4.98}$$

$$\frac{da}{d\tau} + \frac{f(\tau)Pe}{St} = \gamma + \frac{1}{(1-a(\tau))}\frac{\partial T}{\partial x}, \text{ at } x = 0, \tag{4.99}$$

$$T(x,0) = 0, \tag{4.100}$$

$$f(\tau) = \frac{1}{\int_{x=0}^{\frac{b(t)-a(t)}{1-a(t)}} \exp\left(-\lambda(T(x,\tau)-1)\right) dx}. \tag{4.101}$$

Defining

$$\psi(\tau) := -\frac{\gamma}{(1-a(\tau))^2} + \frac{f(\tau)Pe}{St}\frac{a(\tau)}{(1-a(\tau))^2} - \frac{1}{(1-a(\tau))^3}\frac{\partial T}{\partial x}(0,\tau), \tag{4.102}$$

we can write the PDE (4.96) as

$$\frac{\partial T}{\partial \tau} + \psi(\tau)\frac{\partial T}{\partial x} = \frac{1}{St}\frac{1}{(1-a(\tau))^2}\frac{\partial^2 T}{\partial x^2}. \tag{4.103}$$

In the numerical scheme, we first update a by approximating (4.99) using

$$a^{j+1} = a^j + \Delta t\left(\gamma - \frac{f^j Pe}{St} + \frac{1}{1-a^j}\frac{T_1^j - T_G^j}{2\Delta x}\right), \tag{4.104}$$

where j denotes the time point, Δt the timestep, and Δx the spatial step. We calculate the derivative $T_x(0,t)$ by using a ghost point T_G and the first interior point T_1, where T_0 would denote the point on the boundary $x = 0$.

We then determine the coefficient ψ^{j+1} by discretising (4.102), which gives

$$\psi^{j+1} = -\frac{\gamma}{(1-a^j)^2} + \frac{f^j Pe}{St}\frac{a^j}{(1-a^j)^2} - \frac{1}{(1-a^j)^3}\frac{T_1^j - T_G^j}{2\Delta x}. \tag{4.105}$$

The next step is to semi-implicitly find the temperature at the next timestep, T^{j+1}, from the discretised version of (4.96), which reads

$$\frac{T_i^{j+1} - T_i^j}{\Delta t} + \psi^{j+1}\frac{T_{i+1}^{j+1} - T_i^{j+1}}{\Delta x} = \frac{1}{St}\frac{1}{(1-a^j)^2}\frac{T_{i+1}^{j+1} - 2T_i^{j+1} - T_{i-1}^{j+1}}{\Delta x^2}, \tag{4.106}$$

where we have upwinded for the convective term (in this case $\psi < 0$, but if $\psi > 0$ we would have a $T_i^{j+1} - T_{i-1}^{j+1}$ term instead). Note that this scheme is implicit in T but explicit in the coefficients of T derivatives.

We determine b from (4.98). Since T is only defined at grid points in the numerical simulations, we use a piecewise cubic interpolation to approximate the value of x at which $T = T_b$.

The final step within an iteration is to calculate f^{j+1}. We use the trapezium rule to perform the quadrature (4.101), remembering to multiply by the spatial step Δx. Note that if the mesh is not very fine and only the boundary point is hotter than T_b, the necessary quadrature cannot be performed. If this occurs we set f^{j+1} to be the value taken at the previous timestep, f^j.

To improve stability, we run iterative implicit steps before we step forward in time to $j+2$. We first run through the algorithm as explained above to determine an initial approximation for a^{j+1}, T^{j+1}, b^{j+1}, and f^{j+1}. We can use the notation $a^{j+1,1}$ to indicate this is the first solution found. We then refine our solution iteratively. For example, we replace (4.104) with the following

$$a^{j+1,2} = a^j + \Delta t\left(\gamma - \frac{f^{j+1,1}Pe}{St} + \frac{1}{1-a^{j+1,1}}\frac{T_1^{j+1,1} - T_G^{j+1,1}}{2\Delta x}\right), \tag{4.107}$$

and analogously find $T^{j+1,2}$, $b^{j+1,2}$, and $f^{j+1,2}$. We run through this process until the difference between iterations is sufficiently small. In practice, we measure the error as the relative norm of T between successive iterations. Once this falls below a certain tolerance threshold, we then step forward in time to find solutions at time $j+2$. This effectively iteratively solves the implicit backward Euler method.

We choose our timestep based on the CFL condition, letting

$$\Delta t \leq \frac{(1-a_M)^2}{\gamma}\Delta x, \tag{4.108}$$

where a_M is the maximum of the initial condition ($a(0) = 0$) and the steady state value a^*. If the simulations run successfully without oscillations for a larger timestep, then we may choose a larger Δt appropriately. We have run refinement studies with Δt, which show a first order rate of convergence.

We plot the evolution of temperature in both the moving and fixed domains in Figure 4.5. For the parameter values used, the system tends towards a steady state. For early time, $a(t)$ can go negative, as seen by the curve at $t = 0.001$ in the right hand plot. This occurs because of the discontinuity between the initial condition and the lower boundary condition, making the problem hard to resolve numerically for initial timesteps. As the radiative heat from below the charge heats the material, the interface rises and in this case the temperature in the charge tends to a nearly linear profile.

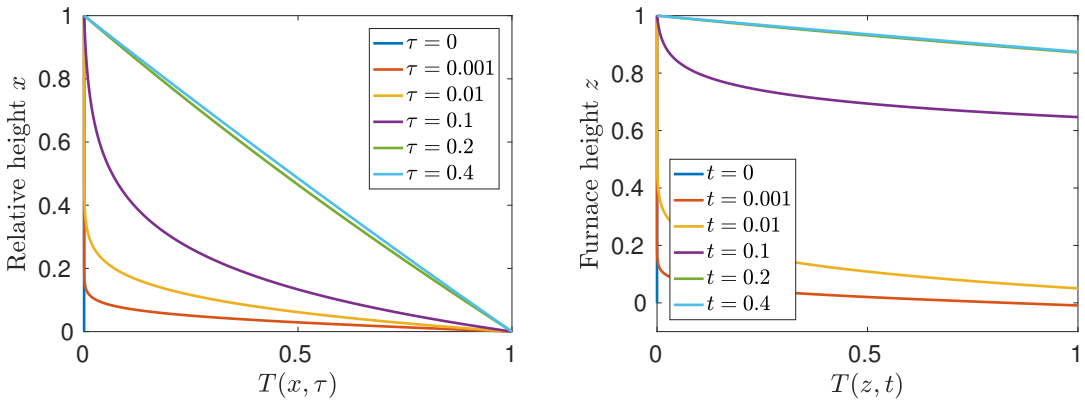


Figure 4.5: Plots showing the evolution of temperature over time. On the left are plots of $T(x,\tau)$ in the fixed domain. On the right are plots of $T(z,t)$ in the original domain. Curves of the same colour are at the same time. Parameter values used are $St = 1$, $Pe = 1$, $\lambda = 0.1$, $T_b = 0.5$, and $\gamma = 20$. A spatial step size of $\Delta x = 4 \times 10^{-3}$ and timestep of $\Delta\tau = 10^{-4}$ are used.

We are mostly interested in the position of the interfaces, with temperature being an intermediate variable to this end. We thus show some example trajectories of $a(t)$ and $b(t)$, each time varying a parameter but keeping the other four fixed. In Figure 4.6 we vary the dimensionless condensation temperature, T_b. Note that for some parameter values the system tends towards a steady state, but for large T_b both interfaces move downwards to $z = -\infty$. In Figure 4.7 we vary the Péclet number Pe. For small values of the Péclet number, the system tends towards a steady state, but the interfaces move downwards for larger values of the Péclet number, since thermal

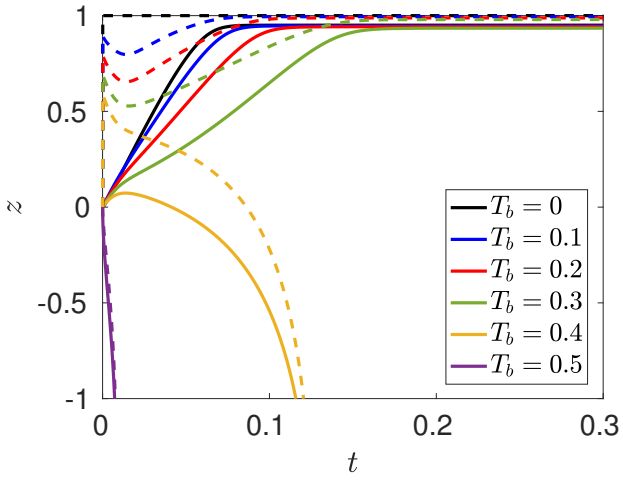


Figure 4.6: Plot showing $a(\tau)$ in solid lines and $b(\tau)$ in dashed lines for varying T_b. Other parameter values used are $St = 0.1$, $Pe = 1$, $\lambda = 0.1$, and $\gamma = 30$. A spatial step size of $\Delta x = 4 \times 10^{-3}$ and timestep of $\Delta\tau = 10^{-4}$ are used.

convection is strong enough to overcome the radiative heating. Note that negative steady states are possible, as demonstrated in Figure 4.8.

In the model we have set initial conditions for the interfaces as $a(0) = b(0) = 0$. Despite the potential numerical problem from having an initially singular viscous domain, the simulations seem to cope, with the interfaces separating in a very fast transient period, as demonstrated in Figures 4.6 and 4.7. These initial conditions are somewhat arbitrary, however, since there is no base of the furnace in the model. In Figure 4.9 we plot trajectories for ten random initial conditions, showing that in each case the system tends to the same pair of steady states a^* and b^*, which are determined by the model parameters.

Numerical simulations of the model thus show that either the interfaces and temperature tend to a steady state, or the interfaces drop indefinitely, and so the charge experiences free fall. When there is free fall, this is not completed in finite time, but the interfaces eventually move at an approximately constant velocity. The steady states shown so far in this chapter appear to be stable, in as much as they can be obtained numerically for different initial conditions, within a given region of attraction. We now turn our attention to examining these steady states.

4.4.2 Steady state solutions

We have observed numerically that solutions of the model (4.87) - (4.92) can tend towards a spatial steady state. We now determine these steady states by neglecting

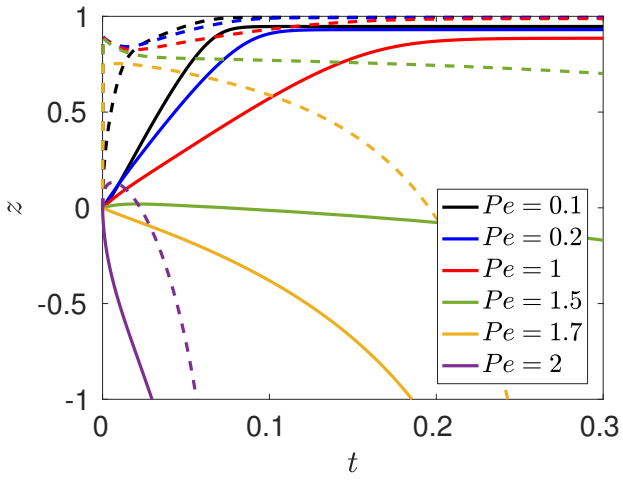


Figure 4.7: Plot showing $a(\tau)$ in solid lines and $b(\tau)$ in dashed lines for varying Pe. Other parameter values used are $St = 0.1$, $\lambda = 0.1$, $\gamma = 20$, and $T_b = 0.1$. A spatial step size of $\Delta x = 4 \times 10^{-3}$ and timestep of $\Delta\tau = 10^{-4}$ are used.

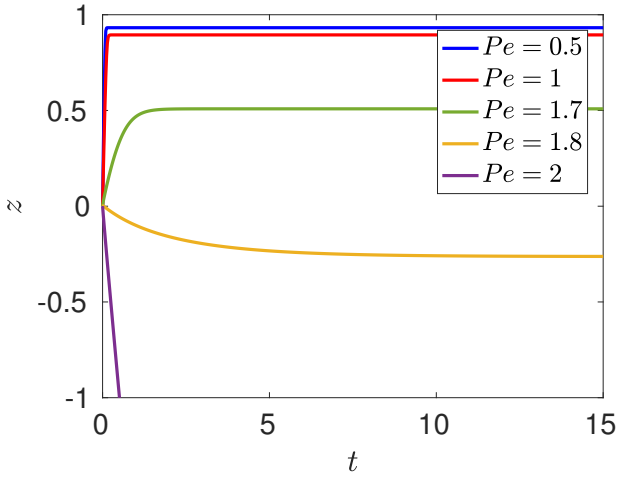


Figure 4.8: Plot showing $a(\tau)$ for varying Pe. Other parameter values used are $St = 0.1$, $\lambda = 0$, $\gamma = 20$, and $T_b = 0$. A spatial step size of $\Delta x = 4 \times 10^{-3}$ and timestep of $\Delta\tau = 10^{-4}$ are used. Note the purple curve for $Pe = 2$ does not tend to a steady state, but decreases to $z = -\infty$.

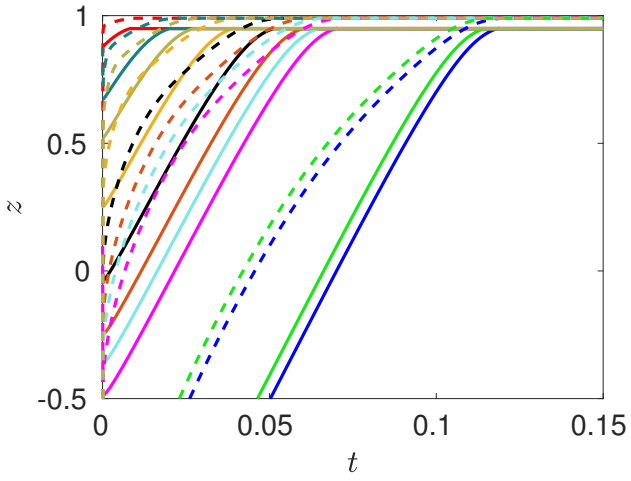


Figure 4.9: Trajectories from ten randomly selected initial positions for $a(t)$ in solid and $b(t)$ in corresponding dashed lines. The initial positions were selected randomly from independent Uniform $[-2, 1]$ distributions. Parameter values used are $\gamma = 30$, $St = 0.1$, $Pe = 0.1$, $\lambda = 0.1$, and $T_b = 0.2$. A spatial step size of $\Delta x = 4 \times 10^{-3}$ and timestep of $\Delta\tau = 10^{-4}$ are used.

time dependence in the system (4.87) - (4.91). For our model, steady state solutions cannot be written in an explicit closed form, but depend upon an implicit equation for f that arises from (4.91), which must be solved numerically. We find two roots to this equation, corresponding to two steady states. We show numerical evidence suggesting that one of these steady states is stable, while the other steady state is unstable. Subsequently, in Section 4.4.3, we plot bifurcation diagrams of the model behaviour in parameter space.

Suppose we look for a steady state solution, so that $a(t) = a^*$, $b(t) = b^*$, $T(z,t) = T^*(z)$, and $f(t) = f^*$. The system (4.87) - (4.92) then becomes

$$-f^* Pe \frac{dT^*}{dz} = \frac{d^2T^*}{dz^2}, \text{ in } a^* \leq z \leq 1, \tag{4.109}$$

$$\frac{f^* Pe}{St} = \gamma + \frac{\partial T^*}{\partial z}, \text{ at } z = a^*, \tag{4.110}$$

$$T^*(a^*) = 1, \quad T^*(1) = 0, \tag{4.111}$$

$$T^*(b^*) = T_b, \tag{4.112}$$

$$f^* = \frac{(1 - a^*)}{\int_{z=a^*}^{b^*} \exp\left(-\lambda(T^* - 1)\right) dz}. \tag{4.113}$$

The equation (4.109) combined with the boundary conditions (4.111) can be solved to find the steady state temperature profile

$$T^*(z) = \frac{\exp\left(-f^* Pe\ z\right) - \exp\left(-f^* Pe\right)}{\exp\left(-f^* Pe\ a^*\right) - \exp\left(-f^* Pe\right)} = \frac{\exp\left(f^* Pe(1 - z)\right) - 1}{\exp\left(f^* Pe(1 - a^*)\right) - 1}. \tag{4.114}$$

We can then use the Stefan condition (4.110) to find an equation for the position of the free boundary, which reads

$$\frac{f^*Pe}{St} = \gamma - f^*Pe\frac{\exp\left(f^*Pe(1-a^*)\right)}{\exp\left(f^*Pe(1-a^*)\right)-1}. \tag{4.115}$$

This can be rearranged to determine that the lower interface is at

$$a^* = 1 + \frac{1}{f^*Pe}\ln\left(1 - \frac{1}{\frac{\gamma}{f^*Pe} - \frac{1}{St}}\right). \tag{4.116}$$

We use the isotherm (4.112) to find that the upper interface is at

$$b^* = 1 - \frac{1}{f^*Pe}\ln\left(1 + T_b\left(\exp\left(f^*Pe(1-a^*)\right)-1\right)\right). \tag{4.117}$$

When $T_b = 0$, the upper interface is at the furnace top ($b^* = 1$). When $T_b = 1$, we find that (4.117) simplifies to give $b^* = a^*$, which is also expected.

We see that if we can find f^*, then we obtain a^* and b^*. To ease the analysis of the equation governing f^*, we introduce the change of variable

$$\vartheta := \frac{\gamma}{f^*Pe} - \frac{1}{St}, \tag{4.118}$$

(where we use ϑ to avoid confusion with the volume fraction θ in Chapter 2). With (4.118), we have

$$a^* = 1 + \frac{1}{f^*Pe}\ln\left(1 - \frac{1}{\vartheta}\right) = 1 + \frac{1}{\gamma}\left(\vartheta + \frac{1}{St}\right)\ln\left(1 - \frac{1}{\vartheta}\right), \tag{4.119}$$

$$b^* = 1 - \frac{1}{f^*Pe}\ln\left(1 + \frac{T_b}{\vartheta - 1}\right) = 1 - \frac{1}{\gamma}\left(\vartheta + \frac{1}{St}\right)\ln\left(1 + \frac{T_b}{\vartheta - 1}\right). \tag{4.120}$$

We must take care to ensure the logarithms in (4.119) and (4.120) are well-defined. The parameters St, Pe, and γ are all positive, $T_b \in [0,1]$, and f^* is non-negative. The logarithm in (4.119) is not well-defined for $\vartheta \in [0,1]$. In the case that $\vartheta < 0$, we have $a^* > 1$ and thus a steady state which is above the top of the furnace, which is evidently not physically attainable. The logarithm in (4.120) is not defined for $\vartheta \in [1-T_b, 1]$. For $\vartheta < 1 - T_b$ we have $b^* > 1$, which is also not physically attainable. Hence, we must have $\vartheta > 1$ for physically relevant steady states to exist.

Note that we have not yet found a^* and b^* explicitly as functions of the parameters Pe, St, γ, T_b, and λ, since (4.116) and (4.117) still have a dependence on f^*. The crucial equation we have not yet used is (4.113), which we write as the implicit integral equation for f^*:

$$f^* = \frac{(1-a^*)}{\int_{z=a^*}^{b^*}\exp\left(-\lambda\left(\frac{\exp(f^*Pe(1-z))-1}{\exp(f^*Pe(1-a^*))-1} - 1\right)\right)dz}. \tag{4.121}$$

We can rearrange (4.121) to

$$f^* e^{\lambda} \int_{z=a^*}^{b^*} \exp\left(-\lambda(\vartheta-1)\left(\exp\left(f^* Pe(1-z)\right)-1\right)\right) dz = -\frac{1}{\gamma}\left(\vartheta+\frac{1}{St}\right)\ln\left(1-\frac{1}{\vartheta}\right). \tag{4.122}$$

Once f^* is determined as a function of Pe, St, γ, T_b and λ, we will then know a^*, b^*, and T^*.

We seek to simplify (4.122), by making the substitution

$$w = -\lambda(\vartheta-1)\exp\left(f^* Pe(1-z)\right), \tag{4.123}$$

and then noting that

$$dw = f^* Pe\lambda(\vartheta-1)\exp\left(f^* Pe(1-z)\right) dz = -f^* Pe\ w\ dz, \tag{4.124a}$$

$$w = -\lambda(\vartheta-1)\exp\left(f^* Pe(1-a^*)\right) = -\lambda\vartheta, \text{ at } z = a^*, \tag{4.124b}$$

$$w = -\lambda(\vartheta-1)\exp\left(f^* Pe(1-b^*)\right) = -\lambda(\vartheta-1+T_b), \text{ at } z = b^*. \tag{4.124c}$$

Then, the change of variable (4.123) transforms (4.122) to

$$\frac{e^{\lambda\vartheta}}{Pe}\int_{-\lambda\vartheta}^{-\lambda(\vartheta+T_b-1)} \frac{e^w}{w} dw = -\frac{1}{\gamma}\left(\vartheta+\frac{1}{St}\right)\ln\left(1-\frac{1}{\vartheta}\right). \tag{4.125}$$

The integral on the left hand side can only be evaluated using special functions. We introduce the exponential integrals $E_1(x)$ and $Ei(x)$ to be

$$E_1(x) := \int_x^{\infty} \frac{e^{-t}}{t} dt, \quad Ei(x) := \int_{-\infty}^{x} \frac{e^{-t}}{t} dt, \tag{4.126}$$

where $E_1(x)$ is defined for $x > 0$ and $Ei(x)$ is defined for $x < 0$. Noting that

$$Ei(-x) = -E_1(x), \text{ for } x > 0, \tag{4.127}$$

after algebraic manipulation, we find that (4.125) can be written as

$$e^{\lambda\vartheta}\left(E_1\left(\lambda(\vartheta-1+T_b)\right) - E_1\left(\lambda\vartheta\right)\right) = \frac{Pe}{\gamma}\left(\vartheta+\frac{1}{St}\right)\ln\left(\frac{\vartheta}{\vartheta-1}\right). \tag{4.128}$$

Since there is a one-to-one mapping between f^* and ϑ (defined in (4.118)), each root of (4.128) for ϑ corresponds to a steady state f^*. Note also that Pe/γ acts as one parameter in (4.128), and so there are only four parameter groupings in (4.128), being St, T_b, λ, and Pe/γ. In exploring this parameter regime we recall we require $\vartheta > 1$, which is equivalent to $\gamma/f^* Pe - 1/St > 1$.

The numerical evidence from simulations of the PDE problem, shown in Section 4.4.1, suggests that there exists at most one steady state for given parameters, and that this steady state is stable. Clearly, however, if unstable steady states exist, then we may not be able to find these numerically from our finite difference scheme. Suppose we introduce the function

$$\phi(\vartheta) := e^{\lambda\vartheta}\left(E_1\left(\lambda(\vartheta - 1 + T_b)\right) - E_1\left(\lambda\vartheta\right)\right) - \frac{Pe}{\gamma}\left(\vartheta + \frac{1}{St}\right)\ln\left(\frac{\vartheta}{\vartheta - 1}\right), \quad (4.129)$$

so that each zero of (4.129) corresponds to a root of (4.128). If the partial derivatives of ϕ were all single-signed then it could have at most one zero. This is true for the derivatives with respect to St, Pe/γ, and T_b, but unfortunately not for λ and ϑ. Instead, to determine the number of roots of (4.128), we plot contours of roots of ϕ for λ against ϑ, for different values of the other parameters. If the contours are monotonic, then only one steady state is possible. However, if several possible ϑ exist for each λ, then multiple steady states are possible. In the parameter space explored, we find curves exhibiting the existence of two steady states. We give an example in Figure 4.10, circling the location of roots for $\lambda = 1$. We plot values of λ within the range $\lambda \in [-10, 10]$ for demonstrative purposes, although in practice we expect the viscosity of the fluid to increase as temperature decreases, and hence require $\lambda > 0$.

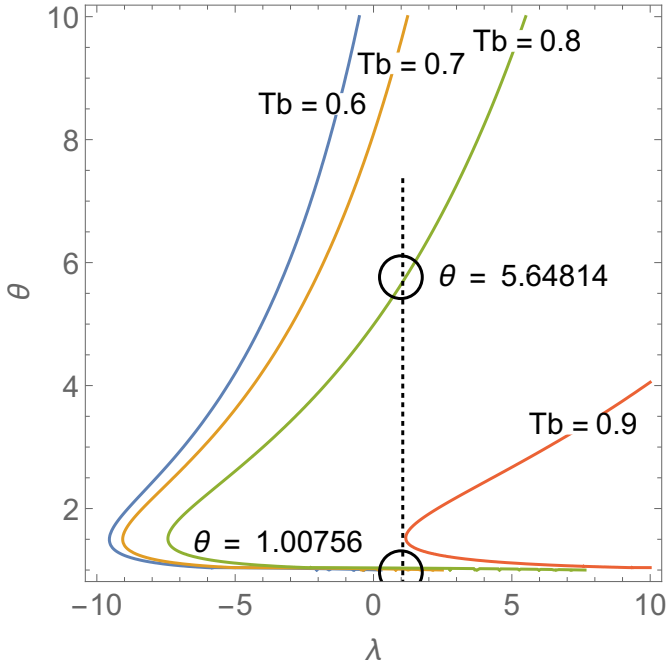


Figure 4.10: Contour plots of roots of (4.129) for ϑ, given a value of λ and T_b, for $Pe = 1$, $St = 2$, and $\gamma = 30$. The multiple roots for $\lambda = 1$ and $T_b = 0.8$ are circled.

Our numerical simulations suggest that the steady state solution corresponding to the larger ϑ root is stable, while the steady state corresponding to the smaller ϑ root is unstable. In Figure 4.11 we plot trajectories starting from steady states corresponding to the circled points shown in Figure 4.10. In each case we set the initial temperature profile as $T^*(z)$. All values used were to five decimal places. The upper trajectories remain at the steady state, but the lower trajectories slowly move away from their respective steady states, before eventually undergoing free fall. This explains why at most one steady state was found from numerical solutions of the PDE problem in Section 4.4.1.

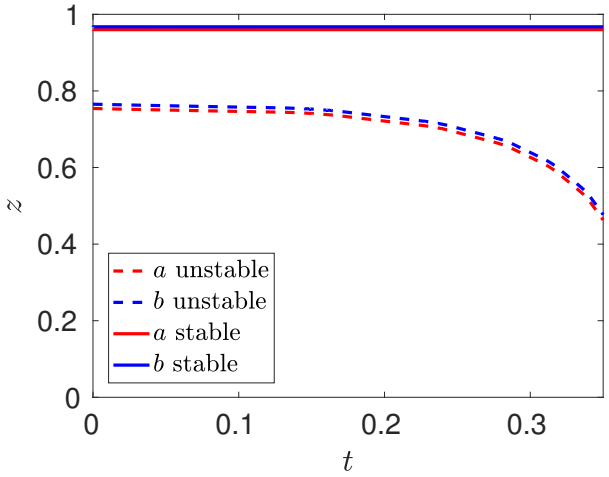


Figure 4.11: Plot showing the evolution of trajectories from a stable steady state (solid) and unstable steady state (dashed) for $a(t)$ (red) and $b(t)$ (blue). Parameter values used are $Pe = 1$, $St = 2$, $\gamma = 30$, $T_b = 0.8$, and $\lambda = 1$. A spatial step size of $\Delta x = 4 \times 10^{-3}$ and a timestep of $\Delta\tau = 10^{-6}$ are used.

For each fixed value of T_b in Figure 4.10, there are values of λ for which one root occurs for ϑ close to 1, and the other for large ϑ. We now examine each of these limits.

For ϑ near 1, we note that

$$\frac{\gamma}{f^* Pe} - \frac{1}{St} \sim 1. \tag{4.130}$$

In particular, for the large Stefan number limit relevant for silicon furnaces, we see that heating and convection are approximately in balance. To analyse the case of $\vartheta \sim 1$ more formally, we set $\vartheta = 1 + \vartheta_\epsilon$, where $0 < \vartheta_\epsilon \ll 1$. Substituting this into

(4.119) and (4.120), and Taylor expanding the relevant quantities, we find

$$\begin{aligned} a^* &= 1 + \frac{1}{\gamma}\left(1 + \vartheta_\epsilon + \frac{1}{St}\right)\ln\left(1 - \frac{1}{1+\vartheta_\epsilon}\right) = 1 + \frac{1}{\gamma}\left(1 + \frac{1}{St}\right)\ln\vartheta_\epsilon + \mathcal{O}\left(\vartheta_\epsilon \ln\vartheta_\epsilon\right), \\ b^* &= 1 - \frac{1}{\gamma}\left(1 + \vartheta_\epsilon + \frac{1}{St}\right)\ln\left(1 + \frac{T_b}{\vartheta_\epsilon}\right) = 1 + \frac{1}{\gamma}\left(1 + \frac{1}{St}\right)\ln\vartheta_\epsilon + \mathcal{O}\left(\vartheta_\epsilon \ln\vartheta_\epsilon\right), \end{aligned} \tag{4.131}$$

and so a^* and b^* can become arbitrarily large in magnitude and negative as $\vartheta \searrow 1$. By reducing the heating, or increasing the convective term, one can lower the steady states. If the heating is too low, however, so that $\vartheta < 1$, then no steady state exists and the interfaces fall indefinitely. Numerical simulations, such as those shown in Figure 4.11, suggest that the root close to $\vartheta = 1$ corresponds to the unstable steady state.

We also obtain a root for large ϑ, so

$$\frac{\gamma}{f^* Pe} - \frac{1}{St} \gg 1. \tag{4.132}$$

This corresponds physically to large heating or small convection. For $\vartheta \gg 1$, we can Taylor expand the logarithms in (4.119) and (4.120), to obtain

$$\begin{aligned} a^* &= 1 + \frac{\vartheta}{\gamma}\left(-\frac{1}{\vartheta}\right) + \mathcal{O}\left(\frac{1}{\vartheta}\right) = 1 - \frac{1}{\gamma} + \mathcal{O}\left(\frac{1}{\vartheta}\right), \\ b^* &= 1 - \frac{\vartheta}{\gamma}\frac{T_b}{\vartheta - 1} + \mathcal{O}\left(\frac{1}{\vartheta}\right) = 1 - \frac{T_b}{\gamma} + \mathcal{O}\left(\frac{1}{\vartheta}\right), \end{aligned} \tag{4.133}$$

and hence $a^* \to 1 - \gamma^{-1}$, $b^* \to 1 - T_b\gamma^{-1}$ as $\vartheta \to \infty$. Thus, we can determine how close to the top of the furnace the interfaces will be if input parameters are chosen to have very large heating or small convection. Note also that this gives us a possible scaling for the dimensional thickness of $1 - a^*$ and $1 - b^*$ as

$$\text{dimensional thickness of } 1 - a^* = \frac{k(T_M - T_c)}{\epsilon_R \sigma_{\text{SB}}(T_h^4 - T_M^4)}, \tag{4.134a}$$

$$\text{dimensional thickness of } 1 - b^* = \frac{k(T_k - T_c)}{\epsilon_R \sigma_{\text{SB}}(T_h^4 - T_M^4)}. \tag{4.134b}$$

Notice that the initial dimensional height h scales out of the problem, which is reassuring since this is artificially imposed. Although in practice the furnace has a floor where the dripped material accumulates before it is tapped away, there is nothing in this model to prevent the interfaces from moving below zero. We suspect that the root corresponding to large ϑ corresponds to the stable steady state.

4.4.3 Bifurcation diagrams

In Figures 4.6 - 4.8 we showed example trajectories that tend to a stable steady state, and others which underwent free fall. It is of interest to determine where in the parameter space stable steady states will occur, and so here we present bifurcation diagrams illustrating where stable steady states can be found.

We first consider the simplified case $\lambda = 0$ and $T_b = 0$. This corresponds to the upper interface fixed at the top of the domain, $z = 1$, and the whole charge being filled with a viscous fluid of constant viscosity. In this limit, we have $f^* = 1$, with the gravity and viscous terms in balance, and so for any values of Pe, St, and γ the location of a^* can be determined from (4.116). We plot how a^* depends on Pe and St for fixed γ, in Figure 4.12. Where a steady state exists, its value is given by the heat map provided. The region where steady states cannot exist is labelled free fall. Note that there is a thin boundary layer where the steady state can be arbitrarily negative, although we have just plotted steady states to a value of $z = -1$, due to difficulties in numerical resolution. The interface between steady state and free fall behaviour is given in parameter space by $\vartheta = 1$. Using (4.118), with $f^* = 1$, we find that this corresponds to $Pe(1 + \frac{1}{St}) = \gamma$, which asymptotes to $Pe = \gamma$ as St becomes large. Thus, for large St, if the Péclet number is sufficiently large then the charge will keep on falling under gravity.

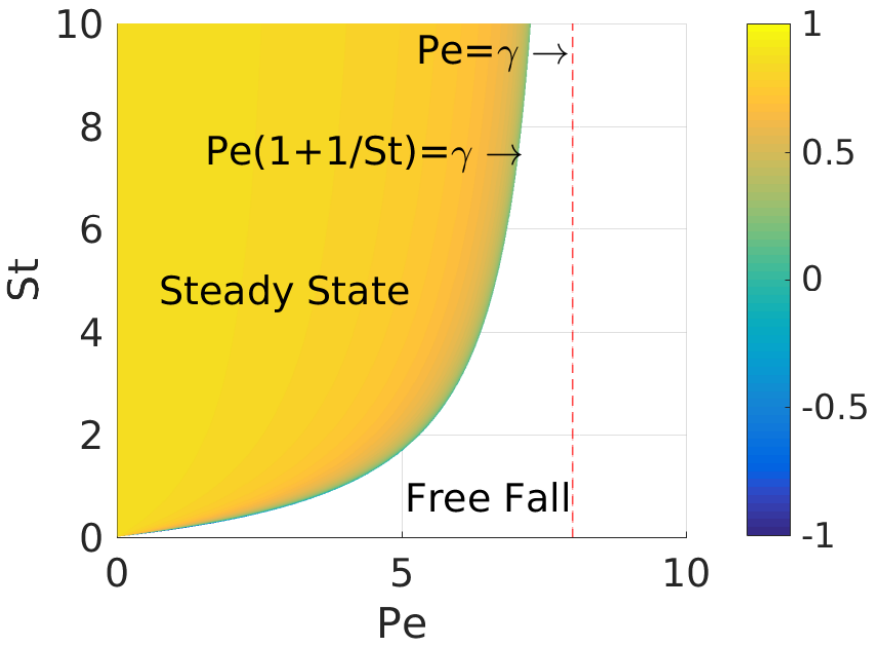


Figure 4.12: Plots of the value of the steady state a^*, comparing Pe and St, for fixed $\gamma = 8$, $\lambda = 0$, and $T_b = 0$.

We can also determine where the steady states a^* and b^* occur for general T_b and λ, and thus where the system undergoes free fall. We know that steady states only exist for $\vartheta > 1$, and that as $\vartheta \searrow 1$ the value of a^* becomes arbitrarily large in magnitude and negative. Since the interface is given by $\vartheta = 1$, we numerically find the root of (4.129) with a value of ϑ slightly greater than $\vartheta = 1$, showing us where the edge of the steady state region is. This allows us to draw bifurcation diagrams, demonstrating where a stable steady state or free fall will occur. We do not plot the value of the steady state, when it occurs, but it will increase with distance from the bifurcation interface. In Figures 4.13 we show bifurcation plots of Pe against St for different λ and for different T_b, and in Figure 4.14 we show plots of Pe against T_b for different γ and for different λ. These plots have been obtained using Mathematica, with a value of $\vartheta = 1 + 10^{-6}$, which is sufficiently close to $\vartheta = 1$.

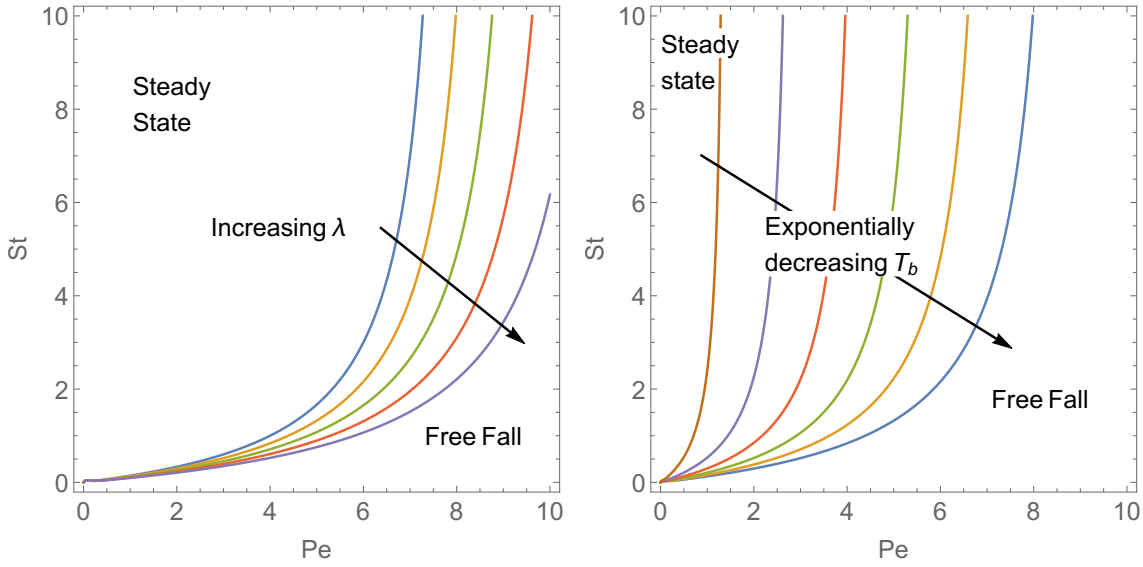


Figure 4.13: Plots showing the interface between where the solutions tend to steady states a^* and b^* and where it undergoes free fall, with $\gamma = 8$ in both cases. Plots were generated in Mathematica by letting $\vartheta = 1 + 10^{-6}$. In the left panel, we vary λ, with values shown $\lambda = 10^{-6}, 0.1, 0.2, 0.3, 0.4, 0.5$, and $T_b = 0$. In the right panel, we vary T_b, with values shown $T_b = 10^{-1}, 10^{-2}, 10^{-3}, 10^{-4}, 0$, and $\lambda = 0.1$.

We have determined that a stable steady state can exist for only certain parameter values. Although an unsteady stable state is possible for some parameter values, we have naturally not been able to obtain these as numerical solutions of the PDE problem. We have given bifurcation diagrams detailing where a stable steady state exists, and where the system goes into free fall. This free fall could occur due to high density or low viscosity of the fluid, or there being insufficient heating from below.

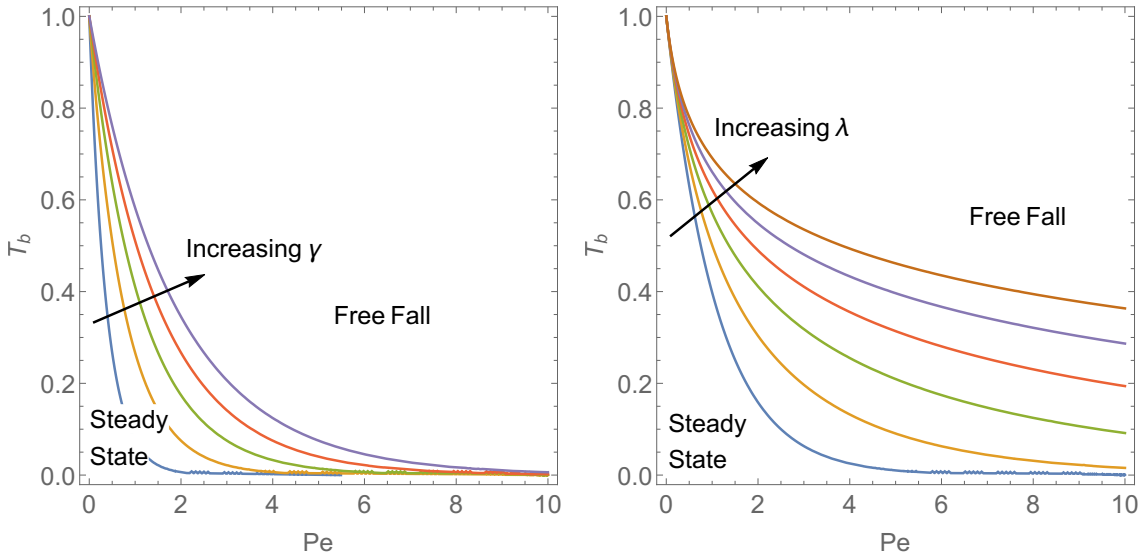


Figure 4.14: Plots showing the interface between where the solutions tend to steady states a^* and b^* and where it undergoes free fall, with $St = 1$ in both cases. Plots were generated in Mathematica by letting $\vartheta = 1 + 10^{-6}$. In the left panel we vary γ, with values shown $\gamma = 10, 20, 30, 40, 50$, and $\lambda = 0.1$. In the right panel we vary λ, with values shown $\lambda = 10^{-6}, 1, 2, 3, 4, 5$, and $\gamma = 30$.

4.5 Special limits of the tall, thin model

We now consider special limits of the tall, thin model. In each case, we assume that the aspect ratio δ is smaller than any other parameter we subsequently take to be small. We list some possible dominant balances which admit steady states in Table 4.1, with ϵ being a small parameter.

Case	$1 - T_b$	Pe	St	γ	λ	f	$1 - a$	$b - a$
A	$1 - T_b = \epsilon \ll 1$	$\mathcal{O}(\epsilon)$	$\mathcal{O}(1)$	$\mathcal{O}(1)$	$\mathcal{O}(1)$	$\mathcal{O}(\epsilon^{-1})$	$\mathcal{O}(1)$	$\mathcal{O}(\epsilon^{-1})$
B	$1 - T_b = \epsilon \ll 1$	$\mathcal{O}(1)$	$\mathcal{O}(1)$	$\gamma \gg 1$	$\mathcal{O}(1)$	$\mathcal{O}(\gamma)$	$\mathcal{O}(\epsilon)$	$\mathcal{O}(\gamma^{-1}\epsilon)$
C	$\mathcal{O}(1)$	$\mathcal{O}(1)$	$\mathcal{O}(\gamma^{-1})$	$\gamma \gg 1$	$\mathcal{O}(1)$	$\mathcal{O}(1)$	$\mathcal{O}(\gamma^{-1})$	$\mathcal{O}(\gamma^{-1})$
D	$\mathcal{O}(1)$	$\mathcal{O}(1)$	$St \gg 1$	$\mathcal{O}(1)$	$\mathcal{O}(1)$	$\mathcal{O}(1)$	$\mathcal{O}(1)$	$\mathcal{O}(1)$
E	$\mathcal{O}(1)$	$Pe \ll 1$	$\mathcal{O}(Pe/\gamma)$	$\gamma \gg 1$	$\mathcal{O}(1)$	$\mathcal{O}(1)$	$\mathcal{O}(\gamma^{-1})$	$\mathcal{O}(\gamma^{-1})$
F	$\mathcal{O}(1)$	$f\,Pe \ll 1$	$\mathcal{O}(1)$	$\mathcal{O}(1)$	$\mathcal{O}(1)$	$f\,Pe \ll 1$	$\mathcal{O}(1)$	$\mathcal{O}(1)$

Table 4.1: Table of dominant balances which give steady states in the model (4.87) - (4.92). Descriptions are given in the list below.

In Table 4.1, we consider the following cases:

- A: The temperature T_b is close to one, so there is a thin crust region. The material is falling slowly, since the Péclet number is small, which could be due to high viscosity or low density, or alternatively high thermal diffusivity.

- B: The temperature T_b is again close to one, so there is a thin crust region, but in this case the radiative heating from underneath the charge is very large.
- C: The radiative heating is large and the Stefan number is small. This could correspond to a small temperature difference between the top and bottom of the charge.
- D: The Stefan number is large. This could be caused by very small latent heat, and is a limit relevant to silicon furnaces.
- E: The radiative heating is large and the Péclet number is small, with the Stefan number being extremely small, balancing the ratio of convection to heating.
- F: The convective term fPe is small and does not balance with other parameters, so this gives a limit without convection.

In this section, we examine these limits. The ratio $(b-a)/(1-a)$ gives the relative thickness of the crust to the total size of the charge, and so in Section 4.5.1 we start by analysing balances A and B, as these lead to a thin crust. Then, in Section 4.5.2, we analyse balances C, D, E, and F, as these cases give rise to an $\mathcal{O}(1)$ crust thickness.

4.5.1 Thin crust limits (cases A and B)

We first consider the cases where there is a thin crust of viscous material holding up a granular region above. We introduce a small parameter, ϵ, defined by

$$\epsilon = 1 - T_b, \tag{4.135}$$

and consider the limit $0 < \epsilon \ll 1$. Since we have already taken the aspect ratio δ to be small, we note that we are taking the limit $0 < \delta \ll \epsilon \ll 1$, so that the thin crust region is still much taller than it is wide. We find it easier to introduce the small parameter in terms of temperature rather than height, but we assume that for $\mathcal{O}(1)$ time, $b(t) - a(t) = \mathcal{O}(\epsilon)$, and so we introduce the $\mathcal{O}(1)$ variable $c(t)$, the scaled crust thickness, such that

$$b(t) = a(t) + \epsilon c(t). \tag{4.136}$$

If we substitute $T_b = 1 - \epsilon$ into (4.128), and expand in terms of ϵ, assuming all other parameters are $\mathcal{O}(1)$, we obtain

$$\frac{\epsilon}{\vartheta} = \frac{Pe}{\gamma}\left(\vartheta + \frac{1}{St}\right)\ln\left(\frac{\vartheta}{\vartheta - 1}\right) + \mathcal{O}(\epsilon^2). \tag{4.137}$$

We need to find a balance for the ϵ term, which cannot be achieved if Pe, St, γ, ϑ, and $\ln(\vartheta/(\vartheta-1))$ are all $\mathcal{O}(1)$ parameters. We note that Pe, γ, and St are all positive, and that in previous analysis we showed that $\vartheta > 1$ is required for physically realistic steady states (i.e. $a^*, b^* \leq 1$). A necessary balance is found in cases A and B, and we now examine these in turn.

4.5.1.1 Case A: Small Péclet number, $Pe = \mathcal{O}(\epsilon)$

If the Péclet number is small, then thermal convection is small compared to thermal conduction, and so the material is falling relatively slowly. We scale $Pe = \epsilon\hat{Pe}$, where $\hat{Pe}$ is an $\mathcal{O}(1)$ constant, and treat St, γ, and λ as $\mathcal{O}(1)$ constants.

We seek to write the system (4.87) - (4.92) in terms of ϵ. We first consider (4.91), obtaining

$$f(t) = \frac{1-a(t)}{\int_{z=a(t)}^{a(t)+\epsilon c(t)} \exp\left(-\lambda(T(z,t)-1)\right) dz} = \frac{1}{\epsilon}\left(\frac{1-a(t)}{c(t)} + \mathcal{O}(\epsilon)\right) \tag{4.138}$$

by the Integral Mean Value Theorem, where we have assumed that $1 - a(t) = \mathcal{O}(1)$. Note that when $\lambda = \mathcal{O}(1)$, we have that the relative thickness of the crust is given by $f(t)^{-1}$, since the weight to viscosity ratio $f(t)$ is just given by the ratio of domain sizes.

For the upper interface, we have

$$T(a(t) + \epsilon c(t), t) = 1 - \epsilon, \tag{4.139}$$

which can be expanded to give

$$T(a(t), t) + \epsilon c(t) T_z(a(t), t) = 1 - \epsilon + \mathcal{O}(\epsilon^2), \tag{4.140}$$

and hence we find

$$c(t) = -\frac{1}{T_z(a(t), t)}, \tag{4.141}$$

providing $T_z(a(t), t)$ is negative and $\mathcal{O}(1)$. We thus have the leading order system

$$\frac{\partial T}{\partial t} + T_z(a(t), t)(1 - a(t))\frac{\hat{Pe}}{St}\frac{\partial T}{\partial z} = \frac{1}{St}\frac{\partial^2 T}{\partial z^2}, \text{ in } a(t) \leq z \leq 1, \tag{4.142}$$

$$\frac{da}{dt} - \frac{\partial T}{\partial z}(1 - a(t))\frac{\hat{Pe}}{St} = \gamma + \frac{\partial T}{\partial z}, \text{ at } z = a(t), \tag{4.143}$$

$$T(a(t), t) = 1, \quad T(1, t) = 0, \tag{4.144}$$

$$T(z, 0) = 0, \quad a(0) = 0. \tag{4.145}$$

We look for steady states as before, finding

$$T^*(z) = \frac{\exp\left(T_z^*(a^*)(1-a^*)\hat{Pe}(z-1)\right)-1}{\exp\left(T_z^*(a^*)(1-a^*)\hat{Pe}(a^*-1)\right)-1}, \tag{4.146}$$

which we can differentiate to find the implicit relationship for $T_z^*(a^*)$:

$$\begin{aligned} T_z^*(a^*) &= T_z^*(a^*)(1-a^*)\hat{Pe}\frac{\exp\left(T_z^*(a^*)(1-a^*)\hat{Pe}(a^*-1)\right)}{\exp\left(T_z^*(a^*)(1-a^*)\hat{Pe}(a^*-1)\right)-1} \\ &= \frac{T_z^*(a^*)(1-a^*)\hat{Pe}}{1-\exp\left(T_z^*(a^*)(1-a^*)^2\hat{Pe}\right)}. \end{aligned} \tag{4.147}$$

Since $T_z^*(a^*) \neq 0$ by assumption, we can rearrange (4.147) to obtain

$$T_z^*(a^*) = \frac{1}{\hat{Pe}(1-a^*)^2}\ln\left(1-(1-a^*)\hat{Pe}\right), \tag{4.148}$$

with the restriction that $(1-a^*)\hat{Pe} < 1$ for the logarithm to be well-defined. The Stefan condition (4.143) gives

$$-T_z^*(a^*)(1-a^*)\frac{\hat{Pe}}{St} = \gamma + T_z^*(a^*), \tag{4.149}$$

and hence we can substitute in $T_z^*(a^*)$ from (4.148) to obtain the implicit equation for $a^*(\gamma, St, \hat{Pe})$, i.e.,

$$\gamma + \frac{\ln\left(1-(1-a^*)\hat{Pe}\right)}{\hat{Pe}(1-a^*)^2}\left(\frac{\hat{Pe}}{St}(1-a^*)+1\right) = 0. \tag{4.150}$$

In our tall, thin model the averaged convection comes from $Pef(t)$, with the downwards motion under gravity caused by the weight of the whole charge, resisted by the viscous layer. When the viscous layer is thin, i.e. there is a thin crust, the weight of the granular region will be too large and the charge will undergo free fall. However, if the thermal convection is slow, due to a small Péclet number, then the gravitational and viscous effects are in balance, $Pef(t) = \mathcal{O}(1)$, and the system is able to run to a steady state.

4.5.1.2 Case B: Large heating, $\gamma \gg 1$

Suppose instead that $Pe = \mathcal{O}(1)$, but that $\gamma \gg 1$, meaning that the radiative heating into the furnace is very large. Again we keep λ and St as $\mathcal{O}(1)$ constants. We look

for balances such that the system tends to a steady state, and so examine the steady state system (4.109) - (4.113). A possible balance from the Stefan condition (4.110) is $f = \mathcal{O}(\gamma)$. However, if $f \gg 1$, then (4.109) and (4.111) cannot be satisfied unless there is a boundary layer of $\mathcal{O}(1/f) = \mathcal{O}(1/\gamma)$. In order to allow matching with the outer solution, the boundary layer has to be at the bottom of the domain, near $z = a$. In this boundary layer $T_z = \mathcal{O}(\gamma)$, and hence all three terms balance in the Stefan condition. We thus consider the scalings

$$f^* = \gamma \hat{f}, \quad z = a + \frac{1}{\gamma} y, \tag{4.151}$$

so that in the boundary layer we have

$$T_{\text{inner}}(y) = \exp\left(-\hat{f}^* Pe\ y\right), \tag{4.152}$$

where we have applied the boundary condition $T(z = a^*) = 1$ and matched with the outer solution $T_{\text{outer}} \equiv 0$. Note that the inner solution is thus the composite solution for the whole region, so

$$T(z) = \exp\left(-\hat{f} Pe \gamma (z - a^*)\right). \tag{4.153}$$

The Stefan condition (4.110) thus gives

$$\hat{f}\gamma \frac{Pe}{St} = \gamma - \hat{f} Pe \gamma, \tag{4.154}$$

so that

$$\hat{f} = \frac{1}{Pe} \frac{St}{1 + St}. \tag{4.155}$$

Applying the boundary condition $T(b^*) = 1 - \epsilon$, we find

$$b^* - a^* = -\left(1 + \frac{1}{St}\right) \frac{1}{\gamma} \ln(1 - \epsilon). \tag{4.156}$$

Since $\lambda = \mathcal{O}(1)$, we have that

$$f^* = \gamma \hat{f} = \frac{1 - a^*}{b^* - a^*}, \tag{4.157}$$

which is the reciprocal of the ratio of the thickness of the viscous crust to the total thickness of the charge (including the crust). Hence, combining (4.155) with (4.157), the thickness of the total charge is

$$1 - a^* = -\frac{1}{Pe} \ln(1 - \epsilon) = \frac{\epsilon}{Pe} + \mathcal{O}(\epsilon^2), \tag{4.158}$$

while the relative thickness of the crust to the total charge is

$$\frac{b^* - a^*}{1 - a^*} = \frac{1}{\gamma} Pe \left(1 + \frac{1}{St}\right), \tag{4.159}$$

which is size $\mathcal{O}(1/\gamma)$. Thus, we have a thin crust for all $\gamma \gg 1$. Notice that these results have not required γ to be of a certain order of ϵ in size, it just has to be large.

4.5.2 Order one crust thickness limits (cases C, D, E, and F)

We now consider dominant balances for which the relative size of the crust to the total charge is not small, but order one. These are cases C, D, E, and F listed in Table 4.1.

4.5.2.1 Case C: Small Stefan number, $St \ll 1$

Suppose that the Stefan number is small, so that we have $0 < St \ll 1$. This could correspond physically to very large latent heat, or to very small specific heat. We rescale our problem onto the fast timescale $t = St\,\hat{t}$, and for a balance we must have large heating, i.e., $\gamma = \hat{\gamma}/St$. With these scalings we obtain the system

$$\frac{\partial T}{\partial \hat{t}} - f(\hat{t})Pe\frac{\partial T}{\partial z} = \frac{\partial^2 T}{\partial z^2}, \text{ in } a(t) \leq z \leq 1, \tag{4.160}$$

$$\frac{da}{d\hat{t}} + f(\hat{t})Pe = \hat{\gamma} + St\frac{\partial T}{\partial z}, \text{ at } z = a(\hat{t}), \tag{4.161}$$

$$T(a(\hat{t}),\hat{t}) = 1, \quad T(b(\hat{t}),\hat{t}) = T_b, \quad T(1,\hat{t}) = 0, \tag{4.162}$$

$$T(z,0) = 0, \tag{4.163}$$

$$f(\hat{t}) = \frac{\big(1 - a(\hat{t})\big)}{\int_{a(\hat{t})}^{b(\hat{t})} \exp\big(-\lambda(T(z,\hat{t}) - 1)\big)\,dz}, \tag{4.164}$$

$$a(0) = 0, \quad b(0) = 0. \tag{4.165}$$

In the limit $St \to 0$, we obtain the usual system, but without the conductive flux in the Stefan condition (4.161). Looking for a steady state solution, we find that from (4.161) we must have $\hat{\gamma} = Pef^*$, and hence the heating from below and the convective term are identically in balance. The intuition behind this statement is that if the heating is too high, or convection to small, all the charge will be melted and the domain will shrink. Conversely, if the heating is too small, or convection too fast, the charge will undergo free fall.

We find the steady state temperature

$$T^*(z) = \frac{\exp(\hat{\gamma}(1-z)) - 1}{\exp(\hat{\gamma}(1-a^*)) - 1}, \tag{4.166}$$

and thus find that the integral equation (4.164) becomes

$$\frac{1 - a^*}{\int_{z=a^*}^{b^*} \exp\left(-\lambda(T^*(z) - 1)\right) dz} = \frac{\hat{\gamma}}{Pe}. \tag{4.167}$$

Note that we cannot determine a^* from the Stefan condition (4.161), since the conductive flux does not feature. Instead, we can rearrange (4.167) using algebraic steps analogous to those used in Section 4.4.2, to obtain

$$e^{\lambda\Theta}\left(E_1\left(\lambda\Theta\right) - E_1\left(\lambda(\Theta - 1 + T_b)\right)\right) = \frac{Pe}{\hat{\gamma}} \ln\left(\frac{\Theta}{\Theta - 1}\right), \tag{4.168}$$

where we have defined

$$\Theta := \frac{\exp(\hat{\gamma}(1 - a^*))}{\exp(\hat{\gamma}(1 - a^*)) - 1}. \tag{4.169}$$

Upon finding a root of (4.168), we then obtain

$$a^* = 1 + \frac{1}{\hat{\gamma}} \ln\left(1 - \frac{1}{\Theta}\right), \tag{4.170}$$

$$b^* = 1 - \frac{1}{\hat{\gamma}} \ln\left(1 + \frac{T_b}{\Theta - 1}\right). \tag{4.171}$$

This is remarkably similar to the method used to find general steady states in Section 4.4.2, but the ordering of the algebraic steps is different. This is because we cannot define the change of variables as in (4.118), because writing $\vartheta := (1/St)(\hat{\gamma}/f^*Pe - 1)$ is not compatible with the condition $\hat{\gamma} = f^*Pe$. Instead, we first take the limit $St \to 0$, and then subsequently make the change of variables (4.169).

4.5.2.2 Case D: Large Stefan number, $St \gg 1$

The case of a large Stefan number, $St \gg 1$, could correspond to the limit of small latent heat. This particular limit is especially appropriate to consider in the study of silicon furnaces. Although we have modelled material melting at the lower interface, in practice the already viscous material drips off, and not much latent heat is released.

If a steady state exists, then it can be explored by taking the limit $St \to \infty$ in (4.116) and (4.117), giving

$$a^* = 1 + \frac{1}{f^*Pe} \ln\left(1 - \frac{f^*Pe}{\gamma}\right), \tag{4.172a}$$

$$b^* = 1 - \frac{1}{f^*Pe} \ln\left(1 + \frac{T_b}{\gamma/f^*Pe - 1}\right). \tag{4.172b}$$

Here f^* can be found from the root of (4.129), with $St \to \infty$ and $\vartheta \to \gamma/f^*Pe$.

We note from (4.172) that we require $f^*Pe/\gamma < 1$ for a steady state to exist. Since the integral term $f^* \geq 1$, we have that no steady states exist if $Pe/\gamma > 1$. For the simplified case of $\lambda = 0 = T_b$, on the bifurcation plot in Figure 4.12 we can see

that for large St all that matters is the value of Pe/γ. This ratio is given in terms of physical dimensional parameters as

$$\frac{Pe}{\gamma} = \frac{Uh/\kappa}{\epsilon_R \sigma_{\mathrm{SB}}(T_h^4 - T_M^4)h/k(T_m - T_c)} = \frac{U\rho C_p(T_M - T_c)}{\epsilon_R \sigma_{\mathrm{SB}}(T_h^4 - T_M^4)}. \tag{4.173}$$

Using the Poiseuille velocity scaling given in (4.30), we can further write

$$\frac{Pe}{\gamma} = \frac{\rho^2 g R^2 C_p(T_M - T_c)}{8\eta_s \epsilon_R \sigma_{\mathrm{SB}}(T_h^4 - T_M^4)}. \tag{4.174}$$

Without specific knowledge of the ferrosilicon process, we can tell that higher density and lower viscosity would lead to a higher value of Pe/γ in (4.174), if the other variables were constant. This could explain why a continuous downwards flow is experienced in some ferrosilicon, but not silicon, production. Of course, the other parameters will not be the same in silicon and ferrosilicon production, but there is uncertainty about what appropriate values might be. A discussion about the application to industrial silicon production is given in Section 6.2.

4.5.2.3 Case E: Large heating and small convection

Suppose $\gamma \gg 1$, $Pe \ll 1$, $St = Pe/\gamma\hat{St}$, with $\lambda = \mathcal{O}(1)$ and $1 - T_b = \mathcal{O}(1)$. This corresponds physically to a case of large latent heat, L, and high source temperature T_h. In this case we have the steady state $T^*(z) = (z-1)/(a-1)$ and $b^* = 1+T_b(a^*-1)$, and can integrate the denominator in f^* to find $f^* = \lambda/\left(\exp(\lambda(1-T_b)) - 1\right)$. There is no way to find a^* from the Stefan condition, unless $1 - a^* = \mathcal{O}(\gamma^{-1})$. We thus set $1 - a^* = \gamma^{-1}\hat{a}$, and from the steady state Stefan condition obtain $\hat{a} = \hat{St}/(\hat{St} - f^*)$, and hence

$$1 - a^* = \frac{1}{\gamma}\frac{\hat{St}}{\hat{St} - \lambda/\left(\exp\left(\lambda(1-T_b)\right) - 1\right)}, \tag{4.175}$$

with $b^* - a^* = (1 - T_b)(1 - a^*)$.

4.5.2.4 Case F: No Convection

Suppose $f\,Pe \ll 1$, for example if the material is very light or highly thermally conductive. Then, for all other parameters being $\mathcal{O}(1)$, we recover a problem similar to the canonical Stefan problem, without convection, but with a radiative flux, namely

$$\frac{\partial T}{\partial t} = \frac{1}{St}\frac{\partial^2 T}{\partial z^2}, \text{ in } a(t) \le z \le 1, \tag{4.176}$$

$$\frac{da}{dt} = \gamma + \frac{\partial T}{\partial z}, \text{ at } z = a(t), \tag{4.177}$$

$$T(a(t),t) = 1, \quad T(b(t),t) = T_b, \quad T(1,t) = 0, \tag{4.178}$$

$$T(z,0) = 0, \tag{4.179}$$

$$a(0) = 0, \quad b(0) = 0. \tag{4.180}$$

This system admits the steady state solution

$$T^*(z) = \frac{z-1}{a-1}, \quad a^* = 1 - \frac{1}{\gamma}, \quad b^* = 1 - \frac{T_b}{\gamma}, \tag{4.181}$$

and hence the ratio of the thickness of the crust to the total charge is given by

$$\frac{b^* - a^*}{1 - a^*} = 1 - T_b. \tag{4.182}$$

Since convection did not enter the problem, the presence of the upper interface b is artificial, since it has no influence on the system, but merely marks where we believe the crust meets the rest of the charge.

4.5.3 Summary of special limits

We have discussed several special limits of the model (4.87) - (4.92) that allow steady state behaviour. When the convective term is small (case A), or the radiative heating is very large (case B), it is possible for a thin crust to support the weight of the granular region. In other limits, order one relative crust thickness is required for the existence of a steady state. These limits are a small or large Stefan number (cases C and D), and small convective term, with or without large radiative heating (cases E and F). We envisage that these limits discussed will be constructive for a range of applications, not just for silicon furnace behaviour.

4.6 Model extensions

We now consider extensions to the one-dimensional tall, thin model developed in Section 4.2 and analysed in Sections 4.4 and 4.5. These include incorporating a radiative flux, chemical reactions, and performing numerical simulations of the full two-dimensional system given in Section 4.2. We examine each of these in turn.

4.6.1 Radiative flux

In the model (4.87) - (4.92) we have assumed that heat transfers by conduction and convection within the charge. However, radiation between particles could be the dominant diffusive thermal mechanism, especially lower down in the furnace. If

instead of being transported by conduction, heat is transferred by radiation, we would replace the dimensional heat flux, $-k\frac{\partial T}{\partial z}$, with

$$-\beta T^3 \frac{\partial T}{\partial z}, \tag{4.183}$$

as used in the energy equation (2.21) in Chapter 2. We estimate the radiative constant by $\beta = 4\epsilon_R \sigma_{\mathrm{SB}} d$, where d is a distance related to the particle size of the porous structure. Using (4.183), we obtain the dimensionless system

$$\frac{\partial T}{\partial t} - \frac{f(t) Pe_R}{St}\frac{\partial T}{\partial z} = \frac{1}{St}\frac{\partial}{\partial z}\left(\left(1 + T_R T\right)^3 \frac{\partial T}{\partial z}\right), \text{ in } a(t) \leq z \leq 1, \tag{4.184}$$

$$\frac{da}{dt} + \frac{f(t) Pe_R}{St} = \gamma_R + \left(1 + T_R T\right)^3 \frac{\partial T}{\partial z}, \text{ at } z = a(t), \tag{4.185}$$

with the same initial and boundary conditions for T, initial conditions for a and b, and the same $f(t)$ given by (4.91). The parameters St, T_b, and λ are the same as in (4.31), but the timescale is now $\tau = \rho L h^2 / 4\epsilon_R \sigma_{\mathrm{SB}} d (T_M - T_c) T_c^3$, and so we would have the new dimensionless parameters

$$Pe_R = \frac{Uh}{4\epsilon_R \sigma_{\mathrm{SB}} T_c^3 d / C_p \rho}, \quad \gamma_R = \frac{h\left(T_h^4 - T_M^4\right)}{4d(T_M - T_c)T_c^3}, \quad T_R = \frac{T_M - T_c}{T_c}. \tag{4.186}$$

This is the same as for the system given in Section 4.3.3 and used throughout this chapter, but with the thermal conductivity (and hence also thermal diffusivity) being a cubic function of temperature. If we look for steady states, we obtain the ODE

$$-f^* Pe_R \frac{dT^*}{dz} = \frac{d}{dz}\left(\left(1 + T_R T\right)^3 \frac{dT^*}{dz}\right), \tag{4.187}$$

which can be integrated twice to obtain

$$\begin{aligned} &\frac{1}{3}\left(1 + T_R T^* + A\right)^3 - \frac{3}{2}A\left(1 + T_R T^* + A\right)^2 + 3A^2\left(1 + T_R T^* + A\right) \\ &+ A^4 \ln\left(1 + T_R T^* + A\right) = z + B, \end{aligned} \tag{4.188}$$

with the arbitrary constants A and B determined from the conditions $T^*(1) = 0$, and $T^*(a^*) = 1$, along with the Stefan condition

$$-f^* \frac{Pe_R}{St} = \gamma_R + \left(1 + T_R T^*\right)^3 \frac{dT^*}{dz}, \text{ at } z = a^*, \tag{4.189}$$

and the usual equation (4.113) for f^*. Thus the behaviour of the radiative model is qualitatively similar to that of the conductive model discussed in this chapter, but is more complicated algebraically.

The main benefits of using conduction are that the analysis is simpler and the results will be transferable to lower temperature applications, where internal radiation does not feature strongly. Perhaps a simpler means of incorporating radiative effects in our results is to set thermal conductivity to be a cubic function of a typical temperature. Letting

$$k = \beta T_c^3 = 4\epsilon_R \sigma_{\mathrm{SB}} d T_c^3, \tag{4.190}$$

which corresponds to taking $T_R = 0$ in (4.187) and (4.189), we find that the potential scalings for the dimensional thickness of $1 - a^*$ and $1 - b^*$ given in (4.134) become

$$\text{dimensional thickness of } 1 - a^* = \frac{4d(T_M - T_c)T_c^3}{T_h^4 - T_M^4}, \tag{4.191a}$$

$$\text{dimensional thickness of } 1 - b^* = \frac{4d(T_k - T_c)T_c^3}{T_h^4 - T_M^4}. \tag{4.191b}$$

4.6.2 Chemical reactions

As well as simplifying the heat transfer, we have also simplified the chemistry. We have assumed that two regions exist in the charge, being a viscous region and a granular region. The viscous region is bounded by a melting temperature, T_M, and a condensation temperature, T_k. In practice, gases condense in this region to form sticky glue-like substances, which hold together solid particles, many of which are expanding and becoming sticky themselves. In this chapter, this has all be represented by a thermally dependent viscosity function, $\eta(T)$. However, further effects could be included, to model how the viscosity depends on distinct phases. Incorporating the seven distinct chemical species modelled in Chapter 2 could be too involved, but extending the model in this chapter to include a distinct solid and liquid phase could be attainable.

Letting ϕ_s and ϕ_l be the volume fractions of the solid and liquid phases, respectively, such that $\phi_s + \phi_l = 1$, we would choose a viscosity function

$$\eta = \eta_T(T)\eta_\phi(\phi_s, \phi_l). \tag{4.192}$$

Such a function could be chosen to be in agreement with literature related to the viscosity of solid suspensions in fluids [11, 17, 18, 52, 58, 62, 79, 93]. We would also introduce a reaction rate, to allow solid material to become liquid, which would be related to the reactions (2.1) - (2.5) modelled in Chapter 2, especially reaction (2.3). A further volume fraction ϕ_g, to represent gas, could also be added, with appropriate reactions included.

4.6.3 Numerics of the full model

In Section 4.2 we presented a model comprising a single-phase Stokes flow fluid with a thermally-dependent viscosity, a heat flow problem with a Stefan condition at the lower boundary, and an upper boundary above which sits a granular region acting as a dead-load. We considered a tall, thin limit to obtain a one-dimensional radially averaged model. However, it would be interesting to study the behaviour of the full two-dimensional model.

We would like to perform numerical simulations of the two-dimensional model, but this is difficult due to the moving boundary at the lower surface of the charge, $z = a(r, t)$. Two possible methods we have considered for obtaining numerical simulations are the boundary mapping method and the phase field method. In the boundary mapping, or front fixing method, the moving domain is mapped to a fixed domain [19], in which the problem can be solved numerically, as we did with the one-dimensional problem in Section 4.4.1. However, the partial differential equations and particularly boundary conditions become more complicated as a result of the transformation. In the phase-field method, an additional 'phase-field' variable is introduced. This is a continuum variable which takes two different values either side of a physical interface [76]. To employ this approach, we would also have to consider some behaviour in the gas region beneath the charge, to account for the boundary conditions on that surface. We have yet to implement either of these methods.

4.7 Conclusions

In this chapter we have developed a thermal and mechanical model that accounts for crust formation, in order to better understand how a viscous and solid mixture can support the granular raw materials fed into the furnace. We modelled the crust as a single-phase incompressible viscous fluid, with thermally-dependent viscosity. The rest of the charge was treated as a region of hydrostatic pressure that moved with the crust. The movement of the lower crust interface was governed by a Stefan condition that allowed for radiation from a hotter furnace base and convection of the charge material downwards. To simplify the analysis a tall, thin limit was taken in Section 4.3, resulting in flat interfaces to leading order. The inner region around the lower interface was considered, leading to an averaged convective term in the outer equations. This convective term accounted for the ratio of gravitational to viscous forces, and so the system presented in Section 4.3.3 is a non-local PDE moving boundary problem.

The dynamics of this system were considered in Section 4.4. We presented numerical simulations in Section 4.4.1 by mapping onto a fixed domain and employing a first order finite difference scheme. Simulations showed that the system can run to a stable steady state, for which the interfaces can be arbitrarily far from the furnace top, or the charge can reach a terminal velocity and undergo free fall. When analysing the steady states in Section 4.4.2, we found that an unstable steady state can occur, although we have not been able to obtain it numerically from the tall, thin PDE system. Numerical evidence suggests that at most one stable steady state exists for a given set of parameter values. We also presented bifurcation diagrams, in order to demonstrate parameter regimes for which the solutions tend to a steady state. We find that increasing the Péclet number would move the system towards free fall, as would decreasing St, γ, λ, and T_b. Physically this means a system with a denser, less viscous charge is less likely to exhibit steady state solutions, potentially explaining why crust formation is occasionally not observed in ferrosilicon furnaces with high iron content. The cooler the base of the furnace, or the thinner the crust region, the more likely a natural flow of raw material to the base of the furnace will be. Indeed, the experimentally observed rising of the charge is captured in our model, in which it is driven by large heating from below.

To bring further insight into potential industrial operating strategies, we examined special limits of the tall, thin model in Section 4.5. Of particular interest is a thin crust, which occurs in silicon production. Unless the Péclet number is small or the radiative heating from below is large, the crust will not be thick enough to support the pressure of the upper charge. Another limit of special interest is the large Stefan number (case D in Section 4.5), which is relevant because of the small latent heat, L, involved in dripping from the base of the furnace charge. In this limit, the locations of stable steady state interfaces depend on the ratio of the Péclet number to the radiative heating, Pe/γ. The smaller this ratio is, the higher in the furnace steady states will form. In practice, steady states are not observed in industrial silicon furnaces, but rather the gas cavity is seen to increase, with the cavity ceiling rising before it is stoked. In our model this would correspond to the early time period when a steady state has not yet been reached, and so the timescale to reach steady state would be slower than the stoking timescale. Similarly, in ferrosilicon furnaces with high iron content, continuous flow is observed. This could correspond to free fall in the model, or to negative steady states for the interfaces, which cannot be obtained in practice since the charge will eventually hit the floor of the furnace.

The model derived and discussed in this chapter is sufficiently general to be useful in other applications. Numerical simulations of the full model, without a small aspect ratio, could determine the shape of the crust interfaces. Applying the model to more complex geometries, including the three electrodes present in industrial operation, would certainly be of interest. We have also chosen to simplify the chemical effects modelled, but by combining this mechanical insight with a multiphase reaction model, one could examine the influence of the specific reaction pathways on the strength of a furnace crust.

Chapter 5

Homogenised Model for Gas-Solid Reactions

5.1 Introduction

In the previous chapters, we have considered models of the pilot furnace. In Chapter 2, we noted the importance of the reaction R_1 (2.1) between solid carbon and gaseous silicon monoxide gas. In particular, we found that using more reactive carbon particles in the process led to lower losses from the system. This analysis was determined by using a parameter r_C representing the reactivity of carbon, which was constant in each simulation. However, in practice this reaction is more complex, since the available surface area of carbon changes over time, and with height in the furnace. We thus seek to develop a better model of this reaction. In this chapter, we frame our modelling in terms of a general reaction between a gas and a solid, which forms a distinct gas and solid. We envisage that the model developed will be useful in a range of settings. We are, though, particularly motivated by the reaction between carbon and silicon monoxide that takes place in silicon furnaces, and so return to this focus at the end of the chapter.

Reactions between gases and solids occur in a wide range of chemical and engineering settings, in addition to silicon production. For example, combustion of solid fuels, roasting of sulphide ores, and incineration of household waste are all listed as applications in the seminal book of Szekely et al. [97]. Reactions between gases and solids are commonplace in industry, and so an improved understanding of the physical and chemical mechanisms involved is valuable. In [34], combustion of char is discussed, with solid carbon reacting with oxygen to form carbon monoxide.

Several modelling approaches have been utilised to understand the behaviour of gas-solid reactions. Reactions between solid particles and a background, or perhaps

flowing, gas will proceed differently to a well-mixed system, since the gas must be transported to the solid material before the reaction takes place, and then reaction products either remain in place, or are transported away, influencing the reaction rate. The simplest means of capturing this interaction is the shrinking core model [43, 95], in which a solid particle is assumed to consist of an inner unreacted core of the solid reactant surrounded by a shell of solid product. The interface between these regions moves inwards, shrinking the core. This model is typically considered in a simplified geometry, either a slab, cylinder, or sphere [90]. The shrinking core model captures gas diffusion and kinetic rates as possible rate-limiting mechanisms, and allows for interactions between these effects. In addition to modelling the reaction between gaseous silicon monoxide and solid carbon particles in the context of silicon production [64, 82], which is our primary concern, shrinking core models are often used in other engineering applications. For example, they have been used to model lithium batteries, as set out by Srinivasan and Newman [92], and further developed in, for example [4, 23, 24, 88]. In a grain model [90, 91, 96], a solid particle is assumed to be composed of many smaller grains, each of which undergoes a shrinking core type reaction. Careful coupling must take place between the dynamics at the microscopic grain level and at the larger particle level. The main distinction between these models is that the shrinking core has a sharp interface between reacted and unreacted regions in the solid, whereas a grain model allows for a diffuse layer on the macroscale, where the macroscale concentration of the reactant solid can vary continuously. Melchiori and Canu [60] compare these models and (with other authors) propose a single particle model including multiple reactions in a porous solid [61]. Random pore models [9, 10] allow for a diffuse reaction front in the solid, whilst incorporating spatially varying pore sizes.

We are interested in deriving a model for the reaction of a gas with a porous solid particle, which we assume is composed of many smaller scale grains. This model will allow for various rate-limiting steps, including gaseous diffusion in the pores and the reaction rate in solid grains. In order to use behaviour on the granular microscale to find effective equations at the macroscale particle level, we employ homogenisation theory, an overview of which can be found in [7, 72]. We use the work of Bruna and Chapman [13] and Dalwadi et al. [21, 22] as a framework for our approach, since they also consider diffusion in spatially varying porous media. In [13, 22], the porous geometry consists of solid cylinders and spheres, with the radius depending on the macroscale. In [21], these solid obstacles can also grow over time, due to a reaction, reducing the region in which diffusion can occur. We consider an external gas outside

the particle to diffuse between the grains and then be transported into the grain to the shrinking core reaction front, where it reacts with the solid core to create a new solid. We first assume that any product gas has no influence on the reaction, and we later show that the models and analysis can easily be extended to include product gas effects.

This chapter is organised as follows. In Section 5.2, we present a mathematical formulation of the canonical shrinking core model, which assumes an inward-moving sharp interface between an unreacted solid core and a reacted solid outer shell. In Section 5.3, we use this shrinking core model as a basis for behaviour at the microscale granular level. We take δ to be the ratio of micro to macroscale lengthscales; in the limit $\delta \to 0$, we obtain a system of homogenised equations that captures behaviour on the macroscale. Two distinguished limits arise depending on the ratio of the gas diffusivity in the grain to that in the pore space, and these are discussed in Section 5.4. The model arising from the more physically relevant distinguished limit is analysed in Section 5.5, with numerical simulations and asymptotics discussed in the cases where the process is diffusion-controlled or reaction-controlled. In Section 5.6, we show how the model development and analysis can be extended to include the dynamics of a product gas. Comparison with results present in the literature are given in Section 5.7. In Section 5.8, we couple our model to the macroscale furnace model in Chapter 2. Finally, conclusions are drawn in Section 5.9. Work given in this chapter has been submitted for publication in [85].

5.2 Shrinking core model

5.2.1 Physical derivation

We are interested in the irreversible chemical reaction between a gas A and solid B, which forms the products of gas F and solid H

$$A_{\text{gas}} + \sigma_1 B_{\text{solid}} \to \sigma_2 F_{\text{gas}} + \sigma_3 H_{\text{solid}}, \tag{5.1}$$

where σ_1, σ_2, and σ_3 are stoichiometric coefficients. We assume that these species are in an idealised spherical particle consisting of a central spherical core of non-porous solid B, surrounded by a shell of porous solid H, with the reaction taking place at the interface between B and H. We further assume that when species B reacts with the gas it creates a solid material of constant porosity ψ. For simplicity, no volumetric changes are modelled, so that when the reaction is complete the spherical particle of solid H is the same size as the initial spherical particle of solid B. We assume

that both gases co-exist in the outer shell, but that no gas is present inside the inner core. We are interested in spherically symmetric behaviour only, and assume that the particle is of radius $r = R_p$ [m], where r is our co-ordinate. The interface between the inner core and the outer shell is given by $r = l(t)$ [m]. Thus there is a sharp divide between the reacted and unreacted regions. A schematic diagram of this is given in Figure 5.1, where P_A and P_F (both kg/ms^2) are the partial pressures of gases A and F, respectively, with external atmospheric partial pressures given by $P_{A0}(t)$ and $P_{F0}(t)$.

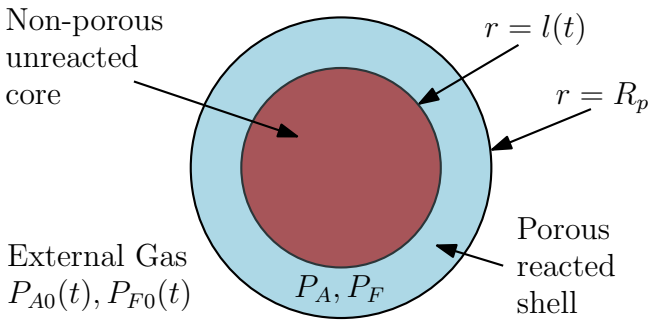


Figure 5.1: Schematic diagram of the shrinking core model, showing the fixed outside radius $r = R_p$ and the moving internal radius $r = l(t)$ of a spherical shell.

For simplicity, we first consider only the reactant gas, and thus assume that P_F has no influence on the dynamics of the reaction. Later, in Section 5.6, we show that the analysis in Sections 5.2 - 5.5 can easily be extended to incorporate the diffusional hindrance of the product gas.

We let the absolute density of A be given by ρ_A [kg/m^3], with the effective density given by $\psi\rho_A$. We assume that gas A will be transported by diffusion from the external atmosphere at $r = R_p$ to the interface $r = l(t)$, then react with the solid B to form gas F and solid H, according to reaction (5.1). Diffusive transport of A implies we have the following equation arising from conservation of mass

$$\frac{\partial(\psi\rho_A)}{\partial t} = D\nabla^2(\psi\rho_A), \quad l(t) \leq r \leq R_p, \tag{5.2}$$

where we assume constant diffusivity D [m^2/s].

We can relate P_A and ρ_A through the ideal gas law, which is

$$P_A = \frac{\rho_A}{M_A} R_g T, \tag{5.3}$$

where we have used R_g to denote the gas constant (8.314 J/molK). M_A [kg/mol] is the molar mass of A and T [K] is the temperature. Thus, assuming that the particle

is isothermal, and noting that porosity is constant, we substitute (5.3) into (5.2) to obtain the diffusion equation for pressure

$$\frac{\partial P_A}{\partial t} = D\nabla^2 P_A, \quad l(t) \leq r \leq R_p. \tag{5.4}$$

At the external boundary the known external pressure implies

$$P_A = P_{A0}(t), \text{ at } r = R_p. \tag{5.5}$$

We let K_A, K_B [mol/m^{2}s] be the rates at which A and B are consumed, per unit time per unit surface area of the unreacted core. By the stoichiometry in (5.1) we have

$$K_A = K_B/\sigma_1. \tag{5.6}$$

For simplicity, we assume that reaction (5.1) follows a first order model, so that

$$K_A = kP_A B_0, \tag{5.7}$$

where B_0 [mol/m^3] is the assumed constant local concentration of B in the unreacted core, and k [m^{2}s/kg] is the reaction constant. B_0 is given in terms of the molar mass M_B [kg/mol] and absolute mass density ρ_B by $B_0 = \rho_B/M_B$. An Arrhenius law or higher order kinetic rates could be used if these are more appropriate for the particular application. Melchiori and colleagues [60, 61] use a general power P_A^α in their continuum model, which we comment on in Section 5.7.4. At the moving reaction interface $r = l(t)$, we have the following conditions, which have been determined by considering the mass flux relative to the interface for A and then B and using (5.3),

$$-\frac{D}{R_g T}\frac{\partial P_A}{\partial r} + \frac{P_A}{R_g T}\frac{dl}{dt} = -K_A, \text{ at } r = l(t), \tag{5.8}$$

$$\frac{\rho_B}{M_B}\frac{dl}{dt} = -K_B, \text{ at } r = l(t). \tag{5.9}$$

Note that $l(t) \geq 0$, so that strictly speaking the right hand side of (5.9) should be $-K_B \mathbb{1}_{l(t)\geq 0}$, where $\mathbb{1}_{l(t)\geq 0}$ is the indicator function, so that the interface stops moving once it reaches $l(t) = 0$. However, from now on we will take this as assumed for brevity of notation. We note that, by (5.6), the right hand side of (5.9) can be written as $-\sigma_1 K_A$.

5.2.2 Dimensionless model

To analyse the problem, we now non-dimensionalise using the scalings

$$t = \tau_s \bar{t}, \quad r = R_p \bar{r}, \quad l = R\bar{l}, \quad P_A = P_{\mathrm{TOT}} \bar{P}_A, \quad P_{A0} = P_{\mathrm{TOT}} \bar{P}_{A0}, \tag{5.10}$$

where P_{TOT} is a constant reference pressure. We introduce three dimensionless parameters, namely

$$\hat{\epsilon} = \frac{R_p^2}{D\tau_s}, \quad \hat{\beta} = \frac{R_g T k B_0 R_p}{D}, \quad \hat{\gamma} = \frac{\sigma_1 k P_{\mathrm{TOT}} \tau_s}{R_p}, \tag{5.11}$$

where the hat notation is to avoid confusion with parameters introduced later in (5.29), and used from Section 5.3 onwards. Dropping the overbar notation from the variables in (5.10), we obtain the system

$$\hat{\epsilon} \frac{\partial P_A}{\partial t} = \nabla^2 P_A, \quad l(t) \leq r \leq 1, \tag{5.12}$$

$$P_A = P_{A0}(t), \text{ at } r = 1, \tag{5.13}$$

$$-\frac{\partial P_A}{\partial r} + \hat{\epsilon} P_A \frac{dl}{dt} = -\hat{\beta} P_A, \text{ at } r = l(t), \tag{5.14}$$

$$\frac{dl}{dt} = -\hat{\gamma} P_A, \text{ at } r = l(t). \tag{5.15}$$

We now discuss some of the behaviour in limiting cases of the dimensionless parameters. The parameter $\hat{\epsilon}$ measures the ratio of the timescale for diffusion within the particle to the timescale for the particle to completely react. Thus, small $\hat{\epsilon}$ means that gas diffuses throughout the particle quickly compared to the particle reaction time, and in particular we do not need to consider the change in the total amount of gas in the particle from the reaction. We are free to choose the timescale τ_s, and so could set any of the dimensionless parameters to unity with an appropriate choice, if desired. However, we will take τ_s to be an experimentally found time (in the setting of interest) for a typical particle to completely react. Typically, such a timescale allows a simplification of our system by using the Quasi-Steady State Assumption (QSSA), sometimes called the pseudo-steady state assumption [108], corresponding to taking the limit $\hat{\epsilon} \to 0$. Xu et al. [111] compare results to solutions found without using a quasi-steady state, with good agreement when the concentration of the reactant gas is low compared to that of the product solid. We use the quasi-steady limit from now on in this chapter.

The parameter $\hat{\beta}$ is a measure of the ratio of the amount of gas A lost from the reaction to the amount of gas transported to the interface by the diffusive flux. Thus,

if $\hat{\beta}$ is large, the reaction is quick compared to the time for gas to get to the interface, and diffusion through the reacted material is the process that determines the overall reaction time. If, however, $\hat{\beta}$ is small, then the chemical reaction time is slower than the diffusive flux, and hence the process is reaction limited. The parameter $\hat{\gamma}$ is a measure of how far the interface moves for a given amount of the gas-solid reaction.

5.2.3 Quasi-steady limit

We now study the system (5.12) - (5.15) in the limit $\hat{\epsilon} \to 0$. This allows us to neglect the left hand side of (5.12), and the second term in (5.14), to give the canonical shrinking core problem that has been studied extensively in literature [90, 95, 97]. We find P_A by integrating (5.12), to obtain

$$r^2 \frac{\partial P_A}{\partial r} = A(t), \quad l(t) \leq r \leq 1, \tag{5.16}$$

where, using (5.14), we have introduced

$$A(t) = \hat{\beta} l(t)^2 P(l(t), t). \tag{5.17}$$

Integrating (5.16) and using (5.13), we find

$$P_A(r,t) = P_{A0}(t) \left[1 - \frac{\hat{\beta} l(t)^2}{1 + \hat{\beta} l(t) \left(1 - l(t)\right)} \left(\frac{1}{r} - 1 \right) \right], \tag{5.18a}$$

$$A(t) = P_{A0}(t) \frac{\hat{\beta} l(t)^2}{1 + \hat{\beta} l(t)(1 - l(t))}. \tag{5.18b}$$

Substituting P_A from (5.18a) into (5.15), we then obtain the ODE for the $l(t)$ problem:

$$\frac{dl}{dt} = -\hat{\gamma} \frac{P_{A0}(t)}{1 + \hat{\beta} l(t)(1 - l(t))}, \quad l(0) = 1. \tag{5.19}$$

Integrating (5.19), we find

$$\hat{\beta} \frac{l(t)^3}{3} - \hat{\beta} \frac{l(t)^2}{2} - l(t) + 1 + \frac{\hat{\beta}}{6} = \hat{\gamma} \int_{u=0}^{t} P_{A0}(u) du. \tag{5.20}$$

Given the external pressure $P_{A0}(t)$, equation (5.20) gives a cubic which can be solved to determine the position of the interface $l(t)$, upon taking the monotonically decreasing real root which starts at $l(0) = 1$. In particular, we can find the time $t = t^*$ when the particle is first fully reacted (that is $l(t^*) = 0$), given by the integral condition

$$\int_{u=0}^{t^*} P_{A0}(u) du = \left(1 + \frac{\hat{\beta}}{6} \right) \frac{1}{\hat{\gamma}}, \tag{5.21}$$

and hence for finite $\hat{\beta}$ and non-zero $\hat{\gamma}$, the particle will always be fully reacted in finite time, as long as the external pressure is non-zero. This is the classic shrinking core model, and we comment further on limits of this simple model in Section 5.7.

The shrinking core assumption, that there is a sharp interface between reacted and unreacted regions, is not always valid, especially for very porous particles where highly diffusive gas may access the inner part of the particle before the outer part has fully converted. This is particularly true for the case for agglomerated solids, where small grains of the reactant solid are compressed together and held in place by a binder. A need to capture interactions between smaller granular and larger particle scales leads us to utilise homogenisation theory.

5.3 Homogenisation of a granular particle

In Section 5.2 we considered a reacting solid particle which has an inward-moving sharp interface between a central unreacted core and a reacted shell. We now consider the reaction of a particle that is composed of many smaller grains, so there may be a diffuse region over which the reaction occurs, instead of a sharp divide. Note that grain models [97] and continuum models [60, 61] have been formed to represent such a situation. However, we use the mathematical technique of homogenisation to systematically derive models, which can then be compared to those previously studied. For ease of notation, from now on we refer to the partial pressures P_A and P_F as P and Q, for gases A and F, respectively, although we will not use Q until Section 5.6.

We follow the methodology of Bruna and Chapman [13], and Dalwadi et al. [21, 22], due to the similar nature of their problems. However, we have diffusion inside solid grains, as well as between them, so discuss the homogenisation in detail. We consider a periodic microscale consisting of three regions. A solid unreacted core occupies the region ω_C, which is surrounded by a porous shell of the solid product ω_S. This is, in turn, surrounded by the void space ω_V, which is filled by gas. The interface between ω_V and ω_S is denoted $\partial\omega_a$, and the interface between ω_S and ω_C is denoted $\partial\omega_b$. We suppose that the ratio of the microscale to macroscale lengthscales is given by $\delta \ll 1$. We allow gas to be present in ω_V, and inside the porous matrix in ω_S (which has fixed porosity), but not to be present inside ω_C. We are interested in the reactant gas pressures inside ω_V and ω_S, denoted by P^V and P^S respectively. A schematic diagram of the geometry is given in Figure 5.2, with a cubic packing of microscale grains used for simplicity. We follow the approach of Bruna and Chapman

[13] to perform a formal homogenisation. We let $\mathbf{x}$ be the macroscale variable, and introduce $\mathbf{y} = \mathbf{x}/\delta$ as the microscale variable, treating $\mathbf{x}$ and $\mathbf{y}$ as independent.

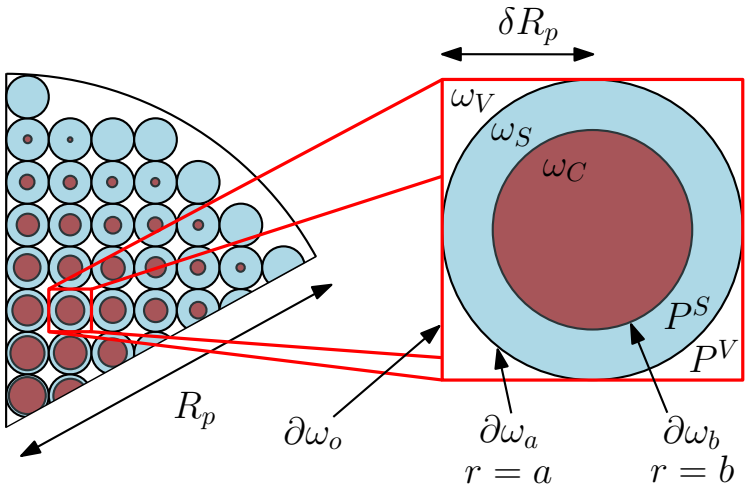


Figure 5.2: Schematic diagram of the problem geometry, with macroscale in the left wedge and microscale in the right square. Note that this is a two-dimensional plane-view of the cubic packing, whereas the problem we are concerned with is three-dimensional.

We consider the scalings

$$P^V = P_{\mathrm{TOT}}\hat{P^V}, \quad P^S = P_{\mathrm{TOT}}\hat{P^S}, \quad t = \tau_s\hat{t}, \quad \mathbf{x} = R_p\hat{\mathbf{x}}, \quad \mathbf{y} = \delta R_p\hat{\mathbf{y}}. \tag{5.22}$$

We assume that the interfaces $\partial\omega_a$ and $\partial\omega_b$ are spheres with centres at the origin of each cell, with radii slowly varying functions of centre position. We allow the position of $\partial\omega_b$ to vary with time. We thus let $b(\mathbf{x}, t) = \mathrm{B}(\mathbf{x}, t)/\delta$ be the radii of the unreacted grains of solid B and $a(\mathbf{x}) = \mathrm{A}(\mathbf{x})/\delta$ be the outer radius of the shells of the solid product H, where lower case a, b denote variables on the microscale, and upper case A, B denote macroscale variables. For simplicity we treat the outer shell radii as constant, so that $a(\mathbf{x}) \equiv a$.

We take the diffusivity in the void D_V [m^2/s], to be a typical dimensional scale, but note that the ratio with the diffusivity in the product shell, D_S [m^2/s], will depend on the specific reaction of interest. We allow for different limits of D_S/D_V to be considered by writing

$$\frac{D_S}{D_V} = \delta^n\nu, \tag{5.23}$$

for ν an $\mathcal{O}(1)$ parameter and $n \in \mathbb{R}$. Typically, we would physically expect $n > 0$, that is $D_S < D_V$, since it is harder for gas to diffuse through the porous matrix than through the void space. However, grains may be held together by a binder which fills

the void space, and so it is possible to have $n < 0$, that is $D_V < D_S$. In this section, we present the two-scale problem using a general n, then consider how the choice of n leads to different homogenised models in Section 5.4.

We find the field equations for $\hat{P}^V$ and $\hat{P}^S$ by using a similar process to that described in Section 5.2. Upon dropping the hat notation, we obtain the equations

$$\epsilon \frac{\partial P^V}{\partial t} = \nabla^2 P^V, \quad \mathbf{y} \in \omega_V, \tag{5.24}$$

$$\frac{\epsilon}{\nu \delta^n} \frac{\partial P^S}{\partial t} = \nabla^2 P^S, \quad \mathbf{y} \in \omega_S. \tag{5.25}$$

We have continuity of pressure and flux at the interface $\partial\omega_a$, so that

$$P^V = P^S, \quad \nabla P^V = \delta^n \nu \nabla P^S, \quad \mathbf{y} \in \partial\omega_a. \tag{5.26}$$

In order to employ homogenisation, we enforce that P^V is periodic in $\mathbf{y}$. We also have the conditions for the interface $\partial\omega_b$, which are analogous to (5.14) and (5.15),

$$-\delta^n \nu \nabla P^S \cdot \mathbf{n} + \epsilon P^S \frac{\partial b}{\partial t} = -\delta \beta P^S, \quad \mathbf{y} \in \partial\omega_b, \tag{5.27}$$

$$\frac{\partial b}{\partial t} = -\gamma P^S, \quad \mathbf{y} \in \partial\omega_b, \tag{5.28}$$

where (5.28) is only defined for $b(t) \geq 0$, so that when $b(t)$ is first zero it remains in that state for all subsequent time. In addition to δ and ν, we also have the dimensionless parameters ϵ, β, and γ. These are given by

$$\epsilon = \frac{R_p^2}{D_V \tau_s}, \quad \beta = \frac{R_g T k_m B_0 R_p}{\delta D_V}, \quad \gamma = \frac{\sigma_1 k P_{\mathrm{TOT}} \tau_s}{R_p}, \tag{5.29}$$

which are the same as the hatted parameters in (5.11), except with D_V replacing D and k_m/δ replacing k. k_m [m^{2}s/kg] is the microscale reaction constant, and is such that $k_m/k = \mathcal{O}(\delta)$. As is similarly argued in [22], there are an $\mathcal{O}(1/\delta^3)$ number of microscale spherical grains in the macroscale particle, each with surface area $\mathcal{O}(\delta^2)$. Thus the overall surface area for the reaction is $\mathcal{O}(1/\delta)$. Hence for an $\mathcal{O}(1)$ overall reaction rate we need the reaction at the microscale interface to be $\mathcal{O}(\delta)$, and the right hand side of (5.27) is accordingly that scale. We let β and γ be order one parameters, but treat ϵ as sufficiently small that it does not enter the analysis, so that $\epsilon = \mathcal{O}(\delta^n)$, for δ^n given in (5.23).

We note that the gradient operator should now incorporate both the macro and micro scales, and so have

$$\nabla \to \nabla_{\mathbf{x}} + \frac{1}{\delta} \nabla_{\mathbf{y}}. \tag{5.30}$$

Similarly, using [22], the unit normal vector at $r = b$ is given by

$$\mathbf{n} = \frac{\mathbf{n_y} - \delta \nabla_{\mathbf{x}} b(\mathbf{x}, t)}{\|\mathbf{n_y} - \delta \nabla_{\mathbf{x}} b(\mathbf{x}, t)\|}, \tag{5.31}$$

where we have defined $\mathbf{n_y} \coloneqq \mathbf{y}/\|\mathbf{y}\|$ as the outward pointing unit normal in $\mathbf{y}$ from the unreacted solid core into the porous solid matrix of the product.

Upon taking ϵ to be suitably small, the field equations are given by

$$0 = \nabla^2_{\mathbf{y}} P^V + \delta \left(\nabla_{\mathbf{x}} \cdot \nabla_{\mathbf{y}} P^V + \nabla_{\mathbf{y}} \cdot \nabla_{\mathbf{x}} P^V \right) + \delta^2 \nabla^2_{\mathbf{x}} P^V, \quad \mathbf{y} \in \omega_V, \tag{5.32}$$

$$0 = \nabla^2_{\mathbf{y}} P^S + \delta \left(\nabla_{\mathbf{x}} \cdot \nabla_{\mathbf{y}} P^S + \nabla_{\mathbf{y}} \cdot \nabla_{\mathbf{x}} P^S \right) + \delta^2 \nabla^2_{\mathbf{x}} P^S, \quad \mathbf{y} \in \omega_S. \tag{5.33}$$

Letting $\mathbf{e}_r$ be the radial unit vector, then the conditions in (5.26) become

$$P^V = P^S, \quad \nabla_{\mathbf{y}} P^V + \delta \nabla_{\mathbf{x}} P^V = \delta^n \nu \nabla_{\mathbf{y}} P^S + \delta^{n+1} \nu \nabla_{\mathbf{x}} P^S, \quad \text{at } \mathbf{y} = a\mathbf{e}_r. \tag{5.34}$$

At the interface $\mathbf{y} = b(\mathbf{x}, t)\mathbf{e}_r$, we have that (5.27) and (5.28) become

$$\begin{aligned} -\nabla_{\mathbf{y}} P^S \cdot \mathbf{n_y} + \delta \big(\nabla_{\mathbf{y}} P^S \cdot \nabla_{\mathbf{x}} b(\mathbf{x}, t) - \nabla_{\mathbf{x}} P^S \cdot \mathbf{n_y} \big) + \delta^2 \nabla_{\mathbf{x}} P^S \cdot \nabla_{\mathbf{x}} b(\mathbf{x}, t) \\ = -\delta^{2-n} \frac{\beta}{\nu} P^S \|\mathbf{n_y} - \delta \nabla_x b(\mathbf{x}, t)\|, \quad \text{at } \mathbf{y} = b(\mathbf{x}, t)\mathbf{e}_r, \end{aligned} \tag{5.35}$$

$$\frac{\partial b(\mathbf{x}, t)}{\partial t} = -\gamma P^S, \text{ at } \mathbf{y} = b(\mathbf{x}, t)\mathbf{e}_r, \tag{5.36}$$

with the initial condition $b(\mathbf{x}, t) = a$.

5.4 Distinguished limits

We now examine the system (5.32) - (5.36), considering different limits of $D_S/D_V = \delta^n \nu$ in turn. For each distinguished limit, we shall expand the pressures in terms of δ, so that

$$P^V = P^V_0 + \delta P^V_1 + \delta^2 P^V_2 + \mathcal{O}(\delta^3), \quad P^S = P^S_0 + \delta P^S_1 + \delta^2 P^S_2 + \mathcal{O}(\delta^3). \tag{5.37}$$

We first consider the limit $n = 2$, and give detailed calculations explaining the derivation of the resulting homogenised model. We then discuss the limits $n = 1$ and $n = 0$, before commenting on other possible limits of the ratio of diffusivities.

5.4.1 The $D_S/D_V = \delta^2\nu$ limit

We begin by examining the limit $D_S/D_V = \delta^2\nu$, so that $n = 2$. In this limit we find that the $\mathcal{O}(1)$ equations give that P_0^V is independent of $\mathbf{y}$, while we also have that P_0^S is given by the solution of

$$\nabla_{\mathbf{y}}^2 P_0^S = 0, \quad \mathbf{y} \in \omega_S, \tag{5.38}$$

$$P_0^S(a, \mathbf{x}, t) = P_0^V(a, \mathbf{x}, t), \tag{5.39}$$

$$\mathbf{n}_{\mathbf{y}} \cdot \nabla_{\mathbf{y}} P_0^S(b(\mathbf{x}, t), \mathbf{x}, t) = \frac{\beta}{\nu} P_0^S(b(\mathbf{x}, t), \mathbf{x}, t). \tag{5.40}$$

In the spherical geometry we employ, the problem (5.38) - (5.40) has the solution

$$P_0^S = \left(\frac{\frac{1}{r} - \frac{1}{a}}{\frac{1}{a} - \frac{1}{b} - \frac{\nu}{\beta b^2}} + 1 \right) P_0^V, \tag{5.41}$$

and, in particular, at $r = b$ we have

$$P_0^S(b(\mathbf{x}, t), \mathbf{x}, t) = \frac{1}{1 + \frac{\beta}{\nu} b \left(1 - \frac{b}{a}\right)} P_0^V. \tag{5.42}$$

At $\mathcal{O}(\delta)$, we have the system

$$\nabla_{\mathbf{y}}^2 P_1^V = 0, \quad \mathbf{y} \in \omega_V, \tag{5.43}$$

$$\nabla_{\mathbf{y}}^2 P_1^S + \nabla_{\mathbf{x}} \cdot \nabla_{\mathbf{y}} P_0^S + \nabla_{\mathbf{y}} \cdot \nabla_{\mathbf{x}} P_0^S = 0, \quad \mathbf{y} \in \omega_S, \tag{5.44}$$

$$P_1^V = P_1^S, \quad \nabla_{\mathbf{y}} P_1^V + \nabla_{\mathbf{x}} P_0^V = 0, \quad \text{at } r = a, \tag{5.45}$$

$$-\left(\nabla_{\mathbf{y}} P_1^S + \nabla_{\mathbf{x}} P_0^S\right) \cdot \mathbf{n}_{\mathbf{y}} = -\frac{\beta}{\nu} P_1^S, \text{ at } r = b(\mathbf{x}, t), \tag{5.46}$$

and that P_1^V is periodic in $\mathbf{y}$. Note that $\mathbf{n}_{\mathbf{y}}$ points outwards away from the origin. If $\mathbf{n}_{\mathbf{y}}$ and $\nabla_{\mathbf{x}} b$ are parallel, then an additional term is present in the right-hand side of (5.46). Thus, if $\mathbf{n}_{\mathbf{y}} = \mathbf{e}_r$ and $\nabla_{\mathbf{x}} b = \frac{\partial b}{\partial R} \mathbf{e}_r$ then the right hand side is given by $-\frac{\beta}{\nu} P_1^S + \frac{\beta}{\nu} \frac{\partial b}{\partial R} P_0^S$. Using the standard homogenisation method [7, 72], and the notation employed in [13], we can write the solution for P_1^V as

$$P_1^V(\mathbf{x}, \mathbf{y}, t) = -\nabla_{\mathbf{x}} P_0^V(\mathbf{x}, t) \cdot \mathbf{\Gamma}(\mathbf{x}, \mathbf{y}, t), \tag{5.47}$$

where components Γ_i of the vector function $\mathbf{\Gamma}(\mathbf{x}, \mathbf{y}, t)$ satisfy

$$\nabla_{\mathbf{y}}^2 \Gamma_i = 0, \quad \mathbf{y} \in \omega_V, \tag{5.48}$$

$$\nabla_{\mathbf{y}} \Gamma_i \cdot \mathbf{e}_{\mathbf{r}} = n_{y,i}, \text{ at } r = a, \tag{5.49}$$

$$\Gamma_i \text{ periodic in } \mathbf{y}, \tag{5.50}$$

where $n_{y,i}$ is the ith component of the unit vector $\mathbf{n_y}$. Since we have a spherical boundary, the appropriate unit vector is given by $\mathbf{n_y} = \mathbf{e}_r$.

To find the necessary solvability condition, we must consider the next order system. At $\mathcal{O}(\delta^2)$, the equations for P_2^V in ω_V are

$$\nabla_{\mathbf{y}}^2 P_2^V + \nabla_{\mathbf{x}} \cdot \nabla_{\mathbf{y}} P_1^V + \nabla_{\mathbf{y}} \cdot \nabla_{\mathbf{x}} P_1^V + \nabla_{\mathbf{x}}^2 P_0^V = 0, \quad \mathbf{y} \in \omega_V, \tag{5.51}$$

$$\nabla_{\mathbf{y}} P_2^V + \nabla_{\mathbf{x}} P_1^V = \nu \nabla_{\mathbf{y}} P_0^S, \text{ at } \mathbf{y} = a\mathbf{e}_r, \tag{5.52}$$

and that P_2^V is periodic in $\mathbf{y}$.

We integrate (5.51) over ω_V, using the divergence theorem and the boundary conditions of periodicity and (5.52), to obtain

$$-\nu \int_{r=a} \nabla_{\mathbf{y}} P_0^S \cdot \mathbf{n_y} dS_{\mathbf{y}} + \nabla_{\mathbf{x}} \cdot \int_{\omega_V} \nabla_{\mathbf{y}} P_1^V + \nabla_{\mathbf{x}} P_0^V d\mathbf{y} = 0. \tag{5.53}$$

Now considering ω_S, we note, using the divergence theorem, that

$$\nu \int_{\omega_V} \nabla_{\mathbf{y}} \cdot \nabla_{\mathbf{y}} P_0^S d\mathbf{y} = \nu \int_{r=a} \nabla_{\mathbf{y}} P_0^S \cdot \mathbf{n_y} dS_{\mathbf{y}} - \nu \int_{r=b} \nabla_{\mathbf{y}} P_0^S \cdot \mathbf{n_y} dS_{\mathbf{y}}. \tag{5.54}$$

The integrand on the left hand side is zero, since P_0^S satisfies Laplace's equation. We can substitute the boundary condition (5.46) into the last integral, to note

$$\nu \int_{r=a} \nabla_{\mathbf{y}} P_0^S \cdot \mathbf{n_y} dS_{\mathbf{y}} = \beta P_0^S \int_{r=b} dS\mathbf{y}. \tag{5.55}$$

Hence, we can re-write (5.53) as

$$\nabla_{\mathbf{x}} \cdot \int_{\omega_V} \nabla_{\mathbf{y}} P_1^V + \nabla_{\mathbf{x}} P_0^V d\mathbf{y} = \beta P_0^S \int_{r=b} dS\mathbf{y}. \tag{5.56}$$

The integral over the surface of the sphere of radius $r = b$ is $4\pi b^2$. As in [13], we introduce $J_{\mathbf{\Gamma}(\mathbf{x},\mathbf{y})}$ as the Jacobian matrix of Γ, namely $(J_{\mathbf{\Gamma}})_{ij} = \frac{\partial \Gamma_i}{\partial y_j}$, so that

$$\nabla_{\mathbf{y}} P_1^V = -J^T_{\mathbf{\Gamma}(\mathbf{x},\mathbf{y})} \nabla_{\mathbf{x}} P_0^V. \tag{5.57}$$

We let $p(\mathbf{x}, t) = P_0^V(\mathbf{x}, t)$ be the homogenised pressure and $D(\mathbf{x})$ the effective diffusion tensor, which is given by

$$D(\mathbf{x}) = I|\omega_V| - \int_{\omega_V(\mathbf{x})} J^T_{\Gamma(\mathbf{x},\mathbf{y})} d\mathbf{y}, \tag{5.58}$$

where I is the identity matrix. However, since a is constant, the right hand side of (5.58) is constant. Letting D_e be the constant effective diffusivity, we have

$$\nabla^2_{\mathbf{x}} p(\mathbf{x},t) = \frac{4\pi\beta}{D_e} \frac{p(\mathbf{x},t) b(\mathbf{x},t)^2}{1+\frac{\beta}{\nu} b(\mathbf{x},t)\left(1-\frac{b(\mathbf{x},t)}{a}\right)}. \tag{5.59}$$

This is coupled, using (5.36) and (5.41), to the equation

$$\frac{\partial b(\mathbf{x},t)}{\partial t} = -\gamma \frac{p(\mathbf{x},t)}{1+\frac{\beta}{\nu} b(\mathbf{x},t)\left(1-\frac{b(\mathbf{x},t)}{a}\right)}. \tag{5.60}$$

We have found these equations by noting that at leading order the pressures in ω_V and ω_S are the same, observing that we can write P_1^V in terms of P_2^V, and integrating the equation for P_2^V to relate the homogenised pressure p to the movement of the boundary b. The initial condition is $b(\mathbf{x},0) = a$, and boundary conditions are $p(1,t) = p_a$ and that p is bounded at the origin.

Using the scalings

$$p = p_a \bar{p}, \quad b = a\bar{b}, \quad t = \frac{a}{\gamma p_a}\bar{t}, \tag{5.61}$$

we find upon dropping the overbar notation and letting $R \in [0,1]$ be the dimensionless macroscale variable,

$$\frac{1}{R^2}\frac{\partial}{\partial R}\left(R^2 \frac{\partial p}{\partial R}\right) = \kappa \frac{p b^2}{1+\lambda b(1-b)}, \quad 0 \le R \le 1, \quad t \ge 0, \tag{5.62}$$

$$\frac{\partial b}{\partial t} = -\frac{p}{1+\lambda b(1-b)}, \quad 0 \le R \le 1, \quad t \ge 0, \tag{5.63}$$

$$p(1,t) = 1, \quad p \quad \text{bounded as } R \to 0, \quad b(R,0) = 1, \tag{5.64}$$

where the dimensionless parameters κ and λ are given by

$$\kappa = 4\pi\beta a^2/D_e, \quad \lambda = a\beta/\nu. \tag{5.65}$$

We can also replace (5.62) with

$$\frac{1}{R^2}\frac{\partial}{\partial R}\left(R^2 \frac{\partial p}{\partial R}\right) = -\kappa \frac{\partial}{\partial t}\left(\frac{b^3}{3}\right), \quad 0 \le R \le 1, \quad t \ge 0, \tag{5.66}$$

which is global conservation of mass. This represents gas moving into the particle to replace the reacting solid.

5.4.2 The $D_S/D_V = \delta\nu$ limit

Returning to the system (5.32) - (5.36), but with $n = 1$, we find that the $\mathcal{O}(1)$ equations give that both P_0^V and P_0^S are independent of $\mathbf{y}$, and that $P_0^V = P_0^S$. At $\mathcal{O}(\delta)$, we find that P_1^S satisfies Laplace's equation instead of (5.44), and that the reaction rate in (5.46) comes in at lower order, so that the right hand side is given by $-\frac{\beta}{\nu}P_0^S$. Equation (5.43) and the boundary conditions in (5.45) remain unchanged. At $\mathcal{O}(\delta^2)$, the interfacial pressure flux from ω_S into ω_V is of a lower order, so that the right hand side of (5.52) becomes $\nu\nabla_{\mathbf{y}}P_1^S + \nu\nabla_{\mathbf{x}}P_0^S$. Integrating (5.51) (which remains unchanged) over ω_V and using analogous methods to what we did before, we can relate the homogeneous pressure $p = P_0^V = P_0^S$ to the interface b, to obtain the same system (5.63) - (5.66), but with $\lambda = 0$. Note that the same model arises if a fractional power of $n \in (0, 2)$ is instead taken, using an asymptotic expansion in the appropriate fractional powers of δ.

5.4.3 The $D_S/D_V = \nu$ limit

If we consider the case where the diffusivities in the void space ω_V and the porous solid ω_S are the same order of magnitude, so $D_S/D_V = \nu$, then examining the system (5.32) - (5.36) with $n = 0$ we find that the pressures and fluxes come in at the same order in each region. The lowest order pressures, P_0^V and P_0^S, are equal and independent of $\mathbf{y}$. We integrate the $\mathcal{O}(\delta^2)$ field equations, using periodicity of P^V along $\partial\omega_o$ and that the macroscale domain of interest is also spherical, so that $\nabla_{\mathbf{x}}$ is parallel to $\mathbf{y}$. This leads to the homogenised equations

$$\nabla \cdot \left((D_e^V + \nu D_e^S)\nabla p\right) = 4\pi\beta b^2 p, \tag{5.67}$$

$$\frac{\partial b}{\partial t} = -\gamma p, \tag{5.68}$$

where

$$D_e^V(\mathbf{x}) = I|\omega_V| - \int_{\omega_V(\mathbf{x})} J^T_{V\,\mathbf{\Gamma}_V(\mathbf{x},\mathbf{y})} d\mathbf{y}, \tag{5.69a}$$

$$D_e^S(\mathbf{x}, t) = I|\omega_S| - \int_{\omega_S(\mathbf{x},t)} J^T_{S\,\mathbf{\Gamma}_S(\mathbf{x},\mathbf{y})} d\mathbf{y}, \tag{5.69b}$$

and J_V and J_S are analogous to the Jacobian used in (5.57), that is $(J_{\mathbf{\Gamma}_V})_{ij} = \frac{\partial \Gamma_{V,i}}{\partial y_j}$ and $(J_{\mathbf{\Gamma}_S})_{ij} = \frac{\partial \Gamma_{S,i}}{\partial y_j}$, where $\mathbf{\Gamma}_V$ and $\mathbf{\Gamma}_S$ are defined in ω_V and ω_S, respectively. Using the same scales as in (5.61), along with $D_e^V = \bar{D_e^V} D_e$ and $D_e^S = \bar{D_e^S} D_e$, we obtain the same system as (5.63) - (5.66), except with a spatially varying diffusivity $\bar{D_e^V} + \nu\bar{D_e^S}$, which is dependent upon the microscale granular behaviour, along with $\lambda = 0$.

5.4.4 Other limits

When $n > 2$, so that the diffusivity in the shell is extremely weak compared to that in the void, we find that p satisfies Laplace's equation and b is spatially independent. Thus, physically it is too hard for the reactant gas to diffuse through ω_S at the granular level to the interface, and so the reaction does not take place. In the case $n < 0$, where it is easier for gas to diffuse through the shell than the void, we find that p is spatially independent and $b_t = -p$. This means that the particle converts linearly in time in a spatially homogeneous manner. Although this limit is physically rare, it could occur if a low-porosity binder is used to glue grains together.

5.4.5 Summary

We can combine each model discussed into a composite model taking the form

$$\nabla \cdot \left((\bar{D_e^V} + \frac{D_S}{D_V} \bar{D_e^S}) \nabla p \right) = -\kappa \frac{\partial}{\partial t} \left(\frac{b^3}{3} \right), \tag{5.70}$$

$$\frac{\partial b}{\partial t} = -\frac{p}{1 + a\beta \frac{D_V}{D_S} \delta^2 b(1-b)}, \tag{5.71}$$

in the domain $0 \leq R \leq 1$, $t \geq 0$, where $\kappa = 4\pi\beta a^2 / D_e$. As δ is the ratio of granular to particle lengthscales, we obtain a homogenised model by taking the limit $\delta \to 0$, with κ, a, and β all $\mathcal{O}(1)$ parameters. If we assume that $D_S/D_V = \mathcal{O}(\delta^2)$ then we will obtain the equations (5.62) and (5.63), since $\bar{D_e^V} = 1$ for this limit. If instead we take $D_S/D_V = \mathcal{O}(1)$, then equation (5.71) becomes $b_t = -p$, but we obtain the granular diffusion terms in the first equation. Taking $D_S/D_V = \mathcal{O}(\delta^n)$ for $n \in (0,2)$ reduces the complexity in (5.70) and (5.71). Since $\lambda = a\beta/\nu$, the $n \in (0,2)$ model can be obtained by taking the $n = 2$ model in the limit $\nu \to \infty$ and the $n = 0$ model in the limit $\nu \to 0$. The $n \in (0,2)$ model is thus a subset of both the $n = 0$ and $n = 2$ models, which are the two distinguished limits of the homogenisation problem. Similarly, taking the $n = 2$ model in the limit $\nu \to 0$ results in the $n > 2$ model, and taking the $n = 0$ model in the limit $\nu \to \infty$ results in the $n < 0$ model. Since the $n = 2$ model is the most physically relevant, along with the sub-limit $\lambda = 0$ corresponding to $n \in (0,2)$, we explore it in the next section.

5.5 Model behaviour

We are interested in the model consisting of equations (5.63) and (5.66) for the spherically symmetric functions $p(R,t)$ and $b(R,t)$, with boundary conditions and initial

condition in (5.64). Upon finding p and b, we can use these quantities to determine the concentration of solid B (mol/m^3) and the extent of the reaction. Letting $C(R,t)$ be the dimensionless molar concentration of solid B, we have $C(R,t) = b(R,t)^3$. The dimensionless extent of the reaction, or degree of conversion, $X(t)$, is the total molar fraction converted, namely

$$X(t) = 3\int_{R=0}^{1}(1-b^3)R^2 dR. \tag{5.72}$$

This is a commonly used metric [60, 64, 70] to summarise the progress of reactions, and we will use it throughout our model analysis. Note that we can utilise equations (5.63) and (5.66) through

$$\frac{dX}{dt} = -9\int_{R=0}^{1}\frac{\partial}{\partial t}\left(\frac{b^3}{3}\right)R^2 dR = \frac{9}{\kappa}\int_{R=0}^{1}\frac{\partial}{\partial R}\left(R^2\frac{\partial p}{\partial R}\right)dR = \frac{9}{\kappa}\frac{\partial p(1,t)}{\partial R}. \tag{5.73}$$

Thus, we can find the extent of the reaction either by solving for b, or finding p_R at the outside of the particle and using the initial condition $X(0) = 0$. We analyse the model behaviour by first showing some numerical simulations in Section 5.5.1 and then finding asymptotic solutions in the limit of small and large κ in Section 5.5.2.

5.5.1 Numerical simulations

We perform numerical simulations using a first order finite difference scheme. In Figure 5.3, we plot p and b for $\kappa = 0.01$, $\kappa = 10$, and $\kappa = 1000$, with $\lambda = 0$ in all cases. We note that for small κ the system is almost spatially homogeneous, with constant pressure $p = 1$ and linearly decreasing b, but for large κ we have an inward-moving wave for b. In Figure 5.4 we plot $X(t)$ for different κ, again with $\lambda = 0$, and also varying λ with fixed $\kappa = 10$. The larger κ is, the longer the reaction takes, but for small κ, the parameter value has little influence on $X(t)$. Similarly, larger λ increases the reaction time, but $X(t)$ is insensitive to changes in λ for small values of the parameter. More details about the dependency of $X(t)$ on κ and λ are given in Section 5.5.2. In Figure 5.5, we show numerical simulations for p and b with different values of κ and λ. We find that including non-zero λ in the model allows for a richer variety of solutions than when κ is the only free parameter.

5.5.2 Asymptotics

We now solve the system (5.63) - (5.66) analytically using asymptotic methods, exploiting the size of κ. We first examine the limit where κ is a small parameter, and

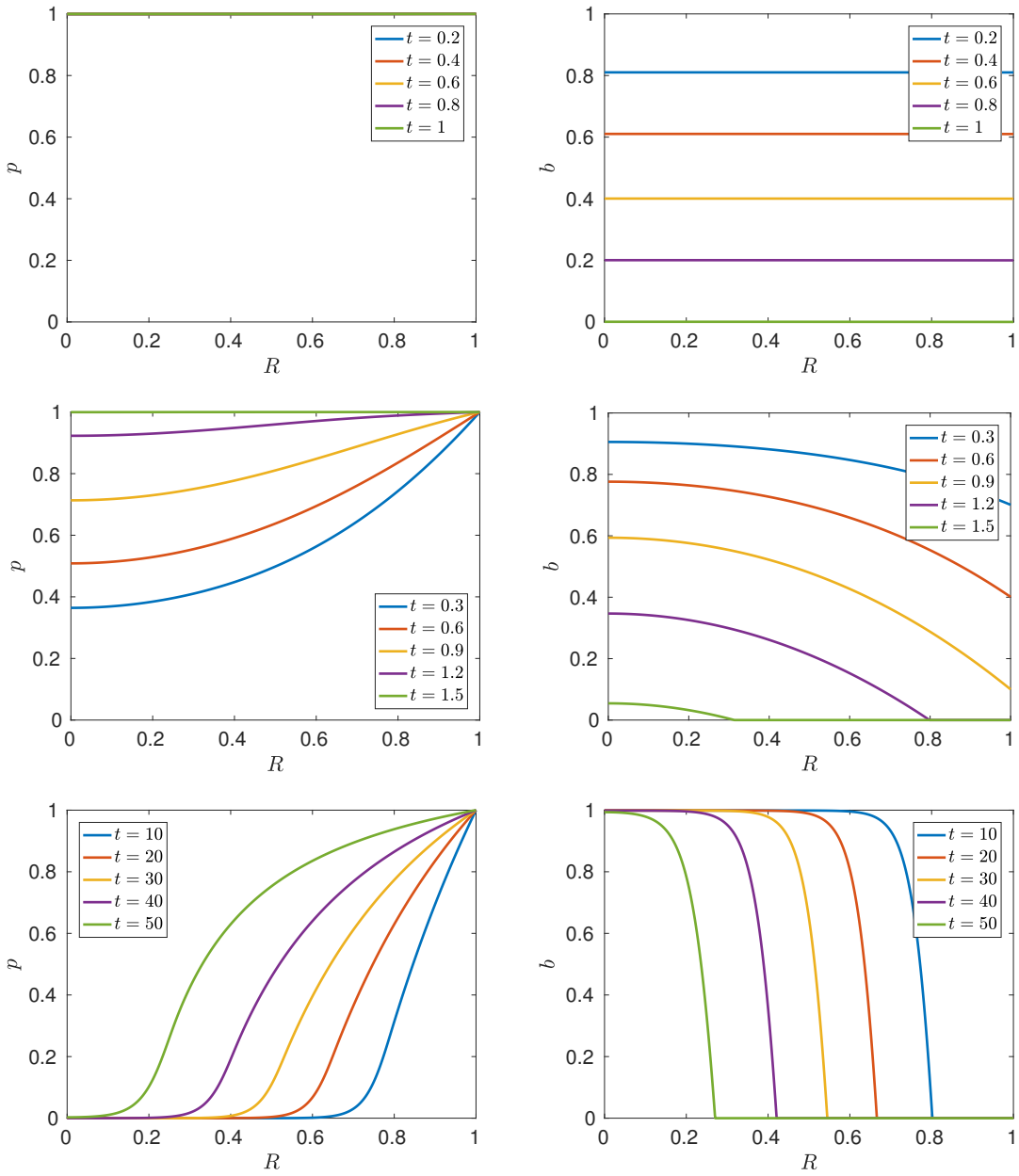


Figure 5.3: Numerical simulations of (5.63) - (5.66), with $\lambda = 0$, for p (left) and b (right). From top to bottom, we tkae $\kappa = 0.01$, $\kappa = 10$, and $\kappa = 1000$. Note how the timescale is different for each choice of κ.

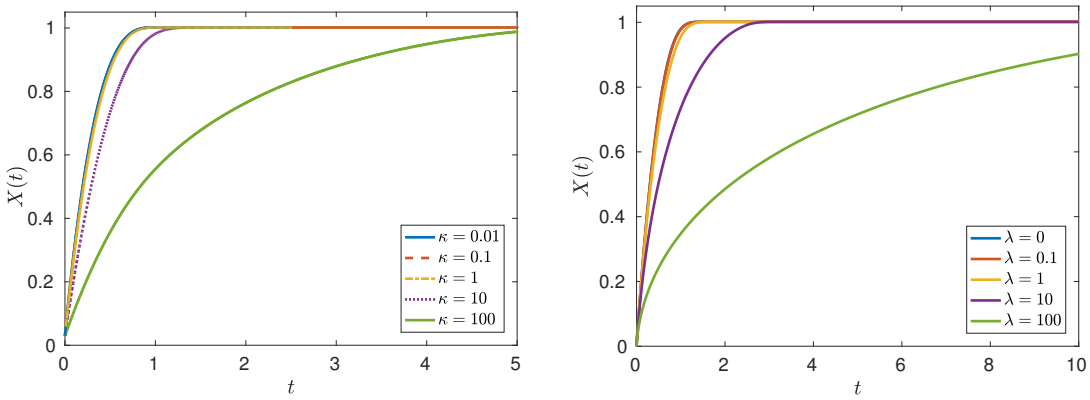


Figure 5.4: Extent of reaction against time. In the left plot, κ is varied, with $\lambda = 0$ fixed. In the right plot, λ is varied, with $\kappa = 10$ fixed.

next consider the limit where κ is a large parameter. In both cases, we treat λ as an $\mathcal{O}(1)$ parameter. In order to make the system easier to solve, we make the substitution $p(R,t) = W(R,t)/R$, which transforms (5.63) - (5.66) to (5.74) - (5.76) below, which are valid for $0 \leq R \leq 1$ and $t \geq 0$.

$$\frac{\partial^2 W}{\partial R^2} = \kappa W b^2, \tag{5.74}$$

$$\frac{\partial b}{\partial t} = -\frac{W}{R}\frac{1}{1+\lambda b(1-b)}, \tag{5.75}$$

$$W(1,t) = 1, \quad W = \mathcal{O}(R), \quad \text{as } R \to 0, \quad b(R,0) = 1. \tag{5.76}$$

Note that for small κ, we find it easier to write (5.74) in the form of (5.62) rather than in conservation of mass form (5.66).

5.5.2.1 Small κ Limit

We consider the limit $0 \leq \kappa \ll 1$, with $\lambda = \mathcal{O}(1)$, which corresponds physically to a parameter regime where diffusion is fast compared to the kinetic rate, so the particle conversion is rate-limited by the chemical reaction. For this limit, it is helpful to replace (5.75) with the time-integrated version

$$b + \frac{\lambda}{2}b^2 - \frac{\lambda}{3}b^3 - \left(1 + \frac{\lambda}{6}\right) = -\frac{1}{R}\int_{\tau=0}^{t} W(R,\tau)d\tau, \tag{5.77}$$

where we integrate over the dummy variable τ. Treating κ as a small parameter, we expand W and b as $W = W_0 + \kappa W_1 + \kappa^2 W_2 + \mathcal{O}(\kappa^3)$, $b = b_0 + \kappa b_1 + \kappa^2 b_2 + \mathcal{O}(\kappa^3)$. For brevity, we list the system arising at each of the first three orders in κ, and then give the combined solutions afterwards.

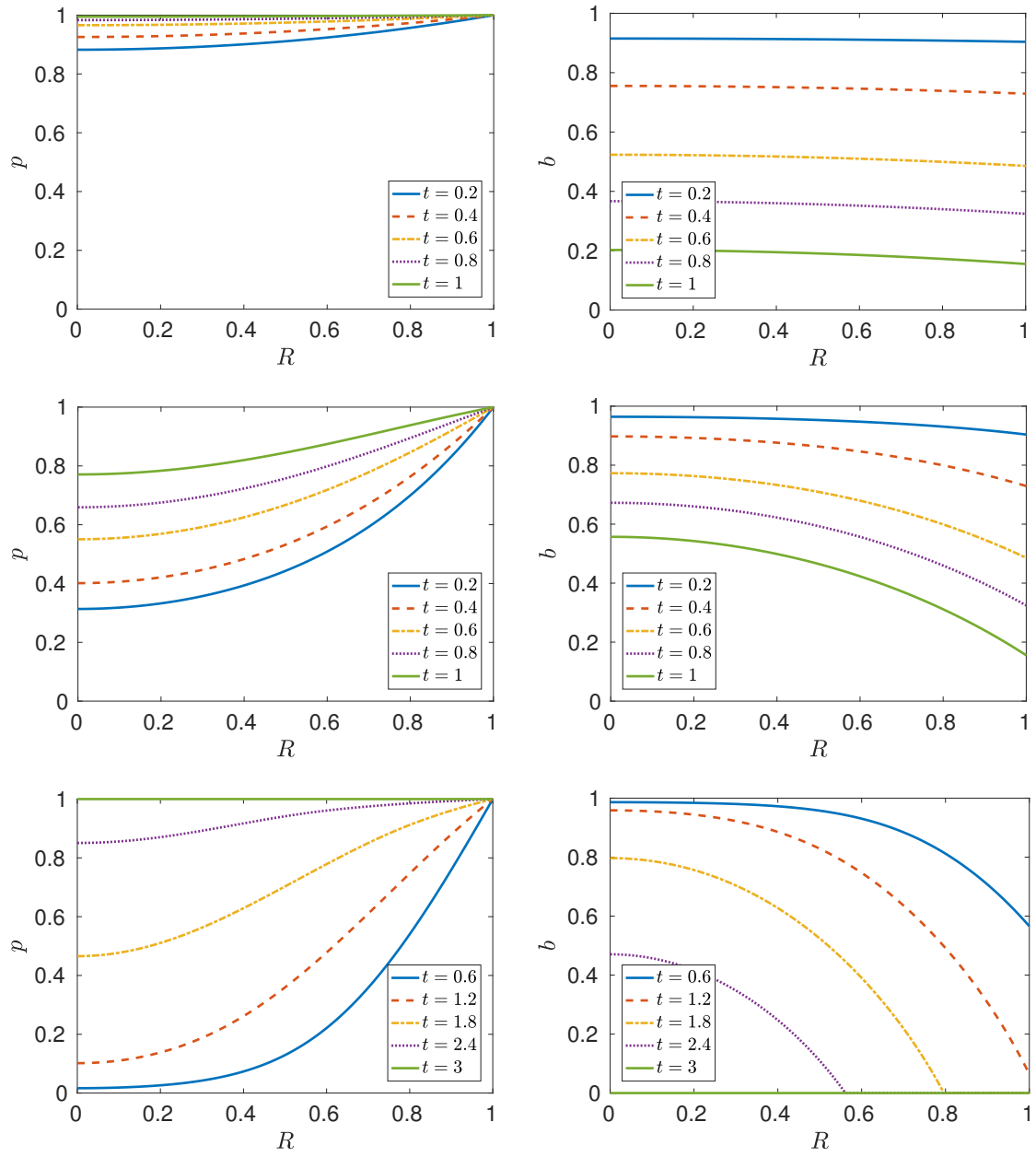


Figure 5.5: Numerical simulations of (5.63) - (5.66), for p (left) and b (right). From top to bottom parameter values used are $\kappa = 1$ and $\lambda = 1$, $\kappa = 10$ and $\lambda = 1$, and $\kappa = 100$ and $\lambda = 20$. Note how the timescale is different in the bottom row.

At $\mathcal{O}(1)$ we obtain the system

$$\frac{\partial^2 W_0}{\partial R^2} = 0, \tag{5.78}$$

$$b_0 + \frac{\lambda}{2} b_0^2 - \frac{\lambda}{3} b_0^3 - \left(1 + \frac{\lambda}{6}\right) = -\frac{1}{R} \int_{\tau=0}^{t} W_0(R, \tau) d\tau, \tag{5.79}$$

$$W_0(1, t) = 1, \quad W_0 = \mathcal{O}(R), \quad \text{as } R \to 0, \quad b_0(R, 0) = 1. \tag{5.80}$$

At $\mathcal{O}(\kappa)$ we obtain

$$\frac{\partial^2 W_1}{\partial R^2} = W_0 b_0^2, \tag{5.81}$$

$$b_1 + \lambda b_0 b_1 - \lambda b_0^2 b_1 = -\frac{1}{R} \int_{\tau=0}^{t} W_1(R, \tau) d\tau, \tag{5.82}$$

$$W_1(1, t) = 0, \quad W_1 = \mathcal{O}(R), \quad \text{as } R \to 0, \quad b_1(R, 0) = 0, \tag{5.83}$$

and at $\mathcal{O}(\kappa^2)$ we find the equations

$$\frac{\partial^2 W_2}{\partial R^2} = W_1 b_0^2 + 2 W_0 b_0 b_1, \tag{5.84}$$

$$b_2 + \frac{\lambda}{2} b_1^2 + \lambda b_0 b_2 - \lambda b_0^2 b_2 - \lambda b_0 b_1^2 = -\frac{1}{R} \int_{\tau=0}^{t} W_2(R, \tau) d\tau, \tag{5.85}$$

$$W_2(1, t) = 0, \quad W_2 = \mathcal{O}(R), \quad \text{as } R \to 0, \quad b_2(R, 0) = 0. \tag{5.86}$$

Upon solving the system at each order, we obtain the solutions

$$W(R, t) = 1 + \frac{\kappa}{6}(R^3 - R) f_0(t; \lambda)^2 + \frac{\kappa^2}{6} \left(\frac{R^5}{20} - \frac{R^3}{6} + \frac{7R}{60}\right) f_0(t) \left(f_0(t)^3 - 2 f_1(t)\right) \mathcal{O}(\kappa^3), \tag{5.87}$$

$$\begin{aligned} b(R, t) =& f_0(t; \lambda) + \frac{\kappa}{6}(1 - R^2) f_1(t; \lambda) \\ & - \kappa^2 \left(\frac{1}{6} \left(\frac{R^4}{20} - \frac{R^2}{6} + \frac{7}{60} \right) f_{21}(t) + \frac{\lambda}{36} (R^2 - 1)^2 f_{22}(t) \right) + \mathcal{O}(\kappa^3), \end{aligned} \tag{5.88}$$

where the function of time $f_0(t; \lambda)$ is given by the real root of the cubic equation

$$f_0^3 - \frac{3}{2} f_0^2 - \frac{3}{\lambda} f_0 + \left(\frac{3}{\lambda}(1 - t) + \frac{1}{2} \right) = 0, \tag{5.89}$$

while $f_1(t; \lambda)$, $f_{21}(t; \lambda)$, and $f_{22}(t; \lambda)$ are given by

$$f_1(t; \lambda) \coloneqq \frac{\int_{\tau=0}^{t} f_0(\tau)^2 d\tau}{1 + \lambda f_0(t) - \lambda f_0(t)^2}, \tag{5.90a}$$

$$f_{21} \coloneqq \frac{\int_{\tau=0}^{t} f_0(\tau)(f_0(\tau)^3 - 2 f_1(\tau)) d\tau}{1 + \lambda f_0(t)(1 - f_0(t))}, \tag{5.90b}$$

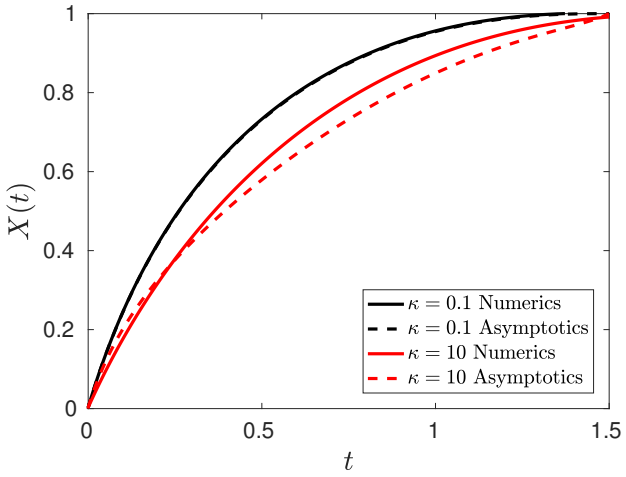


Figure 5.6: Comparison of numerics (solid) and asymptotics (dashed) for the extent of the reaction $X(t)$, with $\lambda = 3$. Even for $\kappa = 10$, the small κ asymptotics give a decent agreement with numerics.

$$f_{22} := \frac{f_1(t)^2(\frac{1}{2} - f_0(t))}{1 + \lambda f_0(t)(1 - f_0(t))}. \tag{5.90c}$$

Using (5.88) in (5.72), we find

$$X(t) = 1 - f_0(t)^3 - \frac{\kappa}{5} f_0^2 f_1 + \frac{2\kappa^2}{105}\left(f_0^2 f_{21} + \lambda f_0^2 f_{22} - f_0 f_1^2\right) + \mathcal{O}(\kappa^3). \tag{5.91}$$

The asymptotic solution (5.91) is compared to numerics in Figure 5.6, for two values of κ, but the same value of λ. The time $t = t^*$ for the reaction to be completed is given implicitly, to leading order, by $f_0(t^*) = 0$, which from (5.89) we find $t^* = 1 + \lambda/6$.

Notice that when $\lambda = 0$ we have

$$f_0(t) = 1 - t, \quad f_1(t) = \frac{1}{3}\left(1 - (1-t)^3\right), \quad f_{21}(t) = \frac{1}{3}\left((1-t)^2 - (1-t)^5\right), \tag{5.92}$$

and so we have the solutions

$$\begin{aligned} W(R,t) =& R - \frac{\kappa}{6}(1-t)^2(R - R^3) + \frac{\kappa^2}{9}\left(\frac{5}{2}(1-t)^4 - (1-t)\right)\left(\frac{R - R^3}{6} - \frac{R - R^5}{20}\right) \\ &+ \mathcal{O}(\kappa^3), \end{aligned} \tag{5.93}$$

$$\begin{aligned} b(R,t) =& (1-t) + \frac{\kappa}{18}\left(1 - (1-t^3)\right)(1 - R^2) \\ &+ \frac{\kappa^2}{18}\left((1-t)^5 - (1-t)^2\right)\left(\frac{1 - R^2}{6} - \frac{1 - R^4}{20}\right) + \mathcal{O}(\kappa^3), \end{aligned} \tag{5.94}$$

$$\begin{aligned} X(t) =& 1 - (1-t)^3 + \frac{\kappa}{15}\left((1-t)^5 - (1-t)^2\right) - \frac{2\kappa^2}{945}\left(4(1-t)^7 - 5(1-t)^4 + (1-t)\right) \\ &+ \mathcal{O}(\kappa^3). \end{aligned} \tag{5.95}$$

Although the results have used the limit $\kappa \to 0$, in practice for $\kappa < 15$ the series (5.95) appears to be a good approximation, but for $\kappa > 15$ the series (5.95) ceases to be asymptotic and it is no longer a helpful approximation. The series given by (5.93), (5.94), and (5.95) are only valid for $t \in [0, 1]$.

5.5.2.2 Large κ Limit

We now consider the case where κ is a large parameter, with λ still $\mathcal{O}(1)$, for the system (5.63) - (5.66). This corresponds to the particle conversion being rate-limited by diffusion, which is slow compared to the kinetic rate. We find that the reaction occurs on an $\mathcal{O}(\kappa)$ timescale, and so we introduce the $\mathcal{O}(1)$ variable $\tau = t/\kappa$. This transforms (5.63) to

$$\frac{\partial b}{\partial \tau} = \begin{cases} \kappa \frac{W}{R} \frac{1}{1+\lambda b(1-b)}, & b \geq 0, \\ 0, & b < 0, \end{cases} \quad 0 \leq R \leq 1, \quad \tau \geq 0, \tag{5.96}$$

where we have included the case $b < 0$ to ensure that b does not become negative, which would be unphysical. Expanding in κ^{-1} like $W = W_0 + \frac{1}{\kappa} W_1 + \mathcal{O}(\frac{1}{\kappa^2})$, $\quad b = b_0 + \frac{1}{\kappa} b_1 + \mathcal{O}(\frac{1}{\kappa^2})$, we obtain

$$b_0(R, \tau) = \begin{cases} 0, & R \geq s(\tau), \\ 1, & R < s(\tau), \end{cases} \tag{5.97a}$$

$$W_0(R, \tau) = \begin{cases} \omega(R, \tau), & R \geq s(\tau), \\ 0, & R < s(\tau), \end{cases} \tag{5.97b}$$

for some unknown function of time $s(\tau)$ and linear function $\omega(R, \tau) = 1 + Y(\tau)(R-1)$.

To determine $s(\tau)$ and $Y(\tau)$, we note that there must be a boundary layer of thickness $\mathcal{O}\left(\frac{1}{\sqrt{\kappa}}\right)$ in R, in order to balance the derivative term in (5.96) with the $\mathcal{O}(\kappa)$ term on the right hand side. To find the behaviour in this boundary layer, we introduce the scalings

$$\eta = \sqrt{\kappa}\left(s(\tau) - R\right), \quad W(R, t) = \sqrt{\kappa} v(\eta, \tau), \quad b(R, t) = h(\eta, \tau), \tag{5.98}$$

and use the conservation form of the equation,

$$\frac{\partial^2 W}{\partial R^2} = -\frac{1}{3} R \frac{\partial}{\partial \tau}\left(b^3\right), \tag{5.99}$$

instead of (5.63). With these scalings, we obtain the system for v, h, and s, for $\tau \geq 0$ and $\eta \geq 0$,

$$\frac{\partial^2 v}{\partial \eta^2} = -s \frac{ds}{d\tau} h^2 \frac{\partial h}{\partial \eta} + \mathcal{O}\left(\frac{1}{\sqrt{\kappa}}\right), \tag{5.100}$$

$$\frac{ds}{d\tau}\frac{\partial h}{\partial \eta} = -\frac{v}{s\left(1+\lambda h(1-h)\right)} + \mathcal{O}\left(\frac{1}{\sqrt{\kappa}}\right), \tag{5.101}$$

$$h(0,\tau) = 0, \quad h \to 1 \quad \text{as } \eta \to \infty, \quad v \to 0 \quad \text{as } \eta \to \infty, \tag{5.102}$$

along with two equations arising from suitable matching of v and W and their derivatives at $\eta = 0$ (that is, $R = s(\tau)$).

Taking the leading order terms from (5.100) and (5.101) (which can be found by expanding $v = v_0 + \mathcal{O}\left(\frac{1}{\sqrt{\kappa}}\right), \quad h = h_0 + \mathcal{O}\left(\frac{1}{\sqrt{\kappa}}\right)$, but we suppress the 0 subscript) then a first integral of (5.100) can be taken to give

$$\frac{\partial v}{\partial \eta} = s\frac{ds}{d\tau}\left(\frac{1}{3} - \frac{h^3}{3}\right). \tag{5.103}$$

Upon integrating, the arbitrary function of time was determined by the last two conditions in (5.102), assuming that v is suitably well behaved so that $\frac{\partial v}{\partial \eta} \to 0$ as $\eta \to \infty$. Since we also have from (5.101) that

$$v = -s\frac{ds}{d\tau}\frac{\partial h}{\partial \eta}\left(1+\lambda h(1-h)\right), \tag{5.104}$$

we can substitute (5.104) into (5.103) to obtain the second order ODE in η for $h(\eta,\tau) = F(\eta)$, which reads

$$\frac{d}{d\eta}\left(\frac{dF}{d\eta}\left(1+\lambda F(1-F)\right)\right) = \frac{F^3}{3} - \frac{1}{3}, \quad F(0) = 0, \quad F(\infty) = 1. \tag{5.105}$$

Note that we can find $F(\eta;\lambda)$ numerically by writing the ODE as a first order system for F and $G = F'$, where $'$ denotes differentiation with respect to η. We then vary the initial value of G until $F(N)$ is sufficiently close to 1, for large N (we shall take $N = 20$). This shooting method is highly sensitive to the initial conditions, since the ODE is unstable at $\eta = \infty$, $F = 1$. This can be seen by letting $F = 1 - \theta$, with $0 < \theta \ll 1$, so that upon linearising (5.105) we find $\theta'' \sim 3\theta$, and hence $\theta \sim A_0 e^{\sqrt{3}\eta} + B_0 e^{-\sqrt{3}\eta}$. In Figure 5.7, we show a plot of F for varying λ.

In the case where $\lambda = 0$, a first integral of (5.105) can be obtained, and this takes the form

$$\frac{dF}{d\eta} = \sqrt{\frac{F^4}{6} - \frac{2F}{3} + \frac{1}{2}}, \quad F(0) = 0, \tag{5.106}$$

where the positive square root is taken because F is an increasing positive function. Since $F(5;0) \sim 0.99$, then when $\lambda = 0$ the boundary layer is of width $\eta \sim 5$, which in radial co-ordinates is $R \sim 5/\sqrt{\kappa}$.

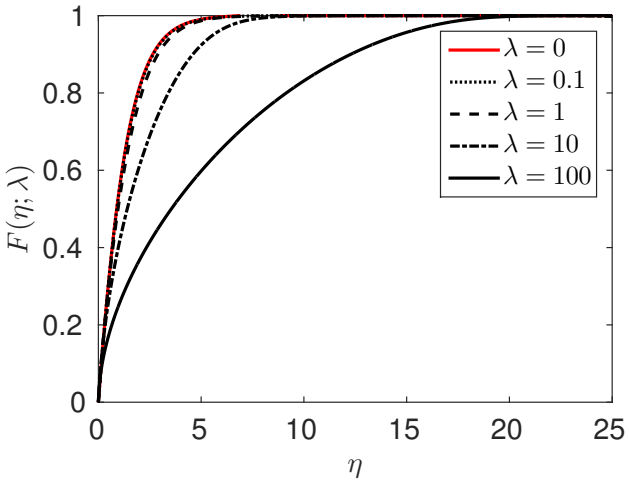


Figure 5.7: Numerical plots of $F(\eta;\lambda)$, for varying λ.

If the parameter λ is increased such that $\lambda \gg 1$, then at leading order (5.105) becomes

$$\frac{d^2}{d\eta^2}\left(\frac{F^2}{2} - \frac{F^3}{3}\right) = 0. \tag{5.107}$$

Integrating (5.107) twice gives $\frac{F^2}{2} - \frac{F^3}{3} = A_1\eta + B_1$, and so F cannot satisfy both boundary conditions $F(0) = 0$ and $F(\infty) = 1$.

Returning to study h and v, using $h(0,\tau) = F(0) = 0$ with (5.103) and (5.104) gives

$$v = -s\frac{ds}{d\tau}\frac{dF}{d\eta}, \quad \frac{\partial v}{\partial \eta} = \frac{s}{3}\frac{ds}{d\tau}, \text{ at } \eta = 0. \tag{5.108}$$

In order to match s from the right hand side, we let $\omega(R,\tau) = 1 + Y(\tau)(R-1)$, with

$$\omega(R,\tau) = \frac{v(\eta,\tau)}{\sqrt{\kappa}}, \quad \frac{\partial \omega(R,\tau)}{\partial R} = \frac{\partial v(\eta,\tau)}{\partial \eta}. \tag{5.109}$$

Thus, by continuity of v and ω, and their derivatives, it is evident that

$$1 + Y(\tau)(s-1) = -\frac{1}{\sqrt{\kappa}}s\frac{ds}{d\tau}\frac{dF}{d\eta}(0), \quad \frac{s}{3}\frac{ds}{d\tau} = Y(\tau). \tag{5.110}$$

Taking the limit $\kappa \to \infty$, and assuming that $F'(0) = o(\sqrt{\kappa})$, so that $F'(0)/\sqrt{\kappa} \to 0$ as $\kappa \to \infty$, we have that $1 + Y(\tau)(s-1) = 0$, and obtain

$$\omega(R,t) = \frac{R - s(\tau)}{1 - s(\tau)}, \tag{5.111}$$

along with the ODE for s,

$$\frac{ds}{d\tau} = -\frac{3}{s(s-1)}, \quad s(0) = 1. \tag{5.112}$$

The ODE (5.112) is solved by the implicit cubic

$$\frac{s(\tau)^3}{3} - \frac{s(\tau)^2}{2} + \frac{1}{6} = 3\tau, \tag{5.113}$$

which in terms of t is

$$\frac{s(t)^3}{3} - \frac{s(t)^2}{2} + \frac{1}{6} = \frac{3t}{\kappa}. \tag{5.114}$$

This result is encouraging, since it is of the same form as the implicit cubic relationship in (5.20), taken in the limit $\hat{\beta} \to \infty$ with $\hat{\beta}/\hat{\gamma}$ finite, and hence the slow diffusion limit of our homogenised model matches the slow diffusion limit of the shrinking core model, up to a timescale. This diffusion-controlled regime is discussed in more depth in Section 5.7.

The time $t = t^*$ for the reaction to be completed is found by setting $s(t^*) = 0$ in (5.114), to give $t^* = \frac{\kappa}{18}$, which, interestingly, is independent of λ. This parameter influences the shape of b in the boundary layer (as seen in Figure 5.7), but has no influence on the time for the reaction to finish. Numerical simulations support this claim, with a relative variation in t^* of 1.03% between $\lambda = 0$ and $\lambda = 10$ for $\kappa = 1000$. However, a larger variation is found when $\lambda \sim \sqrt{\kappa} \sim 31.6$. We can determine when the assumption that $F'(0) = o\left(\sqrt{\kappa}\right)$ is not suitable, and so (5.111) no longer holds, since $F'(0)/\sqrt{\kappa} \not\to 0$ in the limit $\kappa \to \infty$. When $\lambda = 0$, then $F'(0) = \frac{1}{\sqrt{2}}$ which is sufficient. For general $\lambda > 0$ we have

$$F''(0) + F'(0)^2\lambda = -\frac{1}{3}, \tag{5.115}$$

which means that $F''(0) < 0$ and that for large λ we need either $F'(0) = \mathcal{O}(\lambda^{-1/2})$ and $F''(0) = \mathcal{O}(1)$, or $F'(0) = \mathcal{O}(\lambda^{-1})$ and $F''(0) = \mathcal{O}(\lambda^{-1})$. Thus the analysis can break down for $\lambda = \mathcal{O}(\frac{1}{\sqrt{\kappa}})$.

We thus have leading order solutions for b and W, where $\eta = \sqrt{\kappa}\,(s(t) - R)$, which are given by

$$b(R,t) = \begin{cases} 0, & R \geq s(t), \\ F(\eta), & R \leq s(t), \end{cases} \tag{5.116a}$$

$$W(R,t) = \begin{cases} \frac{R-s(t)}{1-s(t)}, & R \geq s(t), \\ \frac{1}{\sqrt{\kappa}}\frac{3}{1-s(t)}F'(\eta)\left(1 + \lambda F(\eta)(1-F(\eta))\right), & R \leq s(t). \end{cases} \tag{5.116b}$$

The extent of reaction $X(t)$ is found from (5.72) by noting $b \to \mathcal{H}(s(t)-R)$ as $\kappa \to \infty$, where $\mathcal{H}$ denotes the Heaviside function, to give

$$X(t) \sim 1 - s(t)^3. \tag{5.117}$$

Asymptotic results for $s(t)$ and $X(t)$ are compared to numerics in Figure 5.8.

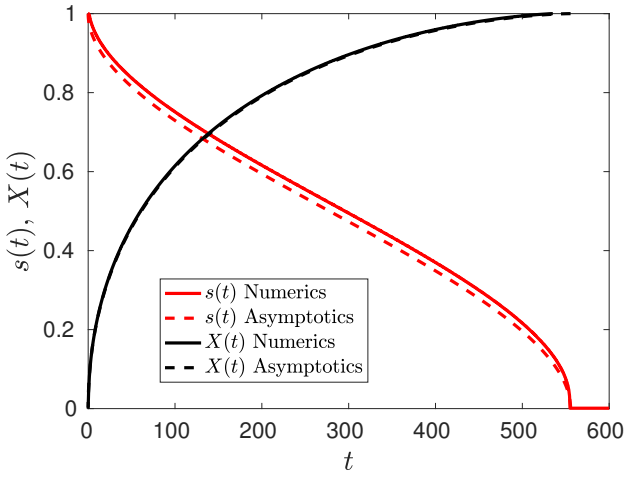


Figure 5.8: Comparison of numerics and asymptotics for $s(t)$ (red) and $X(t)$ (black) for $\kappa = 10^4$ and $\lambda = 0$.

5.5.2.3 Summary of Asymptotics

The system (5.63) - (5.66) arises from considering the distinguished limit $D_S/D_V = \delta^2\nu$ in Section 5.4, and is the most physically relevant model. This model depends on two parameters κ and λ, and has been analysed in the limit $\kappa \to 0$ and $\kappa \to \infty$, with $\lambda = \mathcal{O}(1)$ in each case. When $\kappa \to 0$, we find that the system is spatially homogeneous to leading order. Taking $\lambda = 0$ reduces the complexity of the resulting solutions. For large κ we find a sharp inward-moving wave, separating a reacted exterior from an unreacted core, as with the canonical shrinking core problem discussed in Section 5.2, but with a boundary layer ahead of the interface of size $R = \mathcal{O}\left(1/\sqrt{\kappa}\right)$. Taking $\lambda = 0$ results in a first order ODE to be solved for the shape of b in this boundary layer, rather than a second order ODE when $\lambda > 0$.

In each case, we find a leading order prediction of the overall time for reaction, $t = t^*$. In the limit $\kappa \to 0$, we have $t^* \sim 1 + \lambda/6$, whereas in the limit $\kappa \to \infty$, we have $t^* \sim \kappa/18$. Note that these can be combined to give an overall prediction for t^*, covering the whole range of κ, which is $t^* = 1 + \lambda/6 + \kappa/18$. This combination matches well with numerics, as seen in Figure 5.9.

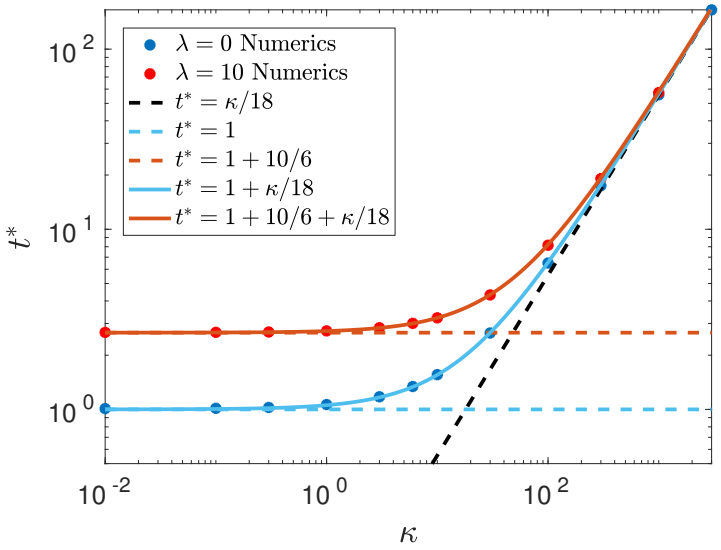


Figure 5.9: Comparison of asymptotics and numerics for time for complete reaction t^* for varying κ, with $\lambda = 0$ in blue and $\lambda = 10$ in red. The plot is on a logarithmic scale. Note how the combined asymptotic result $t^* = 1 + \lambda/6 + \kappa/18$ matches well with the numerics for both values of λ.

5.6 Influence of product gas

In Sections 5.2 - 5.5, we considered a simplified physical set-up where the partial pressure of the product gas F has no influence on the reaction. However, we can easily extend the homogenisation in Section 5.3 to include the effect of binary gas diffusion, and determine the influence on the overall reaction rate, with P and Q referring to the partial pressures of gases A and F, respectively. This is important, since for some reactions the counter-diffusion of the product gas can be the rate limiting step, slowing down the transport of the reactant gas to the reaction fronts. At the microscale reaction interface, one mole of the reactant gas A forms σ_2 moles of the product gas F, according to the reaction (5.1).

Although several models for binary gas diffusion are commonly used [20, 33, 36], we utilise a simple linear Fickian model here, since it allows a straightforward extension of our findings. We assume that dimensionless pressures P^V and Q^V exist in ω_V, while P^S and Q^S exist in ω_S. In both ω_V and ω_S, the diffusion equations will be of the form

$$\zeta \frac{\partial}{\partial t} \begin{pmatrix} P \\ Q \end{pmatrix} = \nabla \cdot \left(\begin{pmatrix} 1 & d_1 \\ d_2 & d_3 \end{pmatrix} \nabla \begin{pmatrix} P \\ Q \end{pmatrix} \right) = \begin{pmatrix} 1 & d_1 \\ d_2 & d_3 \end{pmatrix} \nabla^2 \begin{pmatrix} P \\ Q \end{pmatrix}, \tag{5.118}$$

for some parameter ζ, which is different in each region. We also assume that the diffusivities d_1, d_2, and d_3 are all $\mathcal{O}(1)$ and that the determinant of the diffusion tensor, $d_3 - d_1 d_2$, is $\mathcal{O}(1)$ in size and positive, to ensure positive definiteness of the matrix. If this were not true, the problem would be degenerate, for example in the specific singular case $d_1 = d_2 = d_3 = 0$ the pressure of product gas would remain constant, corresponding to the single gas case considered earlier.

Upon pre-multiplying (5.118) by the matrix inverse (providing the determinant is non-zero), we obtain the rotated equations

$$\frac{\zeta}{d_3 - d_1 d_2} \begin{pmatrix} d_3 & -d_1 \\ -d_2 & 1 \end{pmatrix} \frac{\partial}{\partial t} \begin{pmatrix} P \\ Q \end{pmatrix} = \nabla^2 \begin{pmatrix} P \\ Q \end{pmatrix}. \tag{5.119}$$

Hence, for the top-left entry in the diffusion tensor in ω_V being the dimensional diffusion scale $D_{11} \coloneqq D_V$, then letting $D_S/D_V = \nu\delta^n$ we obtain the system

$$\frac{\epsilon}{d_3 - d_1 d_2} \begin{pmatrix} d_3 & -d_1 \\ -d_2 & 1 \end{pmatrix} \frac{\partial}{\partial t} \begin{pmatrix} P^V \\ Q^V \end{pmatrix} = \nabla^2 \begin{pmatrix} P^V \\ Q^V \end{pmatrix}, \quad \mathbf{y} \in \omega_V, \tag{5.120}$$

$$\frac{\epsilon/\delta^n\nu}{d_3 - d_1 d_2} \begin{pmatrix} d_3 & -d_1 \\ -d_2 & 1 \end{pmatrix} \frac{\partial}{\partial t} \begin{pmatrix} P^S \\ Q^S \end{pmatrix} = \nabla^2 \begin{pmatrix} P^S \\ Q^S \end{pmatrix}, \quad \mathbf{y} \in \omega_S, \tag{5.121}$$

$$\begin{pmatrix} P^V \\ Q^V \end{pmatrix} = \begin{pmatrix} P^S \\ Q^S \end{pmatrix}, \quad \nabla \begin{pmatrix} P^V \\ Q^V \end{pmatrix} = \nu\delta^n \nabla \begin{pmatrix} P^S \\ Q^S \end{pmatrix}, \quad \text{at } r = a, \tag{5.122}$$

$$-\delta^n \nu \begin{pmatrix} 1 & d_1 \\ d_2 & d_3 \end{pmatrix} \nabla \begin{pmatrix} P^S \\ Q^S \end{pmatrix} \cdot \mathbf{n} + \epsilon \begin{pmatrix} P^S \\ Q^S \end{pmatrix} \frac{\partial b}{\partial t} = \delta\beta P^S \begin{pmatrix} -1 \\ \sigma_2 \end{pmatrix}, \text{ at } r = b, \tag{5.123}$$

$$\frac{\partial b}{\partial t} = -\gamma P^S, \quad \text{at } r = b. \tag{5.124}$$

We use the usual multiple scales definitions (5.30) and (5.31), and assume that ϵ is sufficiently small so as to not enter the analysis. With this assumption, we find that the problems for the reactant pressure P and product pressure Q decouple. The systems for P^V, Q^V, P^S, and Q^S are given by

$$0 = \nabla_{\mathbf{y}}^2 P^V + \delta\left(\nabla_{\mathbf{x}} \cdot \nabla_{\mathbf{y}} P^V + \nabla_{\mathbf{y}} \cdot \nabla_{\mathbf{x}} P^V\right) + \delta^2 \nabla_{\mathbf{x}}^2 P^V, \quad \mathbf{y} \in \omega_V, \tag{5.125}$$

$$0 = \nabla_{\mathbf{y}}^2 Q^V + \delta\left(\nabla_{\mathbf{x}} \cdot \nabla_{\mathbf{y}} Q^V + \nabla_{\mathbf{y}} \cdot \nabla_{\mathbf{x}} Q^V\right) + \delta^2 \nabla_{\mathbf{x}}^2 Q^V, \quad \mathbf{y} \in \omega_V, \tag{5.126}$$

$$0 = \nabla_{\mathbf{y}}^2 P^S + \delta\left(\nabla_{\mathbf{x}} \cdot \nabla_{\mathbf{y}} P^S + \nabla_{\mathbf{y}} \cdot \nabla_{\mathbf{x}} P^S\right) + \delta^2 \nabla_{\mathbf{x}}^2 P^S, \quad \mathbf{y} \in \omega_S, \tag{5.127}$$

$$0 = \nabla_{\mathbf{y}}^2 Q^S + \delta\left(\nabla_{\mathbf{x}} \cdot \nabla_{\mathbf{y}} Q^S + \nabla_{\mathbf{y}} \cdot \nabla_{\mathbf{x}} Q^S\right) + \delta^2 \nabla_{\mathbf{x}}^2 Q^S, \quad \mathbf{y} \in \omega_S, \tag{5.128}$$

$$P^V = P^S, \quad Q^V = Q^S, \quad \text{at } \mathbf{y} = a\mathbf{e}_r, \tag{5.129}$$

$$\nabla_{\mathbf{y}} P^V + \delta \nabla_{\mathbf{x}} P^V = \delta^n \nu \nabla_{\mathbf{y}} P^S + \delta^{n+1} \nu \nabla_{\mathbf{x}} P^S, \text{ at } \mathbf{y} = a\mathbf{e}_r. \tag{5.130}$$

$$\nabla_{\mathbf{y}} Q^V + \delta \nabla_{\mathbf{x}} Q^V = \delta^n \nu \nabla_{\mathbf{y}} Q^S + \delta^{n+1} \nu \nabla_{\mathbf{x}} Q^S, \text{ at } \mathbf{y} = a\mathbf{e}_r, \tag{5.131}$$

$$\begin{aligned} -\nabla_{\mathbf{y}} P^S \cdot \mathbf{n}_{\mathbf{y}} + \delta \left(\nabla_{\mathbf{y}} P^S \cdot \nabla_{\mathbf{x}} b(\mathbf{x}, t) - \nabla_{\mathbf{x}} P^S \cdot \mathbf{n}_{\mathbf{y}} \right) + \delta^2 \nabla_{\mathbf{x}} P^S \cdot \nabla_{\mathbf{x}} b(\mathbf{x}, t) \\ = -\delta^{2-n} \frac{d_3 + d_1 \sigma_2}{d_3 - d_1 d_2} \frac{\beta}{\nu} P^S \| \mathbf{n}_{\mathbf{y}} - \delta \nabla_x b(\mathbf{x}, t) \|, \text{ at } \mathbf{y} = b(\mathbf{x}, t)\mathbf{e}_r, \end{aligned} \tag{5.132}$$

$$\begin{aligned} -\nabla_{\mathbf{y}} Q^S \cdot \mathbf{n}_{\mathbf{y}} + \delta \left(\nabla_{\mathbf{y}} Q^S \cdot \nabla_{\mathbf{x}} b(\mathbf{x}, t) - \nabla_{\mathbf{x}} Q^S \cdot \mathbf{n}_{\mathbf{y}} \right) + \delta^2 \nabla_{\mathbf{x}} Q^S \cdot \nabla_{\mathbf{x}} b(\mathbf{x}, t) \\ = \delta^{2-n} \frac{d_2 + \sigma_2}{d_3 - d_1 d_2} \frac{\beta}{\nu} P^S \| \mathbf{n}_{\mathbf{y}} - \delta \nabla_x b(\mathbf{x}, t) \|, \text{ at } \mathbf{y} = b(\mathbf{x}, t)\mathbf{e}_r, \end{aligned} \tag{5.133}$$

where we have obtained (5.132) and (5.133) from (5.123) by pre-multiplying by the inverse of the diffusion matrix. We have that P^V and Q^V are periodic on $\partial\omega_o$, which is the outside boundary of the cell. The interface $b(\mathbf{x}, t)$ moves according to the equation

$$\frac{\partial b(\mathbf{x}, t)}{\partial t} = -\gamma P^S, \text{ at } \mathbf{y} = b(\mathbf{x}, t)\mathbf{e}_r, \tag{5.134}$$

with initial condition $b(\mathbf{x}, 0) = a$.

Introducing the parameter

$$\sigma := \frac{d_3 + d_1 \sigma_2}{d_3 - d_1 d_2}, \tag{5.135}$$

for stoichiometric coefficient σ_2 given in (5.1), then the system (5.125), (5.127), (5.129), (5.130), (5.132), and (5.134), is the same system for P as in (5.32) - (5.36), but with β replaced by $\sigma\beta$. Thus, upon expanding P^V and P^S in terms of δ, we would obtain the same homogenised equations as before, but with $\sigma\beta$ in place of β. Note that $\sigma = 1$ corresponds to $d_1 = 0$ (since $\sigma_2, d_2 \geq 0$). In most practical situations the off-diagonal 'cross-diffusion' terms d_1 and d_2 are equal. Thus, when there is no diffusive interaction between the product and reactant gas, we have the same models as if there were no reactant gas.

We can include binary gas diffusion into the homogenised models by adapting the composite model of equations (5.70) and (5.71) to

$$\nabla \cdot \left((\bar{D_e^V} + \frac{D_S}{D_V} \bar{D_e^S}) \nabla p \right) = -\kappa\sigma \frac{\partial}{\partial t} \left(\frac{b^3}{3} \right), \quad 0 \leq R \leq 1, \quad t \geq 0, \tag{5.136a}$$

$$\frac{\partial b}{\partial t} = -\frac{p}{1 + \sigma a \beta \frac{D_V}{D_S} \delta^2 b(1 - b)}, \quad 0 \leq R \leq 1, \quad t \geq 0. \tag{5.136b}$$

Hence, all of the asymptotic results from Section 5.5.2 still hold, but with the alteration $\kappa \to \sigma\kappa$ and $\lambda \to \sigma\lambda$, and in particular the overall time for reaction is predicted by

$$t^* = 1 + \frac{\sigma\lambda}{6} + \frac{\sigma\kappa}{18}. \tag{5.137}$$

Note that $\sigma \geq 1$ for a positive definite diffusion tensor, so including the reactant gas in the model will always slow down the reaction time. One could consider the singular limit $\sigma \to \infty$, but we do not examine this here, as it is not interesting for our physical results.

5.7 Comparison to existing results

We now compare our findings to those already present in literature. In Section 5.7.1, we compare the shrinking core model of Section 5.2 to existing formulations, noting the simplifications when the limiting step in the process is diffusion or the chemical reaction. In Section 5.7.2, we comment on the times for complete particle reaction found from asymptotic analysis in Section 5.5.2 of the homogenised model equations given in Section 5.3. We then comment on Sohn's 'law of additive reaction times' [89] in Section 5.7.3, and finally we discuss how our homogenised model fits in with other continuum models for gas-solid reactions in Section 5.7.4.

5.7.1 Comparison with existing shrinking core models

The shrinking core model in Section 5.2 is found in the literature [35, 70, 90, 97, 112], where it is often written as a relationship between time, t, and the extent of reaction $X(t)$. This relationship is written in the form $t = h(X)$. An ODE can be found for $X(t)$ upon differentiating this relationship with respect to t, and rearranging. Doing so, we have

$$\frac{dX}{dt} = \frac{1}{h'(X)}. \tag{5.138}$$

The form of h is dependent on the particle geometry and the particular controlling mechanism. In this chapter we have considered models for a spherical geometry. A distinction is often made between when the reaction is controlled by diffusion through the product layer, and when it is controlled by the chemical reaction at the interface $l(t)$. In each case, the slowest process is the controlling factor. When the reaction is diffusion-controlled, h is given by h_d, and when the chemical reaction controls the process h is given by h_r, where typical functional forms for each are given in [35, 70, 90, 97, 112] by

$$h_d = \frac{1}{k_d}\left(1 - 3(1-X)^{2/3} + 2(1-X)\right), \tag{5.139a}$$

$$h_r = \frac{1}{k_r}\left(1 - (1-X)^{1/3}\right). \tag{5.139b}$$

Thus the time for complete reaction t^* in each case is given by $t_d^* = k_d^{-1}$ and $t_r^* = k_r^{-1}$, respectively. Gbor and Jia [35] give

$$k_d = \frac{6\sigma_1 D_{\text{eff}} C_{A0}}{\rho R_p^2}, \quad k_r = \frac{\sigma_1 k_1 C_{A0}^n}{\rho R_p}, \tag{5.140}$$

where D_{eff} [m^2/s] is the effective diffusion coefficient of gas A through the product layer, C_{A0} [mol/m^3] is the concentration of gas A outside the particle, ρ [mol/m^3] is the molar density of B in the solid (the same as $B_0 = \rho_B/M_B$), n is the order of reaction with respect to A, and k_1 [mol$^{(1-n)}$m$^{(3n-2)}$s^{-1}] is the chemical reaction rate constant. Similar constants for k_r and k_d are given in [70]. Szekely et al. [97] include the equilibrium constant K_E, concentration of product gas F outside the particle C_{F0} [mol/m^3], and reaction order m with respect to F, to write

$$k_d = \frac{K_E}{1+K_E}\left(C_{A0} - \frac{C_{F0}}{K_E}\right)^+ \frac{6bD_{\text{eff}}}{\rho R_p^2}, \quad k_r = \frac{\sigma_1 k_1}{\rho R_p}\left(C_{A0}^n - \frac{C_{F0}^m}{K_E}\right)^+, \tag{5.141}$$

where we have added the $^+$ notation to indicate that k_d and k_r cannot be negative. Equation (5.141) is a more general result than (5.140), including thermodynamic effects in the reaction model. However, to keep our model somewhat simple, we ignored these effects in our first order reaction model (5.7).

Note that considering limits of the shrinking core model (5.20), we obtain the results in (5.139a) and (5.139b). Since $l(t) = (1-X)^{1/3}$, then in the limit $\hat{\beta} \to 0$ with constant external dimensionless pressure p_a, we obtain the dimensionless relationship

$$l(t) = 1 - \hat{\gamma} p_a t, \tag{5.142}$$

which rearranges to (5.139b), with k_r as in (5.140). This limit corresponds to infinitely fast diffusion, and so the process is reaction controlled. Instead taking (5.20) in the limit $\hat{\beta} \to \infty$, with $\hat{\beta}/\hat{\gamma}$ finite and for constant pressure p_a, we obtain

$$\frac{l(t)^3}{3} - \frac{l(t)^2}{2} + \frac{1}{6} = \frac{\hat{\gamma}}{\hat{\beta}} p_a t, \tag{5.143}$$

which rearranges to (5.139a), with k_d as in (5.140). This limit corresponds to the kinetic rate $k \to 0$, so that the process is diffusion-controlled. Thus, the simple model outlined in Section 5.2 supports the diffusion-limited and reaction-limited simplifications found in literature.

5.7.2 Physical results from our asymptotics

Composing the original dimensionless time $\hat{t} = t/\tau_s$ (given in (5.22)) and the timescale $\bar{t} = (\gamma p_a/a)\hat{t}$ (given in (5.61)) for the model arising from homogenisation, we then use the dimensionless time $t^* = 1 + \sigma\lambda/6 + \sigma\kappa/18$ to obtain the prediction of the dimensional time for complete reaction $t = t^*_{\text{dim}}$ [s], as

$$t^*_{\text{dim}} = \frac{aR_p}{\sigma_1 k p_a P_{\text{TOT}}} + \sigma\frac{a^2 R_p^2 B_0(k_m/\delta)}{6\sigma_1 k C_A}\frac{\delta^2}{D_S} + \sigma\frac{4\pi a^3}{3D_e}\frac{R_p^2 B_0(k_m/\delta)}{6\sigma_1 k C_A D_V}. \tag{5.144}$$

The first two terms correspond to the small κ limit where diffusion in the void space ω_V is fast compared to the kinetic rate, and the third term corresponds to the large κ limit, where diffusion in the void space is the slow, rate-limiting process. The first term represents the chemical reaction at the microscale granular interface, while the second term represents diffusion through the microscale ω_S solid product matrix. We thus have that the total reaction time is the sum of the time under the limit of three effects, which are the kinetic rate, the microscale diffusion through ω_S, and the macroscale diffusion through ω_V.

Results from existing models only account for the first and third terms. Assuming that $k_m = \delta k$, then for small δ the second term will be negligible. We can relate the time for kinetic control, t^*_1, and pore-diffusion control, t^*_2, to $t^*_r = k_r^{-1}$ and $t^*_d = k_d^{-1}$ respectively, with k_r and k_d found by Gbor and Jia [35] and given in (5.140), through

$$t^*_1 = \sigma\frac{aRB_0}{\sigma_1 k_1 C_A} = \sigma a t^*_r, \quad t^*_2 = \sigma\frac{4\pi a^3}{3D_e}\frac{D_{\text{eff}}}{D_V}t^*_d. \tag{5.145}$$

Here, D_V [m^2/s] is the diffusivity of gas A in a void space, which is a measurable quantity. D_{eff} [m^2/s] is the effective diffusivity of gas A throughout the porous macroscale particle, which is in theory measurable for each type of particle used in experiments relevant to industrial applications. The parameter a is the radius of the reactant solid spherical grain in the microscale, assuming without loss of generality that the microscale cell is of unit volume. Since we have assumed a cubic packing arrangement, then letting each cell be a unit cube we have $a = 1/2$. The effective diffusivity D_e is given by (5.58) (for $D_e = D(\mathbf{x})$). For a cubic packing with $a = 1/2$, Bruna and Chapman [13] have found $D_e = 0.72$ using COMSOL Multiphysics (see Figure 3b of their paper). If a different packing arrangement were used, then the cell problem discussed in Section 5.3 would change accordingly, and a different homogenised model could arise.

Writing the diffusion-controlled cubic (5.114) in terms of the shrinking core timescale $\hat{t}$, and including the influence of the product gas, we obtain

$$\frac{s(\hat{t})^3}{3} - \frac{s(\hat{t})^2}{2} + \frac{1}{6} = \frac{3D_e}{4\pi a^3 \sigma}\frac{\gamma}{\beta} p_a \hat{t}. \tag{5.146}$$

This is the same as the cubic for $l(t)$ in (5.143), up to the timescale, and hence our homogenised model gives the same behaviour as the shrinking core model for diffusion-controlled reactions.

5.7.3 Comparison with the law of additive reaction times

Sohn [89] introduced the 'law of additive reaction times.' This states that, for a shrinking core reaction, the relationship between time and degree of conversion X is the linear sum of the relationships in the diffusion-controlled limit and reaction-controlled limit. The ODE (5.20) in Section 5.2 supports this law, since the diffusion limit ($\hat{\beta} \to \infty$ with $\hat{\beta}/\hat{\gamma}$ finite) and the reaction limit ($\hat{\beta} \to 0$) combine to give the relationship between $l(t)$ and t. The total time for reaction in (5.21) is the sum of the total times in these limits (being $\hat{\beta}/6\hat{\gamma}p_a$ and $1/\hat{\gamma}p_a$, respectively, for constant pressure p_a).

In Section 5.5.2 we analysed a homogenised model developed in Section 5.3, which allows for a diffuse reaction region. In Figure 5.9, we plotted the total time for reaction from the asymptotic limits of $\kappa \to \infty$ and $\kappa \to 0$, which correspond to the $\hat{\beta} \to \infty$ and $\hat{\beta} \to 0$ limits discussed above (namely diffusion and reaction-controlled processes respectively). We find that adding these reaction times together gives a good fit with numerics, adding further weight to Sohn's law.

5.7.4 Continuum models

Melchiori and collaborators (in [60, 61]) develop continuum models and compare them with canonical shrinking core models. Their continuum models are of the form

$$\epsilon_M \frac{\partial C_A}{\partial t} = D_M \nabla^2 C_A - \sigma_1 k_M \frac{C_B^\alpha}{C_{B0}^\alpha} C_A, \quad \frac{\partial C_B}{\partial t} = -k_M \frac{C_B^\alpha}{C_{B0}^\alpha} C_A, \tag{5.147}$$

where we have relabelled parameters ϵ_M, D_M, and k_M to avoid confusion with parameters in this chapter; C_A and C_B are the molar concentrations of gas A and solid B (which we have relabelled to fit with notation in this chapter) and C_{B0} is the initial concentration of solid B. The index α is a general power of the reaction. Since our $b(R,t)$ relates to their C_B through $b^3 = C_B/C_{B0}$, then in the quasi-steady limit

$\epsilon_M \to 0$ we obtain the model with equations (5.63) and (5.66) developed in Section 5.3 and analysed in Section 5.5.2, but with $\alpha = 2/3$ and $\lambda = 0$. They also note in [60, 61] that in the kinetic regime their continuum model gives the same results as a shrinking core model when $\alpha = 2/3$, but that there are differences for any other reaction order. Thus our choice of a first order reaction rate (given in (5.7)), which corresponds to $\alpha = 2/3$ in (5.147), allows this range of sharp interface shrinking core and spatially-homogeneous continuum model behaviour.

In addition, in our model we have included the parameter λ, which allows for a range of behaviour across the diffusive boundary region in the diffusion-controlled reaction arising from the large κ limit (see Figure 5.7). Our model also allows for a richer set of reaction behaviour for general values of κ (see Figure 5.5) and has the ability to better describe experimental results.

Szekely et al. [97] develop a model for porous solids of the form

$$\nabla^2 p = \mu^2 p b^{F_g - 1}, \quad \frac{\partial b}{\partial t} = -p, \tag{5.148}$$

where we have relabelled variables to avoid confusion with those used in this chapter. The key difference from the equations (5.63) and (5.66) with $\lambda = 0$ is the 'shape-factor' F_g, which is given by the dimension of the geometry of interest. For a sphere $F_g = 3$, for a cylinder $F_g = 2$, and for a one-dimensional slab $F_g = 1$. This agrees with (5.66), which has been derived for a three-dimensional particle. Note that if we considered a one or two dimensional model, then we would replace $b^3/3$ in (5.66) with b or $b^2/2$ respectively, as done in (5.148). In the case of a slab ($F_g = 1$), analytical solutions can be found to (5.148) without the need for asymptotics.

5.8 Coupling to a furnace model

We have developed a model of a gas-solid reaction inside a porous sphere, which will have general applications. However, this thesis is focussed on the behaviour of silicon furnaces. We thus seek to couple this reaction model to the one-dimensional pilot furnace model developed in Chapter 2. This means finding a macroscale reaction rate for reaction R_1 between solid carbon and silicon monoxide gas, given in (2.1). To assist the reader, we show this reaction again as

$$\mathrm{SiO(g)} + 2\mathrm{C(s)} \xrightarrow{R_1} \mathrm{SiC(s)} + \mathrm{CO(g)}. \tag{5.149}$$

In Chapter 2, we used the dimensionless reaction rate, first given in (2.34),

$$r_1 = \xi_1 \mathrm{r_C C_C} \left(P_{\mathrm{SiO}} - P_{\mathrm{SiO,equ},1}\right)^+, \tag{5.150}$$

for rate constant ξ_1, reactivity of carbon $\mathrm{r_C}$, effective concentration $\mathrm{C_C}$, and partial pressure difference from equilibrium $(P_{\mathrm{SiO}} - P_{\mathrm{SiO,equ,1}})^+$. In practice, the reactivity of carbon particles depends on factors such as the particle size and porosity, and will change throughout the process. However, for simplicity, we treated $\mathrm{r_C}$ as a constant in simulations, and in the asymptotic analysis of the model in Chapter 3. However, we want to use the results in this chapter to determine an improved macroscale rate for r_1.

We suppose that the carbon content in the furnace is made entirely of spheres, which are partially converted into silicon carbide. Let the number density of these spheres be such that there are n_{C} per 1 m^3 in the furnace, and suppose further that these spheres are of the same constant dimensional radius, R. We note that if we use a canonical shrinking core model, discussed in Section 5.2, with a sharp interface between carbon and silicon carbide, then the volume fraction of carbon in the furnace is given by

$$\theta_{\mathrm{C}} = n_{\mathrm{C}}(z,t)\frac{4\pi}{3}l(z,t)^3R^3, \tag{5.151}$$

where $l(z,t)$ is the dimensionless radius of the inner core of carbon particles at height z and time t. Then, by (2.6), the initial dimensional concentration of carbon scales with the initial volume fraction. This gives us the condition for the dimensionless concentration, namely

$$\mathrm{C_C}(z,t) = l(z,t)^3. \tag{5.152}$$

We thus have that the extent of the reaction is given by

$$X(z,t) = 1 - l(z,t)^3 = 1 - \mathrm{C_C}(z,t). \tag{5.153}$$

In the model SiMod [106], Wasbø and Hammervold write their reactivity of carbon as being proportional to the time rate of change of X. We can utilise similar ideas here. We have the first row in the matrix equation (2.32) describing the change in the concentration of carbon, namely

$$\frac{\partial \mathrm{C_C}}{\partial t} = -2r_1 - r_5. \tag{5.154}$$

This uses the assumption that solid particles do not move in the furnace. If we look at the rate of change of the concentration of carbon due to r_1 alone, we have

$$r_1 = -\frac{1}{2}\frac{\partial \mathrm{C_C}}{\partial t}. \tag{5.155}$$

By (5.152), we thus have

$$r_1 = -\frac{3}{2}l^2\frac{\partial l}{\partial t}. \tag{5.156}$$

We have the ODE (5.19), which we could solve to find $\frac{\partial l}{\partial t}$, and then substitute into (5.156). However, since the functional form of $\frac{\partial l}{\partial t}$ is given from the right hand side of (5.156), we do not need to solve the ODE, but can instead re-write (5.156) as

$$r_1 = \frac{3}{2}\hat{\gamma}\frac{l(z,t)^2}{1+\hat{\beta}l(z,t)(1-l(z,t))}P_{\mathrm{SiO}}(z,t). \tag{5.157}$$

Further, we can utilise the dimensionless scaling $l = \mathrm{C_C}^{1/3}$ from (5.152) to obtain the macroscale rate

$$r_1(z,t) = \frac{3}{2}\hat{\gamma}\frac{\mathrm{C_C}^{2/3}}{1+\hat{\beta}\mathrm{C_C}^{1/3}(1-\mathrm{C_C}^{1/3})}P_{\mathrm{SiO}}(z,t). \tag{5.158}$$

Thus this rate does not have a linear dependence on the concentration of carbon, as used in the original rate given in (5.150), but the function is more complex. The partial pressure difference from equilibrium can easily be included, so that the partial pressure term P_{SiO} in (5.158) is replaced with $(P_{\mathrm{SiO}} - P_{\mathrm{equ,SiO,1}})^+$. Note that this rate does not depend upon the history of the carbon particle, but only the current concentration and external pressure of SiO.

If, instead, we wanted to couple the homogenised model to the one-dimensional furnace model, we could use the system (5.63) - (5.66). Although there is not a sharp interface in general in the model, we can still use (5.153) to write

$$r_1 = -\frac{1}{2}\frac{\partial \mathrm{C_C}}{\partial t} = \frac{1}{2}\frac{\partial X}{\partial t}. \tag{5.159}$$

With this approach, we would have to solve PDEs at each timestep for the local variation in the spherical particles of carbon and silicon carbide. Thus, for every discretised macroscale grid point for height z, we would have a corresponding discretised local mesh for radius R, which would then tell us how the macroscale reaction r_1 is evolving. Clearly this increases the computational complexity, and thus simulation run time, drastically.

An alternative is to use the asymptotic results derived in Section 5.5.2. Experimental evidence suggests that the reaction between carbon and silicon monoxide is diffusion limited, so that κ is large. Thus we could determine $\frac{\partial X}{\partial t}$ directly from (5.117) and (5.114), giving

$$\frac{\partial X}{\partial t} = -3s^2\frac{\partial s}{\partial t} = -\frac{9}{\kappa}\frac{s^2}{s^2-s}, \tag{5.160}$$

where s acts the same as l in the canonical shrinking core model. Incorporating variable external pressure we would thus have

$$r_1 = \frac{9}{2\kappa}\frac{\mathrm{C_C}^{2/3}}{\mathrm{C_C}^{1/3}(1-\mathrm{C_C}^{1/3})}P_{\mathrm{SiO}}. \tag{5.161}$$

This form of the reaction rate causes difficulties at early time when $\mathrm{C_C^{1/3}} \sim 1$ since r_1 would not be finite. The reaction would proceed infinitely quickly initially because we have assumed the process is diffusion controlled, but there is no silicon carbide layer to diffuse through at the start. We avoid this by using the shrinking core formulation (5.158), so that our new reaction rate is

$$r_1 = \frac{3\hat{\gamma}}{2} \frac{\mathrm{C_C^{2/3}}}{1 + \hat{\beta}\mathrm{C_C^{1/3}}(1 - \mathrm{C_C^{1/3}})} \left(P_{\mathrm{SiO}} - P_{\mathrm{SiO,equ,1}}\right)^+, \tag{5.162}$$

where the initial blow-up has been regularised by the additional term in the denominator. We have also included the dependence on the equilibrium partial pressure. We note that in the limit $\hat{\beta} \to \infty$, with $\hat{\gamma}/\hat{\beta}$ finite, we recover the functional form (5.161). In Figure 5.10, we plot how the concentration of carbon changes over time for different values of $\hat{\beta}$, compared to when the original reaction rate is used. We run numerical simulations of the model (2.31) - (2.36), as done in Section 2.3, but replace r_1 used there with (5.162). In each case we use $\hat{\gamma} = 2\mathrm{r_C}\xi_1/3$, for $\mathrm{r_C} = 0.2$, so that the kinetic constant is the same as for the original rate.

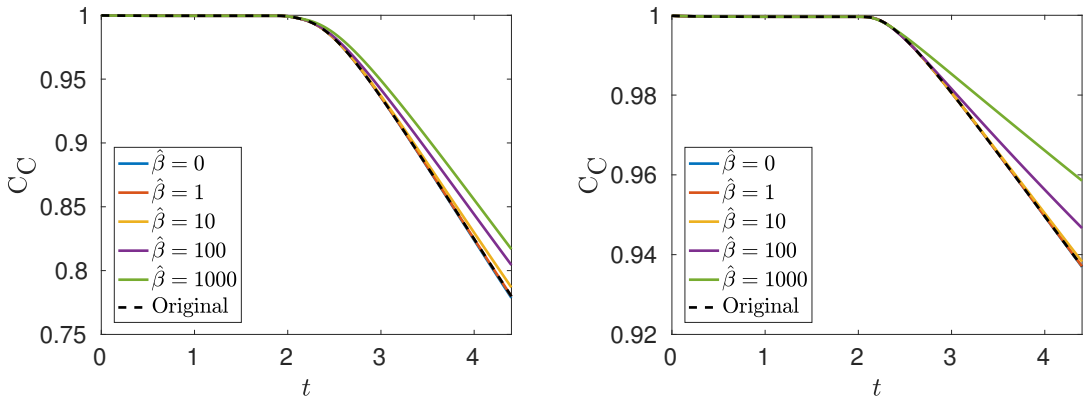


Figure 5.10: Plot of concentration of carbon at $z = 0.3$ (left) and $z = 0.7$ (right). Solid lines are shown of different values of $\hat{\beta}$ in (5.162), with the dashed line found using our original reaction rate, given in (5.150). Note that the vertical axes are different in each case.

When $\hat{\beta}$ is small, we obtain the same behaviour as found using the original model. This is because using $\mathrm{C_C^{2/3}}$ instead of $\mathrm{C_C}$ in the reaction rate has little influence on the dynamics, since reactions R_3 and R_5 dominate the process. However, for larger $\hat{\beta}$, where the microscale reaction is diffusion-limited, there is a small but noticeable difference in the amount of carbon present in the furnace.

The reaction rate (5.162) assumes that the reaction between C and SiO is the only reaction. However, in the base of the furnace, the carbon is mainly reacted away by

liquid quartz, and so even using the improved rate (5.162) for r_1 is a simplification. An improved way to determine reaction rates for the macroscale model would be to perform homogenisation from the particle scale to the furnace scale, as we discuss briefly in Chapter 6. Further, for a macroscale furnace model including motion of carbon particles, an extra convective term would be included in (5.162).

5.9 Conclusions

We have derived a canonical shrinking core model that generalises formulations in the literature, leading to a cubic relationship between the location of the interface and time. This model simplifies in diffusion-controlled and reaction-controlled limits. This canonical shrinking core model has been used as a building block to develop homogenised models of gas-solid reactions which account for interaction between microscale granular behaviour and macroscale particle dynamics. These are developed using the parameter δ as the ratio of the microscale to macroscale lengthscales, with $\mathcal{O}(1)$ and $\mathcal{O}(\delta^2)$ scalings being the resulting distinguished limits for the ratio of diffusivity in the grain to that in the pore space. More detailed analysis was dedicated to the $\mathcal{O}(\delta^2)$ distinguished limit, as it is the more physically relevant limit.

The homogenised model arising from the $\mathcal{O}(\delta^2)$ diffusion scaling agrees with models given by Melchiori et al. [60, 61] and Szekely [97], but with an additional parameter capturing the structure of the reaction given the concentration of the reactant solid. This parameter, λ, governs the shape of the reaction front in the diffusion-controlled process. A boundary layer of $\mathcal{O}\left(\kappa^{-1/2}\right)$ is found across which the solid varies from being fully reactant to fully product. The diffusion-controlled and reaction-controlled times for the reaction to be completed for both the shrinking core model in Section (5.2) and the $\mathcal{O}(\delta^2)$ homogeneous model agree with Sohn's law of additive reaction times. This gives support for the law that the time for a particle reaction is equal to the sum of the time when diffusion dominates and when the chemical reaction dominates.

Most of the modelling and analysis in this chapter have been carried out under the assumption that the product gas has no influence on the reaction dynamics. However, in Section 5.6, we showed that this analysis can be extended to include the effects of the product gas through a parameter σ. This parameter depends on the diffusivity of the product gas, the cross-diffusivities of the two gases, and the stoichiometric coefficient describing how many moles of the product gas are produced per mole of the reactant gas reacted. This extension assumes that the binary gas system is

related through a Fickian diffusion tensor. More accurate diffusion models could be employed, but at the cost of increasing the complexity of the analysis.

The model developed in this chapter allows for a diffuse reaction front, which is an improvement on the sharp interface shrinking core model commonly used. In practice, the solid reactant used may be an agglomerated material, composed of many smaller grains compressed together by a binder material, suggesting that a diffusive reaction front is more appropriate. We have shown how the reaction can be limited by the chemical kinetics, diffusion through the granular solid product matrix, or diffusion through the inter-granular void space or binder. The model captures the influence of gas concentration, solid concentration, particle size, grain size, kinetic rate, stoichiometry, and (binary) gas diffusivities on the reaction time, and also the dynamic transitions towards complete reaction. Thus this model for gas-solid reactions can be used in conjunction with other chemical reactions in process models, which typically consist of coupled reaction-advection-diffusion PDEs for chemical and thermal effects, and allow industrialists to simulate the influence of operational inputs on production levels. In Section 5.8 we demonstrated how one would go about coupling the model to the macroscale furnace model outlined in Chapter 2.

In silicon production, a range of raw materials are used as the source of carbon, including coal, charcoal, char, woodchips, petroleum coke, and agglomerated briquettes. Particle size, porosity, and chemical reactivity are all important considerations when selecting the material. For small particles of charcoal and coke, the canonical shrinking core model compares decently with experiments [64]. In such diffusion-controlled situations, the shrinking core model gives similar behaviour to our homogenised model. However, for other particles, such as large briquettes of compressed agglomerates, where diffusivity in the binder is important, the simple shrinking core approach is not a good representation, and our model is preferred. The role of binder during heat treatment of carbon has been studied in [78]. Since our model allows both sharp interface behaviour and a diffuse reaction front, it is an ideal means of comparing the reactivity of different raw materials. We envisage similar benefits for other metallurgical and chemical processes.

In practice, the conversion of one solid to another through reaction with gas can lead to volumetric increase or decrease of grains within the particle, with the stresses caused by the solid expansion or contraction possibly causing cracks and fracturing of the solid (again see [78]). Such mechanical effects have not been considered in this chapter, due to the difficulty in considering how displacements at the microscale grain level would influence neighbouring grains inside a spherical particle. However,

a study of the interactions with the chemical and diffusional effects considered in this chapter could bring further valuable insight.

Chapter 6

Discussions

We conclude this thesis by highlighting key findings and ways in which our research could be further developed. In Section 6.1 we summarise the mathematical modelling and results. Next, in Section 6.2, we discuss how the models themselves, and results from the models, could be used in practice by Elkem. We consider potential areas for future work in Section 6.3, and close with our outlook in Section 6.4.

6.1 Summary of results

In Chapter 2 we developed a one-dimensional model of a vertical section in a silicon furnace. This is a largely thermo-chemical model, capturing interactions between heat transfer and chemical species and reactions, although gas convection was included as a transport mechanism. We applied the model to the setting of pilot furnace experiments, making the simplification that solid and liquid chemical species remained stationary, and imposing a spatial Heaviside function for the distribution of the external heat source to replicate the energy input from the induction heater. We found that numerical simulations of the model using a finite difference scheme gave a good replication of the experiment, in terms of successfully capturing the location of the lower interface of the furnace charge, to a reasonable level of accuracy. However, since this model does not include any dripping of material from the base of the charge to the liquid pool below, it did not capture the interface between the cavity and crater regions found experimentally, and seen in industrial operation. To further extract value from this model, we performed parameter sweeps, observing the influence of varying input parameters on certain output metrics. Of particular note was the finding that using more reactive carbon particles does indeed reduce the silicon monoxide losses from the furnace, as is expected from industrial experience. Such particles will

also decrease the blockage from crust formation in pilot furnaces, measured in this model through the metric 'solid build-up.'

The model presented and analysed in Chapter 2 is, however, somewhat cumbersome, due to the large number of variables and coupled equations. In addition, the model depends on over thirty parameters, some of which are not well known and have been estimated or data-fitted in the literature. The approach of developing such a complex model is justified, since it was not immediately obvious, *a priori*, which chemical species and reactions dominated the process. In Chapter 3 we performed an asymptotic analysis in order to understand the key chemical and thermal behaviour arising from this model. The asymptotic scalings were motivated by the clear size groupings of chemical concentrations and reactions observed in numerical simulations of the full model. The concentrations of the raw materials of solid carbon and quartz remain larger than those of silicon carbide, silicon, and liquid quartz throughout the furnace. These solid and liquid concentrations are all far greater than the concentration of gas, as expected. Similarly, the melting of quartz and the subsequent reaction between this liquid quartz and carbon are the significant reactions. Thus, asymptotic limits of a fast carbon-quartz reaction compared to the slow melting of quartz, and even faster gas flow, were taken. We found the dominant chemical and gas flow behaviour in early time and order one time in the upper, charge region and the lower, combined cavity and crater region, by prescribing a temperature profile. Further, we established a simplified model that includes thermal variation. This two equation model compared well with the full model, which is encouraging, since much of the main structure of silicon furnaces can be understood from this much simpler model. Later, in Section 6.2, we give suggestions about how this model could be used in practice. Subsequent asymptotic limits of this simplified model were taken, highlighting the key energy balance between the external heating and the endothermic heat sink of the carbon-quartz reaction.

To better understand mechanisms behind the crust formation, we developed a thermo-mechanical model in Chapter 4, treating the crust as a viscous fluid subject to radiative heating from below. The chemistry in this model is simplified, with a condensation isotherm giving the height above which the charge acts as a dead load. The viscosity in the crust region varies exponentially with temperature. The location of the lower interface of the charge is influenced by a Stefan condition, which is a generic approach, supposing that the charge is melting. In practice, the material is dripping, and so a small latent heat limit is relevant for silicon furnaces, and is considered. To simplify our analysis we assumed that the fluid exists within a tall,

thin cylinder. Numerical simulations indicate that the system can either go to a seemingly stable steady state, or the interfaces can proceed to free fall. These results can help to explain the observed disparity between silicon production, where a strong crust forms, requiring periodic stoking, and ferrosilicon production with high iron content, where there is a continual downwards flow in the furnace, and any arising crust is only stoked sporadically. Although steady state behaviour is not observed in silicon furnaces, an initial rising of the charge towards steady state in the model is indicative of the observed rising of the furnace crust prior to stoking. We developed bifurcation diagrams of different model behaviour in parameter space. Denser, less viscous fluid with lower radiative heating could move the charge towards free fall. Further, a thin crust could sustain the large load of the charge above it if the viscosity is highly sensitive to temperature, or there is a small Péclet number in the model.

In Chapter 5, we returned to consider the reaction between silicon monoxide and carbon, which produces carbon monoxide and silicon carbide, which is critical in the production of silicon. We sought to develop a better reaction model than the approach taken in Chapters 2 and 3. With this motivation, we considered general gas-solid reactions. We first presented the canonical shrinking core model, in which there is a sharp interface between the unreacted central core and the reacted product shell. We extended the shrinking core model to allow for a diffuse reaction front by assuming that a spherical particle was composed of many smaller spherical grains, with pores in between. We then utilised homogenisation techniques by assuming a periodic microstructure, that is that the small grains were arranged in a periodic lattice, and that behaviour between grains varied slowly. The resulting macroscale model depends on the scaling between diffusion in the microscale product layer and diffusion in the pores between grains. In the most physically relevant distinguished limit, we obtained a homogenised model that allows for a diffusion-limited sharp interface, chemically kinetic-limited spatially homogeneous dynamics, and behaviour in between. We explored asymptotic limits in each of these extreme cases, showing how our findings compare with the existing literature. We also demonstrated that the model presented can be readily coupled with the larger scale one-dimensional furnace model.

6.2 Industrial applications

We hope that in addition to being of academic interest, our research will be of practical benefit to Elkem. Here we discuss potential ways our models and results could be

implemented and exploited.

6.2.1 Practical use of models

The work in Chapters 2 - 4 is focussed on the pilot furnace experiments, which have simplified geometry and heating mechanisms compared to industrial furnaces. Further, in Chapters 2 and 3, there is no feeding of new material into the top of the furnace. This approach has allowed us to better understand the chemical, thermal, and mechanical interactions, but there are difficulties in applying our findings directly to actual operational situations. Nevertheless, the models developed could have practical uses for Elkem.

Elkem already uses SiMod [106] as a training tool for operators and researchers. Employees can run different 'cases' on the model, exploring the effect of input parameters on the furnace. The one-dimensional model we presented in Chapter 2 built on many of the ideas used in SiMod, and its precursor the dynamic model [39]. If a graphical user interface (GUI) were to be written, the Matlab code we developed for numerical simulations of our model could readily be used in the same manner. Users could enter the required number of grid points, to determine the trade-off between run time and accuracy, as well as varying model inputs for each simulation. Although the model cannot predict furnace dynamics quantitatively to a high degree of accuracy, it does have power to qualitatively distinguish between different behaviour.

Similarly, the simplified model for temperature and concentration of solid quartz, (3.56) - (3.58), could readily be used with a GUI attached for training purposes. Furthermore, this two equation model could be adapted to the complex geometry of industrial furnaces with three electrodes. In addition to using more than one spatial co-ordinate in the Laplacian in (3.56), the functional form of the heat input would need to be modified. Following such adaptation, this model could complement existing energy balance software used by operators during live furnace monitoring.

Likewise, the crust model in Chapter 4 and the gas-solid reaction model in Chapter 5 could be combined with live furnace measurements to improve real-time decision making. Despite the large simplifications involved, the crust model would give an indication as to how the height of the charge and thickness of the crust layer would change based on electrode control strategies, varying the temperature at the bottom of the furnace which radiates up to heat the charge. The homogenised gas-solid reaction model would allow operators to predict how much silicon carbide has formed, based on the type, size, and quantities of carbon fed into the furnace, and select materials accordingly in response to changes in the furnace dynamics.

We now discuss how some of the existing results of the models will be of benefit to Elkem.

6.2.2 Crust formation and the need for stoking

The large Stefan number limit of our crust model is particularly relevant for silicon furnaces, since little latent heat is given off at the interface between the charge and the gas cavity. This limit is discussed in Section 4.5 (case D), but we explore these model results more here.

The crust model predicted that behaviour either went towards steady state, or towards a situation where the charge material fell indefinitely. The key parameter that determined which behaviour occurs is the ratio Pe/γ. This is given in (4.173) and (4.174), but to assist the reader we show this again as

$$\frac{Pe}{\gamma} = \frac{U\rho C_p(T_M - T_c)}{\epsilon_R \sigma_{\mathrm{SB}}(T_h^4 - T_M^4)} = \frac{\rho^2 g R^2 C_p(T_M - T_c)}{8\eta_s \epsilon_R \sigma_{\mathrm{SB}}(T_h^4 - T_M^4)}. \tag{6.1}$$

We can estimate the other parameters, T_b and λ, for silicon production, to determine the critical value of Pe/γ, above which free fall happens.

We estimate the hot and cold temperatures as $T_h = 2400$ K and $T_c = 1500$ K, from Figure 2.4 (left plot) and discussions with Elkem researchers. Similarly we estimate $T_k = 1700$ K as the temperature below which condensation stops in practice. We have from [2] that $T_M = 1996$ K, which is approximately 2000 K. We thus have an estimate for T_b as

$$T_b \approx 0.4. \tag{6.2}$$

We can obtain an estimate for λ by using Figure 2a in Tang and Tangstad [99], where they present viscosity measurements for pure SiO_2. Clearly the viscosity of the charge mixture will be different to the viscosity of quartz, but we use the data to obtain estimates of parameter values. In Figure 6.1, we show how an exponential fit to this data approximates an Arrhenius function well in the temperature interval of interest. From this data we can determine λ by

$$\lambda = \ln(\eta(T_c)) - \ln(\eta(T_M)), \tag{6.3}$$

and so find

$$\lambda \approx 10.4. \tag{6.4}$$

We can find the critical values of Pe/γ for varying λ and T_b in the large Stefan limit by solving (4.129), with $St \to \infty$, with a value of ϑ slightly above one. As

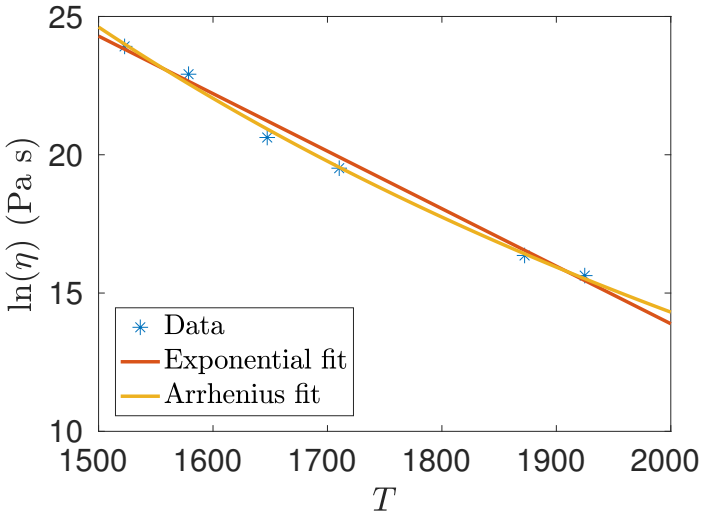


Figure 6.1: Comparison of an Arrhenius and exponential fit for data from Tang and Tangstad [99]. We have read in the data and plotted $\ln(\eta)$ in units of Pa s, rather than Poise.

mentioned in 4.4.2, steady state solutions exist for $\vartheta > 1$ but not for $\vartheta < 1$, so $\vartheta = 1$ gives the bifurcation point. We find that for $\lambda = 10.4$ and $T_b = 0.4$ we require $Pe/\gamma > 7.40$ for there to be free fall in the model. For the constant viscosity and no condensation temperature case $\lambda = T_b = 0$, and as such we only require $Pe/\gamma > 1$. These are demonstrated in Figure 6.2.

Returning to (6.1) we have estimates for the temperatures and the viscosity η_s, and know $g = 9.807$ m/s^2 and the Stefan-Boltzmann constant, $\sigma_{\text{SB}} = 5.670 \times 10^{-8}$ kg s^{-3} K^{-4}, but need to estimate the other parameters. We can use (2.6) to estimate the density of the charge mixture from the initial density in our one-dimensional simulations, as

$$\begin{aligned} \rho &= \sum_i \rho_i(z,0)\theta_i(z,0) \\ &= M_{\text{C}}\text{C}_{\text{C}}(z,0) + M_{\text{SiO}_2\text{(s)}}\text{C}_{\text{SiO}_2\text{(s)}}(z,0) + M_{\text{CO}}\text{C}_{\text{CO}}(z,0) + M_{\text{SiO}}\text{C}_{\text{SiO}}(z,0) \\ &\approx 1493, \end{aligned} \tag{6.5}$$

where, as we expect, including gas has no influence on the four significant figures shown. Rather than calculate a total specific heat, we note we can use (2.22) to find the heat capacity as

$$\begin{aligned} \rho C_p &= \sum_i \text{C}_i(z,0) C_{p,i} \\ &\approx 2.432 \times 10^6, \end{aligned} \tag{6.6}$$

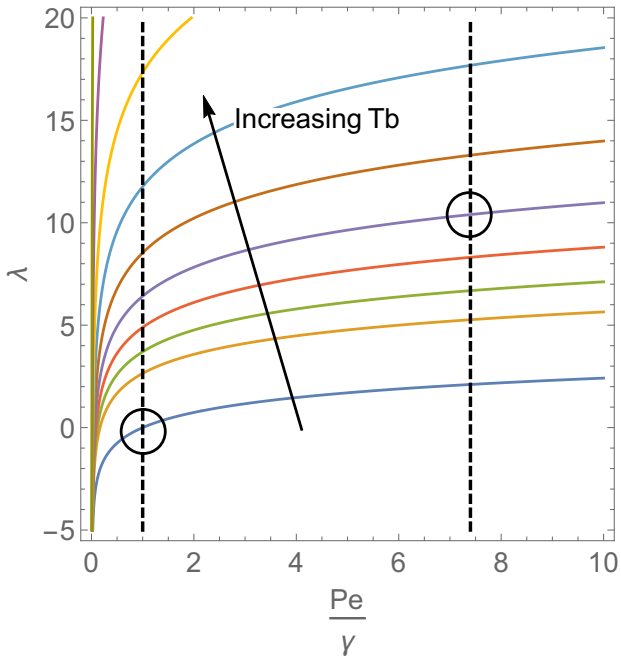


Figure 6.2: Bifurcation plot for Pe/γ against λ, for curves of constant T_b, increasing in intervals of 0.1 from 0 to 0.9. Above and to the left of the curves, steady states are possible, while below and to the right of curves the system is in free fall. Plots were generated in Mathematica by letting $\vartheta = 1 + 10^{-6}$. The left circle is the value for $\lambda = 0$ and $T_b = 0$, corresponding to $Pe/\gamma = 1$. The right circle is the value for $\lambda = 10.4$ and $T_b = 0.4$, corresponding to $Pe/\gamma = 7.40$.

where again the gas only influences the fifth significant figure. Assuming black body radiation, so that $\epsilon_R = 1$, and using the pilot furnace internal radius $R = 0.065$ m, we find that our estimate is

$$\frac{Pe}{\gamma} \approx 10^{-3}. \tag{6.7}$$

We note that (6.7) is nowhere close to the critical value of $Pe/\gamma = 7.40$ needed for continuous downwards motion of the charge. We conclude that the behaviour in a silicon furnace may therefore be going towards a steady state. In practice, this steady state may not be being achieved due to stoking. The steady state may be a very thin charge layer far up the furnace which will not be of practical interest.

We have obtained this result about furnace behaviour by assuming a tall, thin cylindrical geometry, with dimensional radius R. This was appropriate for the pilot furnace, but is clearly not the case for industrial scale furnaces. In the case of an industrial scale furnace, one should instead choose a typical horizontal length scale, R. This could be half the distance between electrodes, or the distance from the electrode to the outer inactive charge, or even the radius of the full furnace. Using the full

furnace radius as $R = 3.5$ m (as given in [82]) gives $Pe/\gamma = 2.649$, which is still too small to predict free fall behaviour. Clearly, though, the assumption of Poiseuille flow breaks down for non-cylindrical geometries, and so it would be better to use a flow rate U in (6.1), if this could be calculated or approximated from knowing the inflow or outflow at relevant boundaries in the more complicated furnace domain.

In this thesis, we have been interested in the production of pure silicon, known in the industry as Si 99, because liquid silicon tapped from the furnace is 99% pure. Elkem also produces ferrosilicon FeSi 75 and FeSi 52, with 75% and 52% weight percentage of silicon, respectively, as well as occasionally producing a less common FeSi 65. In both Si 99 and FeSi 75 production, crust formation occurs with a rising gas cavity, and periodic stoking is required. However, in FeSi 52 production, this gas cavity does not form, and so only intermittent stoking is required. One such FeSi 52 furnace has been operated for extended periods of time without any stoking, but this was done for testing purposes. It is known that the density of the charge increases [26, 68] and viscosity decreases (Figure 9.30 in [27]) as the percentage of Si reduces and Fe increases, and so we expect that the value of Pe/γ increases with iron content. Suppose we are in a parameter regime where we have a steady state. Our model predicts that as we increase the Péclet number (with all other parameters kept constant), the steady state remains fairly insensitive initially. However, eventually the Péclet number increases towards a critical value, beyond which free fall behaviour occurs (see Figures 4.13 and 4.12). We plot an illustrative diagram of this idea in Figure 6.3, with the steady state value of the lower interface given by the red curve.

We have deliberately not put precise values for the different materials onto the axes, since we are demonstrating a potential qualitative explanation. It is also possible that FeSi 52 has a negative steady state in our model, which could also represent a continual flow in practice. From conversations with Elkem employees, we believe that FeSi 65 production has behaviour in-between that observed in FeSi 75 and FeSi 52 production, but this is only anecdotal and needs further exploration.

The ratio of the Péclet number to the radiative heating, Pe/γ, depends on the density squared, as shown in (6.1). One density comes from the weight of the charge, since heavier material will move downwards under gravity faster, regardless of the detailed geometry of the furnace. The other density comes from the heat capacity. The higher the density is, the higher the heat capacity will be, and thus the longer it will take for the radiative heating to melt the charge. Accordingly, a higher heat capacity slows down the rise of the gas cavity. Similarly, Pe/γ is inversely proportional to the viscosity, η_s, as shown in (6.1), since less viscous crust cannot withstand as

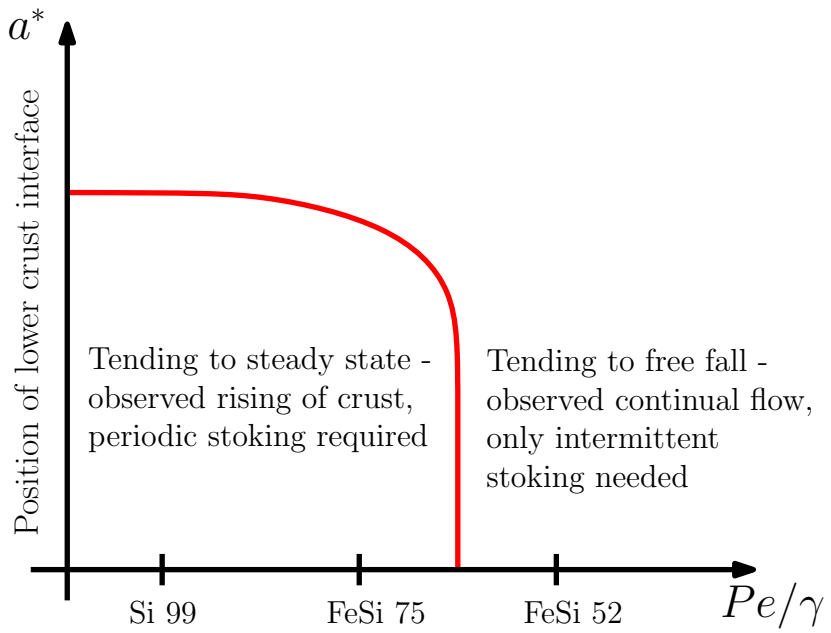


Figure 6.3: Illustration of a possible explanation for the change in furnace behaviour with added iron content.

much weight of the charge. However, this dependence on viscosity is only linear. Thus if one wanted to increase the value of Pe/γ, then increasing the density has a greater effect than reducing the viscosity by the same factor.

We suggest that parameters discussed in this section should be determined from industrial operation. Those that can be changed, either by raw material selection or electrode control, may allow operations to be modified to remove the need for stoking in future silicon production. Our hope is that the crust model gives a framework to understand why the furnace crust forms in silicon production, and correspondingly why it is less of an issue in some ferrosilicon furnaces.

6.2.3 Selection of carbon particles

In Chapter 2, we noted that more reactive carbon particles reduce the silicon monoxide losses from the system, since more convecting gas is captured and reacts to form silicon carbide. In Chapter 5, we developed a homogenised model for gas-solid reactions, which can be applied to the reaction between solid carbon particles and silicon monoxide. We discuss this application here.

A variety of particles are used as carbon sources in silicon production. These include coal, charcoal, char, woodchips, petroleum coke, and charcoal briquettes. In Figure 1.3 in Chapter 1 we showed pictures of pilot furnace experiments using

different types of carbon. The size of particles can also be varied. Elkem have carried out experiments similar to the pilot furnace experiments discussed in Section 1.2, placing different types of carbon particles at different heights in the furnace, to see the influence on the reaction. We do not go into detail about the experimental results here, but use some images for explanatory means.

In Figure 6.4, we show a particle which is larger than those typically used at present. There is a clear separation between unreacted and reacted material, and so the reaction would appear to be diffusion limited. If it were instead chemically-limited, the particle behaviour would be fairly homogeneous. The visible cracks are likely caused by volatiles leaving the particles as gas due to the high temperature, such as seen in [78], rather than as a cause of volume expansion due to the reaction. Thus, the assumption of no volume change in Chapter 5 is appropriate.

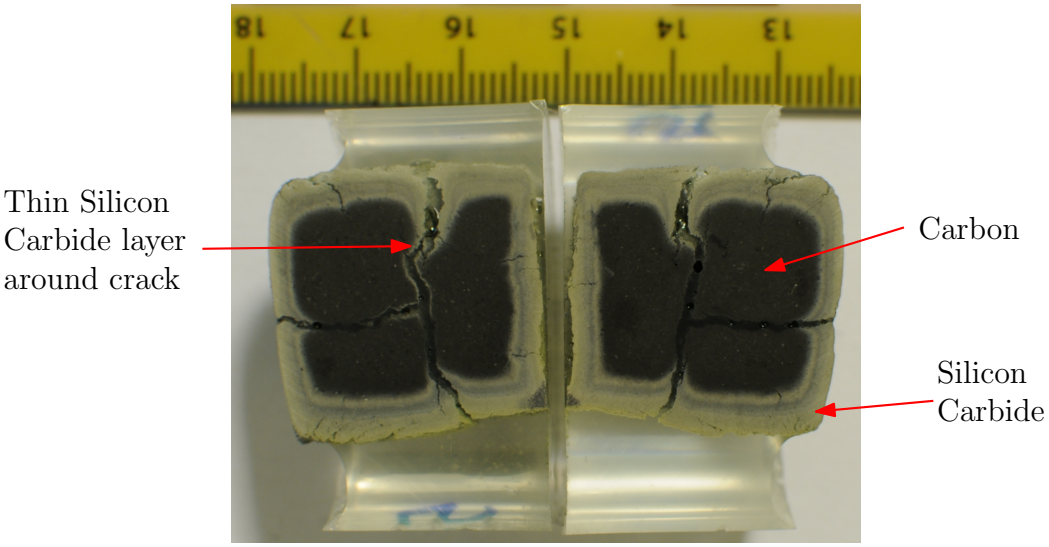


Figure 6.4: Image of a partially reacted carbon cylinder, which has been sliced along its central axis and folded outwards, so that up and down correspond to radial distances. The inner core of unreacted carbon and the outer shell of silicon carbide can be seen. The presence of silicon carbide next to a crack suggests that the cracks were not caused by the reaction. Instead, it is likely that cracks formed to allow moisture and volatiles to escape in the initial heating. We acknowledge Fei Li for conducting the experiment and taking the photograph, whilst working at Elkem Technology.

In Figure 6.5 we show a different carbon particle, which exhibits a transition region. Although the reaction in this particle is also diffusion limited, there is not a sharp interface, since a mixture of carbon and silicon carbide has been found in the black region. Thus the behaviour is qualitatively similar to that in the bottom right plot in Figure 5.3.

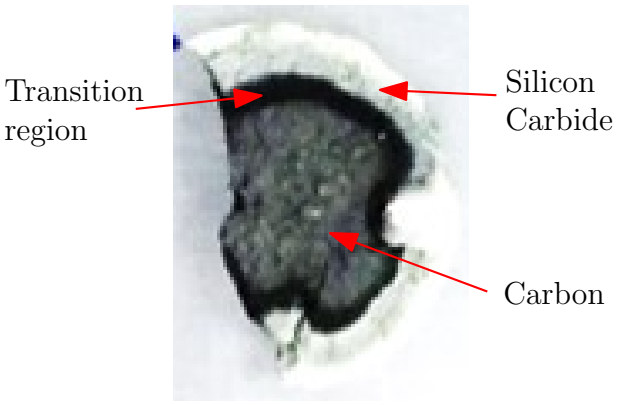


Figure 6.5: Image of a partially reacted carbon particle, which is about 10 mm in diameter. The black region contains a mixture of carbon and some silicon carbide crystals, so is a transition region, despite the colour. We acknowledge Fei Li for conducting the experiment and taking the photograph, whilst working at Elkem Technology.

Our homogenised model consists of equations (5.66) (or (5.62)) and (5.63), and boundary and initial conditions given in (5.64), and depends upon two parameters, κ and λ. Including the influence of the product gas through the parameter σ, which was defined in (5.135), adds no further complexity, since this can be absorbed into κ and λ. Thus, for each type and size of carbon particle, these parameters can be fit to data from conversion experiments, such as those found in doctoral theses by Myrhaug [63] and Li [53]. Individual physical parameters, such as the diffusivity of silicon monoxide in the pores or the average grain size, would not need to be determined. Although our homogenised model assumes a constant external reactant gas pressure, this could be amended through replacing the constant pressure boundary condition in (5.64) with a time-dependent boundary condition, accounting for a varying pressure outside the particle. The model could then be used to aid industrial particle selection.

The dimensional reaction completion time predicted by our model is given in (5.144). We present it again here,

$$t^*_{\text{dim}} = \frac{aR_p}{\sigma_1 k p_a P_{\text{TOT}}} + \sigma \frac{a^2 R_p^2 B_0(k_m/\delta)}{6\sigma_1 k C_A} \frac{\delta^2}{D_S} + \sigma \frac{4\pi a^3}{3D_e} \frac{R_p^2 B_0(k_m/\delta)}{6\sigma_1 k C_A D_V}, \tag{6.8}$$

but do not explain the meaning of each variable again. We can note from this expression how the reaction time will change with different inputs. Of particular interest is the particle radius, R_p, since this can be varied relatively easily in practice. We see that, for small particles, the time approximately varies linearly with particle size, but for larger particles this becomes a quadratic dependence. A schematic diagram of this behaviour is given in Figure 6.6, where we deliberately have not labelled numbers

on the axes. Although the reaction time is always reduced by making the particles smaller, there is a bigger influence in the quadratic diffusion-controlled regime. In practice, though, there is a lower limit to the particle size. If the particles are made too small, they will be blown out of the furnace by the convecting gas, and will not contribute at all to the process.

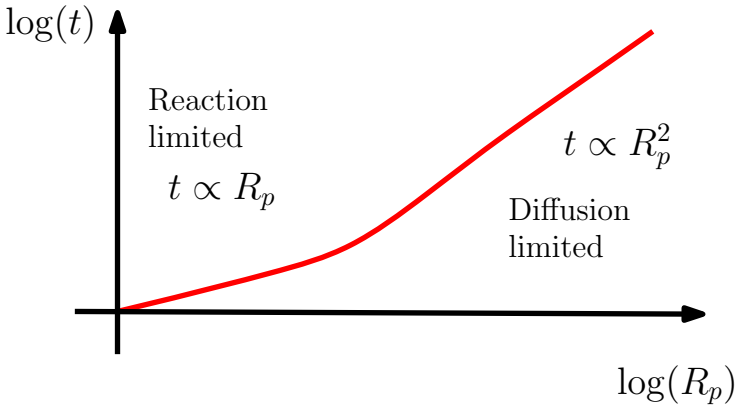


Figure 6.6: Schematic diagram of a log-log plot demonstrating how the reaction completion time varies with the particle radius.

We envisage that our research will help Elkem select the type and size of carbon particles to be fed into silicon furnaces. In particular, since there is an energy cost associated with making raw materials smaller, quantifying the curve in Figure 6.6 for each carbon material would allow Elkem to define an optimum particle size, from a financial perspective.

6.3 Future work

There are a wide variety of ways in which the work in this thesis could be extended, to better understand behaviour in silicon furnaces, and hence to aid industrial decision making. In Section 4.6 we already presented some ways in which the thermo-mechanical crust model could be expanded. Here we discuss other relevant avenues to build on our research.

6.3.1 Homogenised furnace model

In Chapter 2 we derived a macroscale furnace model by assuming an averaged effective concentration of each chemical species at each height. This common continuum approach assumed that there was a mixture of all species everywhere in the furnace, with the volume fractions adding to one. However, an alternative approach would be

to employ similar ideas from Chapter 5, where we used mathematical homogenisation to upscale from microscale behaviour to develop a particle scale model for gas-solid reactions. We could thus upscale a further order of magnitude, by assuming periodic scale on the particle scale to develop homogenised macroscale furnace equations. This would allow us to input further model parameters, such as the size of raw materials. Furthermore, the arising reaction rates would result in more accurate models than those currently used, as was discussed briefly for reaction R_1 in Section 5.8.

6.3.2 Distribution of particle sizes

We demonstrated in Section 5.8 how the homogenised reaction model could be coupled to our furnace model, if all carbon particles are spheres of the same initial radius. However, in practice raw materials are not uniform. Including non-spherical particle geometries is likely too complex, since the orientation of an individual particle may change in the furnace, but it is reasonable to include a variation of particle sizes. Suppose there are n_i spheres of initial dimensional radius $R_{p,i}$ and current dimensional inner core radius $l_i(z,t)R_{p,i}$. Then, the dimensionless concentration of carbon is given by

$$\mathrm{C_C} = \frac{\frac{4\pi}{3}\sum_i n_i l_i^3 R_{p,i}^3}{\frac{4\pi}{3}\sum_i n_i R_{p,i}^3}, \tag{6.9}$$

where the denominator is the initial dimensional concentration. Taking a time partial derivative of (6.9), we have

$$\frac{\partial \mathrm{C_C}}{\partial t} = \frac{\sum_i n_i 3 l_i^2 \frac{\partial l_i}{\partial t} R_{p,i}^3}{\sum_i n_i R_{p,i}^3}. \tag{6.10}$$

The derivatives $\frac{\partial l_i}{\partial t}$ would then be coupled with particle models, as in Section 5.8. Similarly, if the particles are moving, we can take a spatial derivative of (6.9), requiring an extra equation for $\frac{\partial l_i}{\partial z}$. In the case of the canonical shrinking core model, a spatial derivative could be taken of (5.20) (with $l(t)$ replaced with $l_i(z,t)$), to find that the spatial derivative of l_i depends on the time integral of the external pressure flux. We would then find the reaction rate from

$$r_1 = -\frac{1}{2}\frac{\partial \mathrm{C_C}}{\partial t} + \frac{1}{2}U_s \frac{\partial \mathrm{C_C}}{\partial z}. \tag{6.11}$$

This approach requires an extra equation for each initial radius R_i, since we cannot return from l_i to $\mathrm{C_C}$, as done in Section 5.8.

We could further envisage taking a continuous distribution of particle sizes. This would require integrating over a density, instead of the summation in (6.9).

6.3.3 Improved gas-solid reaction model

The gas-solid reaction model in Section 5 is an improvement on the usual shrinking core model used. However, some of the assumptions included in our work could be relaxed to develop a more accurate model. When including the effects of the product gas in Section 5.6, we used a Fickian model, which has a constant diffusion tensor. This is a simplification, however, since the diffusive fluxes are not in general linear in the concentration (or pressure) of the reactant and product gas, unless a dilute limit is appropriate, where there is a third, background gas which is unreactive. As mentioned earlier, there are several multi-component diffusion models, for example [20, 33, 36]. In [33], the non-linear Einstein-Teorell model is deemed a more suitable model than linear Fickian diffusion away from equilibrium. With this model, (5.118) would be replaced with

$$\zeta \frac{\partial}{\partial t} \begin{pmatrix} P \\ Q \end{pmatrix} = \nabla \cdot \left(\begin{pmatrix} 1 & d_1 \frac{P}{Q} \\ d_2 \frac{Q}{P} & d_3 \end{pmatrix} \nabla \begin{pmatrix} P \\ Q \end{pmatrix} \right). \tag{6.12}$$

Since the determinant of the diffusion tensor in (6.12) is the same as that in (5.118), there will also be degeneracy if $d_3 - d_1 d_2 = 0$. Although writing a single particle model for the Einstein-Teorell is feasible, homogenisation from a grain problem would be more complex than our approach. However, such homogenised equations would possibly be of interest.

We have also assumed that the particle is isothermal, which is reasonable considering the typical particle size and temperature variations within the furnace. However, the diffusion coefficients will also vary with temperature, in proportion to $T^{3/2}$ according to Cussler [20]. If the top of the furnace is at around 1500K, and the base of the charge at 2000K, this is a variation of $(1500/2000)^{3/2} \approx 0.65$ of the diffusion rate. Therefore, treating temperature as constant in our model is acceptable, but there may be applications for which thermal variations are crucial.

Similarly, although Figures 6.4 and 6.5 show that our assumption of no volume expansion is valid for the reaction between carbon and silicon monoxide, mechanical effects could be incorporated for general gas-solid reactions. The homogenisation of a three-dimensional granular particle would be particularly difficult, since the expansion of each grain is influenced by the available space left by its neighbours in which to grow.

6.3.4 Crater behaviour

In the furnace model in Chapters 2 and 3, there was no motion of solids or liquids. The crust model developed in Chapter 4 allowed for movement of the charge, and for material to be eaten away. However, we did not track what happens to material once it has dripped into the crater. The crater is well mixed, and so it could be modelled as being spatially homogeneous, with radiative heat emitted and gas convected from the crater reaching the charge. Including crater behaviour would allow for a fully coupled system, with information propagating both ways between the crust and the crater, through the gas cavity. However, the crater found in pilot furnace experiments (shown in Figures 1.3 and 2.1) is a simplification of industrial behaviour. In practice, electric arcs mix and stir the crater, so a liquid pool cannot settle, and hence the dynamics will be different.

6.3.5 Two-dimensional model

The furnace model presented in Chapter 2, and the model analysis of the crust model, given in Chapter 4, have both assumed a one-dimensional vertical geometry. Such an approach has allowed us to understand the dominant thermal, chemical, and mechanical behaviour. The pilot furnaces are not one-dimensional, however, and so it would be of interest to include radial dependence in these models. This would be more difficult computationally, as discussed in Section 4.6.3, but could be worthwhile. For example, if the crust thickness varies radially in a two-dimensional model, Elkem may have a better idea of where to stoke the furnace. Furthermore, the furnace models in this thesis could be combined, so that charge motion would be coupled with chemical behaviour, as well as thermal effects.

6.3.6 Industrial scale furnace geometry and electrical effects

We have focussed the research in this thesis on the pilot furnace experiments, which have a simplified geometry and heating input. Although some of our findings are transferrable to the setting of an industrial scale furnace, it could be useful to extend ideas from our research to model such operational furnaces. The geometry of these furnaces is quite unwieldy, but could be handled in a multiphysics package such as COMSOL. In this way, our research could influence the design of future silicon furnaces. An InFoMM DPhil research project modelling electrical effects in silicon furnaces will start in October 2018. Hopefully this will complement our research,

which neglected electrical effects, and will help to complete the picture of what is taking place inside silicon furnaces.

6.4 Outlook

We believe that silicon will continue to be a sought-after material, and silicon production will remain a significant industry for the forseeable future. As such, furnace behaviour is a rich and crucial setting for scientific and industrial research. We hope that the understanding established in this thesis will aid current operation, particularly through the selection of carbon materials. We also hope it will assist future operation, since our crust model gives a framework for determining which input parameters should be changed to produce silicon without the need for stoking, but instead with a continual flow. There is scope for further mathematical study. New models of electrical behaviour are crucial, since such electrical effects are coupled to chemical dynamics through thermal processes. Also, shape optimisation of furnace geometry could lead to the design of new furnaces, which are more efficient than those used at present.

Appendix A

Further Comments about Species and Reactions

In this thesis we have modelled seven chemical species in the furnace, namely C(s), SiC(s), SiO_2(s), SiO_2(l), Si(l), CO(g), and SiO(g). We have also modelled the reactions

$$\mathrm{SiO(g)} + 2\mathrm{C(s)} \xrightarrow{R_1} \mathrm{SiC(s)} + \mathrm{CO(g)}, \tag{A.1}$$

$$2\mathrm{SiO(g)} \underset{R_{-2}}{\overset{R_2}{\rightleftharpoons}} \mathrm{SiO_2(l)} + \mathrm{Si(l)}, \tag{A.2}$$

$$\mathrm{SiO_2(s)} \xrightarrow{R_3} \mathrm{SiO_2(l)}, \tag{A.3}$$

$$\mathrm{SiO(g)} + \mathrm{SiC(s)} \xrightarrow{R_4} 2\mathrm{Si(l)} + \mathrm{CO(g)}, \tag{A.4}$$

$$\mathrm{SiO_2(l)} + \mathrm{C(s)} \xrightarrow{R_5} \mathrm{SiO(g)} + \mathrm{CO(g)}. \tag{A.5}$$

As with deriving any model, a balance is needed when deciding which effects to include. Here we have sought to establish a good representation of reality, whilst being sufficiently selective as to keep the model tractable, including being able to generate simple scaling laws. Here we discuss some of the assumptions made.

The condensation reaction R_2 is sometimes modelled through a condensate phase $Si.SiO_2$, which subsequently separates into Si(l) and SiO_2(l), for example in [106]. For simplicity we have neglected this intermediate phase and assumed that SiO(g) immediately condenses into Si(l) and SiO_2(l), which in turn can react to evaporate back into SiO(g). Silicon monoxide actually condenses into a solid, and not a liquid. However, in practice the gas condensates in the furnace at temperatures hotter than the melting point of silicon, so any solid silicon will quickly become liquid. The quartz component is very different to the large lumps of rock input to the process, and has been found experimentally to react with carbon. Thus the modelling assumption that

liquid silicon and liquid quartz was formed from the condensation is reasonable, and is also adopted by Andresen [2].

We have chosen to model quartz as having two phases, being solid quartz SiO_2(s) and liquid quartz SiO_2(l), which behave as distinct chemical species. The solid quartz is one of the raw materials input to the furnace and cannot react with any of the other chemical species. The liquid quartz is formed by the melting of solid quartz, through reaction R_3, and the condensation of SiO(g), through reaction R_2, as discussed in the previous paragraph. It can then, in turn, react with C(s) to produce the two gases. In practice, though, the behaviour of quartz is more complex. In this thesis we have used the word 'quartz' as a shorthand for SiO_2 (silicon dioxide or silica), but several different crystalline structural states, or phases, can occur with the same chemical composition, with quartz being the stable state that exists at low temperature and pressure. When the material is heated up in the furnace, the crystalline structure changes to form cristobalite [82]. This transition can occur via an intermediate amorphous, unordered state, and Wiik [109] discusses a model for such transition. During the phase transition, quartz softens and undergoes a volume expansion, with the extent of the expansion dependent on the type of quartz used [77]. If heated sufficiently rapidly cracking can occur. Sometimes pre-heated cristobalite is used as a raw material input to the furnace instead of quartz. The situation is further complicated by the existence of different phases of quartz (α-quartz and β-quartz), and trydimite, which forms in the presence of impurities. In keeping with the aim of this thesis, to understand the main thermal, chemical, and mechanical behaviour in the furnace, we have ignored this complexity and chosen SiO_2(s) and SiO_2(l) to be the sole chemical representations of silicon dioxide in our models.

In addition to (A.1) - (A.5), a further set of reactions (A.6) is believed to occur in industrial furnaces [82]:

$$2SiO_2(l) + SiC(s) \underset{R_{-6}}{\overset{R_6}{\rightleftharpoons}} 3SiO(g) + CO(g). \tag{A.6}$$

The forward reaction, R_6, is a mechanism for gas production in the crater, and the backward reaction, R_{-6}, forms some condensate in the upper charge. However, these are not included in either the dynamic model [39] or SiMod [106]. The justification for their omission is that reactions R_5 and R_{-2} give a pathway for one mole silicon and carbon to react with two moles of liquid quartz to form three moles of silicon monoxide and one mole of carbon monoxide. Thus, R_6 can be seen as the net effect of these reactions, under the assumption that the silicon and carbon molecules in the silicon carbide compound can behave independently. Whilst this is not entirely

satisfactory, the kinetic parameters used in the dynamic model [39] and SiMod [106] have been calibrated to furnace data without using (A.6). As discussed in Section 2.2.8, it is difficult to obtain kinetic data for high temperature reactions such as those found in silicon furnaces, and since we use data obtained from SiMod, we decided to also neglect these reactions. Such a decision is more justifiable for the pilot furnaces, which this thesis is focussed on modelling. Carbon is present throughout almost all the pilot furnace initially, and there is not a large presence of silicon carbide, so reaction R_5 is likely to be the gas-producing mechanism in the pilot furnace crater, rather than R_6, which could be a more important mechanism in industrial furnaces. Regardless, reactions R_6 and R_{-6} could be included in future models once sufficient data has been obtained.

Appendix B

Asymptotic Expansions for Chapter 3

Here we list asymptotic solutions, to leading and first order, for sub-problems considered in Chapter 3. In sections B.1 - B.4 present solutions when the temperature is prescribed. Then, in section B.4, we give solutions for the small diffusion limit of the simplified model.

For simplicity, in the prescribed temperature asymptotics we expand the gas flux as one variable, so that $U_g \mathrm{C}_g = U_g^0 \mathrm{C}_g^0 + \epsilon U_g^1 \mathrm{C}_g^1 + \mathcal{O}(\epsilon^2)$. If instead we had used individual expansions $U_g = U_g^0 + \epsilon U_g^1 + \mathcal{O}(\epsilon^2)$, $\mathrm{C}_g = \mathrm{C}_g^0 + \epsilon \mathrm{C}_g^1 + \mathcal{O}(\epsilon^2)$, then the leading order asymptotics remain the same, but there will be more complex relationships for the first order terms, which include the algebraic no voids condition. For brevity we suppress the notation $T(z)$ and $P_i(T(z))$ in favour of T and P_i, respectively, unless we are integrating over a dummy variable.

B.1 Prescribed temperature - Region IIa

On the early timescale $\hat{t} = t/\epsilon$, the solid and liquid concentrations are given by

$$\mathrm{C_C} = 1 + \epsilon\alpha\left(T - T_m\right)\left(\hat{t} + e^{-\hat{t}} - 1\right) + \mathcal{O}(\epsilon^2), \tag{B.1}$$

$$\mathrm{C_{SiC}} = \epsilon\chi_1\left(\frac{1}{2} - P_1\right)\hat{t} + \mathcal{O}(\epsilon^2), \tag{B.2}$$

$$\mathrm{C_{SiO_2(s)}} = \alpha - \epsilon\alpha\left(T - T_m\right)\hat{t} + \mathcal{O}(\epsilon^2), \tag{B.3}$$

$$\begin{aligned}\mathrm{C_{SiO_2(l)}} = {} & \alpha\left(T - T_m\right)\left(1 - e^{-\hat{t}}\right) + \epsilon\Bigg(\chi_2\left(\frac{1}{2} - P_2\right)^+\left(1 - e^{-\hat{t}}\right) \\ & - \alpha\left(T - T_m\right)^2\left(\hat{t} - 1 + e^{-\hat{t}}\right) \\ & - \alpha^2\left(T - T_m\right)^2\left(\hat{t} - 2 + e^{-\hat{t}}\left(-\frac{\hat{t}^2}{2} + 2\hat{t} + 1\right) + e^{-2\hat{t}}\right)\Bigg) + \mathcal{O}(\epsilon^2),\end{aligned} \tag{B.4}$$

$$\mathrm{C_{Si}} = \epsilon\chi_2 \left(\frac{1}{2} - P_2\right)^+ \hat{t} + \mathcal{O}(\epsilon^2). \tag{B.5}$$

The gas flux and partial pressure are found to be

$$U_g \mathrm{C}_g = 2\alpha \left(1 - e^{-\hat{t}}\right) \int_{y=0}^{y=z} \left(T(y) - T_m\right) dy + 2\epsilon \int_{y=0}^{y=z} r^1_{5,IIa}(\hat{t}, y) - r^0_{2,IIa}(\hat{t}, y) dy + \mathcal{O}(\epsilon^2), \tag{B.6}$$

$$P = \frac{1}{2} - \epsilon \frac{\int_{y=0}^{y=z} r^0_{1,IIa}(\hat{t}, y) + r^0_{2,IIa}(\hat{t}, y) dy}{U^0_g \mathrm{C}^0_g} + \mathcal{O}(\epsilon^2), \tag{B.7}$$

for $U^0_g \mathrm{C}^0_g \neq 0$, i.e. $\hat{t}, z > 0$, where $U^0_g \mathrm{C}^0_g$ is the leading term in (B.6), and

$$r^0_{1,IIa}(\hat{t}, z) = \chi_1 \left(\frac{1}{2} - P_1\right), \quad r^0_{2,IIa} = \chi_2 \left(\frac{1}{2} - P_2\right)^+, \tag{B.8}$$

$$\begin{aligned} r^1_{5,IIa} =& \alpha^2 \left(T - T_m\right)^2 \left(\hat{t} + e^{-\hat{t}} - 1\right) \left(1 - e^{-\hat{t}}\right) + \left(\chi_2 \left(\frac{1}{2} - P_2\right)^+ \left(1 - e^{-\hat{t}}\right)\right. \\ & - \alpha \left(T - T_m\right)^2 \left(\hat{t} - 1 + e^{-\hat{t}}\right) \\ & \left. - \alpha^2 \left(T - T_m\right)^2 \left(\hat{t} - 2 + e^{-\hat{t}} \left(-\frac{\hat{t}^2}{2} + 2\hat{t} + 1\right) + e^{-2\hat{t}}\right)\right). \end{aligned} \tag{B.9}$$

B.2 Prescribed temperature - Region IIb

Since several of the higher order terms in this region can only be written in terms of integrals, we give the $\mathcal{O}(1)$ terms and then the $\mathcal{O}(\epsilon)$ terms. Note that

$$\mathrm{C_{SiO_2(s)}} = \alpha e^{-(T - T_m)t}, \tag{B.10}$$

and so there is no correction term needed for the concentration of solid quartz. Five of the leading order variables are easily found as

$$\mathrm{C^0_C} = \alpha e^{-(T - T_m)t} + (1 - \alpha), \tag{B.11}$$

$$\mathrm{C^0_{SiO_2(l)}} = \frac{(T - T_m)\alpha e^{-(T - T_m)t}}{\alpha e^{-(T - T_m)t} + (1 - \alpha)}, \tag{B.12}$$

$$\mathrm{C^0_{SiO_2(s)}} = \alpha e^{-(T - T_m)t}, \tag{B.13}$$

$$U^0_g \mathrm{C}^0_g = 2\alpha \int_{y=0}^{y=z} e^{-(T(y) - T_m)t} \left(T(y) - T_m\right) dy, \tag{B.14}$$

$$P^0 = \frac{1}{2}. \tag{B.15}$$

The solutions for $\mathrm{C}^0_{\mathrm{SiC}}$ and $\mathrm{C}^0_{\mathrm{Si}}$ are different in the temperature regions $P_2, P_4 \geq \frac{1}{2}$, $P_2 < \frac{1}{2} \leq P_4$, and $P_4 < \frac{1}{2} \leq P_2$. Note that there is no region in $T > T_m$ where P_2 and P_4 are both less than $\frac{1}{2}$.

In $P_2 < \frac{1}{2} \leq P_4$, we have

$$\mathrm{C}^0_{\mathrm{SiC}} = \chi_1 \left(\frac{1}{2} - P_1\right) \left(\frac{\alpha}{T - T_m}\left(1 - e^{-(T-T_m)t}\right) + (1-\alpha)t\right), \tag{B.16}$$

$$\mathrm{C}^0_{\mathrm{Si}} = \chi_2 \left(\frac{1}{2} - P_2\right) \left(\alpha e^{-(T-T_m)t} + (1-\alpha)\right)^{\chi_{-2}} \int_{\tilde{t}=0}^{t=\tilde{t}} \left(\alpha e^{-(T-T_m)\tilde{t}} + (1-\alpha)\right)^{-\chi_{-2}} d\tilde{t}. \tag{B.17}$$

In $P_2, P_4 \geq \frac{1}{2}$, we have that $\mathrm{C}^0_{\mathrm{SiC}}$ is given by (B.16) and that $\mathrm{C}^0_{\mathrm{Si}} = 0$. In $P_4 < \frac{1}{2} \leq P_2$,

$$\mathrm{C}^0_{\mathrm{SiC}} = \begin{cases} \chi_1\left(\frac{1}{2} - P_1\right)\left[\frac{\alpha(e^{-(T-T_m)t} - e^{-\chi_4(\frac{1}{2}-P_4)t})}{\chi_4(\frac{1}{2}-P_4)-(T-T_m)} + \frac{1-\alpha}{\chi_4(\frac{1}{2}-P_4)}\left(1 - e^{-\chi_4(\frac{1}{2}-P_4)t}\right)\right], \\ \qquad\qquad \chi_4(\frac{1}{2} - P_4) \neq (T - T_m), \\ \chi_1\left(\frac{1}{2} - P_1\right)\left[\alpha t + \frac{1-\alpha}{\chi_4(\frac{1}{2}-P_4)}\left(1 - e^{-\chi_4(\frac{1}{2}-P_4)t}\right)\right], \quad \chi_4(\frac{1}{2} - P_4) = (T - T_m), \end{cases} \tag{B.18}$$

$$\mathrm{C}^0_{\mathrm{Si}} = 2\chi_4 \left(\frac{1}{2} - P_4\right) \left(\alpha e^{-(T-T_m)t} + (1-\alpha)\right)^{\chi_{-2}} \int_{\tilde{t}=0}^{\tilde{t}=t} \frac{\mathrm{C}^0_{\mathrm{SiC}}(\tilde{t}, z)}{\left(\alpha e^{-(T-T_m)\tilde{t}} + (1-\alpha)\right)^{\chi_{-2}}} d\tilde{t}. \tag{B.19}$$

To find $\mathrm{C}^1_{\mathrm{C}}$, we note that

$$\frac{\partial \mathrm{C}^1_{\mathrm{C}}}{\partial t} = \frac{\partial \mathrm{C}^0_{\mathrm{SiO_2(l)}}}{\partial t} - 2r^0_1 - r^0_2 - r^0_{-2}, \tag{B.20}$$

which we can integrate to give

$$\begin{aligned} \mathrm{C}^1_{\mathrm{C}} =& \mathrm{C}^0_{\mathrm{SiO_2(l)}} - (T - T_m)\alpha - \chi_2 \left(\frac{1}{2} - P_2\right) t \\ &+ \int_{\tilde{t}=0}^{\tilde{t}=t} -2\mathrm{C}^0_{\mathrm{C}}(\tilde{t}, z) \left(\frac{1}{2} - P_1\right) + \chi_{-2}\mathrm{C}^0_{\mathrm{SiO_2(l)}}(\tilde{t}, z)\mathrm{C}^0_{\mathrm{Si}}(\tilde{t}, z) d\tilde{t}. \end{aligned} \tag{B.21}$$

The other $\mathcal{O}(\epsilon)$ terms are found to be

$$\begin{aligned} \mathrm{C}^1_{\mathrm{SiO_2(l)}} = \frac{1}{\mathrm{C}^0_{\mathrm{C}}} \Bigg(& \frac{\alpha(1-\alpha)(T-T_m)^2 e^{(T-T_m)t}}{\left(\alpha + (1-\alpha)e^{(T-T_m)t}\right)^2} + \chi_2 \left(\frac{1}{2} - P_2\right)^+ \\ & - \chi_{-2}\mathrm{C}^0_{\mathrm{SiO_2(l)}}\mathrm{C}^0_{\mathrm{Si}} - \mathrm{C}^0_{\mathrm{SiO_2(l)}}\mathrm{C}^1_{\mathrm{C}} \Bigg), \end{aligned} \tag{B.22}$$

$$\begin{aligned} U^1_g \mathrm{C}^1_g = 2 \int_{y=0}^{y=z} \Bigg[& \mathrm{C}^1_{\mathrm{SiO_2(l)}}(t, y)\mathrm{C}^0_{\mathrm{C}}(t, y) + \mathrm{C}^0_{\mathrm{SiO_2(l)}}(t, y)\mathrm{C}^1_{\mathrm{C}}(t, y) - \chi_2 \left(\frac{1}{2} - P_2\right)^+ \\ & + \chi_{-2}\mathrm{C}^0_{\mathrm{SiO_2(l)}}(t, y)\mathrm{C}^0_{\mathrm{Si}}(t, y) \Bigg] dy, \end{aligned} \tag{B.23}$$

$$P^1 = \frac{1}{U_g^0 \mathrm{C}_g^0} \int_{y=0}^{y=z} \Bigg[-\chi_1 \mathrm{C}_{\mathrm{C}}^0(t,y) \left(\frac{1}{2} - P_1(T(y))\right) - \chi_2 \left(\frac{1}{2} - P_2(T(y))\right)^+ + \chi_{-2} \mathrm{C}_{\mathrm{SiO_2(l)}}^0(t,y) \mathrm{C}_{\mathrm{Si}}^0(t,y) - \chi_4 \mathrm{C}_{\mathrm{SiC}}^0(t,y) \left(\frac{1}{2} - P_4(T(y))\right)^+ \Bigg] dy, \tag{B.24}$$

$$\mathrm{C}_{\mathrm{SiC}}^1 = \begin{cases} \chi_1 \int_{\tilde{t}=0}^{\tilde{t}=t} \mathrm{C}_{\mathrm{C}}^0(\tilde{t},z) P^1(\tilde{t},y) + \mathrm{C}_{\mathrm{C}}^1(\tilde{t},z) \left(\frac{1}{2} - P_1\right) d\tilde{t}, & P_4 \geq \frac{1}{2}, \\ e^{-\chi_4(\frac{1}{2}-P_4)t} \int_{\tilde{t}=0}^{\tilde{t}=t} e^{\chi_4(\frac{1}{2}-P_4)\tilde{t}} \big(\chi_1 \mathrm{C}_{\mathrm{C}}^0(\tilde{t},z) P^1(\tilde{t},y) + \chi_1 \mathrm{C}_{\mathrm{C}}^1(\tilde{t},z) \left(\frac{1}{2} - P_1\right) & \\ \qquad -\chi_4 \mathrm{C}_{\mathrm{SiC}}^0 P^1\big) d\tilde{t}, & P_4 < \frac{1}{2}, \end{cases} \tag{B.25}$$

$$\mathrm{C}_{\mathrm{Si}}^1 = \left(\alpha e^{-(T-T_m)t} + 1 - \alpha\right)^{\chi_{-2}} \int_{\tilde{t}=0}^{\tilde{t}=t} \Bigg[\left(\alpha e^{-(T-T_m)\tilde{t}} + 1 - \alpha\right)^{-\chi_{-2}} \Big(\chi_2 P^1(\tilde{t},z) \mathbf{1}_{\{P_2 \leq \frac{1}{2}\}} - \chi_{-2} \mathrm{C}_{\mathrm{SiO_2(l)}}^1(\tilde{t},z) \mathrm{C}_{\mathrm{Si}}^0(\tilde{t},z) + \chi_4 \mathrm{C}_{\mathrm{SiC}}^1(\tilde{t},z) \big(\frac{1}{2} - P_4\big)^+ + \chi_4 \mathrm{C}_{\mathrm{SiC}}^0(\tilde{t},z) P^1(\tilde{t},z) \mathbf{1}_{\{P_4 \leq \frac{1}{2}\}} \Big) \Bigg] d\tilde{t}. \tag{B.26}$$

B.3 Prescribed temperature - Region Ia

On the early timescale $\hat{t} = t/\epsilon$, we find

$$\mathrm{C}_{\mathrm{C}} = 1 + \mathcal{O}(\epsilon^2), \tag{B.27}$$

$$\mathrm{C}_{\mathrm{SiC}} = \epsilon \chi_1 \left(\frac{1}{2} - P_1\right) \hat{t} + \mathcal{O}(\epsilon^2), \tag{B.28}$$

$$\mathrm{C}_{\mathrm{SiO_2(s)}} = \alpha, \tag{B.29}$$

$$\mathrm{C}_{\mathrm{SiO_2(l)}} = \epsilon \chi_2 \left(\frac{1}{2} - P_2\right) \left(1 - e^{-\hat{t}}\right) + \mathcal{O}(\epsilon^2), \tag{B.30}$$

$$\mathrm{C}_{\mathrm{Si}} = \epsilon \chi_2 \left(\frac{1}{2} - P_2\right) \hat{t} + \mathcal{O}(\epsilon^2), \tag{B.31}$$

$$U_g \mathrm{C}_g = U_{g,IIa}^0 \mathrm{C}_{g,IIa}^0(\hat{t}, z_m) + \epsilon \left(2 \int_{y=z_m}^{y=z} r_{5,Ia}^1(\hat{t},y) - r_{2,Ia}^0(\hat{t},y) dy + U_{g,IIa}^1 \mathrm{C}_{g,IIa}^1(\hat{t}, z_m) \right) + \mathcal{O}(\epsilon^2), \tag{B.32}$$

$$P = \frac{1}{2} - \epsilon \left(\frac{\int_{y=z_m}^{y=z} r_{1,Ia}^0(\hat{t},y) + r_{2,Ia}^0(\hat{t},y) dy}{U_{g,IIa}^1 \mathrm{C}_{g,IIa}^1(t, z_m)} - P_{IIa}^1(\hat{t}, z_m) \right) + \mathcal{O}(\epsilon^2), \tag{B.33}$$

where the functions $U^0_{g,IIa}\mathrm{C}^0_{g,IIa}$ and $U^1_{g,IIa}\mathrm{C}^1_{g,IIa}$ are the $\mathcal{O}(1)$ and $\mathcal{O}(\epsilon)$ terms in (B.6), P^1_{IIa} is the $\mathcal{O}(\epsilon)$ term in (B.7), and the reaction rates are given by

$$r^0_{1,Ia}(\hat{t},z)=\chi_1\left(\frac{1}{2}-P_1\right),\;\; r^0_{2,Ia}=\chi_2\left(\frac{1}{2}-P_2\right),\;\; r^1_{5,Ia}=\chi_2\left(\frac{1}{2}-P_2\right)\left(1-e^{-\hat{t}}\right). \tag{B.34}$$

B.4 Prescribed temperature - Region Ib

In this region, we have solutions

$$\mathrm{C_C}=1-\epsilon\left(2\chi_1\left(\frac{1}{2}-P_1\right)+\chi_2\left(\frac{1}{2}-P_2\right)\right)t+\mathcal{O}(\epsilon^2), \tag{B.35}$$

$$\mathrm{C_{SiO_{2(s)}}}=\alpha, \tag{B.36}$$

$$\mathrm{C_{SiO_{2(l)}}}=\epsilon\chi_2\left(\frac{1}{2}-P_2\right)+\mathcal{O}(\epsilon^2), \tag{B.37}$$

$$U_g\mathrm{C}_g=U^0_{g,IIb}\mathrm{C}^0_{g,IIb}(t,z_m)+\epsilon U^1_{g,IIb}\mathrm{C}^1_{g,IIb}(t,z_m)+\mathcal{O}(\epsilon^2), \tag{B.38}$$

where $U^0_{g,IIb}\mathrm{C}^0_{g,IIb}$ and $U^1_{g,IIb}\mathrm{C}^1_{g,IIb}$ are the functions in Region IIb, given in (B.14) and (B.23), respectively. We also have

$$P=\frac{1}{2}+\epsilon\left(P^1_{IIa}(t,z_m)-\frac{\int_{y=z_m}^{y=z}\chi_1\left(\frac{1}{2}-P_1(T(y))\right)+\chi_2\left(\frac{1}{2}-P_2(T(y))\right)dy}{U^0_{g,IIb}\mathrm{C}^0_{g,IIb}(t,z_m)}\right)+\mathcal{O}(\epsilon^2), \tag{B.39}$$

$$\begin{aligned}\mathrm{C_{SiC}}=&\chi_1\left(\frac{1}{2}-P_1\right)t+\epsilon\Bigg(\chi_1\int_{\tilde{t}=0}^{\tilde{t}=t}P^1(\tilde{t},z)d\tilde{t}\\&-\left(\chi_1^2\left(\frac{1}{2}-P_1\right)^2+\frac{\chi_1\chi_2}{2}\left(\frac{1}{2}-P_1\right)\left(\frac{1}{2}-P_2\right)\right)t^2\Bigg)+\mathcal{O}(\epsilon^2),\end{aligned} \tag{B.40}$$

where P^1 is the $\mathcal{O}(\epsilon)$ term in (B.39). We also have

$$\mathrm{C_{Si}}=\chi_2\left(\frac{1}{2}-P_2\right)t+\epsilon\left(\int_{\tilde{t}=0}^{\tilde{t}=t}\chi_2P^1(\tilde{t},z)d\tilde{t}-\frac{\chi_{-2}\chi_2^2}{2}\left(\frac{1}{2}-P_2\right)^2t^2\right)+\mathcal{O}(\epsilon^2). \tag{B.41}$$

B.5 Simplified model asymptotics - small diffusion limit

Expanding variables in terms of K, we have in Region A

$$T^A(z,t)=-1+\omega F(z)t+\omega\sum_{n=1}^{\infty}K^nF^{(2n)}(z)\frac{t^{n+1}}{(n+1)!},\;\; C^A(z,t)=0, \tag{B.42}$$

and that the position of the interface is given by

$$\begin{aligned} s(t) =& F^{-1}\left(\frac{1}{\omega t}\right) - \frac{K}{2}\frac{F''(s_0(t))}{F'(s_0(t))}t \\ &+ K^2\left(\frac{F''(s_0(t))F'''(s_0(t))}{4(F'(s_0(t)))^2} - \frac{F^{IV}(s_0(t))}{6F'(s_0(t))} - \frac{(F''(s_0(t)))^3}{8(F'(s_0(t)))^3}\right)t^2 + \mathcal{O}(K^3). \end{aligned} \tag{B.43}$$

In Region B, we have the leading order terms

$$C_0^B(z,t) = \frac{\exp\left(-\frac{2+b}{2\omega F(z)} + (b+1)\,t - \frac{b\omega F(z)}{2}t^2\right)}{1 + \sqrt{\frac{\pi}{2b\omega F(z)}}\exp\left(\frac{1}{2b\omega F(z)}\right)\left[\operatorname{erf}\left(\frac{1}{\sqrt{2b\omega F(z)}}\right) + \operatorname{erf}\left(\frac{b\omega F(z)t-b-1}{\sqrt{2b\omega F(z)}}\right)\right]}, \tag{B.44}$$

$$T_0^B = \frac{1}{b}(C_0^B - 1) - 1 + \omega F(z)t. \tag{B.45}$$

The first order terms satisfy equations

$$b\frac{\partial T_1^B}{\partial t} - \frac{\partial C_1^B}{\partial t} = b\frac{\partial^2 T_0^B}{\partial z^2}, \quad \frac{\partial C_1}{\partial t} = -b(C_0^B T_1^B + C_1^B T_0^B), \tag{B.46}$$

with initial conditions

$$T_1^B + s_1(t)\frac{\partial T_0^B}{\partial z} = 0, \quad C_1^B + s_1(t)\frac{\partial C_0^B}{\partial z} = 0, \quad \text{on } t = \frac{1}{\omega F(z)}. \tag{B.47}$$

We can integrate the first equation in (B.46) to obtain

$$T_1^B = \frac{1}{b}C_1^B + \frac{F''(z)}{2\omega F(z)^2} + \int_{\tilde{t}=1/\omega F(z)}^{\tilde{t}=t} \frac{\partial^2 T_0^B}{\partial z^2}(z,\tilde{t})d\tilde{t}, \tag{B.48}$$

where the spatial function $F''(z)/\left(2\omega F(z)^2\right)$ has been determined using (B.47), (3.77), and (3.71), with $s_0(t) = z$ and $t = 1/\left(\omega F(z)\right)$. Equation (B.48) can be substituted into the second equation in (B.46), to find

$$\begin{aligned} C_1^B(z,t) =& \frac{1}{I(z,t)}\int_{\tilde{t}=1/\omega F(z)}^{\tilde{t}=t} I(z,\tilde{t})\Bigg[-\frac{bC_0^B(z,\tilde{t})F''(z)}{2\omega F(z)^2} \\ &- bC_0^B(z,\tilde{t})\int_{u=1/\omega F(z)}^{u=\tilde{t}} \frac{\partial^2 T_0^B}{\partial z^2}(z,u)du\Bigg]d\tilde{t} \\ &+ \frac{I(z,(\omega F(z))^{-1})}{I(z,t)}\frac{F''(z)}{2\omega F'(z)F(z)}\left.\frac{\partial C_0^B}{\partial z}\right|_{t=(\omega F(z))^{-1}}, \end{aligned} \tag{B.49}$$

where the integrating factor I is given by

$$I(z,t) = \exp\left(\int^{\tilde{t}=t} bT_0^B(z,\tilde{t}) + C_0^B(z,\tilde{t})d\tilde{t}\right). \tag{B.50}$$

The solution in (B.49) can then be substituted into (B.48), in order to determine T_1^B.

Bibliography

[1] J. T. Abrahamson and M. S. Strano. Analytical solution to coupled chemical reaction and thermally diffusing systems: applicability to self-propagating thermopower waves. *The Journal of Physical Chemistry Letters*, 1(24):3514–3519, 2010.

[2] B. Andresen. *Process model for carbothermic production of silicon metal.* PhD thesis, The Norwegian Institute of Technology, Trondheim, 1995.

[3] E. S. Antoniou, J. K. Bechtold, and M. Matalon. A diffusional-thermal theory of near-stoichiometric premixed flames. *SIAM Journal on Applied Mathematics*, 64(4):1434–1456, 2004.

[4] H. Arunachalam, S. Onori, and I. Battiato. On veracity of macroscopic lithium-ion battery models. *Journal of The Electrochemical Society*, 162(10):A1940–A1951, 2015.

[5] G. P. Benham, K. Hildal, C. P. Please, and R. A. Van Gorder. Penetration of molten silicon into a bed of fines. *International Communications in Heat and Mass Transfer*, 75:323–327, 2016.

[6] G. P. Benham, K. Hildal, C. P. Please, and R. A. Van Gorder. Solidification of silicon in a one-dimensional slab and a two-dimensional wedge. *International Journal of Heat and Mass Transfer*, 98:530–540, 2016.

[7] A. Bensoussan, J.-L. Lions, and G. Papanicolaou. *Asymptotic analysis for periodic structures*, volume 374. American Mathematical Soc., 2011.

[8] T. Bergstrøm, S. Cowley, A. C. Fowler, and P. E. Seward. Segregation of carbon paste in a smelting electrode. *IMA Journal of Applied Mathematics*, 43(1):83–99, 1989.

[9] S. K. Bhatia and D. D. Perlmutter. A random pore model for fluid-solid reactions: I. Isothermal, kinetic control. *AIChE Journal*, 26(3):379–386, 1980.

[10] S. K. Bhatia and D. D. Perlmutter. A random pore model for fluid-solid reactions: II. Diffusion and transport effects. *AIChE Journal*, 27(2):247–254, 1981.

[11] H. C. Brinkman. The viscosity of concentrated suspensions and solutions. *The Journal of Chemical Physics*, 20(4):571–571, 1952.

[12] F. Brosa Planella, C. P. Please, and R. A. Van Gorder. Instability in the self-similar motion of a planar solidification front. *IMA Journal of Applied Mathematics*, 83(1):106–130, 2017.

[13] M. Bruna and S. J. Chapman. Diffusion in spatially varying porous media. *SIAM Journal on Applied Mathematics*, 75(4):1648–1674, 2015.

[14] H. M. Byrne and J. Norbury. Stable solutions for a catalytic converter. *SIAM Journal on Applied Mathematics*, 54(3):789–813, 1994.

[15] M. Ceseri and J. M. Stockie. A three-phase free boundary problem with melting ice and dissolving gas. *European Journal of Applied Mathematics*, 25(4):449–480, 2014.

[16] A. C. D. Chaklader and A. L. Roberts. Transformation of quartz to cristobalite. *Journal of the American Ceramic Society*, 44(1):35–41, 1961.

[17] C. Chang and R. L. Powell. Effect of particle size distributions on the rheology of concentrated bimodal suspensions. *Journal of Rheology*, 38(1):85–98, 1994.

[18] J. S. Chong, E. B. Christiansen, and A. D. Baer. Rheology of concentrated suspensions. *Journal of Applied Polymer Science*, 15(8):2007–2021, 1971.

[19] J. Crank. *Free and moving boundary problems*. Oxford University Press, 1987.

[20] E. L. Cussler. *Diffusion*. Cambridge University Press, 1997.

[21] M. P. Dalwadi, M. Bruna, and I. M. Griffiths. A multiscale method to calculate filter blockage. *Journal of Fluid Mechanics*, 809:264–289, 2016.

[22] M. P. Dalwadi, I. M. Griffiths, and M. Bruna. Understanding how porosity gradients can make a better filter using homogenization theory. *Proceedings of the Royal Society A*, 471(2182):20150464, 2015.

[23] S. Dargaville and T. W. Farrell. Predicting active material utilization in LiFePO4 electrodes using a multiscale mathematical model. *Journal of the Electrochemical Society*, 157(7):A830–A840, 2010.

[24] S. Dargaville and T. W. Farrell. A comparison of mathematical models for phase-change in high-rate LiFePO4 cathodes. *Electrochimica Acta*, 111:474–490, 2013.

[25] J. Dowden, M. Davis, and P. Kapadia. Some aspects of the fluid dynamics of laser welding. *Journal of Fluid Mechanics*, 126:123–146, 1983.

[26] C. Dumay and A. W. Cramb. Density and interfacial tension of liquid Fe-Si alloys. *Metallurgical and Materials Transactions B*, 26(1):173–176, 1995.

[27] Verlag Stahleisen GmbH (editor). *Slag Atlas 2nd ed.* Dusseldorf, Germany, 1995.

[28] Entegris. Properties and characteristics of graphite. `https://www.entegris.com/resources/assets/6205-7329-0513.pdf`, May 2013. Accessed: 25 August 2016.

[29] N. T. Fadai, C. P. Please, and R. A. Van Gorder. Asymptotic analysis of a multiphase drying model motivated by coffee bean roasting. *SIAM Journal on Applied Mathematics*, 78:418–436, 2018.

[30] A. D. Fitt and P. D. Howell. The manufacture of continuous smelting electrodes from carbon-paste briquettes. *Journal of Engineering Mathematics*, 33(4):353–376, 1998.

[31] N. D. Fowkes and A. P. Bassom. Batch processing in a glass furnace. *The ANZIAM Journal*, 57(02):175–188, 2015.

[32] D. R. Gaskell. *Introduction to metallurgical thermodynamics*. Hemisphere Publishing Corporation New York, NY, 1981.

[33] R. Gaur, L. Mishra, and S. K. Sen Gupta. Diffusion and transport of molecules in living cells. In *Modelling and Simulation of Diffusive Processes*, pages 27–49. Springer, 2014.

[34] G. R. Gavalas. Analysis of char combustion including the effect of pore enlargement. *Combustion Science and Technology*, 24(5-6):197–210, 1980.

[35] P. K. Gbor and C. Q. Jia. Critical evaluation of coupling particle size distribution with the shrinking core model. *Chemical Engineering Science*, 59(10):1979–1987, 2004.

[36] A. N. Gorban, H. P. Sargsyan, and H. A. Wahab. Quasichemical models of multicomponent nonlinear diffusion. *Mathematical Modelling of Natural Phenomena*, 6(5):184–262, 2011.

[37] R. W. Griffiths. The dynamics of lava flows. *Annual Review of Fluid Mechanics*, 32(1):477–518, 2000.

[38] V. V. Gubernov, J. J. Sharples, H. S. Sidhu, A. C. McIntosh, and J. Brindley. Properties of combustion waves in the model with competitive exo-and endothermic reactions. *Journal of Mathematical Chemistry*, 50(8):2130–2140, 2012.

[39] S. A. Halvorsen, A. Schei, and J. H. Downing. A unidimensional dynamic model for the (ferro)silicon process. In *Electric Furnace Conference Proceedings*, volume 50, pages 45–59, 1992.

[40] T. Hannesson. *The Si Process Drawings*. Elkem Iceland, May 2016.

[41] A. M. Hassanein, G. L. Kulcinski, and W. G. Wolfer. Surface melting and evaporation during disruptions in magnetic fusion reactors. *Nuclear Engineering and Design. Fusion*, 1(3):307–324, 1984.

[42] W. M. Hayne. CRC Handbook of Chemistry and Physics, 92 edn, 2011.

[43] S. Homma, S. Ogata, J. Koga, and S. Matsumoto. Gas–solid reaction model for a shrinking spherical particle with unreacted shrinking core. *Chemical Engineering Science*, 60(18):4971–4980, 2005.

[44] H. E. Huppert. Phase changes following the initiation of a hot turbulent flow over a cold solid surface. *Journal of Fluid Mechanics*, 198:293–319, 1989.

[45] M. Kadkhodabeigi. *Modeling of Tapping Processes in Submerged Arc Furnaces*. PhD thesis, The Norwegian University of Science and Technology, Trondheim, 2011.

[46] M. Kadkhodabeigi, H. Tveit, and K. H. Berget. Silicon process-new hood design for tapping gas collection. In *Twelfth International Ferroalloys Congress*, pages 109–119, 2010.

[47] M. Kadkhodabeigi, H. Tveit, and S. T. Johansen. CFD modelling of the effect of furnace crater pressure on the melt and gas flows in the submerged arc furnaces used for silicon production. *Progress in Computational Fluid Dynamics, an International Journal*, 10(5-6):374–383, 2010.

[48] M. Kadkhodabeigi, H. Tveit, and S. T. Johansen. Modelling the tapping process in submerged arc furnaces used in high silicon alloys production. *ISIJ International*, 51(2):193–202, 2011.

[49] N. E. Kamfjord. *Mass and Energy Balances of the Silicon Process*. PhD thesis, The Norwegian University of Science and Technology, Trondheim, 2012.

[50] J. R. King and D. S. Riley. Asymptotic solutions to the stefan problem with a constant heat source at the moving boundary. *Proceedings of the Royal Society of London A: Mathematical, Physical and Engineering Sciences*, 456(1997):1163–1174, 2000.

[51] A. V. Kostanovskiy, M. E. Kostanovskaja, and M. G. Zeodinov. Thermal conductivity of graphite at high temperatures. In *Seventeenth European Conference on Thermophysical Properties, Bratislava, Slovak Republic*, 2005.

[52] I. M. Krieger and T. J. Dougherty. A mechanism for non-newtonian flow in suspensions of rigid spheres. *Transactions of the Society of Rheology*, 3(1):137–152, 1959.

[53] F. Li. *SiC Production using SiO_2 and C agglomerates*. PhD thesis, The Norwegian University of Science and Technology, Trondheim, 2017.

[54] D. R. Lide. CRC Handbook of Chemistry and Physics, 84 edn, 2004. *Section*, 4:4–1.

[55] D. R. Lide. CRC Handbook of Chemistry and Physics, 86 edn, 2005. *Section*, 4:4–1.

[56] J. R. Lister and P. J. Dellar. Solidification of pressure-driven flow in a finite rigid channel with application to volcanic eruptions. *Journal of Fluid Mechanics*, 323:267–283, 1996.

[57] B. F. Lund. *Rigorous simulation models for improved process operation*. PhD thesis, The Norwegian University of Science and Technology, Trondheim, 2005.

[58] H. M. Mader, E. W. Llewellin, and S. P. Mueller. The rheology of two-phase magmas: a review and analysis. *Journal of Volcanology and Geothermal Research*, 257:135–158, 2013.

[59] B. P. Marchant and J. Norbury. Discontinuous travelling wave solutions for certain hyperbolic systems. *IMA Journal of Applied Mathematics*, 67(2):201–224, 2002.

[60] T. Melchiori and P. Canu. Improving the quantitative description of reacting porous solids: critical analysis of the shrinking core model by comparison to the generalized grain model. *Industrial & Engineering Chemistry Research*, 53(22):8980–8995, 2013.

[61] T. Melchiori, F. Gallucci, M. van Sint Annaland, and P. Canu. Reacting porous solids with phase segregation. *Chemical Engineering Science*, 132:200–214, 2015.

[62] S. Mueller, E. W. Llewellin, and H. M. Mader. The rheology of suspensions of solid particles. *Proceedings of the Royal Society of London A: Mathematical, Physical and Engineering Sciences*, page 20090445, 2009.

[63] E. H. Myrhaug. *Non-fossil reduction in the silicon process - properties and behaviour*. PhD thesis, The Norwegian University of Science and Technology, Trondheim, 2003.

[64] E. H. Myrhaug, J. Tuset, and H. Tveit. Reaction mechanisms of charcoal and coke in the silicon process. In *Proceedings: Tenth International Ferroalloys Congress*, volume 1, pages 108–121, 2004.

[65] J. Norbury and A. M. Stuart. A model for porous-medium combustion. *Quarterly Journal of Mechanics and Applied Mathematics*, 42(1):159–178, 1989.

[66] H. Ockendon and J. R. Ockendon. Variable-viscosity flows in heated and cooled channels. *Journal of Fluid Mechanics*, 83(1):177–190, 1977.

[67] J. Ockendon, S. Howison, A. Lacey, and A. Movchan. *Applied Partial Differential Equations*. Oxford University Press, 2003.

[68] E. Ott. *Solidification of two Ferroalloys, FeSi 75wt% Si and MC-FeMn; Formation of Microstructure and Cracks*. PhD thesis, The Norwegian University of Science and Technology, Trondheim, 2003.

[69] HSC Outokumpu. HSC Chemistry® for Windows, 4.0, 1999.

[70] J. Y. Park and O. Levenspiel. The crackling core model for the reaction of solid particles. *Chemical Engineering Science*, 30(10):1207–1214, 1975.

[71] P. Patnaik. Handbook of inorganic chemical compounds. *McGraw-Hill Professional*, page 1086, 2002.

[72] G. Pavliotis and A. Stuart. *Multiscale methods: averaging and homogenization*. Springer Science & Business Media, 2008.

[73] J. R. A. Pearson. Variable-viscosity flows in channels with high heat generation. *Journal of Fluid Mechanics*, 83(1):191–206, 1977.

[74] C. P. Please, P. S. Hagan, and D. W. Schwendeman. Light-off behavior of catalytic converters. *SIAM Journal on Applied Mathematics*, 54(1):72–92, 1994.

[75] C. P. Please, F. Liu, and D. L. S. McElwain. Condensed phase combustion travelling waves with sequential exothermic or endothermic reactions. *Combustion Theory and Modelling*, 7(1):129–143, 2003.

[76] N. Provatas and K. Elder. *Phase-field methods in materials science and engineering*. John Wiley & Sons, 2011.

[77] E. Ringdalen. Changes in quartz during heating and the possible effects on si production. *The Journal of The Minerals, Metals and Materials Society (TMS)*, 67(2):484–492, 2015.

[78] L. Roberts, E. Nordgård-Hansen, Ø. Mikkelsen, S. A. Halvorsen, and R. A. Van Gorder. A heat and mass transfer study of carbon paste baking. *International Communications in Heat and Mass Transfer*, 88:9–19, 2017.

[79] R. Roscoe. The viscosity of suspensions of rigid spheres. *British Journal of Applied Physics*, 3(8):267, 1952.

[80] A. Schei and S. A. Halvorsen. A stoichiometric model of the silicon process. In *Proceedings from Ketil Motzfeldt Symposium, The Norwegian Institue of Technology, Trondheim, Norway*, pages 41–56, 1991.

[81] A. Schei and K. Larsen. A stoichiometric model of the ferrosilicon process. In *Electric Furnace Conference Proceedings*, volume 39, pages 301–309, 1981.

[82] A. Schei, J. Kr. Tuset, and H. Tveit. *Production of high silicon alloys*. Tapir, Trondheim, Norway, 1998.

[83] L. A. Segel and M. Slemrod. The quasi-steady-state assumption: a case study in perturbation. *SIAM Review*, 31(3):446–477, 1989.

[84] J. J. Sharples, H. S. Sidhu, A. C. McIntosh, J. Brindley, and V. V. Gubernov. Analysis of combustion waves arising in the presence of a competitive endothermic reaction. *IMA Journal of Applied Mathematics*, 77(1):18–31, 2012.

[85] B. M. Sloman, C. P. Please, and R. A. Van Gorder. Homogenisation of a shrinking core model for gas-solid reactions in granular particles. *Submitted on 4/12/2017.*

[86] B. M. Sloman, C. P. Please, and R. A. Van Gorder. Asymptotic analysis of a silicon furnace model. *SIAM Journal on Applied Mathematics*, 78(2):1174–1205, 2018.

[87] B. M. Sloman, C. P. Please, R. A. Van Gorder, A. M. Valderhaug, R. G. Birkeland, and H. Wegge. A heat and mass transfer model of a silicon pilot furnace. *Metallurgical and Materials Transactions B*, 48(5):2664–2676, 2017.

[88] R. B. Smith and M. Z. Bazant. Multiphase porous electrode theory. *Journal of The Electrochemical Society*, 164(11):E3291–E3310, 2017.

[89] H. Y. Sohn. The law of additive reaction times in fluid-solid reactions. *Metallurgical and Materials Transactions B*, 9(1):89–96, 1978.

[90] H. Y. Sohn. Chemical reaction engineering in the chemical processing of metals and inorganic materials part I. advances in fluid-solid reaction analysis. *Korean Journal of Chemical Engineering*, 20(2):185–199, 2003.

[91] H. Y. Sohn and J. Szekely. A structural model for gas-solid reactions with a moving boundary-III: A general dimensionless representation of the irreversible reaction between a porous solid and a reactant gas. *Chemical Engineering Science*, 27(4):763–778, 1972.

[92] V. Srinivasan and J. Newman. Discharge model for the lithium iron-phosphate electrode. *Journal of the Electrochemical Society*, 151(10):A1517–A1529, 2004.

[93] J. J. Stickel and R. L. Powell. Fluid mechanics and rheology of dense suspensions. *Annual Review of Fluid Mechanics*, 37:129–149, 2005.

[94] Y. M. Stokes, E. O. Tuck, and L. W. Schwartz. Extensional fall of a very viscous fluid drop. *The Quarterly Journal of Mechanics and Applied Mathematics*, 53(4):565–582, 2000.

[95] J. Szekely and J. W. Evans. A structural model for gas-solid reactions with a moving boundary. *Chemical Engineering Science*, 25(6):1091–1107, 1970.

[96] J. Szekely and J. W. Evans. A structural model for gas-solid reactions with a moving boundary-II: The effect of grain size, porosity and temperature on the reaction of porous pellets. *Chemical Engineering Science*, 26(11):1901–1913, 1971.

[97] J. Szekely, J. W. Evans, and H. Y. Sohn. *Gas–solid reactions*. Academic Press, New York, 1976.

[98] M. Takla, N. E. Kamfjord, H. Tveit, and S. Kjelstrup. Energy and exergy analysis of the silicon production process. *Energy*, 58:138–146, 2013.

[99] K. Tang and M. Tangstad. Modeling viscosities of ferromanganese slags. In *INFACON XI: Innovations in the Ferro Alloy Industry*, volume 53, pages 344–357, 2007.

[100] M. Tangstad, M. Ksiazek, V. Andersen, and E. Ringdalen. Small scale laboratory experiments simulating an industrial silicon furnace. In *Twelfth International Ferroalloys Congress*, pages 661–669, 2010.

[101] The Engineering ToolBox. Densities of solids. `http://www.engineeringtoolbox.com/density-solids-d_1265.html`, 2007. Accessed: 25 August 2016.

[102] E. O. Tuck, Y. M. Stokes, and L. W. Schwartz. Slow slumping of a very viscous liquid bridge. *Journal of Engineering Mathematics*, 32(1):27–40, 1997.

[103] A. M. Valderhaug. *Modelling and control of submerged-arc ferrosilicon furnaces*. PhD thesis, The Norwegian Institute of Technology, Trondheim, 1992.

[104] A. M. Valderhaug and P. Sletfjerding. A non-interacting electrode current controller for submerged-arc furnaces. In *Electric Furnace Conference Proceedings.*, volume 49, pages 311–320, 1991.

[105] H. Van Wijngaarden, J. F. Dijksman, and P. Wesseling. Non-isothermal flow of a molten polymer in a narrow rectangular cavity. *Journal of Non-Newtonian Fluid Mechanics*, 11(1-2):175–199, 1982.

[106] S. O. Wasbø and A. Hammervold. SiMod - a Silicon Furnace Process Model. Personal Communication, 2014.

[107] W. Wee, H. Sidhu, J. Sharples, I. Towers, and V. Gubernov. Properties of reaction fronts in a non-adiabatic two stage exothermic-endothermic competitive reaction scheme. *ANZIAM Journal*, 54:646–663, 2013.

[108] C. Y. Wen. Noncatalytic heterogeneous solid-fluid reaction models. *Industrial & Engineering Chemistry*, 60(9):34–54, 1968.

[109] K. Wiik. *Kinetics of reaction between silica and carbon.* PhD thesis, The Norwegian Institute of Technology, Trondheim, 1990.

[110] J. J. Wylie and J. R. Lister. The effects of temperature-dependent viscosity on flow in a cooled channel with application to basaltic fissure eruptions. *Journal of Fluid Mechanics*, 305:239–261, 1995.

[111] Z. Xu, X. Sun, and M. A. Khaleel. A generalized kinetic model for heterogeneous gas-solid reactions. *The Journal of Chemical Physics*, 137(7):074702, 2012.

[112] S. Yagi and D. Kunii. Studies on combustion of carbon particles in flames and fluidized beds. In *Symposium (international) on Combustion*, volume 5, pages 231–244. Elsevier, 1955.